The Cosmological Evolution of Galaxies

Ian Waddington

Doctor of Philosophy
University of Edinburgh
1999

Abstract

The results of an extensive optical and infrared investigation of a complete sub-sample of the Leiden-Berkeley Deep Survey of radio sources at 1.4 GHz are presented. Optical counterparts have been identified for 69 of the 73 sources in the two Hercules fields, and redshifts obtained for 49 of them. Photometric redshifts are computed from the $griK$ data for the remaining 20 sources.

Redshifts have been measured for fifteen sources in the brighter Parkes Selected Regions radio survey, in order to test the accuracy of redshift estimates based on the K–z relation for brighter radio sources. The results enhance the evidence for a high-redshift cut-off in the 2.7 GHz radio luminosity function.

The data from the LBDS Hercules sample is compared with the radio luminosity functions (RLFs) of Dunlop and Peacock (1990). Two of the RLF models successfully trace the evolution of the radio sources with redshift, but there is some disagreement between the luminosity-dependence of the models and the data. The observed RLF for the lower luminosity population ($\log_{10} P_{2.7} < 26$) shows evidence for a cut-off at lower redshifts ($z \sim 0.5$–1.5) than for the more powerful objects in the Parkes Selected Regions survey.

The spectral evolution of these radio sources is investigated, with particular emphasis on modelling the red envelope of galaxies. Together with a sample of passively-evolving galaxies believed to be at $z \simeq 2.4$, these data are used to show that the oldest galaxies at high-redshift are incompatable with a critical-density ($\Omega_0 = 1$) universe, unless there is a significant cosmological constant.

Declaration

I declare that this thesis has been composed by myself and that it reports my own original work, except where explicitly stated otherwise.

Acknowledgments

I wish to thank my supervisors James Dunlop and John Peacock for their teaching and guidance throughout the course of my postgraduate studies. I also thank Rogier Windhorst for the assistance he has given me with the Leiden-Berkeley Deep Survey, and for the additional motivation to complete this work (a job!).

The observations that contribute to this thesis have been provided by many people, to whom I am very grateful: James Dunlop, John Peacock, Rogier Windhorst, David Koo, Marc Oort, Scott Anderson, Steve Rawlings and Marek Kukula. I thank Raul Jimenez for providing access to his new spectral synthesis models for my use, prior to publication. Keck Telescope spectra (§5.4) were provided by Hyron Spinrad, Arjun Dey and Dan Stern to whom I give my thanks. Thanks also to Tom Keck for performing the bias-subtraction and flat-fielding stages for parts of the Four-Shooter data (§2.2), as part of an undergraduate project. The assistance of the support astronomers and the night assistants at the telescopes is also acknowledged.

Financial support for this thesis has been provided by: a research studentship from the U.K. Particle Physics and Astronomy Research Council (PPARC), my wife and my parents.

The *Anglo-Australian Telescope* is operated by the Anglo-Australian Observatory on behalf of the PPARC and the Australian government. The *Hale Telescope* at Palomar Observatory is owned and operated by the California Institute of Technology. The *United Kingdom Infrared Telescope* is operated by the Joint Astronomy Centre on behalf of the PPARC. The *William Herschel Telescope* is operated on the island of La Palma by the Isaac Newton Group in the Spanish Observatorio del Roque de los Muchachos of the Instituto de Astrofisica de Canarias.

And finally, special thanks to my wife, Alison, for her endless support and patience during the time I have spent working on this thesis, particularly during the frantic final stages.

When I consider your heavens, the work of your fingers, the moon and the stars, which you have set in place, what is man that you are mindful of him, the son of man that you care for him?

Psalm 8 : 3–4

The science of cosmology, which is based on testable, quantitative predictions, is now at the intriguing point where we can start to discuss, in some detail, what appear to be the physical processes following the birth of our Universe.

E. S. Cheng (1992)

Contents

3 Spectroscopy in the PSR and LBDS samples 105

4 Evolution of the radio luminosity function 137

Chapter 1

An introduction to galaxy evolution

The basic observations and models underlying modern cosmology are briefly reviewed. The theory of galaxy formation in a cold dark matter universe is described before turning to observational studies of galaxy evolution. The use of radio galaxies as a probe of cosmological evolution is surveyed. Evolutionary synthesis models of galaxies are discussed. Their use in determining the ages of galaxies, and thus placing limits on the age of the universe and the epoch of galaxy formation, is examined.

1.1 Basic cosmology

The purpose of this thesis is to investigate the cosmological evolution of galaxies from two complementary perspectives. The first is to follow the evolution of the radio source population at 1.4 GHz, with particular emphasis on the high-redshift behaviour of the radio luminosity function (RLF) and the possible existence of a redshift cut-off in the RLF. Secondly, the spectral evolution of these sources will be investigated. Together with a possible group of passively-evolving galaxies at $z \simeq 2.4$, these radio sources enable the red envelope of galaxies to be traced from $z = 0$ to $z \simeq 3$, placing constraints on the epoch of galaxy formation and the age of the universe.

This first chapter will present the background to the thesis and some of the analysis techniques that will be used later. The evidence for an expanding isotropic universe will be summarised and the cosmological model that results will be discussed (§1.1). In section 1.2, the theories underlying the modern picture of galaxy formation and evolution will be presented and compared with the observations. The use of radio galaxies to probe the high-redshift universe will be introduced (§1.3), and the methods of spectral synthesis of evolving stellar populations will be summarised in section 1.4. Finally, an outline of the thesis is given in §1.5.

1.1.1 The expanding isotropic universe

Modern cosmology probably began with the discovery that the galaxies we observe around us are, in general, receding from our own Galaxy (Slipher 1917) and furthermore that the more distant a galaxy is, the faster it is receding (Hubble 1929). Hubble discovered that the universe is expanding in such a way that the recessional velocity of a galaxy v is proportional to its distance d

$$v = \mathrm{H}_0 d \qquad [1.1]$$

where the constant of proportionality H_0 is known as Hubble's constant. At large distances this equation must be modified to take into account relativistic effects but it remains one of the most fundamental discoveries in cosmology.

There has been much work since 1929 to test equation [1.1] and to determine H_0. The velocity of a galaxy is measured from the redshift z of its spectrum, where $v = cz$ for small v. The distance is measured from the inverse square law for galaxy apparent magnitudes, and thus one must know the absolute magnitude of a galaxy in order to determine d. Herein lies the difficulty in measuring the Hubble constant, as galaxies have a considerable spread in absolute magnitudes (intrinsic luminosities) and a method of determining the intrinsic luminosity of a galaxy, independently of the redshift, is required.

The first approach is to identify a class of galaxies whose luminosities have a nearly standard value. Humason et al. (1956) observed a sample of galaxies that extended to twenty-times the distance of Hubble's original paper and discovered that if they used only the brightest members of clusters of galaxies then the data followed equation [1.1] with very little scatter. This method was successfully used by Sandage (1968; 1988) out to $z \approx 0.5$. At higher redshifts ($z < 1.8$), Lilly and Longair (1984) showed that powerful radio galaxies also followed Hubble's law, using the infrared K magnitudes as a distance indicator (§1.3).

The second approach to determining a galaxy's absolute magnitude is to use variants of the Faber and Jackson (1976) and Tully and Fisher (1977) relations between the intrinsic luminosity and internal velocity of elliptical and spiral galaxies respectively. The results from such studies (e.g. Mould et al. 1991; Peebles 1988) once again show the linear nature of equation [1.1] to be correct, but the uncertainty in the absolute calibrations produce large errors in the value of H_0.

All these methods rely on using the global properties of a galaxy to determine its luminosity and thus distance. A different approach to measuring d has been to calculate the distance to individual stars in a galaxy, using either Cepheid variable stars or supernovae. Leavitt (1912) showed that Cepheids follow a very tight correlation between their luminosities and periods, thus by measuring the period of a Cepheid variable observed in a galaxy one can deduce its absolute magnitude and hence find its distance. Until recently it was only possible to apply this technique to nearby galaxies, but with the *Hubble Space Telescope* and new high-resolution ground-based cameras it is now possible to resolve individual stars within galaxies at a significant distance. Recent observations of Cepheids in the Virgo and Leo I clusters have continued to produce somewhat disparate values for H_0 from the different groups, for example, 80 ± 17 km s^{-1} Mpc^{-1} (Freedman et al. 1994), 87 ± 7 km s^{-1} Mpc^{-1} (Pierce et al. 1994), 69 ± 8 km s^{-1} Mpc^{-1} (Tanvir et al. 1995).

Another method of measuring the distance of galaxies that has come to the forefront of cosmology has been to use supernovae of type Ia. This class of supernova is well understood to have a constant absolute magnitude at the maximum of the light-curve. By regular monitoring of galaxy samples, it has been possible to identify supernovae in external galaxies before maximum light thus enabling detailed imaging and spectroscopic observations to be made of them at maximum. Type Ia supernovae can then be distinguished from the other types and their apparent magnitudes at maximum measured, enabling determination of their distance. Values of the Hubble constant from these studies have generally been lower than those measured by the Cepheid observers, for example, 57 ± 4 km s^{-1} Mpc^{-1} (Sandage et al. 1996), 63 ± 3 km s^{-1} Mpc^{-1} (Hamuy et al. 1996), <78 km s^{-1} Mpc^{-1} (Kim et al. 1997).

The Hubble expansion is the first observation to be explained by any cosmological model. The second is the isotropy of the universe — that is, it looks the same in all directions.

The most direct evidence for isotropy comes from observations of the cosmic microwave background radiation (CMBR). Penzias and Wilson (1965) discovered an "excess antenna temperature" of 3.5 ± 1.0 K at a wavelength of 7 cm using the Holmdel radio telescope of Bell Telephone Laboratories, that was isotropic, of constant amplitude throughout the year and could not be attributed to any terrestrial source. It was interpreted by Dicke et al. (1965) as being blackbody radiation left over from the dense early stages of the expanding universe. The source of this radiation will be discussed more fully in §1.1.3 below, but the key point is that the first results showed it to be isotropic and of cosmological origin.

Much work then ensued to measure just how smooth the CMBR actually is. Progress was slow due to the fact that the radiation peaks in the millimetre region of the spectrum where the atmosphere is bright and highly variable, and the data had to be obtained either at longer wavelengths, high altitude or using short balloon flights. Furthermore, these experiments were limited to observing a very small fraction of the sky. The results revealed a dipole anisotropy, such that the brightness-temperature T of one half of the sky differs from that of the other half by $\delta T/T \simeq 10^{-3}$. This is due to the Doppler shift from the motion of the Galaxy relative to the CMBR and implies that we are moving towards Leo at about 360 km s^{-1}. Multiple experiments failed to detect any further anisotropies below this level. (For reviews, see Cheng 1994; White et al. 1994).

The breakthrough came with the launch in November 1989 of NASA's Cosmic Background Explorer satellite (COBE). With three far-infrared and microwave (mm-wavelength) detectors, COBE produced the best measurements of the CMBR ever obtained. After removing the effects of the dipole anistropy and the Galactic emission, the COBE team discovered brightness fluctuations of $\delta\mathrm{T}/\mathrm{T} \simeq 10^{-5}$ (Smoot et al. 1992; Bennett et al. 1996). That is, after correcting for the Earth's motion the CMBR is isotropic to within one part in 100,000 *across the whole sky*, at the 7° resolution of COBE. An important point to note is that this isotropy is a fundamental property of the universe. The event horizon at the surface of last scattering (from where we see the CMBR) was $0\overset{\circ}{.}5$–$1\overset{\circ}{.}5$, thus there could be no physical process that occured at the surface of last scattering that could produce such a smooth distribution.

Before turning away from the CMBR, another important result from COBE is worth recording. The spectrum of the background radiation over 0.5–10 mm was found to be a perfect blackbody with a temperature of 2.736 K (Mather et al. 1990). This implies that the radiation must have been in thermal equilibrium with the matter at some point in the past, as predicted by Dicke et al. (1965).

The largescale isotropy of the universe has also been established at much more recent cosmological times, via the distribution of galaxies and quasars. The distribution of infrared-bright galaxies in the IRAS survey was found to be smooth on scales of ~ 60 Mpc (Strauss et al. 1992). The APM optical survey of Maddox et al. (1990) reached a greater depth than the IRAS survey and found results comparable with that infrared data. The angular distribution of the 31,000 brightest radio sources in the catalogue of Gregory and Condon (1991) also revealed that the universe is isotropic over the scale of a Hubble length.

In addition to the expansion of the universe and its isotropy, a third requirement is added to any realistic cosmological model — that of homogeneity. This simply means that not only does the universe *look* the same in all directions, but that it *is* the same at all locations. Our own Galaxy is not at any special place in the universe. Were we to be anywhere else, then the same physical laws would apply and the universe would look the same (on the largescale) as it does from here. This requirement is supported by the COBE observations of the CMBR. As noted above, the CMBR is smooth on scales much larger than the horizon distance at the surface of last scattering, demonstrating that the same physics applied to all parts of the (observable) universe.

The requirement of homogeneity and isotropy is known as the Cosmological Priciple. Together with the expansion of the universe, these form the basis of the Hot Big Bang model of the universe which will now be discussed.

1.1.2 Useful results from relativistic cosmology

The field equations of general relativity can be solved to give the metric for the case of an isotropic and homogeneous curved space-time (note that the expansion of the universe is predicted as a consequence of the models). The derivation of the Robertson-Walker metric, as it is known, is given in any of the standard cosmology texts, for example Berry (1989), Longair (1984), Peebles (1993) or Schutz (1990). In terms of comoving coordinates $(r,\ \theta,\ \phi)$ the metric is

$$ds^2 = c^2dt^2 - R^2(t)\left(\frac{dr^2}{1-kr^2} + r^2d\theta^2 + r^2\sin^2\theta d\phi^2\right) \qquad [1.2]$$

where $k = 0,\ \pm1$ is the curvature of the universe. The dynamics of the expanding universe are contained in the scale-factor $R(t)$, which depends upon the current rate of expansion (Hubble's constant H_0), the density of matter Ω_0 and the value of the cosmological constant Λ. These parameters also determine the curvature.

$R(t)$ is illustrated in figure 1.1 for the case of $\Lambda = 0$. If $k = -1$ ($\Omega_0 < 1$) there is not enough mass in the universe to halt the expansion and it will continue to expand forever. If

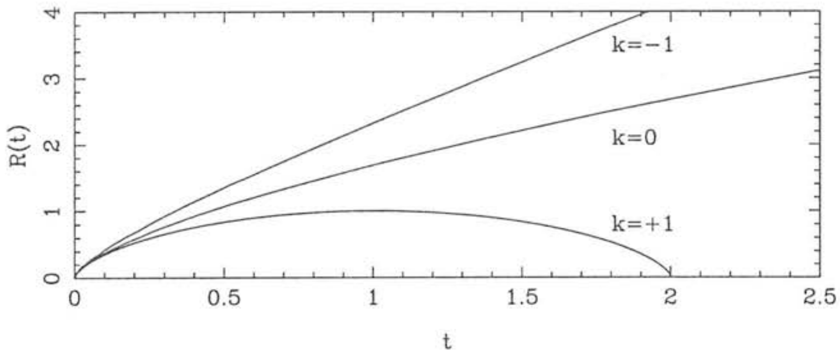

Figure 1.1 The cosmological scale-factor $R(t)$ as a function of time, for the three possible curvatures: open ($k = -1$), critical ($k = 0$) and closed ($k = +1$). They have been scaled such that the maximum radius of the closed model is $R = 1$ at $t = 1$.

$k = +1$ ($\Omega_0 > 1$) then there is sufficient mass that gravity will halt the current expansion and the universe will collapse back into itself. The case $k = 0$ ($\Omega_0 = 1$) is the critical point between these two — the universe will expand forever but only just ($dR/dt \to 0$ as $t \to \infty$). This is a relatively simple solution to the field equations and is preferred by many cosmologists for its elegance, although there is currently insufficient observational evidence to empirically determine the curvature. A positive cosmological constant has the opposite effect of gravity — it will reduce the rate at which the universe decelerates, increasing the age of the universe (to first order, "stretching" the t-axis of figure 1.1).

In order to relate the metric to observable quantities, it is helpful to use the redshift z. Light emitted at a wavelength $\lambda_{\rm emit}$ will be shifted to a longer wavelength λ by the cosmological expansion. The redshift is related to the scale-factor via

$$\frac{\lambda}{\lambda_{\rm emit}} = 1 + z = \frac{R_0}{R(t)} \qquad [1.3]$$

where $R_0 = R(t_0)$ is the value of the scale-factor today.

The Robertson-Walker metric [1.2] can then be evaluated in order to express the geometry of the expanding universe in terms of observables. The key equations that will be used in this thesis are summarised here — see the above text books for derivations. The results for two cosmologies are given: (i) an open universe $\Omega_0 = 0$ ($k = -1$), and (ii) the critical case $\Omega_0 = 1$ ($k = 0$, also known as the Einstein–de Sitter solution), both for zero cosmological constant.

The "effective distance" is defined as

$$D = \frac{2c}{H_0 \Omega^2 (1+z)} \left(\Omega z + (\Omega - 2)[(\Omega z + 1)^{0.5} - 1]\right) \qquad \text{for } \Omega_0 \neq 0;$$

$$D = \frac{cz(1 + z/2)}{H_0(1+z)} \qquad \text{for } \Omega_0 = 0 \qquad [1.4]$$

The flux density [W m^{-2} Hz^{-1}] of a source of monochromatic luminosity $L(\nu)$ [W Hz^{-1}], at a redshift z is given by

$$S(\nu) = \frac{L(\nu(1+z))}{4\pi D^2(1+z)} \tag{1.5}$$

If the spectrum of the source is a power-law $L(\nu) \propto \nu^{-\alpha}$ then this reduces to

$$S(\nu) = \frac{L(\nu)}{4\pi D^2(1+z)^{1+\alpha}} \tag{1.6}$$

The luminosity distance is defined to be $D_L = D(1+z)$. With this definition, the relation between bolometric luminosity and bolometric flux density (integrate [1.5] or [1.6] over all ν) looks like an inverse-square law:

$$S_{\text{bol}} = \frac{L_{\text{bol}}}{4\pi D_L^2} \tag{1.7}$$

The angular size of an object of proper length d perpendicular to the line-of-sight is

$$\Delta\theta = \frac{d(1+z)}{D} \tag{1.8}$$

The comoving volume enclosed by the universe [Mpc^3 sr^{-1}] out to a redshift z is given by

$$V(z) = \frac{8c^3}{3H_0^2}\left(1 - \frac{1}{\sqrt{1+z}}\right)^3 \qquad \text{for } \Omega_0 = 1;$$

$$V(z) = \left(\frac{c}{H_0}\right)^3 \left(\frac{1}{8}(1+z)^2 - \frac{1}{2}\log_{10}(1+z) - \frac{1}{8(1+z)^2}\right) \qquad \text{for } \Omega_0 = 0 \tag{1.9}$$

If a non-zero cosmological constant is included in the field equations, then these relations are modified. See, for example, Berry (1989) or the appendix of Peacock et al. (1998). This thesis will not explicitly consider a $\Lambda \neq 0$ cosmology and so those equations are not given here.

1.1.3 The early universe

To conclude this introduction to cosmology, the evolution of the universe in its earliest phase will be reviewed. Although the early universe is not open to direct observation, the remnants of this phase are seen today in the cosmic microwave backgound (CMBR) and the very matter of the universe.

It is seen in figure 1.1 that the scale-factor $R(t)$ decreases as one goes farther back in time, approaching the limit $R \to 0$ as $t \to 0$. As the space between particles decreases, their density increases, as does their temperature. Similarly, the energy density of the CMBR increases as t becomes smaller. The matter density scales as R^{-3} and the radiation density goes as R^{-4} (the extra factor of R^{-1} being due to the redshifting of the photons). Thus there was a time when the radiation density was higher than the density of matter. This occurred at a redshift of $z \sim 10^4$. Prior to that time, the matter and radiation were in thermal equilibrium, at temperatures $\geq 3 \times 10^4$ K.

The evolution of the early universe at these epochs was dominated by quantum, nuclear and thermodynamic physics. The details can be found in the standard cosmology texts, in particular Weinberg (1993). Prior to 10^{-43} s, quantum and gravitational effects were comparable and the current laws of physics break down. At that time the temperature was $\sim 10^{31}$ K and the universe consisted of photons, leptons, free quarks and a multitude of exotic particles. By $\sim 10^{-5}$ s the temperature had fallen sufficiently that free quark states were no longer possible and the baryons formed. Electro-weak interactions became dominant and the universe entered thermal equilibrium. At $t \sim 1$ s the neutrinos became decoupled from the radiation and shortly afterwards electron–positron pairs annihilated. Nucleosynthesis occurred at a temperature of $\sim 10^9$ K when the universe was ~ 100 s old. Most of the light elements (D, ^{3}He, ^{4}He, ^{7}Li) that are observed today formed at that time, their abundances being determined by the ratio of the number of photons to baryons. A comparison of the observed abundances with theoretical predictions led to the conclusion that the baryonic matter has a density parameter of $\Omega_0 \simeq 0.05$–0.1 (Wagoner 1973; Walker et al. 1991).

At an age $\sim 10^6$ years ($z \sim 10^4$) the dynamics of the universe became dominated by the matter rather than the radiation. After about 10 million years, at $z \simeq 1500$, the free electrons were able to combine with the hydrogen nuclei and the universe became transparent to the radiation. This was the "recombination epoch" or "surface of last scattering". The radiation subsequently cooled with the expansion of the universe, reaching its present temperature of 2.7 K. Following recombination, the matter was free to collapse under gravity (being no longer supported by radiation pressure) and the first structures formed. This will be the topic of the next section.

1.2 Galaxy evolution

One of the foundations of the Hot Big Bang model is that the universe is homogeneous on the largest scales. On small scales it is clearly inhomogeneous — there are stars, galaxies and clusters of galaxies. The formation of these structures following the epoch of recombination will be discussed from two directions. First, the theory of structure formation will be reviewed (§1.2.1) and then some of the observational evidence related to galaxy formation and evolution will be addressed (§1.2.2).

1.2.1 A theoretical picture

The most successful theories at present suggest that the formation of galaxies and the growth of structure (clusters and superclusters of galaxies) resulted from the gravitational collapse of initial density fluctuations in a universe whose dynamics are dominated by cold dark matter (CDM). Whilst there is no empirical evidence from physics for the weakly-interacting massive particles of which CDM consists, CDM has become popular among cosmologists for a number of theoretical reasons and has led to detailed models of structure formation with testable predictions (Ostriker 1993). Some form of dark matter is required in order to explain the flat rotation curves of galaxies at large radii. This form of dark matter could be baryonic. However if the universe has the Einstein-de Sitter critical mass then it must be dominated by non-baryonic matter — the nucleosynthesis results noted above do not allow values of $\Omega_{\rm baryon} \gtrsim 0.1$. CDM has so far been the most successful form of dark matter that has been studied in detail.

In the CDM models it is assumed that at some point during the radiation-dominated era of the early universe, small quantum fluctuations in the density of the cold dark matter appeared. While perturbations in the baryonic matter were kept small by the strong matter–radiation coupling before recombination, the weakly-interacting dark matter could collapse freely. With the standard scale-invariant power spectrum ($P(k) \propto k$), small objects (haloes) are the first to form which then amalgamate into progressively larger systems, a process known as hierarchial clustering. Following recombination at $z \simeq 1500$, the baryonic matter falls into the dark matter potential wells. This condensation of the gas leads to the formation of rotationally supported discs within the haloes. As the haloes merge, so do the gas discs forming galaxy-sized concentrations of gas which will eventually develop into the galaxies we see today. N-body/hydrodynamical simulations of the process do have flaws, as pointed out by Navarro et al. (1995), but as a model of galaxy formation it is widely accepted (for a full description see Efsthathiou 1990).

As the gas collapses into the dark matter potential wells, the density increases to a point at which star formation can begin to take place. Whether this occurs before or after most of the mass of the galaxy has come together is a matter of considerable debate. Studies of a high-redshift group of galaxies have suggested that the former is correct — star formation begins in small clumps which then merge into galaxies at $z \sim 2$ (Pascarelle et al. 1996b). Other studies have shown that at least some massive galaxies were assembled very early in the history of the universe, at $z \gtrsim 5$ (Dunlop et al. 1996; Spinrad et al. 1997).

Once the first stars have formed, the evolution of the stars themselves and their effect on the interstellar medium (ISM) become the dominant processes. Nucleosynthesis in stellar cores builds up the abundances of the metals (elements heavier than hydrogen and helium), which are then ejected into the interstellar medium by mass-loss processes such as supernovae, novae and powerful stellar winds. The chemically enriched ISM will then be incorporated into the next generation of stars which will further enrich the ISM with heavy elements as they evolve and so on, in a continuous feedback process. Modelling of this stage of galaxy evolution is much harder than the CDM-dominated early stages, and observational work currently dominates the literature on these topics.

1.2.2 Observational clues

The empirical clues as to the processes involved in galaxy evolution are many and only a few of the more recent ones will be addressed here. One of the first methods used to investigate "galaxies" at very high redshifts was the study of quasar absorption lines. The spectra of high-redshift quasars have many narrow and broad lines shortward of Lyα, due to absorption of the quasar continuum by intervening gas clouds along the line of sight. Three distinct types of absorbers have been identified, based on the H I column density Σ and corresponding line shape: Lyα forest clouds with $\Sigma \sim 10^{14}$ atoms cm^{-2} (Impey 1998), Lyman-limit systems with $\Sigma \sim 10^{17}$ cm^{-2} (Lanzetta 1991) and damped Lyα (DLA) systems with $\Sigma \gtrsim 10^{20}$ cm^{-2}. These various systems may represent galaxies in various stages of collapse. At $z \sim 2$ the Lyα absorbers are as common as luminous galaxies and represent most of the baryons in the universe (Impey 1998). The DLA systems have column densities comparable to the interstellar gas in a spiral galaxy at the present and may be massive galaxies seen prior to the onset of major star formation (Wolfe and Prochaska 1998).

One of the most important breakthroughs in the study of high-redshift galaxies was the discovery of a population of star-forming galaxies at $3.0 < z < 3.5$, using broad-band filters to select galaxies with a Lyman-limit break at those redshifts (Steidel et al. 1995; Steidel et al. 1996b). This was rapidly followed by the Hubble Deep Field (HDF; Williams et al. 1996), the deepest exposure of the universe ever made. Numerous studies of the high-redshift universe have resulted from the HDF, for example: studies of the faint number counts (Metcalfe et al. 1996); morphological separation of the counts (Driver et al. 1998); and a determination of the star formation history of the universe (Madau et al. 1998). This last paper also used results from the Canada-France Redshift Survey (CFRS; Lilly et al. 1995). This and subsequent papers presented the results of a complete survey of several thousand objects brighter than $I_{AB} < 22.5$, that has enabled the evolution of galaxies to be studied in detail at redshifts $z \lesssim 1$.

Further observational results will be discussed throughout the thesis as they become relevant to particular discussions. In the next section, attention will turn away from studies of the general galaxy population to focus upon the use of radio galaxies in investigating the evolution of galaxies.

1.3 Radio galaxies as probes of evolution

Only with the advent of the *Hubble Space Telescope* has it been possible to begin to study ordinary galaxies at redshifts $z \gtrsim 0.5$. Before this, the only objects known in any large number at these redshifts were the radio galaxies (RGs) and quasars. The optical light of quasars is dominated by the active nucleus and they are of little use for studying their host galaxies at high redshifts. The radio galaxies however have a much smaller contribution to their optical–infrared light from the active nucleus than do quasars and it is the stellar populations of the galaxies which we can observe directly. In addition, radio galaxy samples have well defined and understood selection criteria based on their radio emission and they often have strong emission lines making the determination of their redshifts far easier than for normal galaxies at comparable distances. At low redshifts, luminous radio galaxies are almost exclusively giant ellipticals. Although the mechanism that triggers the powerful radio emission in some galaxies rather than others is not fully understood, it is reasonable to suppose that the same mechanism would occur throughout the universe and that radio galaxies at high redshifts are also associated with giant ellipticals. For these reasons, radio galaxies have played a crucial role in our understanding of galaxy evolution, being the only massive galaxies visible at large lookback times. For an extensive review of the properties of high redshift radio galaxies see McCarthy (1993).

The process of collecting together a statistically complete sample of radio galaxies is a time consuming but very necessary one in order to draw firm conclusions about the nature and evolution of RGs. As detailed in McCarthy (1993) there are around 12 radio surveys at frequencies 151 MHz $< \nu <$ 5 GHz, with flux limits $0.001 < S_\nu < 10$ Jy. These surveys, or selected areas of them, vary widely in their optical completeness — the percentage of radio sources with confirmed optical (or infrared) identifications and spectroscopic redshifts. The most complete and widely studied of these is the 3CR survey (Laing et al. 1983; Spinrad et al. 1985) which, together with additional samples at lower flux limits of ~1 Jy, provided the first evidence for a redshift cut-off and was used for the first studies of the stellar populations of distant radio galaxies.

However, it became apparent that the very properties which made RGs visible at high redshifts, also made them very different from "normal" giant ellipticals and from low-redshift RGs. For example, a strong correlation was found between [O II] 3727 Å (Spinrad 1986) or [O III] 5007 Å (Rawlings et al. 1989) emission line luminosity and radio luminosity, resulting in more distant RGs being more active than their nearby counterparts. McCarthy et al. (1987) found that the optical (rest-frame UV) *continuum* emission of the 3CR galaxies was elongated and aligned with the axis of radio emission. This "alignment effect", as it is known, has been variously attributed to jet-induced star formation, scattering of light from the active nucleus or dynamical coupling between the radio and gravitational axes. Detections of highly polarized light from many of these galaxies supports the model of scattered nuclear emission, whilst there is also strong evidence that much of the (rest-frame) UV can be explained by star formation (McCarthy 1993). It is likely that both make an important contribution and it is necessary to distinguish the two effects.

In order to overcome the drawbacks of using the most powerful radio galaxies, attention is now focussed on the radio surveys with lower flux limits. Of particular interest to the present work are the Parkes Selected Regions (PSR; Downes et al. 1986; Dunlop et al. 1989b) and the Leiden-Berkeley Deep Survey (LBDS; Windhorst 1984; Windhorst et al. 1984b), with flux limits of 0.1 Jy at 2.7 GHz and 0.001 Jy at 1.4 GHz respectively. The optical identification of sources in the PSR is essentially complete, with an ongoing programme to measure their redshifts. Chapter 2 will report on the completion of the optical identifications for a sub-sample of the LBDS and progress on the redshift content will be presented in chapter 3.

The advantage of using these surveys is two-fold. Firstly, at low and moderate redshifts the galaxies have intrinsically less powerful radio emission than the 3CR sources. Thus their emission and morphological properties are found to more closely resemble those of normal giant ellipticals nearby, that are unaffected by an AGN. In particular their optical/infrared continuum is less strongly aligned with their radio emission and their colours are redder than most of the 3CR galaxies, consistent with a reduction in the aligned blue component associated with radio activity (Dunlop and Peacock 1993). Also, their emission lines are weaker and more comparable to low redshift radio galaxies, as expected from the [O II]/radio luminosity correlation noted earlier. The second advantage of these low-flux surveys is that the powerful sources ($P_{2.7} > 10^{27}$ W Hz^{-1} sr^{-1}) as seen in the 3CR sample, should be observable at redshifts $z \gtrsim 3$ in the Parkes Selected Regions and at redshifts $z \gtrsim 10$ in the Leiden-Berkeley Deep Survey. Observations of a population of RGs with a wide range of intrinsic radio powers at the same redshift ($z \sim 1$–3) will facilitate a better understanding of their properties, and the ability to see powerful RGs at very high redshift is of crucial importance to study the redshift cut-off.

One of the motivations behind using radio galaxies as cosmological probes is the relative ease with which their redshifts can be measured from emission lines. The very fact that the PSR and LBDS galaxies are less active than their 3CR counterparts means they have weaker emission lines which are thus harder to detect and measure a redshift from. This will become all too apparent in chapter 3 below. To overcome this problem and to reduce the need for the time-intensive observations required to obtain faint spectra, methods of estimating the redshift of a RG from either its infrared magnitude or its broadband colours have been developed.

One of the earliest and most widely used tests to measure the curvature of the universe is the redshift–magnitude, or Hubble, diagram. The idea underlying this is to find some "standard candle", for example the brightest galaxy in a cluster, that is assumed to have a constant absolute magnitude and to plot its apparent magnitude against redshift. Over large distances, such a diagram is sensitive to spatial curvature, and it was hoped that this would be the most direct method for measuring Ω_0 (see Sandage 1988 for a review). However, galaxies evolve and it is no longer certain that such standard candles exist. Evolutionary models produce a variation in the diagram that is as large as the variation between $\Omega_0 = 0$ and $\Omega_0 = 2$ models, which thus masks the cosmological curvature. The Hubble diagram is now used primarily as a tool for exploring the formation epoch and evolution of galaxies.

The optical Hubble diagram is of limited use at high redshifts as the light is dominated by the rest-frame UV from rapidly evolving starbursts or possible scattered from an AGN. However, the light in the infrared K-band (2.2 μm) is, in general, dominated by an old stellar population where evolutionary effects are small and there is less sensitivity to the change in rest-frame bandpass (the k-correction). The infrared Hubble (K–z) diagram has thus been used to study evolution in RGs.

In particular, Lilly and Longair (1984) showed for the 3CR sample that the K–z relation is well-defined with approximately constant dispersion to redshifts $z > 1$ and indicates evolution in the galaxies' luminosity of about a magnitude at $z \sim 1$, if $\Omega_0 = 1$. They concluded that the luminosity evolution could be accounted for by passive evolution of the main sequence turn-off mass. Again it was important to extend the observations to RGs with a lower flux limit. Lilly et al. (1985) looked at the K magnitudes and redshifts of 16 radio galaxies from the 1-Jansky survey of Allington-Smith (1982) and found that they have the same absolute magnitudes as the 3CR radio galaxies, giving no evidence for a correlation between radio power and optical luminosity. They found an empirical fit to the combined 3CR and 1-Jansky Hubble diagram of

$$\log_{10} z = -5.368 + 0.384K - 0.00385K^2 \qquad [1.10]$$

They then turned the problem around and used equation [1.10] to estimate the redshifts of the remaining galaxies in their sample from their K magnitudes.

The Parkes Selected Regions sources are an order of magnitude fainter in their radio emission than the 1-Jansky galaxies. This makes it all the more difficult to measure emission line redshifts for them: as of 1989 only 46% had spectroscopic redshifts, of which the majority were quasars or low-redshift galaxies (Dunlop et al. 1989b). In order to study the evolution of these RGs at lower flux limits it was necessary to estimate the redshifts of the remaining 54% of the sample (mostly RGs). Dunlop and Peacock (1990) showed that those PSR galaxies with known redshifts were consistent with the Hubble diagram of Lilly et al. (1985). Equation [1.10] was then adopted as an estimator for the redshifts of the PSR galaxies, the majority of which had K magnitudes. The test of this estimation procedure is to obtain further spectroscopic redshifts of the PSR galaxies and compare them to the estimates (§§3.1 and 4.2).

More recently, Eales et al. (1997) compared the K-band Hubble diagram for the 3C survey with a sample of weaker radio sources with virtually complete redshifts. This sample consisted of 80 sources drawn from the B2/1-Jansky (Allington-Smith 1982) and 6C (Eales 1985) surveys with flux limits of 1 Jy at 408 MHz and 2.2 Jy at 151 MHz respectively. They found that at low redshifts ($z < 0.6$) the fainter sources followed the same K–z relation as the 3C sources, but at higher redshifts the B2/6C galaxies were on average ~ 0.6 magnitudes fainter at K than the 3C galaxies. Two possible models were offered to explain this effect. First, the K-band emission of radio galaxies could be due to two components — the stellar population of the galaxy, plus a non-stellar component whose strength is proportional to the radio luminosity of the galaxy. The non-stellar component could be attributed to either emission lines or scattered light from a buried quasar. Second, the B2/6C galaxies at $z > 0.6$ could be less massive than the 3C galaxies at the same epochs. This would simultaneously explain both the brighter K-magnitudes and the greater radio luminosity of the 3C galaxies, as it is likely that the most massive galaxies (having the brightest stellar K-band emission) would contain the most extensive and densest distributions of gas (required for producing the most luminous radio emission). This latter explanation is strongly favoured by the results of Roche et al. (1998), who found that a subsample of ten 6C sources at $z \sim 1.1$ were significantly smaller than the 3C galaxies at the same redshift.

One of the most important aims of cosmology is to observe how galaxies evolve over time. At large distances (lookback times) this can be done by observing populations of AGN, in particular the space distributions, or luminosity functions, of quasars and radio galaxies. The luminosity function is defined as the number of sources per comoving Mpc^3 per unit interval of magnitude or $\log_{10}(\mathrm{RadioPower})$, for quasars or RGs respectively, in a given redshift range. Optical studies of quasars suggested that their luminosity function peaked at about $z \sim 2.5$ and then fell off (Green 1989; Hartwick and Schade 1990). Whether this cut-off corresponds to a reduction in the real space density of quasars, a systematic change in their intrinsic luminosity, or is an apparent effect due to increasing obscuration by dust, is an open question.

In an attempt to overcome the many selection effects inherent in optically selected samples, attention switched to the luminosity function of radio sources. As described above, complete identification and redshift data, well defined selection criteria, as well as the lack of obscuration due to dust at radio wavelengths, suggested the study of the radio luminosity function (RLF) could yield an unambiguous insight into the redshift cut-off. Peacock (1985) looked at a number of complete samples of radio galaxies and radio-loud quasars with flux limits ~ 1 Jy. He found that for the class of compact, flat spectrum sources ($\alpha < 0.5$, where $S \propto \nu^{-\alpha}$), the data required a redshift cut-off with the RLF ceasing to evolve at $z \simeq 2$ and being reduced at $z = 4$ by a factor of > 3 from its peak value.

To extend this conclusion to other classes of radio source required a complete sample with a lower flux limit, which would contain substantial numbers of high redshift objects unless the observed cut-off applied to all radio sources. This was the motivation behind the work to obtain complete identification and redshift data for the Parkes Selected Regions (Dunlop et al. 1989b). At an order of magnitude fainter than the samples used in Peacock (1985) and with a higher selection frequency of 2.7 GHz, both flat- and steep-spectrum sources would have been observable out to $z \gtrsim 3$ in the absence of a cut-off in the RLF.

Dunlop and Peacock (1990) modelled the PSR radio luminosity function and concluded that *all* high luminosity radio sources show a cut-off in their redshift distributions beyond $z \simeq 2$. They also demonstrated that the cut-off for steep-spectrum sources (dominated by RGs) is less abrupt than that for flat-spectrum sources (dominated by radio-loud quasars) and that there is some evidence that the redshift at which the RLF peaks is a function of radio luminosity. However, these results are dependent upon the accuracy of their redshift estimation and confirmation of these redshifts is very desirable (see §§3.1 and 4.2). For the steep-spectrum sources (RGs) only the most powerful ($P_{2.7} > 10^{27}$ W Hz^{-1} sr^{-1}) could be observed at $z > 3$ in the PSR sample, illustrating the need to go to even fainter flux limits to confirm the steep-spectrum cut-off. The LBDS sample, with a flux limit of 1 mJy, will be the next step in this investigation. The following chapters will discuss the LBDS in detail, but first the use of spectral synthesis models in the analysis of the stellar populations of galaxies will be introduced.

1.4 Spectral synthesis models of galaxies

Modelling the evolution of a galaxy spectrum as a function of stellar population and redshift, and comparing the models to the observed broadband colours of galaxies enables important conclusions to be drawn about their ages and star formation history. The spectral evolution models most widely used are those of Bruzual (1983; Bruzual and Charlot 1993), Guiderdoni and Rocca-Volmerange (1987), Arimoto and Yoshii (1987) and Worthey (1994). In these spectral synthesis models, analytical expressions are assumed for the star formation rate and initial mass function, which together determine the number of stars of a given mass formed during a given time interval. Theoretical evolutionary tracks are used to calculate the stellar population content of the model galaxy at any given time. A galaxy spectrum is then synthesized from a library of observed or model spectra of different stellar types. This spectrum can then be redshifted and combined with the spectral responses of the required broadband filters to simulate an observed multi-colour spectral energy distribution (SED).

One of the greatest freedoms in these models is the choice of star formation rate (SFR). The SFR used is usually either a burst model in which all of the mass of gas is converted to stars within $\lesssim 1$ Gyr, or an exponentially decreasing model (characterized by the fractional mass consumed in the first Gyr), or a combination of the two. Spinrad and Djorgovski (1987) and Dunlop et al. (1989a) fitted these models to their 3CR, 1-Jansky and PSR samples and concluded that the single burst models could not explain both the optical and the near-infrared colours simultaneously. The objects with the bluest $R-K$ colours require a formation redshift of $z_{\rm form} < 2$, the reddest $R-K$ colours require $z_{\rm form} \simeq 5$–7, while the $J-K$ colours of the reddest galaxies require $z_{\rm form} \simeq 20$ (even if $\Omega_0 = 0$) (McCarthy 1993).

Dunlop et al. (1989a) found that the simplest model to explain the wide range in colours was to decouple the old and young stellar populations. In this "old galaxy plus burst" model, the majority of stars formed in a burst (< 1 Gyr duration) at $z \gg 2$, but with a low rate of star formation continuing thereafter. The blue optical colours (rest-frame UV) could then be explained by the addition of a small ($\sim 1\%$ of the total mass) burst of star formation in the otherwise passive galaxy. While the bluest colours could be explained by a variety of starburst or scattered light models, the reddest infrared colours can only be attributed to a well developed 4000-Å break, due to an old, evolved population of stars. It is the age of these stars, that is, the time it takes the 4000-Å break to develop in the models, that has important implications for cosmology. For example, the reddest $R-K$ colours in the PSR sample could only be reproduced if the bulk of the stars in the galaxy formed ~ 18.5 Gyr ago, requiring $H_0 < 35$ km s^{-1} Mpc^{-1} for $\Omega_0 = 1$ or $z_{\rm form} \simeq 20$ if $H_0 = 50$ km s^{-1} Mpc^{-1} and $\Omega_0 = 0$ (using the 1-Gyr burst models of Guiderdoni and Rocca-Volmerange (1987)).

These spectrophotometric models can also be used to estimate redshifts from multi-waveband photometry, a potentially more accurate method of estimation than using the K–z relation of equation [1.10]. Lilly (1989) showed how a two-component model (with separate blue and red fluxes) could be used to fit an observed SED by varying both the redshift ($z_{\rm est}$) and the relative contribution of the two components at 5000 Å (f_{5000}). This model fitting was principally used by Lilly to investigate the level of activity in the 3CR and 1-Jansky samples via determination of f_{5000}, but it was also used to estimate redshifts for a number of the 1-Jansky galaxies.

Estimating the redshifts of the PSR radio sources has been particularly important given that only one-half had spectroscopic redshifts. In their investigation of the alignment effect and optical activity in a subsample of the full PSR, Dunlop and Peacock (1993) re-estimated the radio galaxy redshifts using this photometric fitting technique. For the red, or "old", component they used a 10 Gyr old galaxy from the models of Guiderdoni and Rocca-Volmerange (1987), and for the blue, or "young", component a flat power-law spectrum ($f_\nu \propto \nu^{-0.2}$) was used. For the eight radio galaxies in the subsample with measured redshifts, a comparison between the estimated ($z_{\rm est}$) and spectroscopic ($z_{\rm true}$) redshifts showed them to be in excellent agreement $\langle z_{\rm est}/z_{\rm true}\rangle = 0.97 \pm 0.11$. On average, these estimates were found to be a factor of ~ 0.8 smaller than the K–z estimates used in Dunlop and Peacock (1990).

In order to investigate the properties of radio galaxies of lower luminosity than the PSR sources, the LBDS sample also requires accurate determination of the redshifts. As will be discussed in chapter 3, spectroscopy of these faint galaxies is very difficult and accurate estimation of their redshifts from their optical/infrared colours will be necessary. The development of the redshift estimation technique will be presented in section 4.3.

In addition to the spectral synthesis models noted above, this thesis will make considerable use of the new models of Jimenez et al. (1999). As these models are not yet widely known, a few details will be given here. Most of the disagreement between the existing stellar evolution codes originates with the difficulty of modelling the post main-sequence evolution (Charlot et al. 1996). Jimenez et al. improve this aspect of the models by applying an algorithm which includes proper modelling of the horizontal branch (HB), taking accurate account of the formation of carbon stars on the asymptotic giant branch (AGB), and using the properties of real star clusters to calibrate the mixing-length parameter and the mass-loss rate. New stellar evolutionary tracks were computed using an "adaptive mesh" of sampling points, that enabled the rapid stages of evolution to be calculated with higher resolution in mass than is possible with fixed sampling of the model. The stellar spectra were calculated using theoretical stellar photospheres (Kurucz 1992; Helling et al. 1996).

Using these ingredients, Jimenez et al. (1999) can compute synthetic stellar populations of arbitrary age, metallicity, initial mass function (IMF) and star formation rate. The models that will be used later in the thesis are all instantaneous burst models. Two different IMFs are used (Salpeter and Miller-Scalo), for six metallicities ($Z = 0.0002, 0.004, 0.02$ (solar), 0.05 and 0.1) and twenty ages (0.01, 0.03, 0.07, 0.1, 0.3, 0.7, 1, 2, ..., 13, 14 Gyr).

1.5 Outline of the thesis

The purpose of this thesis is to address two issues: (i) to confirm or refute the existence of a high-redshift decline in the radio source population beyond $z \simeq 2$; and (ii) to determine if the stellar populations of radio hosts (and massive ellipticals in general) were formed at the same time as the rise in AGN activity.

The first aim will be pursued from two directions. Firstly, the accuracy of the K–z relation (equation [1.10]) for sources in the PSR will be tested. Recall that Dunlop and Peacock (1990) used that relation to estimate the redshifts of sources in the PSR — the evidence for a cut-off in the radio luminosity function (RLF) was crucially dependent upon the accuracy of those estimates. Secondly, by studying a radio sample with a lower flux density limit, the RLF can be investigated at higher redshifts and lower luminosities. A sub-sample of the Leiden-Berkeley Deep Survey, with $S_{1.4} \geq 1$–2 mJy, will be used to trace the RLF to $z \sim 10$ and $\log_{10} P_{1.4} \sim 20$.

The second aim of the thesis will be addressed in two ways. The spectral evolution of the LBDS radio sources will be investigated, with particular emphasis on the reddest radio galaxies in the survey. Secondly, the results of a search to find the reddest companions around the radio galaxy 53W002 at $z = 2.390$ will be discussed.

The layout of the thesis is as follows. In chapter 2, the results of an extensive optical and infrared imaging programme in the Hercules field of the LBDS will be reported. This will essentially complete the optical identification of this sub-sample, and provide nearly complete infrared K-band data on the sources. The radio/optical/infrared properties of the sample will be summarised. The following chapter will report the results of spectroscopic campaigns to measure redshifts for sources in the PSR and the LBDS samples. The spectra from the two surveys will be compared, emphasising the differences that are most likely due to the lower radio luminosity of sources in the LBDS.

Chapter 4 will begin the second half of the thesis, dealing with the analysis of the results presented in chapters 2–3. The radio luminosity functions of Dunlop and Peacock (1990) will be reviewed. The implications of the new redshift measurements in the PSR will be discussed with reference to the accuracy of the K–z relation for the PSR sources, and the consequences for the redshift cut-off. A technique for estimating the redshifts of the LBDS sources will be presented, and the results used to construct the observed radio luminosity function for the LBDS Hercules sample. The observations will be compared with the models of Dunlop and Peacock (1990).

The spectral evolution of the LBDS sources will be investigated in chapter 5. This will be done via a study of the optical and infrared Hubble diagrams, and modelling of the envelope of the reddest galaxies. The results of an investigation of the two oldest galaxies at high redshift will be reviewed, and the conclusions drawn together to place limits on the possible cosmologies allowed by the ages of these sources. Chapter 6 will present the results of deep infrared imaging around the radio galaxy 53W002 which revealed the presence of a number of red companions to this source at high redshift. The possibility that these companions could be passively-evolving galaxies seen within 2 Gyr of the Big Bang will be investigated.

Finally, the conclusions of the thesis will be drawn together in chapter 7, and some possible extensions of the work will be explored.

Chapter 2

Imaging the LBDS Hercules field

The Leiden–Berkeley Deep Survey of milli-Jansky radio sources at 1.4 GHz is reviewed, with particular emphasis on the 73-source complete sample in Hercules. An extensive programme of optical and infrared imaging of these sources is reported. This sample is now almost completely identified in g, r, i and K, with some additional data available at J and H. The magnitude distributions extend down to $r \simeq 26$, $K \simeq 21$. The K-band magnitude distributions for the radio galaxies and quasars are compared with those of other radio surveys. The sources span a broad range of colour, with a significant number being very red ($r - K > 5$).

2.1 The Leiden–Berkeley Deep Survey

The purpose of the Leiden–Berkeley Deep Survey (hereafter "the LBDS") was to gain a better understanding of the nature of faint radio galaxies and quasars, and to determine their cosmological evolution. In this section, the radio data is reviewed and the status of the optical/infrared follow-up work is summarised. The completion of the optical identification of the Hercules sample is presented in §2.2 and the infrared data on these sources follows (§2.3). The general properties of the sample are discussed in §2.4, and the images, finding charts and results tables are given at the end of the chapter (§2.5).

2.1.1 Introduction

As discussed in §1.3, a radio survey with milli-Jansky flux limits is required in order to probe weak radio sources ($P_{2.7} \lesssim P^*_{2.7} = 10^{25}$ W Hz^{-1} sr^{-1}) at cosmologically interesting redshifts ($z \gtrsim 1$). Galaxies at such distances will also be faint in the optical, thus deep optical images are required in order to identify the hosts of the radio sources. This is traditionally done by selecting a region of sky for a radio survey and then following that by an optical search. However the LBDS was designed in the opposite manner. A collection of good multi-colour prime focus plates had been acquired with the 4 m Mayall telescope at Kitt Peak for the purpose of faint galaxy and quasar photometry (Kron 1980; Koo and Kron 1982). Several high latitude fields were chosen in the selected areas SA57, SA68, SA28 (referred to as the Lynx field) and an area in Hercules. The fields were selected on purely optical criteria, such as high galactic latitude ($b^{II} \gtrsim 35°$) and minimum H I column density, resulting in a random area of sky from the radio perspective.

Nine of these fields were then surveyed with the 3 km Westerbork Synthesis Radio Telescope (WSRT) at 21 cm (1.412 GHz) with a 12.″5 beam (Windhorst et al. 1984b). These observations yielded noise limited maps with σ = 0.12–0.28 mJy in 12 hours, with absolute uncertainties in position of order 0.″4 and in flux of order 3–5%. A total of 471 sources were found, out of which a complete sample of 306 sources was selected. This complete sample is defined by (1) a peak signal-to-noise $S_p/N \geq 5\sigma$ (corresponding to 0.6–1.0 mJy) and (2) a limiting primary beam attenuation of -7 dB (corresponding to a radius of 0.°464, or an attenuation factor $A(r) \leq 5$). With this attenuation radius the WSRT field then covers the same area as the Mayall 4-m plates. Images were also made at the resolution of the 1.5 km WSRT (σ = 0.27 mJy; Windhorst et al. 1984b) and at 50 cm (0.609 GHz) with the 3 km WSRT (σ = 0.48 mJy; Windhorst 1984). The radio data for the two Hercules fields are summarised in table 2.4 (p. 52).

Following this selection of the radio sample, the photographic plates were searched for optical counterparts to the radio sources (Windhorst et al. 1984a). Large astrographic plates were used to measure the positions of 30–40 secondary standards based on the positions of AGK-3 astrometric standard stars. These secondary standards were then used to calibrate the Mayall prime focus plates for each field in the survey. The radio and optical position errors combine to give an error ellipse around the co-ordinates of the radio source within which one expects to find the optical identification of the source. For the complete sample, 171 of the 306 radio sources were identified in this way with the expected number of real identifications being 53%, whilst for the Hercules fields the identification percentage was somewhat higher at 65% (47 out of 73 sources).

Magnitudes for each of these objects were measured from digital scans of the plates (Kron et al. 1985). Absolute calibrations were made for most of the fields using photoelectric observations of stars in the fields and transforming the derived UBV zero-points to the photographic $U^+J^+F^+N^+$ system. For the two Hercules fields, however, no photoelectric zero-points were available. They had to be estimated by assuming that the sensitivity of the Hercules plates was the same as for plates (with the same emulsion and filter) taken of another field for which photometric calibrations were available. The resulting errors in the photometry ($\simeq$ 0.2–0.3 mags) are thus larger for Hercules than the rest of the sample. Redshifts were measured for ~60 of the LBDS identifications, of which 16 were in Hercules.

One of the major limiting factors in using the LBDS for statistical studies of radio source evolution has been the incomplete optical identification of the sample and the limited number of redshifts available. To obtain complete identification and spectroscopic data on the whole ~300 source survey is a major long-term project (led by Windhorst and collaborators), so in this thesis, attention is focused on a sub-sample of 73 sources. The two Hercules fields were chosen for this detailed study because they had the largest number of optical identifications already available. In addition, the highest redshift object yet known in the LBDS (53W002 at $z = 2.390$) was found in these fields. Unpublished optical and infrared observations were made available to the author, and additional imaging and spectroscopic data have been acquired over the past few years. This chapter will discuss the processing and analysis of the imaging data, whilst the spectroscopic data is presented in the next. First, some of the highlights of previous work in the LBDS will be reviewed and the radio observations of Hercules will be summarised.

2.1.2 Previous work in the LBDS

Initial results from the photographic identifications were presented by Kron et al. (1985). About 20% of the identifications were quasars and there were two stars. The galaxies were separated into bright ($F^+ < 18$) and faint ($18 < F^+ < 21.5$), red ($J^+ - F^+ > 1.2$–2.8) and blue ($J^+ - F^+ < 1.2$–2.8) classes. The red radio galaxies (both bright & faint classes) were identified as giant ellipticals with extended radio emission — "classical" powerful radio galaxies. The bright, blue galaxies were exclusively spirals with unresolved radio structure and a very narrow range in power $\log_{10} P_{2.4} = 22.1 \pm 0.1$. The faint, blue galaxies frequently had irregular optical morphologies (interactions, mergers or compact galaxies), and higher radio/optical flux ratios than normal spirals, suggesting they were a population distinct from the brighter blue sources.

Thuan et al. (1984) observed 48 sources in the LBDS in the near-infrared JHK-bands, down to $K \simeq 17.5$. They discovered that the optical–infrared colours of the faint radio galaxies were due to their stellar populations, showing no correlation with their radio flux or power. Less than 10% of the red radio galaxies had evidence for non-thermal IR emission. The colours of the red galaxies were consistent with those of distant ($z \gtrsim 0.2$) non-evolving or passively-evolving luminous giant ellipticals, such as observed in the 3CR survey. The optical/IR colours of the faint blue radio galaxies were indicative of low-luminosity and/or star-forming galaxies.

Deep VLA observations at 1.4 GHz were made of the Lynx-2 field ($08^{\rm h}\ 42^{\rm m}\ +44^\circ 47'$) by Windhorst et al. (1985). This area is devoid of sources stronger than 10 mJy, allowing observations to be made that were not limited by dynamic range effects. A complete sample of 93 sources was found, with a 5-σ limiting flux of 0.2 mJy. The normalised differential source counts were found to flatten below 5 mJy — an effect that could not be explained by ordinary spiral and Seyfert galaxies, nor by the giant elliptical or quasar contribution that dominates at higher flux densities. The "sub-mJy" counts were shown to be dominated by the faint blue galaxies that first appeared in the LBDS proper. The fraction of blue galaxies increases from 30% above 10 mJy to ~70% below 3 mJy.

Windhorst et al. (1993) used the VLA to observe the Lynx-2 field and an area in Cepheus down to an rms noise of ~4 μJy at 8.44 GHz. They found that the slope of the differential source counts ($dN/dS \propto S^{-\gamma}$) remained unchanged at $\gamma = 2.3 \pm 0.2$ over three orders of magnitude in flux density, $4 \lesssim S < 1000\ \mu$Jy. These "micro-Jansky" sources were identified as faint blue galaxies. Their median spectral index was $\alpha_{\rm med} = 0.35 \pm 0.15$ and their median angular size $\Theta_{\rm med} = 2\farcs6 \pm 1\farcs4$ (or 5–40 kpc at the expected median redshift of 0.5–0.8, for reasonable cosmologies).

High-resolution maps of many of the LBDS sources were obtained at 1.4 GHz with the

VLA, in order to investigate the radio morphologies of weak radio sources (Oort et al. 1987; Oort 1988). The median angular size of the radio samples was found to decrease with decreasing flux density, to $\sim 2''$ at 1–10 mJy and $\lesssim 1''$ at 0.4–1.0 mJy. This was attributed to the combined effects of a change in the population and a decrease in the intrinsic size of radio sources at lower (radio) luminosity. Approximately 90% of the red galaxies were resolved by the $1\farcs4$ beam, but half the blue radio galaxies remained unresolved. There was evidence in the sample for a decrease in intrinsic size with increasing redshift — a factor of 4 from $z = 0$ to $z = 0.5$. The morphological information and radio positions from this survey have been incorporated into table 2.4 (p. 52). Surveys have also been made of the LBDS at additional frequencies, for example: 4.86 GHz (6 cm) by Donnelly et al. (1987), 327 MHz (92 cm) by Oort et al. (1988).

The discovery of the most distant source in the LBDS to date was published by Windhorst et al. (1991). The steep-spectrum, compact radio source 53W002 was identified as a $z = 2.390$ galaxy. Multi-wavelength imaging and optical spectroscopy revealed a compact galaxy ($\sim$10–35 kpc in size) with a more extended Lyman-α cloud aligned with the radio emission. Several independent age estimates gave a value of $\sim$0.3 Gyr, suggesting that it was undergoing its first major starburst at that redshift. *Hubble Space Telescope* WFPC images showed that it has an $r^{1/4}$ de Vaucouleur's profile consistent with that of nearby luminous early-type galaxies (Windhorst et al. 1992). Such a regular light profile suggested that the dynamical collapse of the galaxy started about the same time as its star-formation began.

Hubble Space Telescope observations of the $z = 0.331$ radio galaxy 53W044 were made to study its structure and stellar population (Keel and Windhorst 1993). The WFC images showed the presence of a dim disk, leading to its classification as an S0 galaxy. A close companion at $\sim 2''$ from the nucleus showed evidence that it is interacting with the radio source. A FOC image and ground-based spectroscopy revealed a stellar population consistent with that seen in nearby E/S0 galaxies, and no indication of a nuclear blue-continuum source (due to its AGN).

Further *Hubble Space Telescope* and ground-based observations of 53W002, 53W044 and 53W046 ($z = 0.528$) were presented by Windhorst et al. (1994). Both 53W044 and 53W046 had the colours and spectra of early-type galaxies with $r^{1/4}$ de Vaucouleur's profiles. Unlike 53W044, there was no evidence for an exponential disk in 53W046 and it was classified as an elliptical. 53W002 was shown to have $\lesssim$30% of its V and I flux concentrated in the central kiloparsec due to its (weak) AGN, while most of its light followed a symmetric $r^{1/4}$ profile. Optical–infrared colours suggested the age of the stellar population increased with radius, from $\sim$0.3 Gyr at $r \lesssim 2$ kpc to 0.5–1.0 Gyr at $r \gtrsim 10$ kpc.

The detection of CO in 53W002 was first reported by Yamada et al. (1995). They made a weak detection of the $J = 1$–0 line at a redshift of 2.392, from which a molecular gas (H_2) mass of 2.2×10^{11} $M_\odot$ was calculated (using $q_0 = 0.5$, $H_0 = 75$ km s^{-1} Mpc^{-1}). Scoville et al. (1997) observed the CO $J = 3$–2 line at $z = 2.394$ and derived a gas mass of 7.4×10^{10} $M_\odot$, somewhat lower than the Yamada et al. result. The CO emission was extended at the same position angle as the radio continuum and optical emission, though with a radius of $\sim 3''$ it is about three times larger. A velocity gradient across the line was indicative of a (possibly forming) disk.

A total of 67 orbits of the *Hubble Space Telescope* have now been devoted to 53W002 and its companions. Windhorst et al. (1998) used these data to investigate the alignment effect and evolution of this relatively weak high-redshift radio galaxy. They placed stronger limits on the amount of AGN light from the unresolved nuclear point source ($\lesssim$ 20–25% in BVI) and found that an additional resolved ($r_e \sim 0''.05$) component — which they call a "core" — was required to match the central light distribution. After subtracting the nuclear source, the core and an $r^{1/4}$ profile (with $r_e \simeq 0''.25$) there remained two blue "clouds" aligned with the Lyα, radio continuum and CO line emission. The shape of the larger blue cloud suggested a reflection cone from the AGN, the smaller blue cloud may be separated from the nucleus by a red dust lane. All the evidence suggests that jet-induced star-formation and reflection in the AGN cone caused the alignment effect. These features are much the same as have been observed in the more (radio) powerful 3CR sources, but at much smaller angular sizes and lower optical-UV luminosities.

Long spectroscopic observations of two sources from the LBDS Hercules field have enabled detailed modelling of their spectra to be used to determine their ages. 53W091 was found to be 3.5 Gyr old at $z = 1.552$ (Dunlop et al. 1996; Spinrad et al. 1997), and an age of 4.0 Gyr was determined for 53W069 at $z = 1.432$ (Dey 1997; Dunlop 1999). These results will be discussed further in chapter 5.

Parts of the LBDS have also be used for other studies. Deep CCD observations of the Lynx-3 field (08^h 45^m $+44°36'$) were used to measure the galaxy two-point correlation function to $g \simeq 25$ (Neuschaefer et al. 1991; Neuschaefer 1992; Neuschaefer and Windhorst 1995a). Narrow-band images of the field around 53W002 led Pascarelle et al. (1996a,b) to discover a group of emission-line objects at $z \simeq 2.4$ around the radio source. A discussion of Pascarelle's work is to be found later in chapter 6.

2.1.3 Sample completeness and source weights

Before summarising the radio properties of the LBDS Hercules field, it is necessary to discuss the completeness of the sample and the associated weighting of radio sources. Given the selection criteria of the LBDS ($S_p/N \geq 5\sigma$, attenuation ≤ 5), the sample will be complete only for certain ranges in total flux density S_ν, angular size ψ and the component flux ratio f. A detailed discussion of the completeness is to be found in Windhorst et al. (1984b).

Due to the primary beam attenuation (i.e. the sensitivity of the telescope decreases with radial distance from the pointing centre), the signal-to-noise of a given source will depend on where it is on the map. For example, a source that lies just above the 5-σ cut at the centre of the map would have fallen below the cut if it happened to lie at the edge, and it would then not be included in the sample. Assuming the primary beam is isotropic then the correction for this incompleteness is a weight in the source counts and optical identification statistics. Every radio source is weighted inversely proportional to the area over which it could have been seen, before it dropped below the 5-σ threshold.

This primary beam weight is

$$W_{\rm pb} = \left(\frac{0.464}{r_{lim}}\right)^2 \qquad [2.1]$$

where r_{lim} is the distance from the beam centre (in degrees) at which the source would fall below the 5-σ cut:

$$r_{lim} = \frac{1}{61.191\nu} \arccos\left[\left(\frac{S_{\rm p}}{N}\right)\frac{A(r_{obs})}{5}\right]^{-\frac{1}{6}}. \qquad [2.2]$$

ν is the frequency in GHz, $S_{\rm p}/N$ is the observed peak signal-to-noise, and the attenuation (A) at the distance (r_{obs}) from the beam centre where the source was observed is given by

$$A(r_{obs}) = \cos^{-6}(61.191 \times \nu \times r_{obs}). \qquad [2.3]$$

A second, more complicated, source of incompleteness is the resolution/population bias — a resolved source of a given sky flux $S_{\rm TOT}^{\rm SKY}$ will drop below the 5-σ cut-off more easily than a point source of the same $S_{\rm TOT}^{\rm SKY}$. Thus the completeness depends on the distribution of source angular sizes and component flux ratios. The determination of, and statistical corrections for, this incompleteness were found by processing Monte Carlo simulations of artificial data using the same algorithms as the real data. They are detailed in Windhorst et al. (1984b), to which one is referred. High-resolution (arcsecond) VLA images have subsequently shown that the median angular size of radio sources is a function of flux density, decreasing monotonically from ∼20″ at 1 Jy to ∼2″ below 1 mJy. Windhorst et al. (1990) showed that this resulted in an overestimate of the original resolution correction, in the sense that the correction should have been $1+\epsilon$ rather than $1+3\epsilon$. The revised source weights were computed following equation (14) of Windhorst et al. (1984b) incorporating this adjustment:

$$W_{\rm res} = 1 + \frac{58''}{{\rm HPBW}_\alpha} \exp\left(\frac{-2.71(S_{\rm TOT}/N)}{(S_{\rm p}/N)_{\rm cut-off}}\right) \qquad [2.4]$$

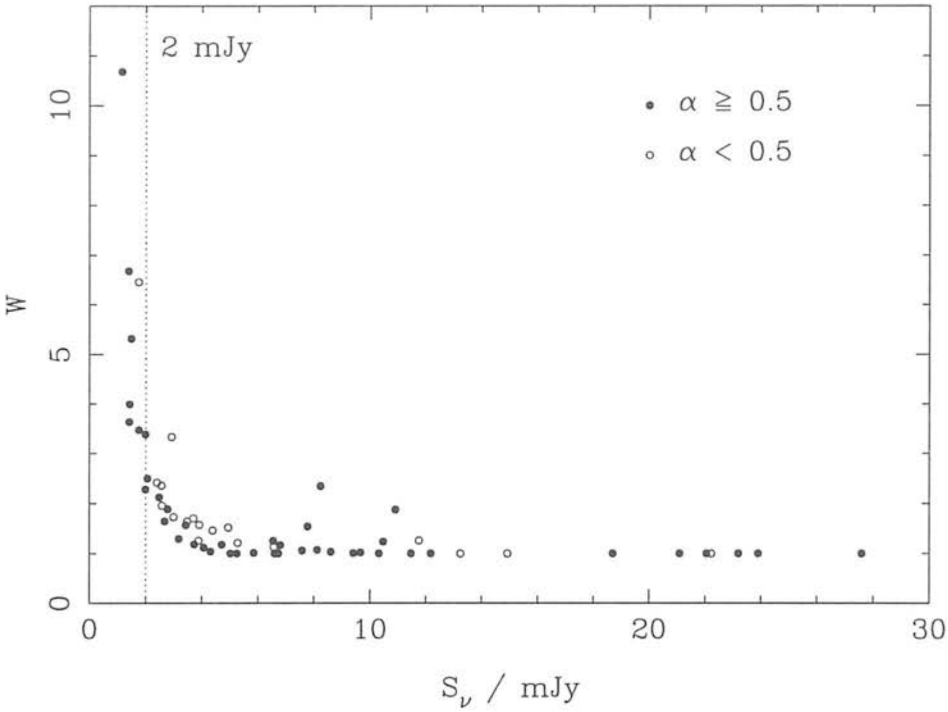

Figure 2.1 Source weights as a function of flux density for the complete Hercules sample of 73 objects. Applying the additional selection criterion $S_\nu \geq 2$ mJy excludes virtually all sources with $W \gtrsim 2.5$. Solid and open symbols denote steep-spectrum ($\alpha \geq 0.5$) and flat-spectrum ($\alpha < 0.5$) sources respectively.

where $\mathrm{HPBW}_\alpha = 12''$ is the half-power beam-width of the observations, (S_{TOT}/N) is the total signal-to-noise of the source and $(S_{\mathrm{p}}/N)_{\mathrm{cut-off}} = 5$ is the selection criterion of the sample. The statistical errors are a few percent at the $S_{\mathrm{TOT}} \simeq 10\sigma$ level, increasing to about 10% at $S_{\mathrm{TOT}} \simeq 5\sigma$.

The total weight of each source is then the multiple of the primary beam and resolution weights:

$$W = W_{\mathrm{pb}} \times W_{\mathrm{res}}. \qquad [2.5]$$

These revised weights are given in the last column of table 2.4, and are plotted in figure 2.1. This figure clearly shows how the weights rise exponentially near the survey flux density limit of 1 mJy. By applying a flux density limit of 2 mJy to the sample, the "completeness" is increased significantly from 56% to 76% — here defining the "completeness" as the ratio of the number of sources actually detected to the total weighted number of sources. There are 9 sources with $1 \leq S_\nu < 2$ mJy that are excluded, with an average weight of 5 (a "completeness" of 20%). Being the faintest objects, they have the largest errors and their effect on the sample is greatly exaggerated by the high weights. Therefore a "2-mJy sample" is defined, consisting of those 64 sources with $S_{1.4} \geq 2$ mJy. This is used in preference to the full Hercules sample in some of the statistical studies that follow.

It must be emphasized that following application of the weights, the incompleteness of the sample is fully corrected for and it is, in effect, *complete*. The agreement between the LBDS differential number counts and those of other surveys demonstrates the accuracy of the weights, even for $1 \leq S_\nu < 2$ mJy (see figure 2.2 and Windhorst and Waddington 1999).

2.1.4 Radio properties of the Hercules sample

The radio data for the Hercules sample is summarized in table 2.4 (p. 52). The co-ordinates are from the VLA 1.4 GHz observations where available (Oort et al. 1987; Oort 1988), otherwise the WSRT co-ordinates are used (Windhorst et al. 1984b). The 1.4 and 0.6 GHz fluxes ($S_{1.4}$ and $S_{0.6}$ respectively) and the resulting spectral indices ($\alpha_{0.6}^{1.4}$) are from the WSRT data (Windhorst et al. 1984b; Windhorst 1984). The radio morphological data are taken from Oort et al. where available, otherwise the WSRT data are shown. Column 6 ($\mathcal{R}$) notes whether the source is unresolved (U), resolved (R) or extended (E). An unresolved source consists of one component that is not distinguishably larger than the WSRT beam; a resolved source consists of one component whose extent is larger than the beam; and a source is classified as extended if it is clearly resolved into two (the classical double) or more components. Column 7 is the largest angular size (ψ) of the source in arcseconds, or an upper limit to ψ for unresolved sources. The position angle (ϕ) of the largest angular size is given in degrees east of north. The weights (W) have been recalculated as discussed in the previous section and are given in the final column.

The flux density distribution of all 73 sources is presented as a histogram in figure 2.2. The median flux is 3.0 mJy, and for the 2-mJy sample the median is 6.6 mJy. The dashed line in the figure is the predicted distribution based on a 5th-order polynomial fit to the 1.4 GHz differential source counts of Windhorst and Waddington (1999). The fit was based on a sample of 10575 sources drawn from a large number of recent radio surveys. The good agreement between data and model is indicative that the Hercules sample being used here is a fair representation of the full LBDS and indeed other surveys. The excess of bright sources ($S_\nu \gtrsim 80$ mJy) is not statistically significant, given the small area of the Hercules field.

In figure 2.3 the distribution of 1.4–0.6 GHz (21–50 cm) spectral indices is plotted, for both the full Hercules sample and the 2-mJy sample (taking $S_\nu \propto \nu^{-\alpha}$). Not all sources were detected at 50 cm and thus have only upper limits to their spectral index (indicated by the hatched histogram). The median spectral index of those sources with detections at both

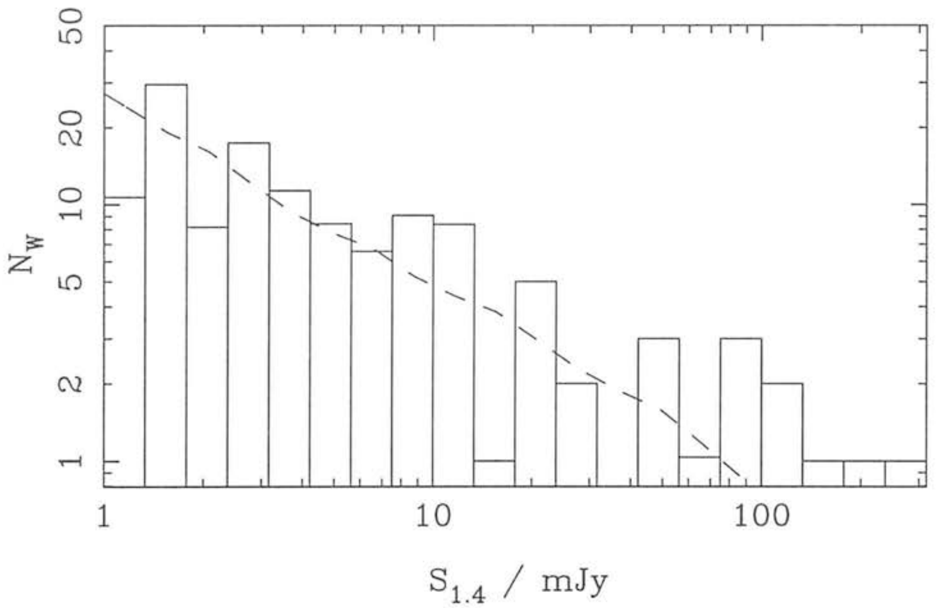

Figure 2.2 The flux density distribution for the Hercules field. The histogram is the observed data; the dashed line is the expected distribution based on the 1.4 GHz source counts (Windhorst and Waddington 1999).

frequencies (i.e. *excluding* upper limits) is $\alpha_{\rm med} \simeq 0.8$ for both samples. Taking into account the flux limits gives an upper limit to the median spectral index itself: $\alpha_{\rm med} < 0.74$ for the full sample, and $\alpha_{\rm med} < 0.79$ for the 2-mJy sample. Given the relatively few sources without spectral indices in the 2-mJy sample, the true $\alpha_{\rm med}$ will not be significantly less than 0.79 — this is then the value which will be used in the following work. Nearly half the full Hercules sample is without spectral index information, thus it is possible that $\alpha_{\rm med}$ may be significantly less than 0.74 for $S_\nu \geq 1$ mJy. This is unlikely, however, given that Donnelly et al. (1987) found that the median spectral index in the Lynx-2 area of the LBDS remains at $\alpha_{\rm med} \simeq 0.75$ down to $S_{1.4} \simeq 0.25$ mJy.

2.2 Optical identifications and photometry

Twenty-six of the seventy-three sources in Hercules were unidentified on the multi-colour Mayall photographic plates. These deep, sky limited plates reached limiting magnitudes of $23^{\rm m}_{\cdot}3$ for U^+, $23^{\rm m}_{\cdot}7$ for J^+, $22^{\rm m}_{\cdot}7$ for F^+ and $21^{\rm m}_{\cdot}1$ for N^+, roughly corresponding to a giant elliptical galaxy at $z \lesssim 1$ (Windhorst et al. 1984a; Kron et al. 1985). Thus the unidentified sources were potentially the most important for investigating the cut-off in the radio luminosity function at $z \sim 2$. In order to complete the survey, deep CCD images were obtained of the unidentified radio sources.

(a) Full sample

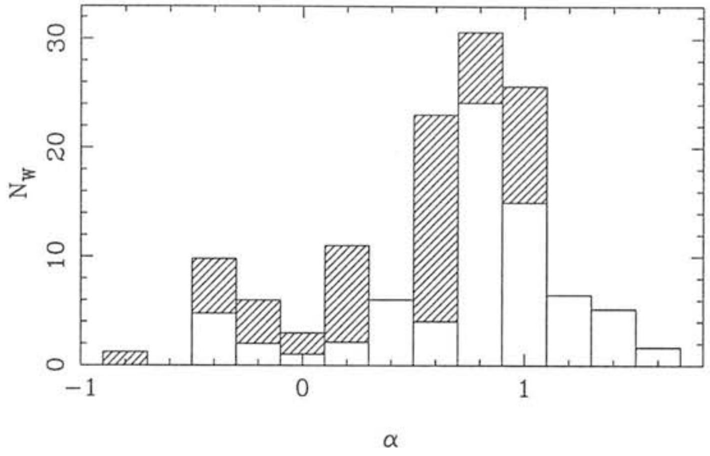

(b) 2 mJy sample

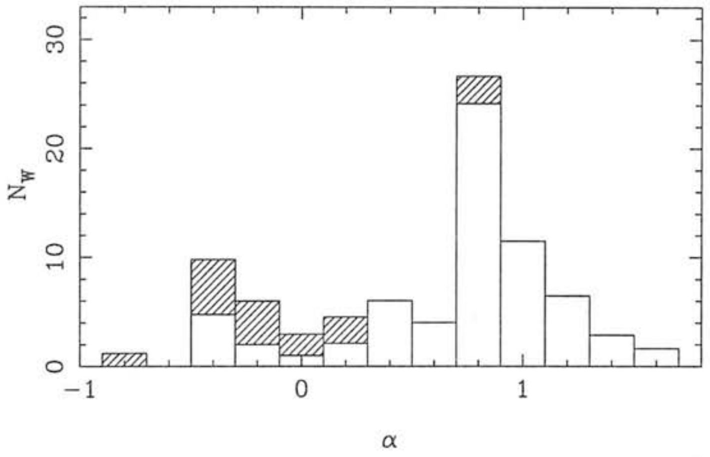

Figure 2.3 The distribution of 21–50 cm spectral indices for: (a) the complete Hercules sample ($S_{1.4} \geq 1$ mJy); and (b) the 2-mJy sample. Hatched histograms denote sources that were not detected at 50 cm and thus only have upper limits to α.

2.2.1 Observations with the Palomar 200-inch

The Hercules field was observed on the 200-inch Hale telescope at Palomar Observatory between 1984 and 1988 (table 2.1), using the Four-shooter CCD camera. This camera consists of four simultaneously exposed 800×800 pixel Texas Instruments CCDs, covering a nearly contiguous field of $\sim 9' \times 9'$, with a pixel scale of 0.332 arcsec pixel^{-1}. The total field of view is split by a reflecting pyramid into four separate beams which go to one each of the detectors. Poor reflections at the edges of the pyramid results in a strip of $\approx 10\farcs0$ of sky between the CCDs which is not exposed, but >95% of the field is imaged by the detectors. One simultaneous

Table 2.1 Palomar Observing Runs

Date	Observers	Notes
1984 July 31 – August 2	Windhorst, Koo	Liquid N_2 on pyramid
1985 June 16 – June 18	Windhorst, Koo	2/3 photometric nights
1986 July 31 – August 3	Windhorst, Koo	2/5 photometric nights
1987 May 27 – May 28	Windhorst, Koo, Anderson	53W043, 1/2 phot. nights
1987 July 26 – July 29	Windhorst, Koo, Rosema	Mostly spectroscopic data
1988 June 7 – June 8	Windhorst, Koo, Mathis	Photometric *i*-band data

exposure of the four CCDs is defined as a *frame*.

Sixteen separate pointings of the telescope were used in order to observe all of the unidentified radio sources (figure 2.4). Multiple observations were made through Gunn g, r and i filters over the six runs. Photometric standard stars were observed each night, normally at the start, middle and end of observing. Many of the nights were not photometric, though in almost all cases at least one photometric frame was obtained in each filter for each source. During the 1984 run, a problem with the the Four-shooter resulted in liquid nitrogen coolant being spilled onto the pyramid thus obscuring much of the frame — although taken in otherwise photometric conditions, these 'blotchy' images were only occasionally used in the analysis. The May 1987 run was principally an attempt to observe 53W043 by occulting a very bright star in the field that obscured the radio source. The July 1987 run was mostly spectroscopic data but it also contained a few images.

2.2.2 Data reduction methods

The first stage in processing the images was to get the data onto disk in a format that IRAF will read. This normally trivial stage was very time-consuming due to the age of the data. Two copies of the observations at the telescope were saved onto a multitude of half-inch reel-to-reel tapes at 1600 bpi density (about 28 images per tape) and a back-up copy of the data was saved at 6250 bpi. For the 1984, 1985 & 1986 observations, these tapes were copied to DAT tape in FITS format a number of years ago and thus the data could be read directly by IRAF. For the 1987 runs, the 6250 bpi back-up tapes were read using a microvax at Arizona State University and the resulting FITS files were then transferred to the Unix workstation and converted to IRAF format. The final observing run, June 1988, posed the greatest difficulty. Only one high-density tape existed, which was read by the Vax without difficulty, with the remaining three-quarters of the data only available on the 1600 bpi format. Only about half the files on

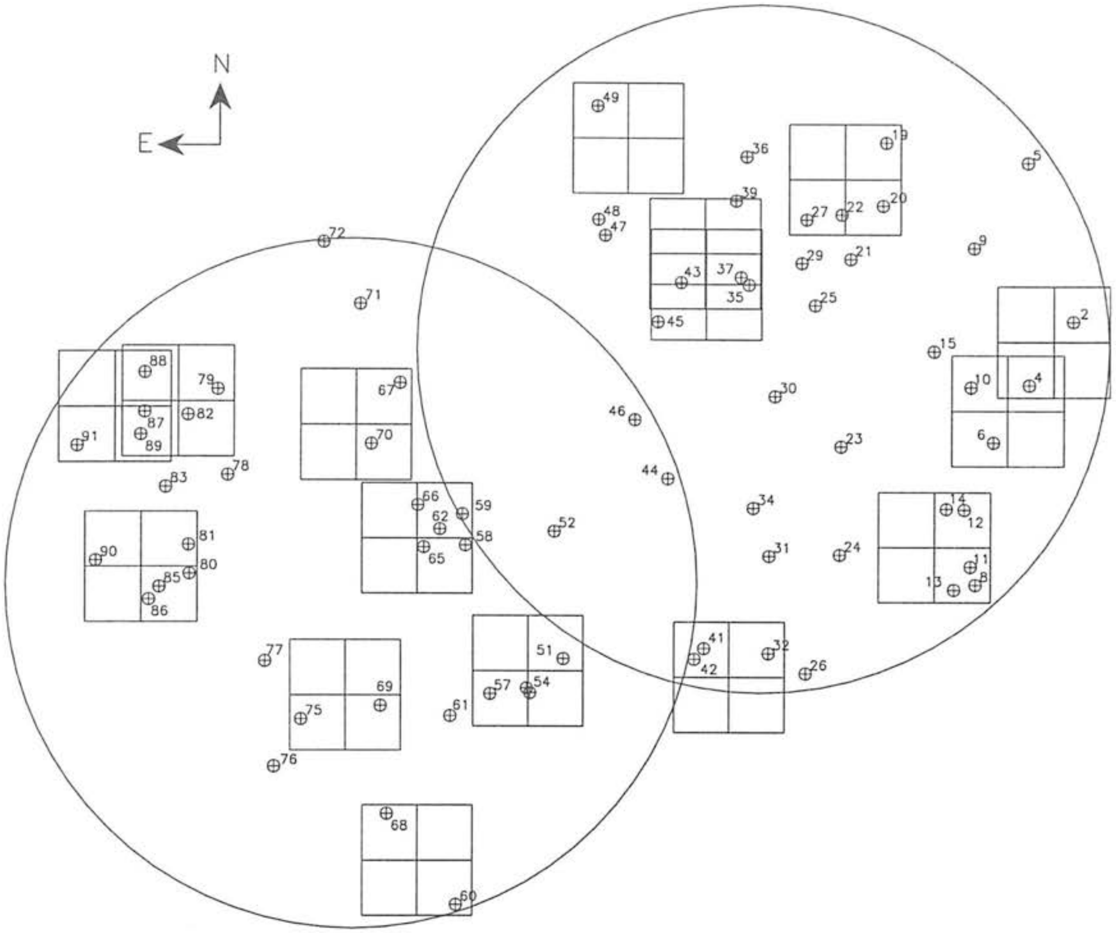

Figure 2.4 Schematic map of the Hercules field. Each radio source in the complete sample is denoted by an encircled cross. The two large circles show the radial limit of the radio observations (at the -7dB attenuation radius of $0\overset{\circ}{.}464$). The boxes show the positions of the Four-shooter observations. The centres of the two fields are $17^{\rm h}\,18^{\rm m}\,58^{\rm s}$ $+49^\circ\,58'\,00''$ and $17^{\rm h}\,15^{\rm m}\,33^{\rm s}$ $+50^\circ\,17'\,00''$ (1950).

each of these low-density tapes could be read in batch mode, the rest had to be read one file at a time using the image reduction package "CASSANDRA" by D. P. Schneider. Between one and ten of the files on each of these tapes proved to be unreadable by any method, but only in five cases were both copies of the file corrupted. The lost data was not essential to the project.

The images were processed in a standard manner (Neuschaefer 1992; Neuschaefer and Windhorst 1995b), but with some important differences. The first step in the reduction is to remove the bias level from each exposure. Examination of several bias frames confirmed that there was no two-dimensional structure to the bias (the mean counts in a 10×10 pixel box varied by $\lesssim 0.3\%$ across the image). Each CCD has a 'bias strip' of 16 columns width along one edge, so for each exposure a first order spline was fitted to this and then the bias subtracted from across the image. The bias strip was removed producing a square 800×800 pixel array.

The next step is normally to remove the dark current — a two-dimensional pattern across the CCD produced by thermal noise in the electronics, which scales with exposure time. For these data there were only one or two dark frames taken each run, generally of short exposure time and poor quality. The Four-shooter CCDs have a very low dark current, which the observers considered to be negligible. Tests on the two best dark frames showed that the counts were comparable to the noise in the bias frames for exposures of about 1000s (corresponding to a dark current of $\sim 10^{-3}$ e^{-} s^{-1} pixel^{-1}). To have used the darks that were available would have severely degraded the signal-to-noise in the data, thus no correction for the very small dark current was made.

Construction of high quality flat-fields was one of the most important parts of the image processing. Flat-field images of the inside of the telescope dome were made at the beginning and end of each night. These images were the average of eight exposures of 7–10 seconds each for g and 2–4 seconds each for r and i. For each observing run, the mean of *all* the flat-field images was calculated, after scaling and rejection of deviant pixel values, to give a single flat-field for the whole of the run. Each of the individual flat-field images was then divided by this mean flat-field. In most cases this produced a perfectly flat, though noisy, image as expected, but occasionally significant patterns remained demonstrating that the individual flat-field was not really flat at all. This was most likely due to temperature changes in the camera, as most of the deviant flats appeared at the start of a run, shortly after the Four-shooter had been installed on the telescope and before the dewar had fully cooled down. The mean flat-field was then constructed a second time, excluding such deviant images. The mean value of all the pixels in all four CCDs of the flat-field frame was calculated, and each image scaled by this single value. Scaling in this way corrected for the global sensitivity differences between the four CCDs.

Following subtraction of the bias, each science frame was divided by the appropriate flat-field for that CCD and filter. This produced images that were corrected for pixel-to-pixel sensitivity variations, removing most of the defects visible in the raw image. However, in some of the g and r images and in almost all the i images, large-scale gradients remained across the CCDs. Neuschaefer and Windhorst (1995b) determined that the features in g and r were due to scattered light rather than sensitivity variations in the CCDs. As this project concerns individual sources, such global gradients are not important and no attempt was made to remove them (the photometry routine described below takes account of localized variations in the sky background).

The features in the i-band images that remained after flattening posed a more serious problem, as they appeared to have two distinct sources. First, there were large-scale gradients across the images of a few percent of the sky background (larger than in the g and r images), and very similar in appearance to the flat-field pattern itself. Rather than being scattered light, it is suggested that this is due to the different spectral characteristics of the night sky compared to the lamp used to illuminate the flat-fields, an idea supported by the observation that the problem was most significant near twilight when the sky was changing most rapidly. This is then an extra *multiplicative* correction. The second problem with the i images is that of fringing — the strong night sky lines interfere in the CCD producing Newton's fringes, seen as brightness variations on a smaller scale than the large gradients. This is an *additive* correction that scales with the brightness of the sky background.

Following Neuschaefer and Windhorst (1995b), who actually only considered the fringing, an i-band 'superflat' was constructed. Most of the i-band data were taken in the June 1988 run, in which there are approximately 50 science frames. Observations of the same region of sky were offset by 10–20 arcsec each time and repeated no more than three or four times during the run, thus all the frames were effectively pointing at different parts of the sky. Just as with infrared imaging, a flat-field (or "superflat") was constructed from the median of all 50 frames, using a ± 3-σ rejection on each pixel. This produced a high signal-to-noise picture of the sky flat-field, devoid of all sources. Each CCD was scaled by a single mean value to give a normalised superflat.

The superflat was divided into the flattened i-band images in order to remove the large-scale gradients, which it did successfully. The fringing pattern was also removed by this process, although it is really an additive error. If fringing had been the dominant problem, then a scaled version of the superflat should have been subtracted from the image to remove the fringes. This was done for several frames and the results compared with those obtained by dividing by the superflat. There was no visible difference between the results of the two methods, nor were they statistically different (both methods increased the sky noise by 0.5–1.0%). For the i-band observations in earlier years there were not enough independent exposures to construct a superflat, however using the 1988 superflat often improved the images from these earlier runs.

The final stage of the processing was to combine the images from different years to produce an image of each radio source in the g, r and i filters. Before combination, each image was edited to remove bad lines or columns, trimmed to remove the unexposed parts of the CCD, and the shadow of the Four-Shooter guide-arm was interpolated over where necessary. The images were registered using three or four unsaturated stars — most images only required a X–Y offset, although the 1988 data also needed a $0\overset{\circ}{.}7$ rotation to be applied. The images were added together as they were generally of different exposure times, although for a few cases a clipped average was possible.

2.2.3 Astrometry

The astrometry was performed on the r-band images in general. Occasionally the radio source was not visible in r, in which case either the g or i image was used. The Cambridge APM Guide Star Catalogue (Lewis and Irwin 1997) was used to find 10–20 secondary standards in each image of interest. This catalogue is based on digitised scans of the first epoch Palomar Observatory Sky Survey O (blue) and E (red) survey plates. The astrometry is calibrated by using 200+ PPM astrometric standards per Palomar field, resulting in an internal accuracy of 0.1–0.2 arcsec, and accurate to 0.5 arcsec externally. The co-ordinates used were taken from the red plates so as to most closely match the Four-shooter r-band observations.

The centroid of each secondary standard was measured on the image and matched with its co-ordinates from the catalogue. A six coefficient linear model was fitted to the data using the program ASTROM (Wallace 1994). Any sources that had residuals greater than $1''$ were deleted from the list and a new solution computed. This step removed wrong catalogue identifications, saturated stars with a poorly-defined centroid and stars with a non-negligible proper motion. Occasionally a third iteration was required. No more than five sources were removed from a list, and all final solutions used at least eight secondary standards. The root-mean-square residuals for the astrometric solutions were 0.5 ± 0.1 arcsec.

2.2.4 Optical identifications

The 21 cm radio co-ordinates from table 2.4 were converted to pixel co-ordinates on the Four-shooter images. The errors in the radio positions are typically $0''.5$–$1''.0$. Combining these in quadrature with the optical astrometry errors defines a circle about the predicted co-ordinates of the source, with a radius (σ) of $0''.7$–$1''.2$, within which the optical counterpart to the radio source is expected to be found. Strictly, the errors in Right Ascension and Declination are not equal and the search area should be an ellipse (Windhorst et al. 1984a), however with an ellipticity of typically 0.1–0.2 the assumption of symmetrical errors was adequate for all identifications.

An optical identification was considered to be real if the source was within 3-σ of the radio position *and* if it was detected in at least two passbands. In many cases the positional agreement was better than 1-σ.

A total of 48 sources were observed, of which 26 had not been identified on the Mayall photographic plates. Of these sources, optical identifications for 19 of them are proposed here, 3 have been published elsewhere (53W002, 53W069, 53W091) and only 4 sources remain unidentified (53W006, 53W037, 53W043, 53W087). Of the new identifications, 53W054 which was previously classified as a two-component radio source has now been reclassified as two independent objects with solid IDs (53W054A & 53W054B). In addition, two sources have new identifications compared with those in Windhorst et al. (1984a): 53W051 has a good ID where it was previously associated with a source offset along the radio axis; and 53W022 is identified with a fainter source $5''$ to the NW of the original candidate.

The co-ordinates of the identifications are given in table 2.5 and the images are presented in figures 2.10–2.53, together with the Four-shooter finding charts (section 2.5).

2.2.5 Photometry

The photometric calibration of the Four-shooter images was done in two stages, due to the non-photometric conditions during a significant number of the observing nights. For most of the sources, at least one exposure had been taken on a photometric night which could therefore be calibrated accurately. This calibrated exposure was then used to bootstrap a zero-point for the non-photometric mosaic of all the exposures.

The apparent magnitude of a source (m) is defined by

$$m = m_{\mathrm{inst}} + k \cdot \overline{\sec z} + C \cdot (g - r) + z_p \qquad [2.6]$$

where the instrumental magnitude is

$$m_{\mathrm{inst}} = -2.5 \log \left(\frac{DN}{t} \right) + 25.65 \qquad [2.7]$$

DN is the number of counts in the source (i.e. flux), t is the exposure time, "25.65" is a constant chosen to be close to the zero-point of all three filters, k is the extinction coefficient, $\overline{\sec z}$ is the time-averaged airmass, C is the colour coefficient, $(g - r)$ is the instrumental colour of the source, and z_p is the zero-point correction (relative to a zero-point of 25.65). Higher order terms are not included due to the limited number of standard star observations available. For a derivation of these equations see, for example, Henden and Kaitchuck (1982).

For each night of the observing runs, there were between three and eight observations of Gunn standard stars made. These were taken throughout the night at different airmasses and in all three filters. Instrumental magnitudes in a 30–40 arcsec circular aperture were measured for each star, on every night that the log sheets recorded as being 'photometric' or 'clear'. True apparent magnitudes (m_0) were taken from a list of both published and unpublished standards available at the telescope. The magnitude equation [2.6] was then fitted to the data

Table 2.2 Mean extinction & colour coefficients

Filter	$\overline{k}$	$\overline{C}$
g	-0.28 ± 0.05	0.16 ± 0.02
r	-0.14 ± 0.03	0.10 ± 0.01
i	-0.11 ± 0.02	0.05 ± 0.01

($m_0 - m_{\rm inst}$, sec$z$, $g - r$) using a linear least squares method. This gave best-fit values for k, z_p and C for each night. The colour coefficients are not expected to change from night to night and the fitted values were indeed consistent, thus a weighted average over all the nights in a run was used. A second least squares fit was then performed with C fixed at its average value, and values for k and z_p were found for each photometric night.

The next stage was to calculate apparent magnitudes for a number of sources in each photometric image containing a radio source. This was done using the automated image detection program PISA (Draper and Eaton 1996). The search parameters were chosen such that a source was defined as having at least eight contiguous pixels with values greater than 5-σ above the background, resulting in 20–80 detections per exposure. The fluxes were then converted to apparent magnitudes using the calibrations described above. This process was then repeated on the corresponding non-photometric mosaic. The extinction and colour coefficients used for the mosaics were taken as the mean of the values over all the runs (table 2.2). The zero-point of the mosaic image was then found from the mean difference between the magnitudes from the non-photometric mosaic and the calibrated magnitudes from the photometric exposure. Only sources in the magnitude ranges $18 < g < 23$, $18 < r, i < 22$ were used for the comparison to avoid possible saturation at the bright end and poorly determined fluxes at the faint end (recall that magnitudes were calculated from the lowest isophote which is 5-σ above the background — the photometric image is not as deep, therefore the isophote is smaller and the flux enclosed is less than in the mosaic image).

For six sources (53W006, 10, 19, 20, 22, 27), only r-band observations from the 1984 run are available so no colour correction could be applied to them. In addition, only two standard star observations were available for each of the two nights, which was inadequate to determine both the extinction and zero-points. Thus, the mean extinction coefficient from table 2.2 was adopted, and the zero-point calculated from the observed magnitudes of the standards. For five other sources (53W080, 81, 85, 86, 90), no photometric calibrations were available for the g and r images. The zero-points adopted for these mosaics were taken as the mean of the zero-points for all the other observations in the sample. This is reflected in the slightly larger errors in the magnitudes for these sources.

The most crucial stage in measuring the flux of a faint source is to accurately subtract the sky emission from beneath the object. This was done using a method based upon the image reduction package "CASSANDRA" by D. P. Schneider, here adapted to run as an IRAF task using the APPHOT package for the numerical work. The first step in measuring the instrumental magnitude was to select a rectangular box (typically $10''$–$20''$ a side) surrounding the source and excluding any other objects, which was then cut out of the mosaic image. A plane was fitted to this box, excluding a circle centered on the source with a radius $1''$ larger than the required aperture. This fitted sky was then subtracted from the image. Photometry was performed using a circular aperture of $4\overset{''}{.}0$, $7\overset{''}{.}5$ or $10\overset{''}{.}0$ diameter (depending on the extent of the source), with the sky statistics determined over the remainder of the box. This enabled a large asymmetric sky aperture to be used, which is not possible with the basic APPHOT, in addition to providing a better measure of the sky background than is possible with an annulus around the object.

During testing of this method an error was found in the way that APPHOT calculates magnitude errors for faint objects. APPHOT makes the approximation $\log(1+\Delta) \approx \Delta$ which for faint sources overestimates the error by as much as 0.1–0.2 magnitudes. This was corrected by including the second, and for good measure the third, order terms in the expansion: $\log(1+\Delta) \approx \Delta - \Delta^2/2 + \Delta^3/3$. The apparent magnitude was then calculated from equation [2.6] using the coefficients in table 2.2 and the appropriate zero-points. The results are presented in table 2.5 (p. 56). The errors quoted are the quadratic sum of the instrumental magnitude errors from APPHOT (shot-noise in the object aperture, sky-noise), and the errors in the determination of k, C and z_p.

In order to compare those radio sources with photographic magnitudes, $J^+F^+N^+$, to those sources with Four-shooter Gunn magnitudes, gri, it is necessary to convert one photometric system to another. Windhorst et al. (1991) derive transformations from the Gunn system to the photographic system, and inverting these gives the required equations:

$$\begin{aligned} g &= 0.69J^+ + 0.31F^+ - 0.19 \\ r &= 1.14F^+ - 0.14J^+ + 0.34 \\ i &= N^+ + 0.75 \end{aligned} \qquad [2.8]$$

For those sources without Four-shooter observations, the optical magnitudes in table 2.5 are photographic magnitudes from Kron et al. (1985) transformed to the Gunn system using these equations. An error of 0.3 magnitudes is assigned to each of these values, corresponding to the quadratic sum of the error in the transformations ($0\overset{\mathrm{m}}{.}1$) and the error in the photographic

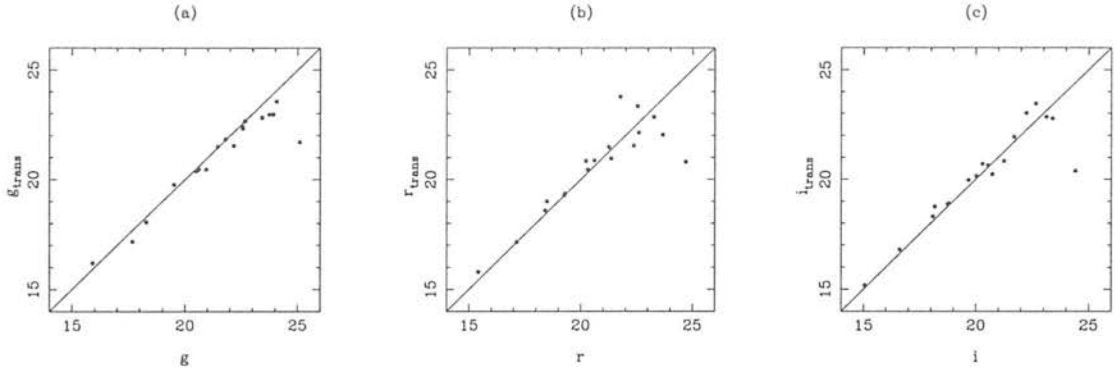

Figure 2.5 Accuracy of the photometric transformations from $J^+F^+N^+$ to gri for the eighteen sources with measurements in both systems. $g_{\rm trans}$, $r_{\rm trans}$ and $i_{\rm trans}$ are the photographic magnitudes transformed to the Gunn system with equations [2.8], g, r and i are the observed Four-shooter magnitudes.

magnitudes ($0^{\rm m}.2$–$0^{\rm m}.3$). For the eighteen sources with both photographic and Four-shooter Gunn photometry, the transformed photographic magnitudes are compared with the Four-shooter data in figure 2.5. It can be seen that the transformations are in good agreement with the data for $gri \lesssim 22$–23; fainter than this, the $J^+F^+N^+$ magnitudes are close to the detection limits of the photographic plates and are less reliable.

2.3 Infrared photometry

Infrared data are crucial to understanding high-redshift galaxies. Beyond a redshift of ~1, optical observations sample the restframe ultraviolet emission of galaxies and the restframe optical emission has shifted into the near-infrared. Thus in order to properly compare sources at high-z with those at low-z, the analysis must move to longer wavelengths. As explained in the first chapter (§1.4), the K-band has long been recognized as a valuable window through which to investigate radio galaxies, and so this project has sought to obtain K magnitudes for the complete Hercules sample.

2.3.1 Observations with the UK Infrared Telescope

Approximately half the sample has been observed during three major observing runs at the 3.8 m UK Infrared Telescope, Mauna Kea, Hawaii (table 2.3). The first two runs (1992 & 1993) used the infrared camera IRCAM, a 62×58-pixel InSb array with a pixel scale of 0.62 arcsec/pixel. All these observations were done in the K-band. The 1997 run used the upgraded camera IRCAM3, which now has 256×256 pixels with a scale of 0.286 arcsec/pixel. Deep K

Table 2.3 UKIRT Observing Runs

Date	Observer	Filters
1992 July	Dunlop	K
1993 May 15 – May 17	Dunlop	K
1997 June 1 – June 4	Waddington	H K

images were obtained for sources which had not previously been detected, together with H-band observations of several galaxies for which H was particularly important for constraining the redshift. Additional observations of some sources were made during associated projects and via the UKIRT Service Observing programme.

A standard jittering procedure was used to obtain a median-filtered sky flat-field simultaneously with the data. Nine 3-minute exposures were made, each offset by $8''$ (1992 & 1993) or $15''$ (1997) from the first position, resulting in a central area around the radio source with a maximal exposure time of 27 minutes, surrounded by a border of low signal-to-noise data. This was repeated two or three times for the faintest sources. Observations of faint standard stars were taken to calibrate the data.

2.3.2 Data reduction and calibration

For all three runs, the image processing stage in the reduction was performed at the telescope by the observers. This consisted of the following steps: (i) a dark frame observed prior to the nine-exposure sequence was subtracted from each image; (ii) a normalised flat-field was constructed by taking the median of the nine exposures; (iii) each exposure was then divided by the flat-field; (iv) an extinction correction was applied; (v) the images were registered and finally combined into a mosaic after rejection of known bad pixels.

The standard star observations were reduced in the same manner, and the instrumental magnitude (corrected for extinction) calculated. Comparison with the known apparent magnitude then yielded a zero-point. Standards were observed regularly and the zero-points were found to vary by $\lesssim 0\overset{\mathrm{m}}{.}05$ throughout each photometric night. Colour coefficients are small in the infrared and were not determined.

Photometry was performed on each of the mosaics using the same method as for the optical data (§2.2.5), with the exception of the 1992 observations for which Dunlop provided calibrated magnitudes. The results are presented in table 2.5 and figures 2.10–2.53. In addition to the 36 new observations described here, table 2.5 contains infrared data published by Thuan et al. (1984) for sixteen sources, unpublished data from Neugebauer et al. and Katgert et al. for a further twenty sources, and data on five other galaxies referenced in the notes to the table.

2.4 Analysis of the multi-colour photometry

The results of the optical and infrared photometry will be discussed in this section, and compared with both earlier results from the LBDS and with results from other radio surveys. Discussion of redshift-dependent properties will be postponed until chapters 4 & 5, following analysis of the new spectroscopic data.

2.4.1 Notes on individual sources

Before investigating the photometric properties of the sample as a whole, it is necessary to make some comments on the optical/infrared/radio observations of individual sources.

53W002 This $z = 2.390$ radio galaxy has been the subject of much study (see §2.1.2). Comparing the optical and infrared colours recorded in Windhorst et al. (1991) with those here, shows that they are fully consistent within the errors, although there is some discrepancy between the optical magnitudes. This may be explained by noting that Windhorst et al. use "total" magnitudes which are brighter than the $4''$ aperture magnitudes in table 2.5 — indeed, application of Windhorst's method to this data produces consistent results. It is important to note that the *colours* of faint sources are not significantly affected by aperture size so long as the aperture is larger than the seeing disk, which it is in all cases here.

53W006 This radio source may not be real. It lies close to 53W007 (not in the complete sample) and is not detected at 2-σ in a poor quality VLA map. There is no optical candidate in the 600s r-band image.

53W011 This radio source may not be real (due to possible confusion with the grating rings), however it does have an optical counterpart and so is retained in the sample.

53W013 This radio source may not be real (due to possible confusion with the grating rings), however it does have an optical counterpart and so is retained in the sample.

53W014 Optical ID is at 3.1-σ from the radio position. A second object, $5''$ to the NE, at 3.7-σ, may also be a possible ID.

53W022 New ID compared to Windhorst et al. (1984a). This object looks as if it could be physically associated with the brighter old ID in the r-band, but at K the two objects are very similar.

53W032 $z = 0.370$ galaxy at the centroid of a double radio source. The Four-shooter images reveal extended emission to the NE, reminiscent of a tidal tail. Note also that component A is coincident with an $r \simeq 20.3$ source, although component B does not have a separate ID.

53W035 This source appeared on two independent mosaics, enabling the accuracy of the photometry to be tested — the two sets of magnitudes are fully consistent with one another.

53W043 Radio source is $8''$ away from a very bright star. Even with this star occulted by the guide arm, the scattered light obscured the expected position of the ID.

53W054A & 53W054B Originally classified as the lobes of a "classical" double radio source (Windhorst et al. 1984b), they are now considered as two objects. Both have solid IDs in the optical, and 53W054A is clearly identified in the infrared also.

53W057 K is a 2-σ detection at the NE end of the elongated source in g. The brighter source at $6''$ to the W is also a possible ID, at 2-σ from the radio position.

53W058 Radio source in the arm of a bright spiral galaxy at $z = 0.034$.

53W067 This identification is based on spectroscopic results from the Keck telescope (Spinrad, Dey & Stern, 1997, private communication). The ID is $4\overset{''}{.}8$ (8-σ) from the radio position but has [OII] and Ca H & K lines identified in the spectrum, at a redshift of 0.759. The fainter source to the SE, originally proposed as the ID (at 1.2-σ), was found to be an M-type star.

53W069 A 4.5 Gyr-old galaxy at $z = 1.432$ — see chapter 5 for further discussion of this source.

53W089 ID is the fainter of the two objects in the centre of the images. This source appeared on two independent mosaics, enabling the accuracy of the photometry to be tested — the two sets of magnitudes are fully consistent with one another.

53W091 A 3.5 Gyr-old galaxy at $z = 1.552$ — see chapter 5 for further discussion of this source.

2.4.2 General properties of the sample

The apparent magnitude distribution is of cosmological interest because it is closely related to the radio source redshift distribution. Broadly speaking, the fainter a source is, the more distant it is expected to be. Although complicated by evolutionary effects, in the absence of spectroscopic data the magnitude distribution has been an important tool in studying radio galaxies.

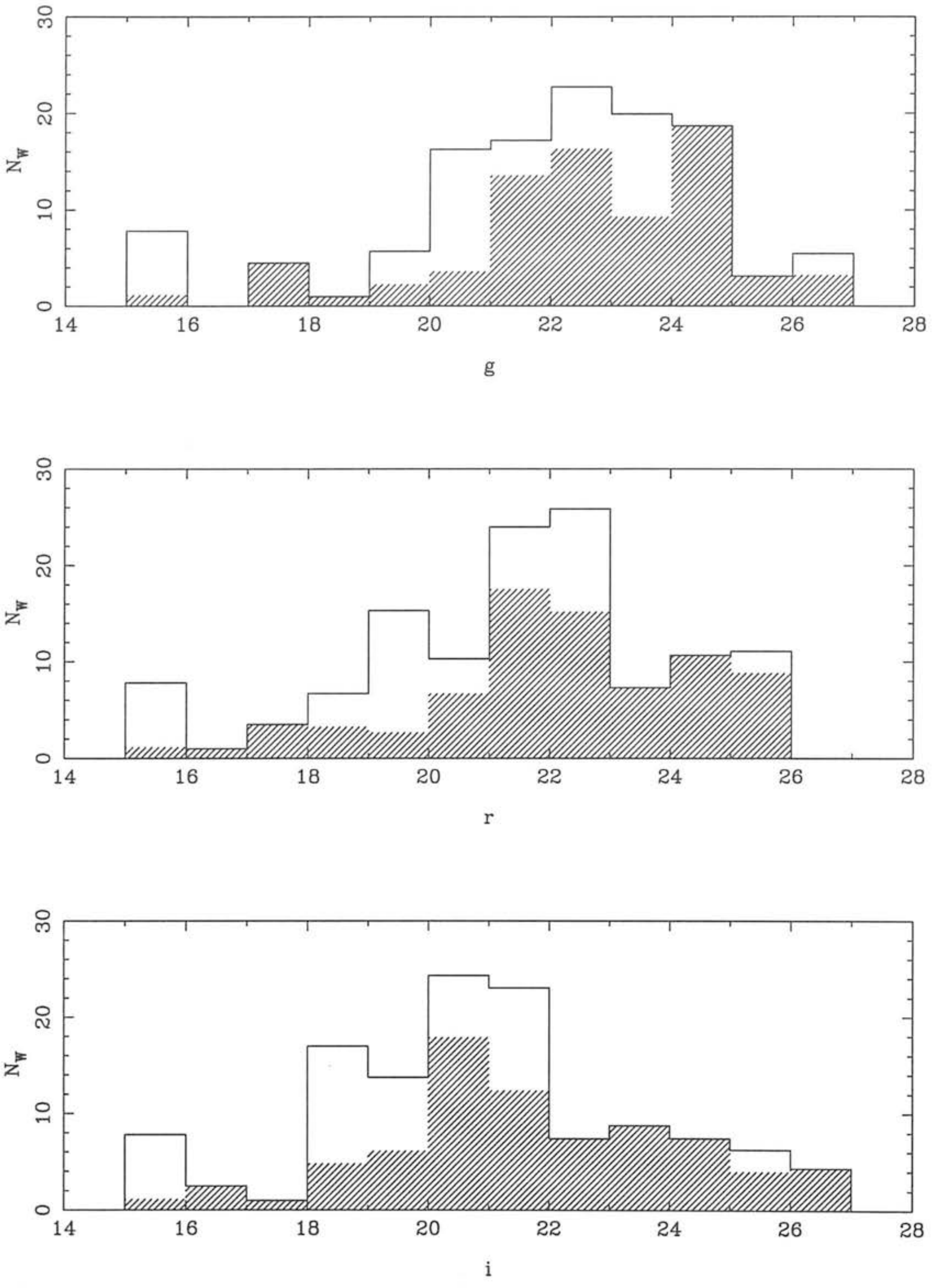

Figure 2.6 Magnitude distributions for the three optical bands (g, r, i). Shaded histograms show the 2-mJy sample data, open histograms show the full Hercules data. Photographic magnitudes have been transformed to the Gunn system using equations [2.8]. The limits of the photographic data correspond to $g \simeq 23.0$, $r \simeq 22.3$ and $i \simeq 21.5$.

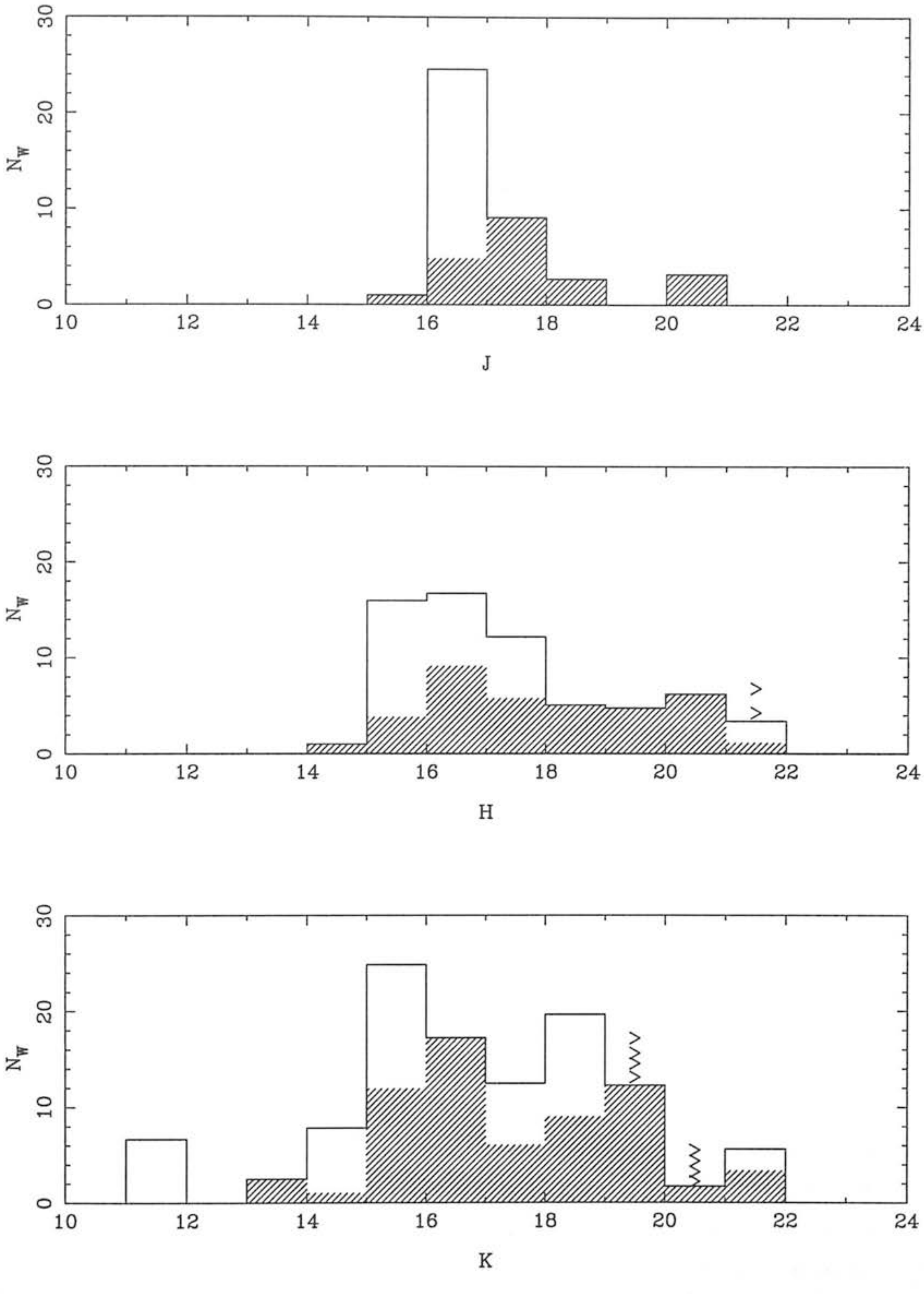

Figure 2.7 Magnitude distributions for the three infrared bands (J, H, K). Shaded histograms show the 2-mJy sample data, open histograms show the full Hercules data. Arrows denote 3-σ upper limits.

The optical data is shown in figure 2.6 and the infrared data in figure 2.7. In addition to the full Hercules distributions, the 2-mJy sample is shown as hatched histograms. The first thing that is apparent from these figures is the greater depth of the new observations. The limiting magnitudes of the Kron et al. (1985) photographic data correspond to $g \simeq 23.0$, $r \simeq 22.3$ and $i \simeq 21.5$. The Four-shooter data extend some four magnitudes fainter in all passbands. The infrared K-band data are similarly about four magnitudes deeper than the Thuan et al. (1984) results. The $griK$ data are essential complete, whilst approximately half the sources have H-band measurements and only one-third of the sample has been observed in J.

It is clear from figures 2.6 & 2.7 that the number of galaxies per magnitude interval does not continue to increase down to the magnitude limit, but rather turns over at $r \sim 22$. This immediately points to evolution of some form in the radio source population — if the radio sources formed an homogeneous class of object present throughout the history of the universe, the numbers would continue to increase towards the magnitude limit. This turnover was hinted at in the N^+ magnitude distribution of the whole LBDS (Windhorst et al. 1984a) and is clearly confirmed for the Hercules subsample here. Excluding the $1 \leq S_{1.4}(\mathrm{mJy}) < 2$ sources does not significantly change the shape of the magnitude distributions, but it does *increase* the median magnitude — i.e. the faintest radio sources are not in general the faintest sources at optical/IR wavelengths. This would suggest that the faintest radio sources are lower (radio) luminosity objects at lower redshift, rather than radio-powerful objects at high redshift. Some caution must be applied to this conclusion however, given that these sources are few in number (9) but have large weights ($\gtrsim$2.5).

In figure 2.8, the LBDS K-band magnitude distribution is compared with the results of three other radio samples with near complete infrared data. The Parkes Selected Regions (PSR) data are principally taken from Dunlop et al. (1989b). Only sources in their four-region subsample, for which the K-band data are essentially complete, are used (the 12^{h} and 13^{h} regions are poorly covered in the infrared). Further discussion of the PSR sample will be found in §3.1 below. The 1-Jansky sample of Allington-Smith (1982) is a complete sample of 59 radio sources with 1 Jy $< S_\nu <$ 2 Jy at 408 MHz. Lilly et al. (1985) presented infrared observations of 53 of these sources, which are plotted in the third panel of figure 2.8. Finally, a complete sample of 90 radio galaxies was selected from the 173-source 3CR catalogue of Laing et al. (1983). Nearly complete K-band data was obtained for this 3CR sub-sample (Lilly and Longair 1984), which excludes all quasars, and is shown in the last panel of the figure. For the first three samples, both galaxies and quasars are shown. The LBDS panel also includes the 2-mJy sample for comparison.

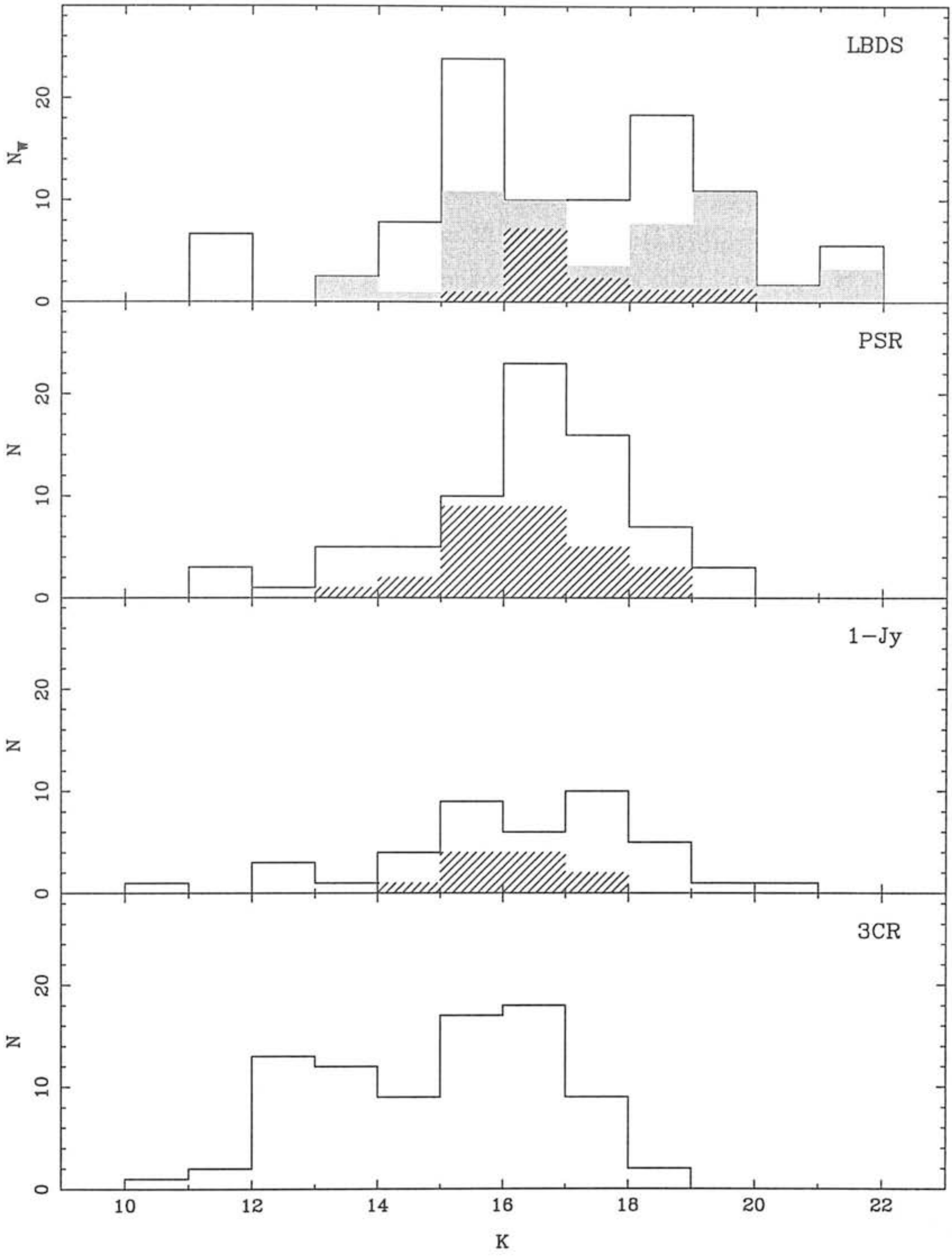

Figure 2.8 Comparison of the K-band magnitude distributions for the LBDS Hercules ($S_\nu \geq 0.001$ Jy at 1.4 GHz), PSR ($S_\nu \geq 0.1$ Jy at 2.7 GHz), 1-Jansky ($S_\nu \geq 1$ Jy at 0.408 GHz) and 3CR ($S_\nu \geq 10$ Jy at 0.178 GHz) samples. Open histograms are the galaxies and uncertain IDs (G, G? or ?), hatched histograms are the quasars (Q or Q?), and the shaded histogram in the top panel is the 2-mJy Hercules sample (note that all the LBDS quasars have $S_{1.4} \geq 2$ mJy).

As first pointed out by Dunlop et al. (1989b), the 1-Jansky radio galaxies are biased towards larger K magnitudes than the (radio) brighter 3CR galaxies. However, a similar shift is not seen between the 1-Jansky and PSR sources, a further factor of two fainter in flux. Dropping another factor of $\sim$200 in flux, the LBDS galaxies are seen here to have much the same distribution as the 1-Jansky and PSR galaxies. The median K magnitudes for the four samples are 15.3 (3CR), 16.5 (1-Jy), 16.5 (PSR) and 16.8 (LBDS). To the extent that the K magnitude of a powerful radio galaxy is a good estimator of its redshift, this result implies that although the 1-Jansky galaxies are consistent with being high-redshift counterparts of the 3CR galaxies, these same sources are not seen at even higher redshifts in the fainter samples. (Note that a median spectral index of $\alpha = 0.8$ was used to bring the flux limits of the samples to a common frequency for this comparison.)

Although the number of sources is small, the same effect is not seen in the quasar distributions. The median K magnitude of quasars in the fainter three samples increases with decreasing flux limit: 16.1 (1-Jy), 16.3 (PSR) and 16.8 (LBDS). This may suggest that the quasar population is not changing as rapidly as the radio galaxy population. It must be noted, however, that the decrease in restframe optical/infrared flux between the 1-Jansky and LBDS quasars (a factor of $\sim$2) is certainly not comparable to the drop in radio flux (a factor of $\sim$400) — i.e. if the K magnitude is a fair redshift estimator, the LBDS quasars must be less luminous in the radio than the 1-Jansky quasars.

Figure 2.9 presents colour–magnitude diagrams for the Hercules sample. To compare these results with those of Kron et al. (1985), note that the colours are related by $(g - r) \sim (J^+ - F^+) - 0.5$ and $(r - i) \sim (F^+ - N^+) - 0.4$ (from equations 2.8). It can be seen that the colours of the new identifications are comparable to those of the photographic identifications at $r \lesssim 22$. There is some bias towards bluer $g - r$ (and to a lesser extent, $r - i$) colours at the fainter magnitudes — perhaps a continuation of the faint blue radio galaxy population that Kron et al. (1985) found.

The sources classified as quasars (Q & Q?) tend to have bluer optical colours on average than the galaxies, as one would expect from the dominance of the AGN at UV/optical wavelengths in such sources. (Recall that the classification was based on morphology, not colour.) The "galaxy" class includes objects of unknown identity (?), which dominate at the faintest magnitudes. Figures 2.9(a), (b) & (f) suggest that the bluest of these objects may in fact be quasars. Figure 6 of Dunlop et al. (1989b) shows that essentially all PSR sources with $K \gtrsim 15$ and $R - K \lesssim 3$ are quasars. Comparing that figure with figure 2.9(f) here, shows that the same cannot be said for the LBDS — only one of these faint blue objects is of uncertain classification (53W068) and one is a probable quasar (53W036), while the other three are G

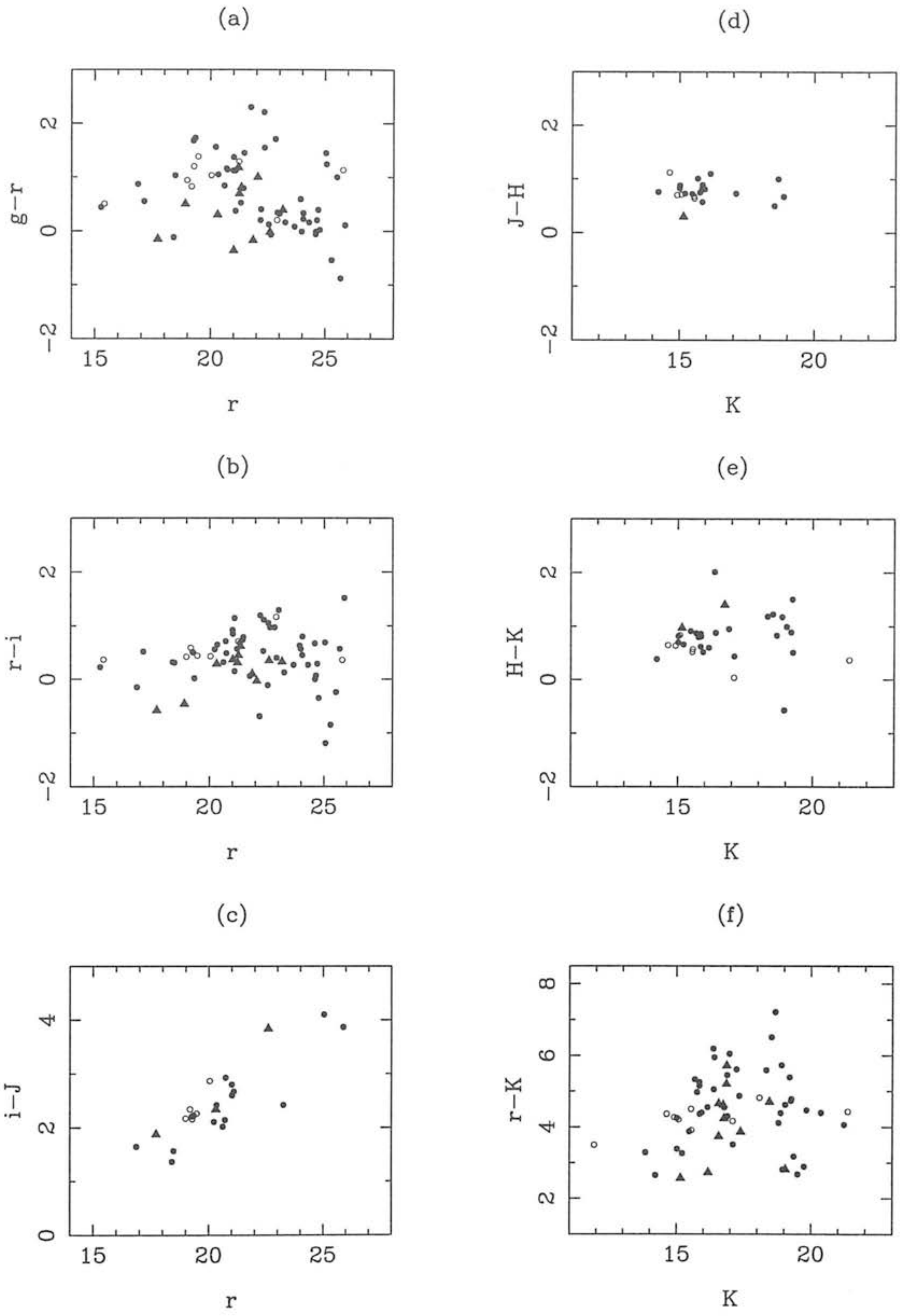

Figure 2.9 Colour–magnitude diagrams for the LBDS Hercules sample. Solid circles denote galaxies (G, G? or ? types) in the 2-mJy sample. Open circles denote galaxies with $1 \leq S_{1.4} < 2$ mJy. Triangles denote quasars (Q or Q?), all of which have $S_{1.4} \geq 2$ mJy.

(53W034, 53W067) or G? (53W027). The LBDS quasars have a much broader range of colours than those in the PSR, perhaps a consequence of their weaker AGN.

Figures 2.9(c), (d) & (e) suggest that there is a much smaller dispersion in the $i-J$, $J-H$ and $H-K$ colours of the sources, compared with the other colours. This is possibly due to the very incomplete J & H infrared data on sources fainter than $r \gtrsim 21$ or $K \gtrsim 17$. Nevertheless, this may also suggest that the radio galaxies form quite an homogenous population. The small scatter may reflect an expectation that the IR emission is due to stellar light rather than the AGN which tends to dominate at the bluer wavelengths.

2.5 Tables, images and finding charts

The data tables and images are grouped together in this final section for convenience. Table 2.4 summarises the radio data on the Hercules sample, principally taken from Windhorst et al. (1984b), Windhorst (1984), Oort et al. (1987) and Oort (1988). A full discussion of the columns was given in section 2.1.4.

Table 2.5 presents the optical/infrared data. The co-ordinates are of the optical identifications that are either presented here for the first time or are from Windhorst et al. (1984a). The redshifts (z) are taken from the literature, previously unpublished results and the new spectroscopy to be presented in chapter 3. The references are as follows: [a] Kron et al. (1985); [b] Windhorst et al. (1991); [c] Dunlop et al. (1996); [d] Dey (1997) & Dunlop (1999); [e] Windhorst et al. (1994); [f] Butcher (1982, priv. comm.); [g] Hall et al. (1996); [h] Spinrad (1997, priv. comm.); [i] Chapter 3 here; [j] Windhorst (1998, priv. comm.).

The object classification ("Type") is based on the optical/infrared appearance, and spectral features when available. The sources are divided into "galaxies" and "quasars" where: G (G?) is a clearly (most likely) extended source; Q (Q?) is a (most likely) stellar object; and sources denoted as ? are too faint to classify. The optical (gri) and infrared (JHK) magnitudes have been assembled from the results of this chapter, published results from the literature and unpublished results from Windhorst and collaborators. Photographic data from Kron et al. (1985) have been transformed to the Gunn system using equations [2.8]. Magnitudes have been measured in apertures of $4''$, $7\farcs5$ or $15''$, depending on the extent of the source. One-sigma errors are given. Footnotes to the table provide references to the sources of the photometry data.

The optical and infrared images for the sources observed during the course of this thesis are presented in figures 2.10–2.53. Each of these figures consists of a finding chart followed by the individual images of the source. The finding charts are generally r-band images (a few are g or i) of a single Four-shooter chip $\sim 4\farcm5 \times 4\farcm5$ square. This is followed by the g, r and i images (top row, left to right), and finally the J, H and K images (bottom row, left to right). These images are all $30''$ on a side; some have been smoothed by a $1''$ (FWHM) gaussian. All figures are orientated with North to the top, East to the left.

Table 2.4 LBDS Hercules Complete Sample Radio Data

Name	RA (1950)	$S_{1.4}$ mJy	$S_{0.6}$ mJy	$\alpha_{0.6}^{1.4}$	$\mathcal{R}$	ψ ''	ϕ °	W
	Dec (1950)	ΔS	ΔS	$\Delta\alpha$		$\Delta\psi$		
53W002	17 12 59.76	50.1	126.1	1.10	R	0.8	90	1.00
	50 18 51.7	(4.3)	(7.0)	(0.12)		(0.2)		
53W004	17 13 21.46	54.5	64.5	0.20	U	< 1.4	78	1.00
	50 13 46.1	(4.2)	(3.6)	(0.11)		-		
53W005	17 13 22.25	7.6	19.0	1.09	E	11.9	56	1.06
	50 31 43.2	(1.3)	(1.9)	(0.23)		-		
53W006[1,2]	17 13 39.12	2.4	< 3.0	< 0.27	U	< 9.8	139	2.42
	50 9 8.2	(0.5)	-	-		-		
53W008	17 13 47.95	306.6	597.2	0.79	R	1.9	58	1.00
	49 57 36.4	(26.9)	(31.0)	(0.12)		(0.5)		
53W009[1]	17 13 48.89	92.7	128.1	0.38	R	20.0	36	1.00
	50 24 49.2	(6.7)	(7.0)	(0.11)		(2.1)		
53W010[1]	17 13 50.30	8.1	15.1	0.73	R	11.0	100	1.07
	50 13 36.8	(0.8)	(1.2)	(0.16)		(4.5)		
53W011[1,3]	17 13 50.44	3.5	< 2.8	< 0.28	U	< 8.8	0	1.64
	49 59 4.3	(0.7)	-	-		-		
53W012	17 13 53.51	47.6	67.3	0.41	E	20.0	49	1.00
	50 3 43.5	(3.8)	(3.6)	(0.11)		-		
53W013[1,3]	17 13 58.55	3.7	< 2.7	<−0.39	U	< 10.5	125	1.70
	49 57 12.7	(0.8)	-	-		-		
53W014	17 14 2.38	5.3	< 2.7	<−0.81	E	2.9	169	1.21
	50 3 48.0	(0.7)	-	-		-		
53W015[1]	17 14 8.58	184.6	355.1	0.78	R	16.1	126	1.00
	50 16 29.7	(11.8)	(18.6)	(0.10)		(1.6)		
53W019	17 14 32.66	6.8	12.5	0.72	E	3.2	139	1.17
	50 33 21.7	(0.9)	(1.4)	(0.20)		-		
53W020	17 14 34.25	6.7	16.6	1.07	R	4.0	45	1.00
	50 28 15.1	(0.6)	(1.4)	(0.14)		(0.5)		
53W021	17 14 50.26	4.7	11.6	1.07	E	12.9	25	1.18
	50 23 54.9	(0.4)	(1.0)	(0.14)		-		
53W022[*,1]	17 14 54.81	11.8	16.9	0.43	E	21.8	67	1.26
	50 27 31.1	(1.0)	(1.4)	(0.14)		-		
53W023[1]	17 14 54.89	109.9	229.1	0.87	R	9.3	65	1.00
	50 8 47.1	(6.3)	(11.7)	(0.09)		(1.0)		
53W024	17 14 55.47	10.3	16.4	0.55	U	< 1.4	11	1.00
	50 0 1.8	(0.8)	(1.0)	(0.12)		-		
53W025[1,3]	17 15 7.93	1.1	< 2.7	< 1.03	U	< 8.7	0	10.68
	50 20 10.0	(0.2)	-	-		-		

Table 2.4 *continued*

Name	RA (1950) Dec (1950)	$S_{1.4}$ mJy ΔS	$S_{0.6}$ mJy ΔS	$\alpha_{0.6}^{1.4}$ $\Delta\alpha$	$\mathcal{R}$	ψ ″ $\Delta\psi$	ϕ °	W
53W026	17 15 12.23	21.1	39.2	0.74	R	3.5	138	1.00
	49 50 24.6	(2.0)	(2.1)	(0.13)		(4.0)		
53W027[*,1]	17 15 12.36	8.3	16.2	0.80	E	26.8	127	2.35
	50 27 6.4	(1.1)	(1.8)	(0.20)		-		
53W029	17 15 14.65	22.2	18.3	-0.23	U	< 1.4	0	1.00
	50 23 33.8	(1.3)	(1.2)	(0.10)		-		
53W030	17 15 27.91	1.4	< 2.3	< 0.60	U	< 1.0	0	3.63
	50 12 51.0	(0.2)	-	-		-		
53W031	17 15 30.63	116.5	210.2	0.70	R	4.1	111	1.00
	49 59 54.9	(6.9)	(10.6)	(0.09)		(0.5)		
53W032[*,1]	17 15 30.93	10.5	20.5	0.80	E	22.4	155	1.23
	49 52 2.0	(2.1)	(1.6)	(0.26)		-		
53W034[*,1]	17 15 38.65	10.9	25.3	1.00	E	40.2	38	1.88
	50 3 49.1	(1.4)	(1.8)	(0.17)		-		
53W035	17 15 41.09	4.4	3.0	-0.44	U	< 1.3	133	1.46
	50 21 49.3	(0.4)	(0.6)	(0.27)		-		
53W036[1]	17 15 42.28	3.2	9.0	1.24	U	< 6.5	0	1.29
	50 32 12.4	(0.3)	(0.9)	(0.18)		-		
53W037	17 15 45.09	6.6	16.3	1.07	E	3.6	66	1.00
	50 22 25.7	(0.4)	(1.2)	(0.12)		-		
53W039	17 15 47.66	3.4	6.8	0.82	U	< 11.4	2	1.57
	50 28 38.3	(0.4)	(1.0)	(0.22)		-		
53W041	17 16 3.19	9.4	19.8	0.88	U	< 1.4	151	1.01
	49 52 26.5	(0.9)	(1.1)	(0.14)		-		
53W042	17 16 8.08	6.6	16.1	1.07	R	1.3	0	1.26
	49 51 33.9	(0.8)	(1.0)	(0.17)		(0.5)		
53W043	17 16 15.09	2.7	9.6	1.52	E	2.7	0	1.65
	50 22 0.2	(0.3)	(0.9)	(0.17)		-		
53W044	17 16 21.55	1.8	3.8	0.92	R	2.0	0	3.47
	50 6 11.5	(0.3)	(0.5)	(0.23)		(0.5)		
53W045	17 16 26.72	1.5	< 2.4	< 0.58	U	< 1.0	17	5.32
	50 18 50.5	(0.3)	-	-		-		
53W046	17 16 38.16	63.1	112.6	0.69	R	3.2	143	1.03
	50 10 57.1	(3.2)	(5.7)	(0.09)		(0.5)		
53W047	17 16 53.49	23.9	42.0	0.67	R	1.4	94	1.00
	50 25 49.2	(1.6)	(2.3)	(0.10)		(0.5)		
53W048	17 16 56.84	11.5	22.6	0.81	R	1.3	90	1.00
	50 27 5.5	(1.1)	(1.7)	(0.14)		(0.5)		

Table 2.4 *continued*

Name	RA (1950)	$S_{1.4}$ mJy	$S_{0.6}$ mJy	$\alpha_{0.6}^{1.4}$	$\mathcal{R}$	ψ ″	ϕ °	W
	Dec (1950)	ΔS	ΔS	$\Delta\alpha$		$\Delta\psi$		
53W049	17 16 57.36	95.1	188.9	0.81	E	30.9	78	1.00
	50 36 18.2	(8.0)	(10.2)	(0.12)		-		
53W051[1]	17 17 14.23	141.6	294.3	0.87	R	19.6	30	1.00
	49 51 35.6	(8.3)	(14.8)	(0.09)		(1.6)		
53W052	17 17 18.70	8.6	16.1	0.74	R	2.2	9	1.03
	50 1 55.8	(0.6)	(1.0)	(0.10)		(0.5)		
53W054A[1,4]	17 17 31.05	3.9	2.8	-0.39	U	< 12.5	50	1.57
	49 48 51.5	(0.6)	(0.4)	(0.24)		-		
53W054B[1,4]	17 17 33.82	3.0	2.1	-0.42	U	< 12.5	50	1.73
	49 49 14.1	(0.4)	(0.3)	(0.25)		-		
53W057	17 17 51.28	2.9	< 2.2	< -0.36	R	1.0	122	3.33
	49 48 45.5	(0.6)	-	-		(0.5)		
53W058[1]	17 18 3.63	1.4	< 2.2	< 0.52	U	< 11.3	45	6.68
	50 0 47.4	(0.3)	-	-		-		
53W059	17 18 5.10	18.7	40.0	0.90	U	< 3.0	97	1.00
	50 3 18.7	(1.0)	(2.1)	(0.09)		-		
53W060	17 18 8.27	9.7	21.1	0.93	U	< 1.4	66	1.02
	49 31 43.8	(1.4)	(1.3)	(0.19)		-		
53W061[1]	17 18 11.26	2.6	< 2.3	< -0.15	R	12.3	72	2.35
	49 46 58.7	(0.4)	-	-		(5.4)		
53W062	17 18 16.56	1.7	< 2.2	< 0.28	U	< 1.4	0	6.46
	50 2 5.1	(0.3)	-	-		-		
53W065	17 18 24.64	5.3	14.5	1.21	U	< 1.4	0	1.00
	50 0 37.4	(0.4)	(0.9)	(0.11)		-		
53W066	17 18 27.66	4.1	8.8	0.91	U	< 1.4	0	1.12
	50 4 2.3	(0.3)	(0.7)	(0.13)		-		
53W067	17 18 36.79	23.2	45.8	0.81	E	12.6	101	1.00
	50 13 52.6	(1.4)	(2.5)	(0.10)		-		
53W068	17 18 43.28	3.9	5.1	0.33	U	< 1.0	31	1.26
	49 39 6.2	(0.5)	(0.6)	(0.20)		-		
53W069	17 18 46.45	3.7	7.8	0.87	R	1.6	0	1.18
	49 47 47.6	(0.3)	(0.9)	(0.17)		(0.5)		
53W070	17 18 51.12	2.6	< 2.5	< -0.04	U	< 1.4	107	1.96
	50 8 57.9	(0.3)	-	-		-		
53W071	17 18 56.81	2.8	9.3	1.43	U	< 1.4	132	1.89
	50 20 12.9	(0.6)	(0.9)	(0.26)		-		
53W072	17 19 15.30	6.6	7.6	0.17	U	< 1.4	25	1.13
	50 25 32.1	(1.3)	(1.0)	(0.29)		-		

Table 2.4 *continued*

Name	RA (1950)	$S_{1.4}$ mJy	$S_{0.6}$ mJy	$\alpha_{0.6}^{1.4}$	$\mathcal{R}$	ψ ″	ϕ °	W
	Dec (1950)	ΔS	ΔS	$\Delta\alpha$		$\Delta\psi$		
53W075	17 19 26.36	96.1	185.3	0.78	U	< 1.2	0	1.00
	49 46 42.6	(6.0)	(9.6)	(0.10)		-		
53W076[1]	17 19 39.88	1.4	< 3.0	< 0.89	R	1.0	0	3.99
	49 42 53.7	(0.3)	-	-		(0.5)		
53W077[1]	17 19 44.40	7.8	16.1	0.87	R	16.8	82	1.54
	49 51 23.7	(0.8)	(1.6)	(0.17)		(4.2)		
53W078	17 20 3.10	2.0	< 3.1	< 0.53	R	0.7	0	3.38
	50 6 26.2	(0.4)	-	-		(0.5)		
53W079	17 20 8.02	13.3	13.9	0.05	U	< 1.4	39	1.00
	50 13 22.0	(1.0)	(1.3)	(0.14)		-		
53W080	17 20 22.08	27.6	54.2	0.80	E	10.4	35	1.00
	49 58 26.8	(1.8)	(3.0)	(0.10)		(0.5)		
53W081	17 20 22.56	12.2	24.7	0.84	U	< 1.4	0	1.00
	50 0 47.6	(0.8)	(1.6)	(0.11)		-		
53W082	17 20 22.85	2.0	6.5	1.41	U	< 1.4	0	2.28
	50 11 17.3	(0.4)	(1.0)	(0.29)		-		
53W083	17 20 33.89	5.0	9.0	0.70	U	< 1.4	0	1.00
	50 5 28.9	(0.5)	(1.1)	(0.19)		-		
53W085	17 20 37.05	4.3	12.8	1.29	U	< 1.4	0	1.04
	49 57 23.1	(0.4)	(1.1)	(0.16)		-		
53W086	17 20 42.21	4.9	6.7	0.35	R	1.3	124	1.52
	49 56 22.7	(0.7)	(1.1)	(0.26)		(0.5)		
53W087	17 20 44.29	5.8	15.8	1.18	E	2.9	106	1.02
	50 11 31.8	(0.8)	(1.6)	(0.20)		-		
53W088	17 20 44.22	14.9	13.7	−0.10	U	< 1.4	22	1.00
	50 14 41.6	(1.4)	(1.2)	(0.15)		-		
53W089	17 20 46.26	2.5	7.3	1.29	E	3.2	178	2.12
	50 9 41.1	(0.5)	(1.1)	(0.30)		-		
53W090[1]	17 21 8.53	2.1	< 4.1	< 0.83	U	< 9.3	0	2.50
	49 59 30.8	(0.4)	-	-		-		
53W091	17 21 17.81	22.1	66.0	1.30	E	4.0	0	1.00
	50 8 47.4	(2.0)	(3.9)	(0.13)		-		

[*] Source has multiple radio components. [1] WSRT data only — all other sources have VLA positions and morphologies (Oort et al. 1987; Oort 1988). [2] Source not detected by VLA — probably not real. [3] Source may not be real (possible grating ring confusion), but it does have an optical counterpart. [4] These sources (53W054A & 53W054B) were originally considered to be a single two-component source (53W054*), but are now believed to be distinct objects.

Table 2.5 LBDS Hercules Complete Sample Optical Data

Name	RA (1950)			z	g	r	i	J	H	K
	Dec (1950)			Type	Δg	Δr	Δi	ΔJ	ΔH	ΔK
53W002	17	12	59.71	2.390[b]	23.42	23.26	23.13	20.71[8]	20.04[8]	18.87[8]
	50	18	51.2	G	(0.12)	(0.09)	(0.10)	(0.16)	(0.17)	(0.12)
53W004	17	13	21.42	-	24.38	24.05	23.25	-	19.78[2]	19.27[3]
	50	13	45.2	G	(0.22)	(0.16)	(0.11)	-	(0.16)	(0.27)
53W005	17	13	22.37	0.95[j]	23.34[1]	23.02[1]	21.73[1]	-	-	16.97[4]
	50	31	42.8	G	(0.30)	(0.30)	(0.30)	-	-	(0.25)
53W006	-	-	-	-	-	-	-	-	-	-
	-	-	-	-	-	-	-	-	-	-
53W008	17	13	47.98	0.733[f]	20.61	20.31	20.02	17.68[4]	-	16.57[4]
	49	57	36.0	Q	(0.06)	(0.04)	(0.05)	(0.28)	-	(0.21)
53W009	17	13	48.90	1.090[a]	17.57[1]	17.72[1]	18.30[1]	16.42[4]	16.12[4]	15.15[4]
	50	24	48.6	Q	(0.30)	(0.30)	(0.30)	(0.10)	(0.11)	(0.11)
53W010	17	13	50.17	0.48[j]	21.08[1]	19.35	19.33[1]	17.10[4]	16.38[4]	15.47[4]
	50	13	37.4	G	(0.30)	(0.05)	(0.30)	(0.14)	(0.15)	(0.07)
53W011	17	13	50.21	-	21.45	20.61	20.29	18.27[6]	17.54[6]	17.10[6]
	49	59	3.3	G	(0.06)	(0.04)	(0.05)	(0.15)	(0.12)	(0.15)
53W012	17	13	53.47	1.328[i]	23.97	23.98	23.41	-	20.75[2]	19.25[9]
	50	3	43.0	G	(0.11)	(0.11)	(0.10)	-	(0.39)	(0.40)
53W013	17	13	58.44	-	24.79	24.77	25.12	-	>21.05[2]	20.37[3]
	49	57	13.8	G	(0.18)	(0.19)	(0.33)	-	-	(0.51)
53W014	17	14	2.17	-	23.55	23.16	22.83	-	-	18.46[3]
	50	3	46.5	Q	(0.08)	(0.06)	(0.07)	-	-	(0.16)
53W015	17	14	8.62	1.129[j]	19.41[1]	18.91[1]	19.37[1]	-	-	16.18[6]
	50	16	29.5	Q	(0.30)	(0.30)	(0.30)	-	-	(0.16)
53W019	17	14	32.64	0.542[i]	22.40[1]	21.22	20.91[1]	-	-	16.57[6]
	50	33	21.0	Q?	(0.30)	(0.06)	(0.30)	-	-	(0.25)
53W020	17	14	34.19	0.100[a]	17.73[1]	16.86	17.01[1]	15.36[4]	14.60[4]	14.21[4]
	50	28	14.3	G	(0.30)	(0.05)	(0.30)	(0.07)	(0.06)	(0.06)
53W021	17	14	50.12	-	-	22.56[1]	21.51[1]	-	18.38[4]	16.37[4]
	50	23	55.6	G	-	(0.32)	(0.30)	-	(0.45)	(0.15)
53W022	17	14	54.54	0.528[i]	21.84[1]	21.32	20.64[1]	-	-	16.78[9]
	50	27	30.4	G	(0.30)	(0.06)	(0.30)	-	-	(0.06)
53W023	17	14	54.99	0.57[j]	22.12[1]	21.00[1]	20.08[1]	17.28[6]	16.71[6]	15.85[6]
	50	8	46.5	G	(0.30)	(0.30)	(0.30)	(0.17)	(0.14)	(0.08)
53W024	17	14	55.46	1.961[g]	20.65[1]	21.01[1]	20.64[1]	-	-	16.77[6]
	50	0	1.7	Q	(0.30)	(0.30)	(0.30)	-	-	(0.32)
53W025	17	15	7.87	-	23.10[1]	22.90[1]	21.74[1]	-	-	18.09[6]
	50	20	11.3	?	(0.30)	(0.30)	(0.30)	-	-	(0.60)

Table 2.5 *continued*

Name	RA (1950)			z	g	r	i	J	H	K
	Dec (1950)			Type	Δg	Δr	Δi	ΔJ	ΔH	ΔK
53W026	17	15	12.12	0.55^{i}	22.23^{1}	21.44^{1}	20.70^{1}	-	-	16.39^{4}
	49	50	24.0	G	(0.30)	(0.30)	(0.30)	-	-	(0.21)
53W027	17	15	12.07	0.403^{i}	22.56^{1}	22.63	21.66^{1}	-	-	19.74^{3}
	50	27	5.4	G?	(0.30)	(0.09)	(0.30)	-	-	(0.38)
53W029	17	15	14.63	-	23.06^{1}	22.06^{1}	22.09^{1}	-	-	16.86^{6}
	50	23	33.7	Q	(0.30)	(0.30)	(0.30)	-	-	(0.32)
53W030	17	15	27.88	0.35^{j}	21.07^{1}	20.04^{1}	19.61^{1}	16.74^{6}	16.06^{6}	15.54^{6}
	50	12	50.8	G	(0.30)	(0.30)	(0.30)	(0.16)	(0.11)	(0.11)
53W031	17	15	30.69	0.628^{a}	22.21^{1}	21.09^{1}	19.95^{1}	17.28^{6}	16.46^{6}	15.84^{9}
	49	59	54.1	G	(0.30)	(0.30)	(0.30)	(0.08)	(0.07)	(0.04)
53W032	17	15	31.09	0.37^{j}	19.51	18.48	18.17	16.60^{6}	15.87^{6}	15.21^{6}
	49	51	57.4	G	(0.07)	(0.07)	(0.04)	(0.12)	(0.10)	(0.14)
53W034	17	15	38.94	0.281^{i}	22.38^{1}	22.18^{1}	22.87^{1}	-	-	19.50^{9}
	50	3	44.3	G	(0.30)	(0.30)	(0.30)	-	-	(0.25)
53W035	17	15	41.08	-	23.74	23.66	23.39	-	20.03^{2}	19.04^{3}
	50	21	48.6	?	(0.10)	(0.09)	(0.13)	-	(0.20)	(0.25)
53W036	17	15	42.38	-	21.69^{1}	21.86^{1}	21.76^{1}	-	-	19.05^{9}
	50	32	13.1	Q?	(0.30)	(0.30)	(0.30)	-	-	(0.20)
53W037	-	-	-	-	-	-	-	-	-	$>20.74^{2}$
	-	-	-	-	-	-	-	-	-	-
53W039	17	15	47.26	0.402^{a}	20.94	19.26	18.75	16.54^{6}	15.71^{6}	15.01^{9}
	50	28	38.2	G	(0.09)	(0.05)	(0.03)	(0.11)	(0.10)	(0.06)
53W041	17	16	3.02	-	26.31	25.07	26.26	-	-	$>20.78^{2}$
	49	52	25.8	?	(0.43)	(0.23)	(0.91)	-	-	-
53W042	17	16	8.03	-	24.80	25.68	25.11	-	-	$>20.81^{2}$
	49	51	30.7	?	(0.17)	(0.47)	(0.37)	-	-	-
53W043	-	-	-	-	-	-	-	-	-	-
	-	-	-	-	-	-	-	-	-	-
53W044	17	16	21.53	0.311^{e}	19.93^{1}	18.99^{1}	18.57^{1}	16.40^{5}	15.28^{5}	14.63^{5}
	50	6	11.5	G	(0.30)	(0.30)	(0.30)	(0.19)	(0.07)	(0.08)
53W045	17	16	26.76	0.30^{j}	20.49	19.29	18.79	16.63^{6}	15.92^{6}	15.08^{6}
	50	18	49.3	G	(0.06)	(0.03)	(0.03)	(0.12)	(0.11)	(0.11)
53W046	17	16	38.26	0.528^{e}	21.39^{1}	20.34^{1}	19.69^{1}	17.27^{5}	16.46^{5}	15.94^{5}
	50	10	57.5	G	(0.30)	(0.30)	(0.30)	(0.10)	(0.08)	(0.12)
53W047	17	16	53.49	0.534^{j}	21.87^{1}	20.73^{1}	20.24^{1}	17.31^{6}	16.56^{6}	15.76^{6}
	50	25	49.5	G	(0.30)	(0.30)	(0.30)	(0.12)	(0.10)	(0.12)
53W048	17	16	56.85	0.676^{i}	22.38^{1}	21.01^{1}	20.16^{1}	17.56^{6}	16.55^{6}	15.68^{6}
	50	27	5.8	G	(0.30)	(0.30)	(0.30)	(0.12)	(0.07)	(0.06)

Table 2.5 *continued*

Name	RA (1950) Dec (1950)			z Type	g Δg	r Δr	i Δi	J ΔJ	H ΔH	K ΔK
53W049	17	16	57.39	0.23[j]	21.86	20.70	19.99	17.85[6]	16.75[6]	16.15[6]
	50	36	17.1	G	(0.09)	(0.03)	(0.03)	(0.15)	(0.12)	(0.15)
53W051	17	17	14.32	-	24.55	22.84	21.87	-	-	17.23[3]
	49	51	33.3	G?	(0.11)	(0.05)	(0.04)	-	-	(0.07)
53W052	17	17	18.66	0.46[j]	22.37[1]	21.20[1]	20.63[1]	-	17.85[4]	16.90[4]
	50	1	53.7	G	(0.30)	(0.30)	(0.30)	-	(0.32)	(0.16)
53W054A	17	17	31.25	-	24.52	23.93	23.30	-	19.52[2]	18.34[3]
	49	48	50.3	G	(0.26)	(0.16)	(0.13)	-	(0.14)	(0.13)
53W054B	17	17	34.05	-	24.26	24.04	23.59	-	20.79[2]	>19.77[3]
	49	49	16.2	?	(0.18)	(0.15)	(0.17)	-	(0.34)	-
53W057	17	17	51.12	-	24.75	25.29	26.14	-	>21.90[2]	21.22[2]
	48	48	44.8	G	(0.15)	(0.21)	(0.59)	-	-	(0.51)
53W058	17	18	3.22	0.034[a]	15.92	15.42	15.05	-	-	11.92[2]
	50	0	40.6	G	(0.09)	(0.05)	(0.04)	-	-	(0.01)
53W059	17	18	4.96	-	24.53	24.59	23.92	-	20.09[2]	19.20[3]
	50	3	19.8	G?	(0.17)	(0.18)	(0.18)	-	(0.20)	(0.19)
53W060	17	18	8.50	-	26.52	25.52	25.76	-	-	>20.77[2]
	49	31	45.0	G	(0.53)	(0.26)	(0.45)	-	-	-
53W061	17	18	11.29	-	21.95[1]	21.26[1]	20.81[1]	-	-	17.39[4]
	49	46	58.6	Q?	(0.30)	(0.30)	(0.30)	-	-	(0.26)
53W062	17	18	16.51	0.61[j]	22.54	21.25	20.54	-	17.13[6]	17.09[4]
	50	2	4.8	G	(0.11)	(0.06)	(0.05)	-	(0.20)	(0.25)
53W065	17	18	24.31	1.185[i]	23.26	22.92	22.52	-	-	18.80[2]
	50	0	37.4	G	(0.08)	(0.06)	(0.05)	-	-	(0.21)
53W066	17	18	27.64	-	24.59	24.60	24.60	-	21.34[2]	>19.28[3]
	50	4	0.9	G?	(0.18)	(0.20)	(0.32)	-	(0.32)	-
53W067	17	18	36.72	0.759[j]	24.06	21.76	21.70	-	18.38[2]	18.95[9]
	50	13	52.8	G	(0.13)	(0.07)	(0.05)	-	(0.06)	(0.20)
53W068	17	18	43.22	(0.048)[j]	22.66	22.54	22.65	-	-	19.36[3]
	49	39	6.0	?	(0.08)	(0.05)	(0.05)	-	-	(0.28)
53W069	17	18	46.48	1.432[d]	26.49	25.04	24.35	20.25[2]	19.75[2]	18.53[3]
	49	47	47.5	G	(0.60)	(0.22)	(0.14)	(0.14)	(0.18)	(0.11)
53W070	17	18	51.01	-	24.55	22.34	21.81	-	-	16.89[3]
	50	8	57.9	G	(0.20)	(0.10)	(0.05)	-	-	(0.07)
53W071	17	18	56.89	0.287[a]	21.46[1]	21.09[1]	20.94[1]	-	18.83[6]	-
	50	20	13.2	G	(0.30)	(0.30)	(0.30)	-	(0.26)	-
53W072	17	19	15.28	0.019[a]	15.71[1]	15.27[1]	15.04[1]	-	-	-
	50	25	32.5	G	(0.30)	(0.30)	(0.30)	-	-	-

Table 2.5 *continued*

Name	RA (1950)			z	g	r	i	J	H	K
	Dec (1950)			Type	Δg	Δr	Δi	ΔJ	ΔH	ΔK
53W075	17	19	26.29	2.150^a	22.16	21.35	20.73	-	18.14^4	16.74^4
	49	46	42.3	Q	(0.08)	(0.05)	(0.04)	-	(0.37)	(0.23)
53W076	17	19	39.75	0.390^a	20.85^1	19.47^1	19.03^1	16.77^4	16.13^4	15.56^4
	49	42	55.4	G	(0.30)	(0.30)	(0.30)	(0.11)	(0.11)	(0.10)
53W077	17	19	45.53	0.80^j	22.92^1	21.47^1	20.68^1	-	17.86^6	-
	49	51	26.6	G	(0.30)	(0.30)	(0.30)	-	(0.20)	-
53W078	17	20	3.12	0.27^j	20.00^1	19.18^1	18.59^1	16.25^4	15.55^4	14.91^4
	50	6	26.3	G	(0.30)	(0.30)	(0.30)	(0.09)	(0.11)	(0.06)
53W079	17	20	8.07	0.548^a	21.79	20.23	19.67	17.56^6	16.67^6	15.86^6
	50	13	20.9	G	(0.07)	(0.04)	(0.03)	(0.09)	(0.09)	(0.09)
54W080	17	20	22.05	0.546^a	18.29	18.41	18.09	16.72^4	15.84^4	15.02^4
	49	58	26.2	G	(0.12)	(0.10)	(0.04)	(0.06)	(0.10)	(0.09)
53W081	17	20	22.53	2.060^h	24.84	24.64	24.57	-	-	18.91^3
	50	0	46.7	?	(0.20)	(0.23)	(0.29)	-	-	(0.21)
53W082	17	20	22.77	1.409^h	26.92	25.79	25.43	-	21.73^2	21.36^2
	50	11	17.0	G	(0.60)	(0.38)	(0.31)	-	(0.34)	(0.68)
53W083	17	20	33.81	0.628^i	22.60^1	22.20^1	21.01^1	-	-	17.34^3
	50	5	28.9	G	(0.30)	(0.30)	(0.30)	-	-	(0.10)
53W085	17	20	37.05	1.35^j	22.57	22.59	22.24	18.40^6	-	16.87^4
	49	57	22.3	Q	(0.11)	(0.11)	(0.05)	(0.32)	-	(0.16)
53W086	17	20	42.14	0.40^j	23.91	22.36	21.25	-	17.29^4	16.41^4
	49	56	21.9	G	(0.13)	(0.11)	(0.04)	-	(0.21)	(0.10)
53W087	-	-	-	-	-	-	-	-	-	$>19.27^3$
	-	-	-	-	-	-	-	-	-	-
53W088	17	20	44.25	1.773^h	24.46	24.30	24.03	-	-	19.83^3
	50	14	40.5	G?	(0.12)	(0.13)	(0.13)	-	-	(0.29)
53W089	17	20	46.11	0.635^i	25.09	24.70	24.41	-	-	$>19.21^3$
	50	9	39.6	?	(0.21)	(0.19)	(0.33)	-	-	-
53W090	17	21	8.68	0.094^a	17.68	17.13	16.61	-	-	13.84^2
	49	59	29.0	G	(0.12)	(0.11)	(0.04)	-	-	(0.02)
53W091	17	21	17.79	1.552^c	25.99	25.88	24.37	20.5^7	19.5^7	18.67^3
	50	8	47.0	G	(0.49)	(0.48)	(0.19)	(0.1)	(0.1)	(0.13)

[1] Transformed from $J^+F^+N^+$ data using equations [2.8]. [2] IRCAM3 June 1997. [3] IRCAM1 May 1993. [4] Thuan et al. (1984). [5] Windhorst et al. (1994). [6] Neugebauer et al., Katgert et al., unpublished results. [7] Spinrad et al. (1997). [8] See chapter 6 here. [9] IRCAM1 July 1992. [*a*–*j*] See introduction to §2.5 for key to the redshift references.

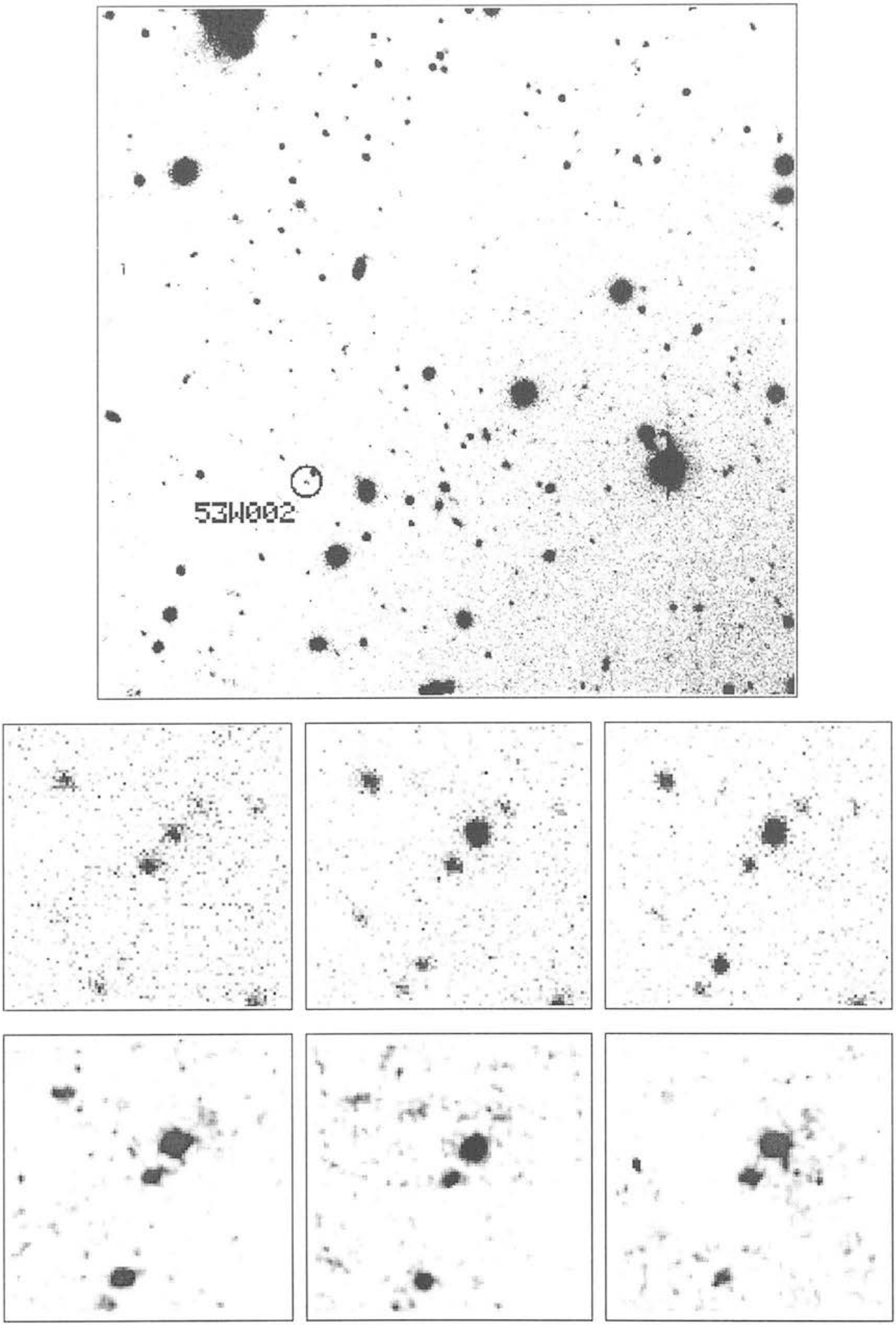

Figure 2.10 53W002

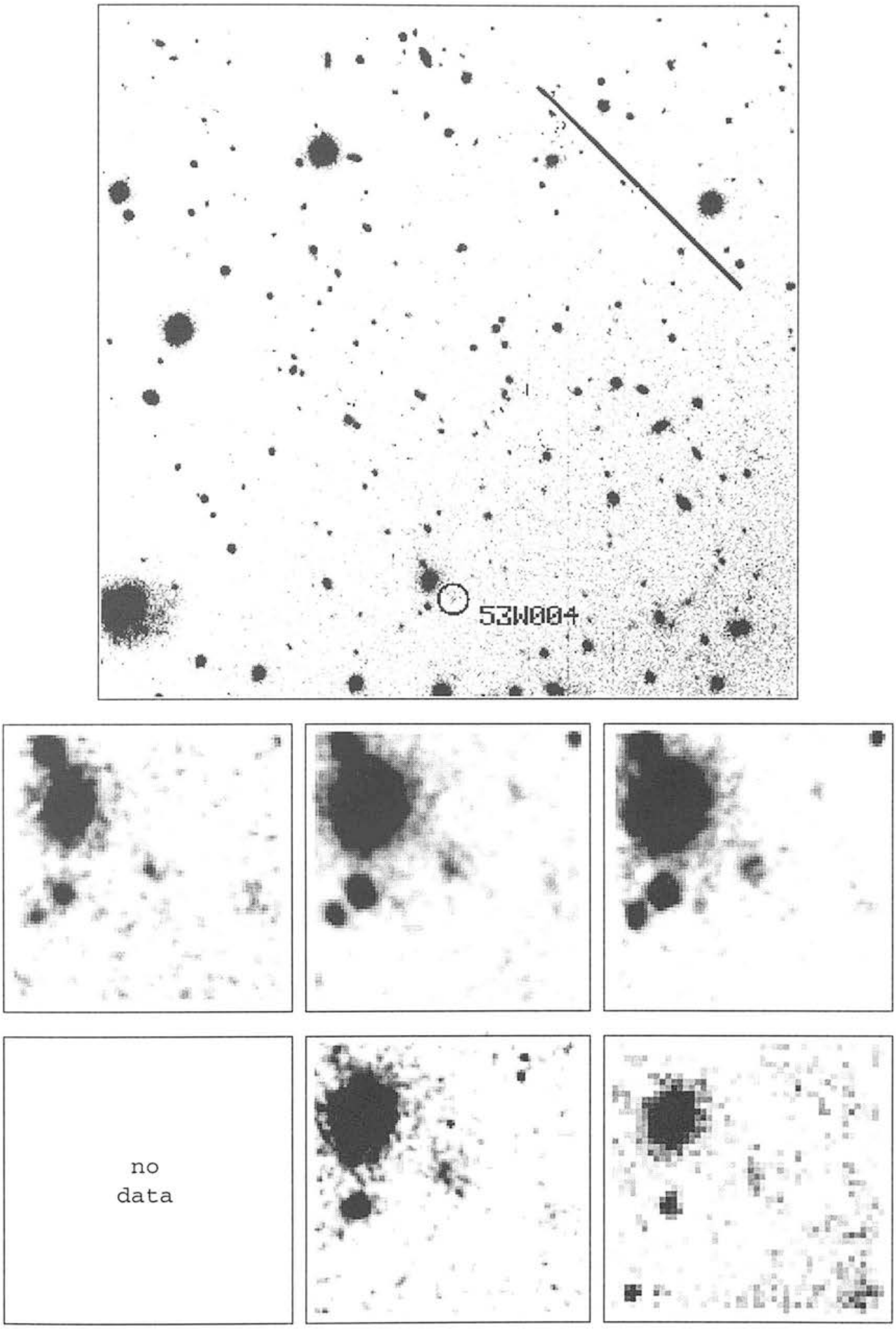

Figure 2.11 53W004

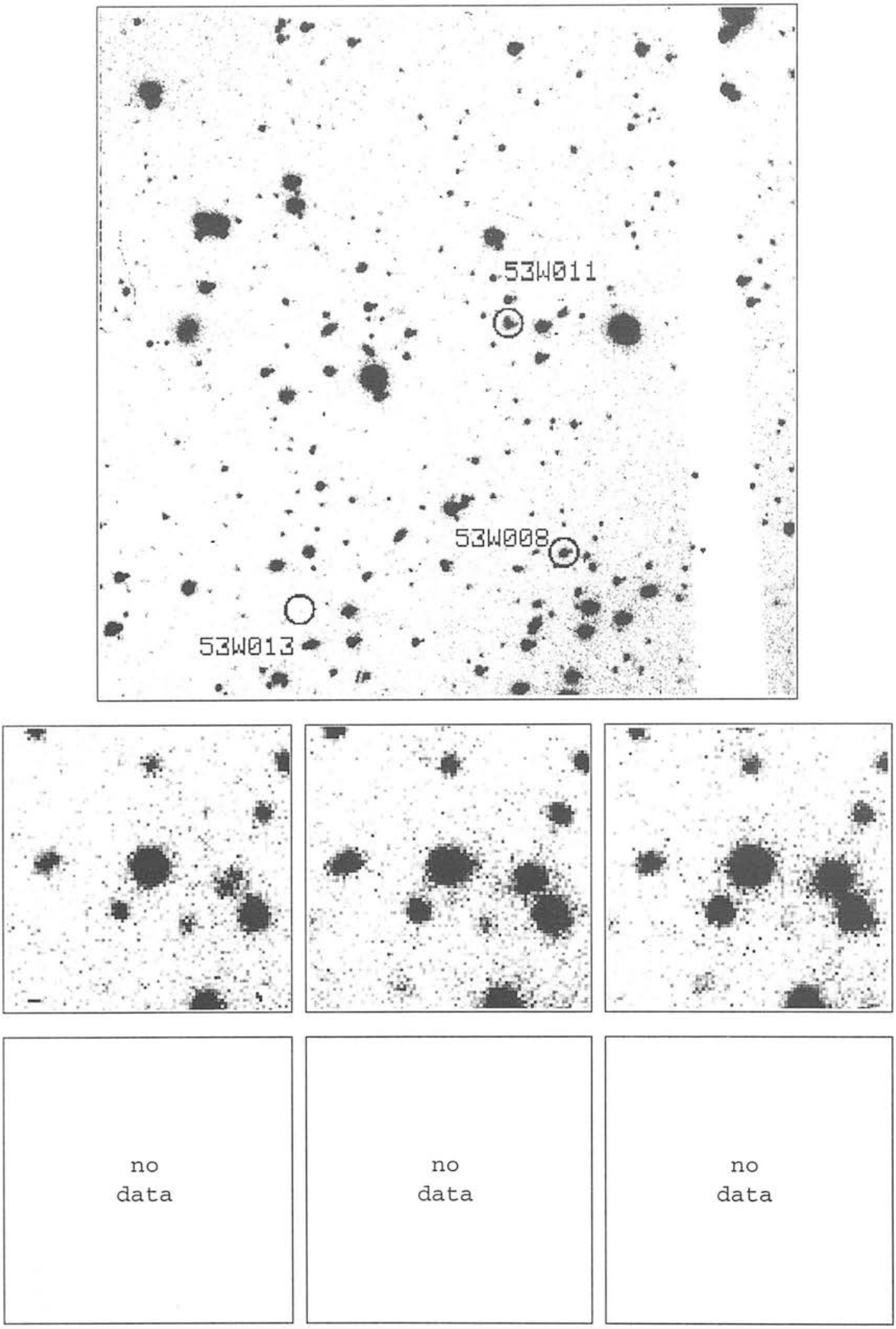

Figure 2.12 53W008

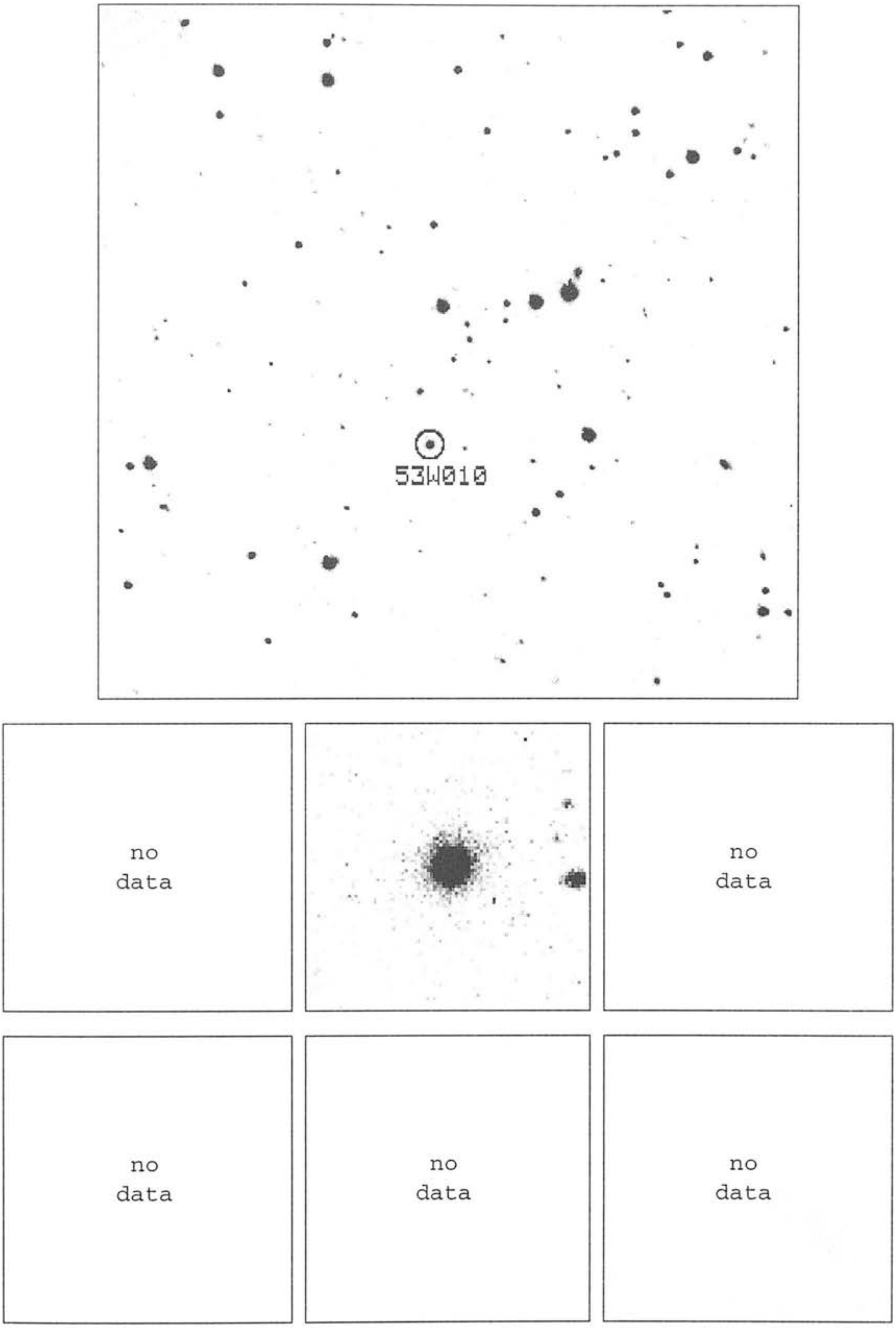

Figure 2.13 53W010

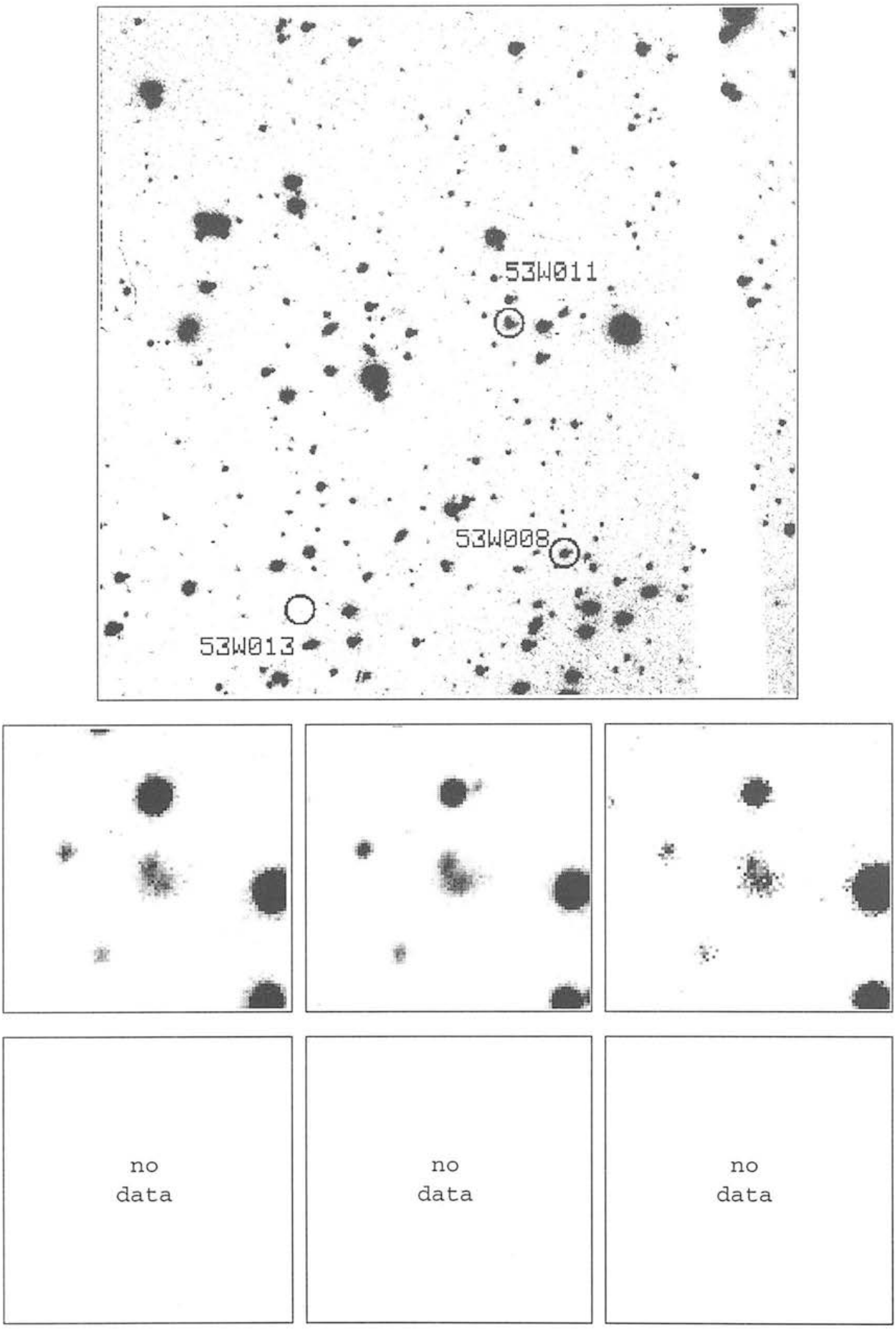

Figure 2.14 53W011

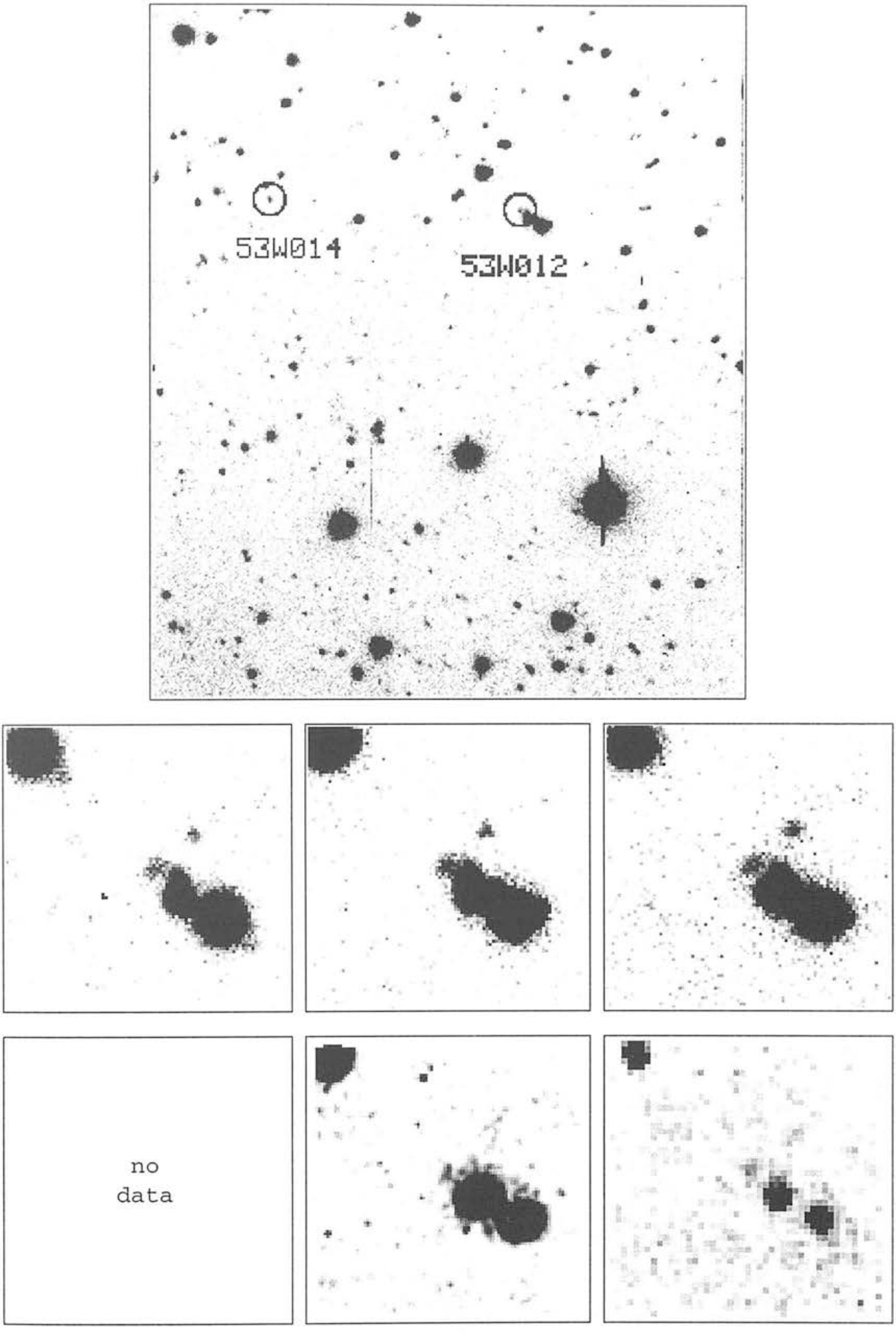

Figure 2.15 53W012

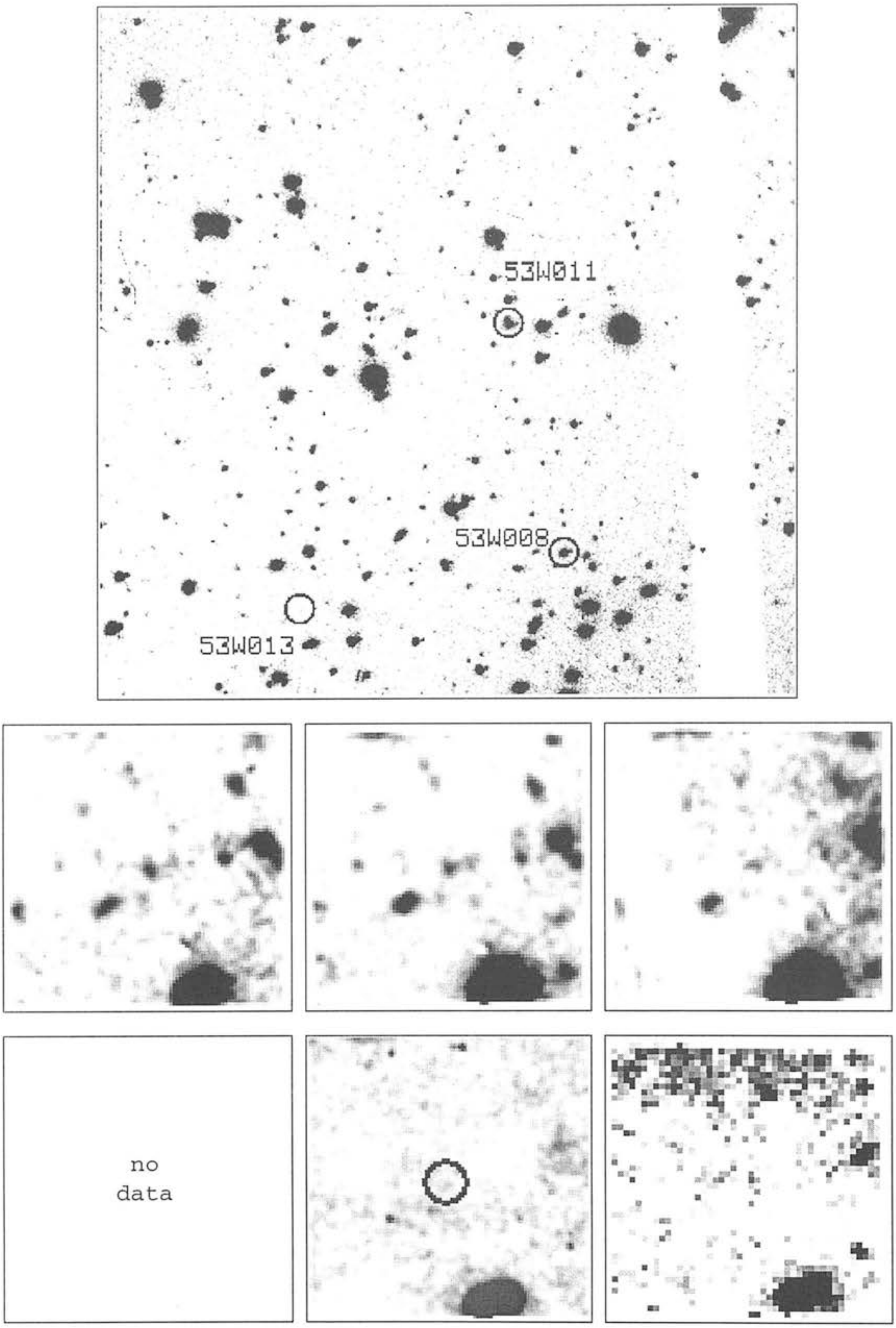

Figure 2.16 53W013

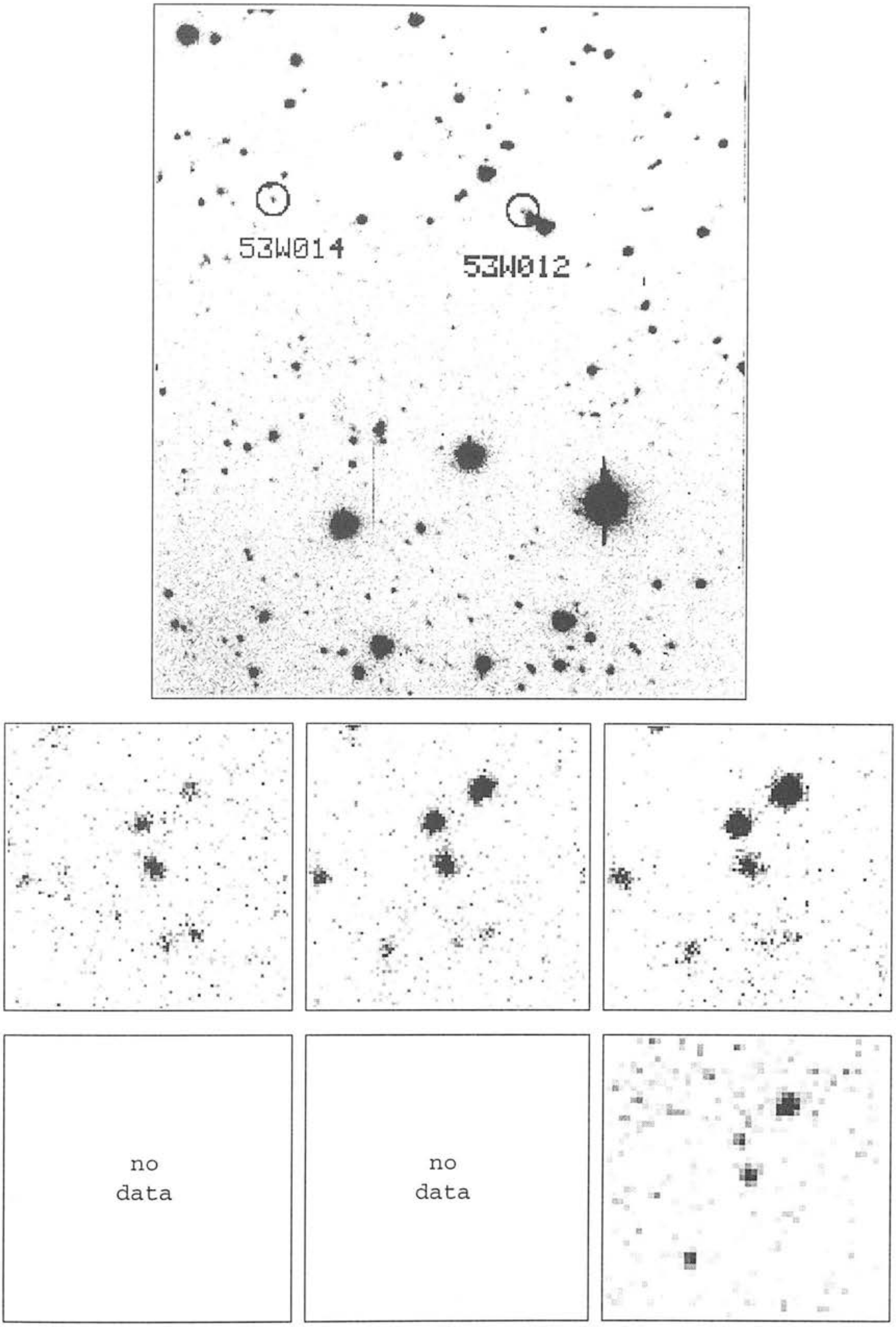

Figure 2.17 53W014

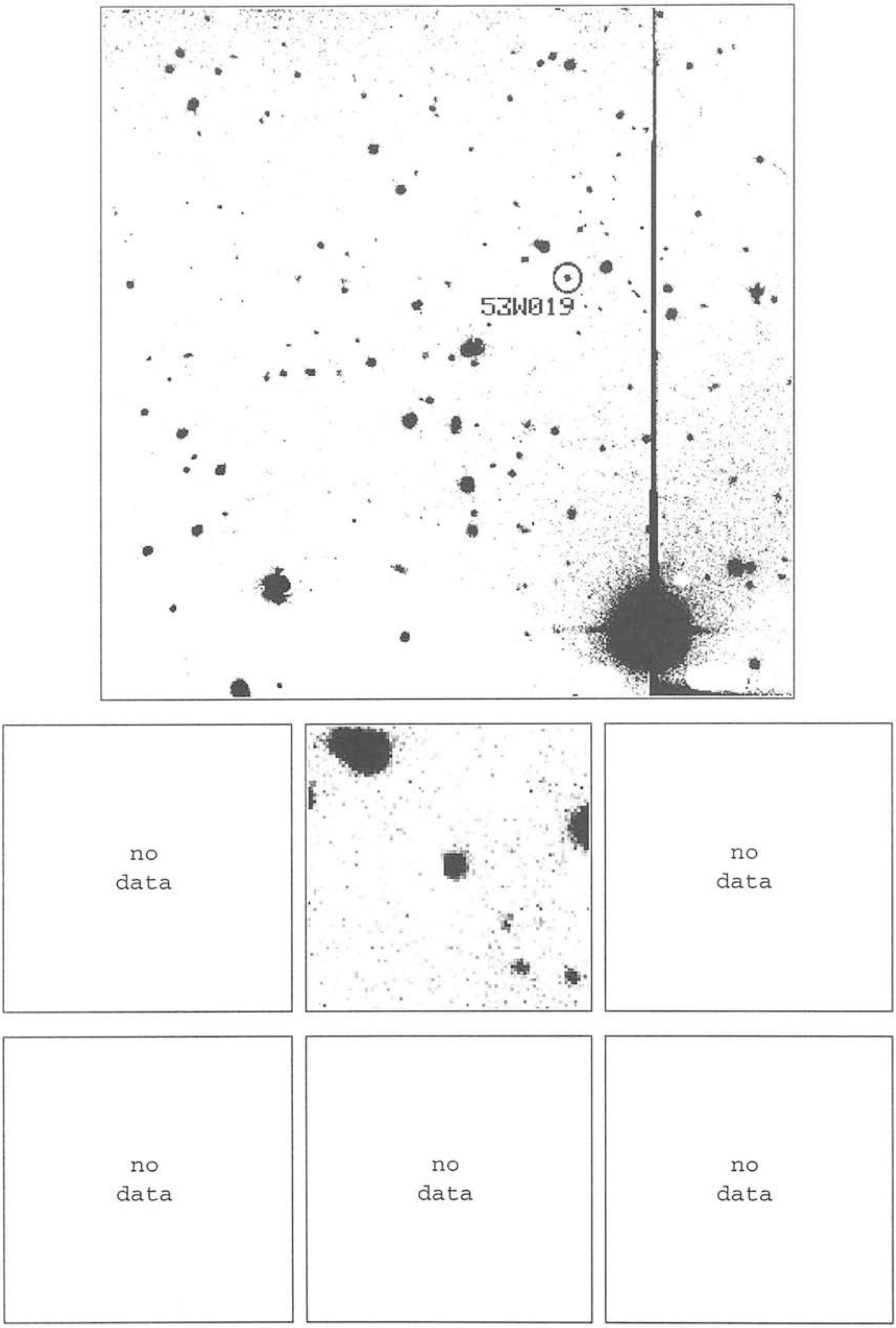

Figure 2.18 53W019

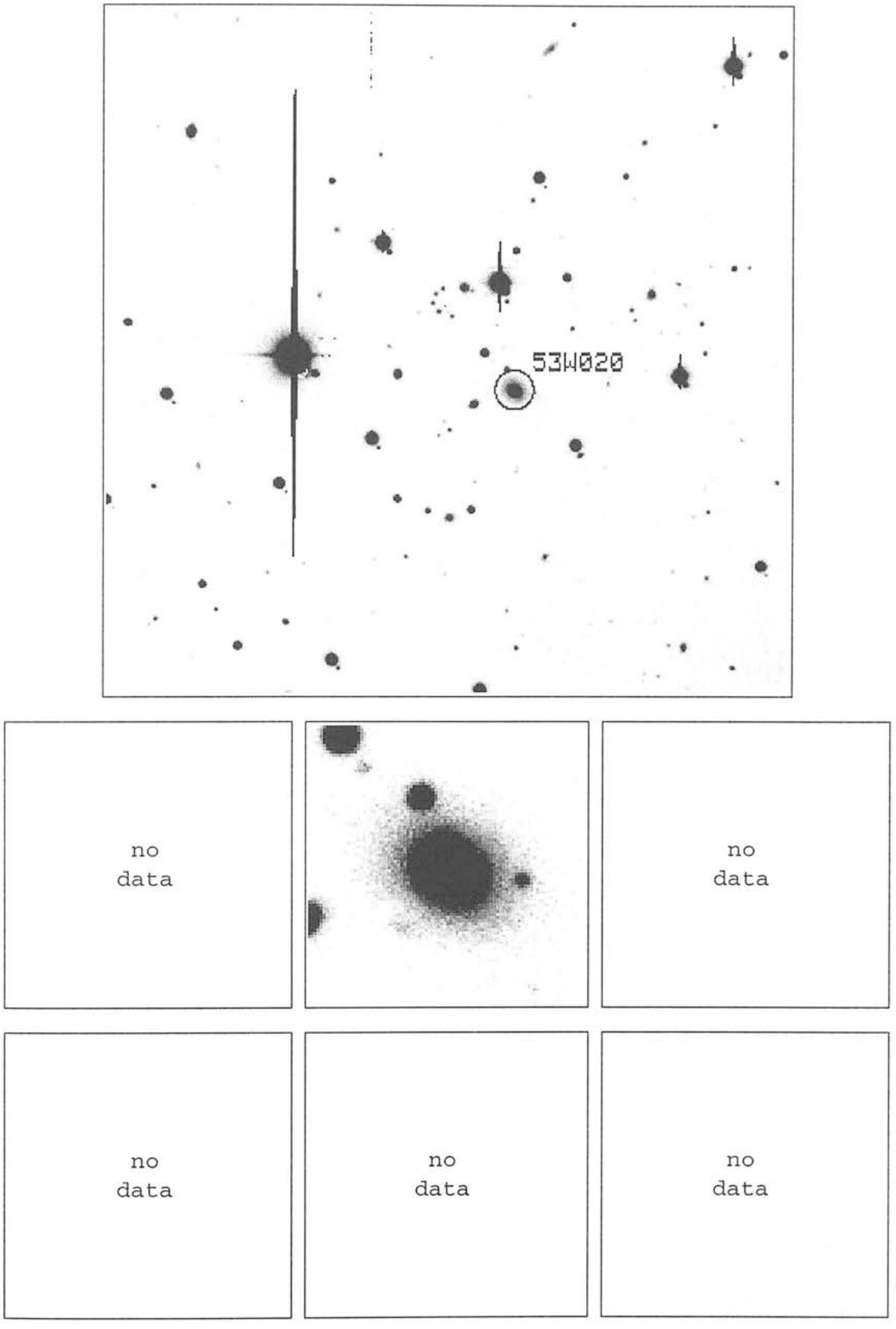

Figure 2.19 53W020

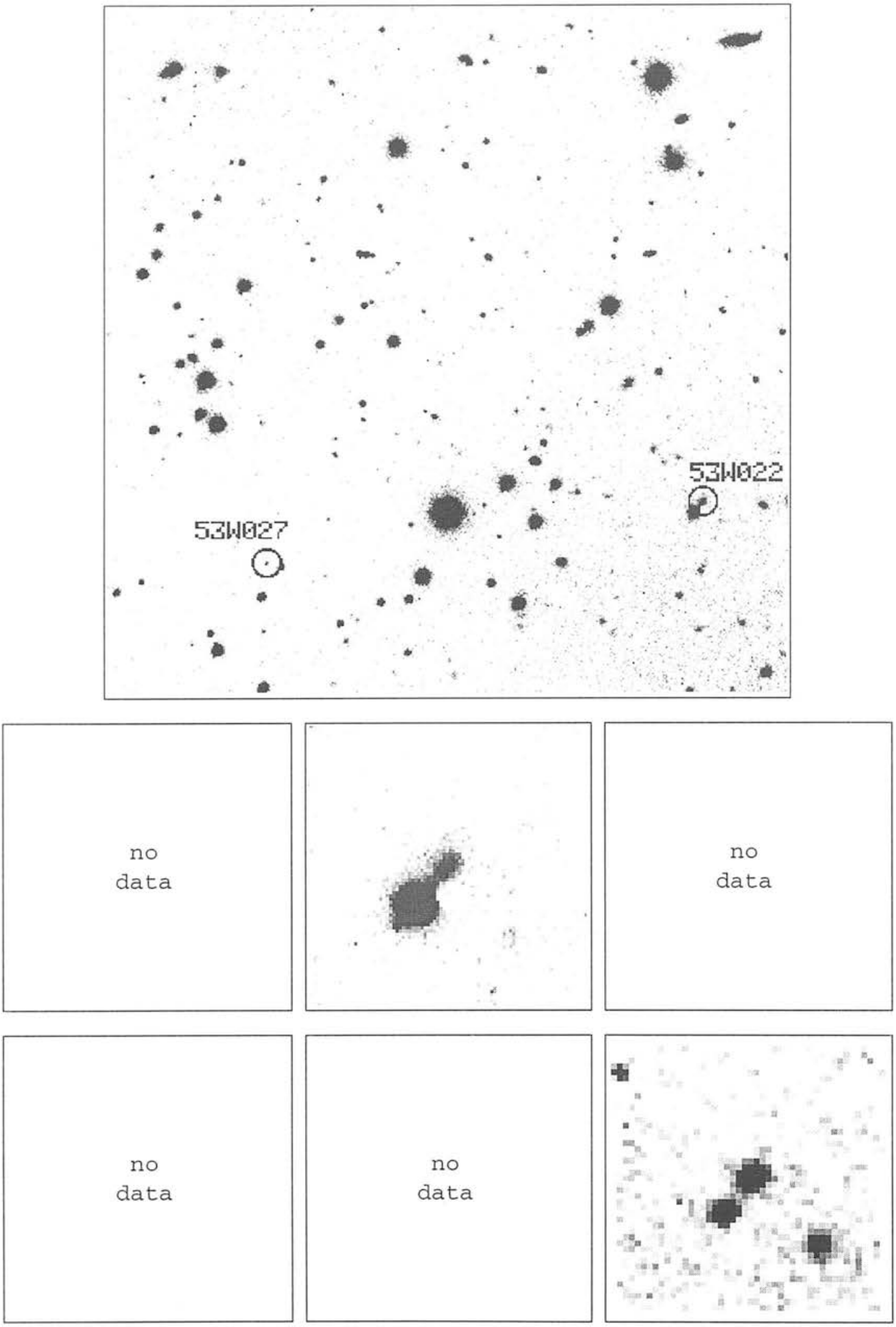

Figure 2.20 53W022

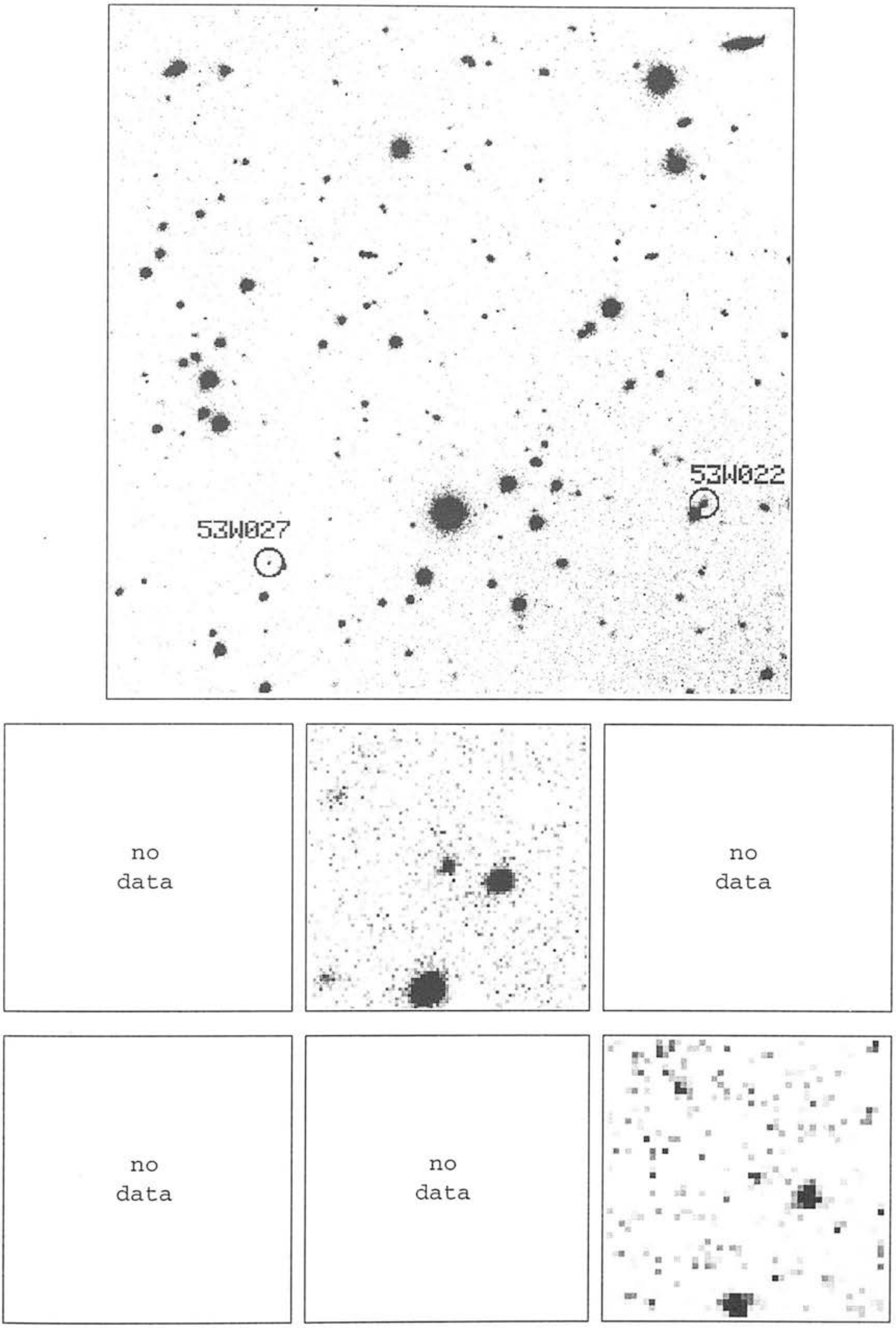

Figure 2.21 53W027

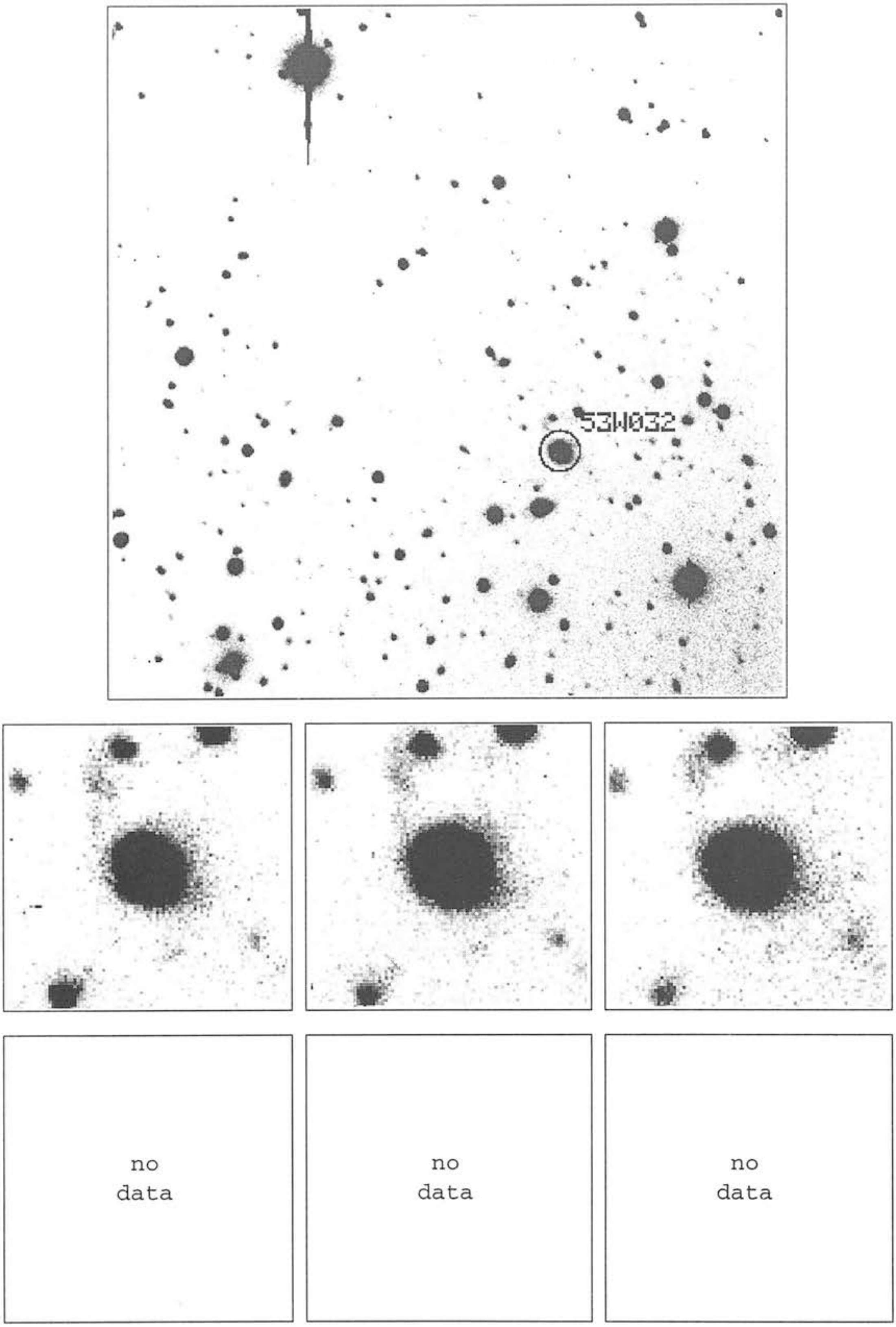

Figure 2.22 53W032

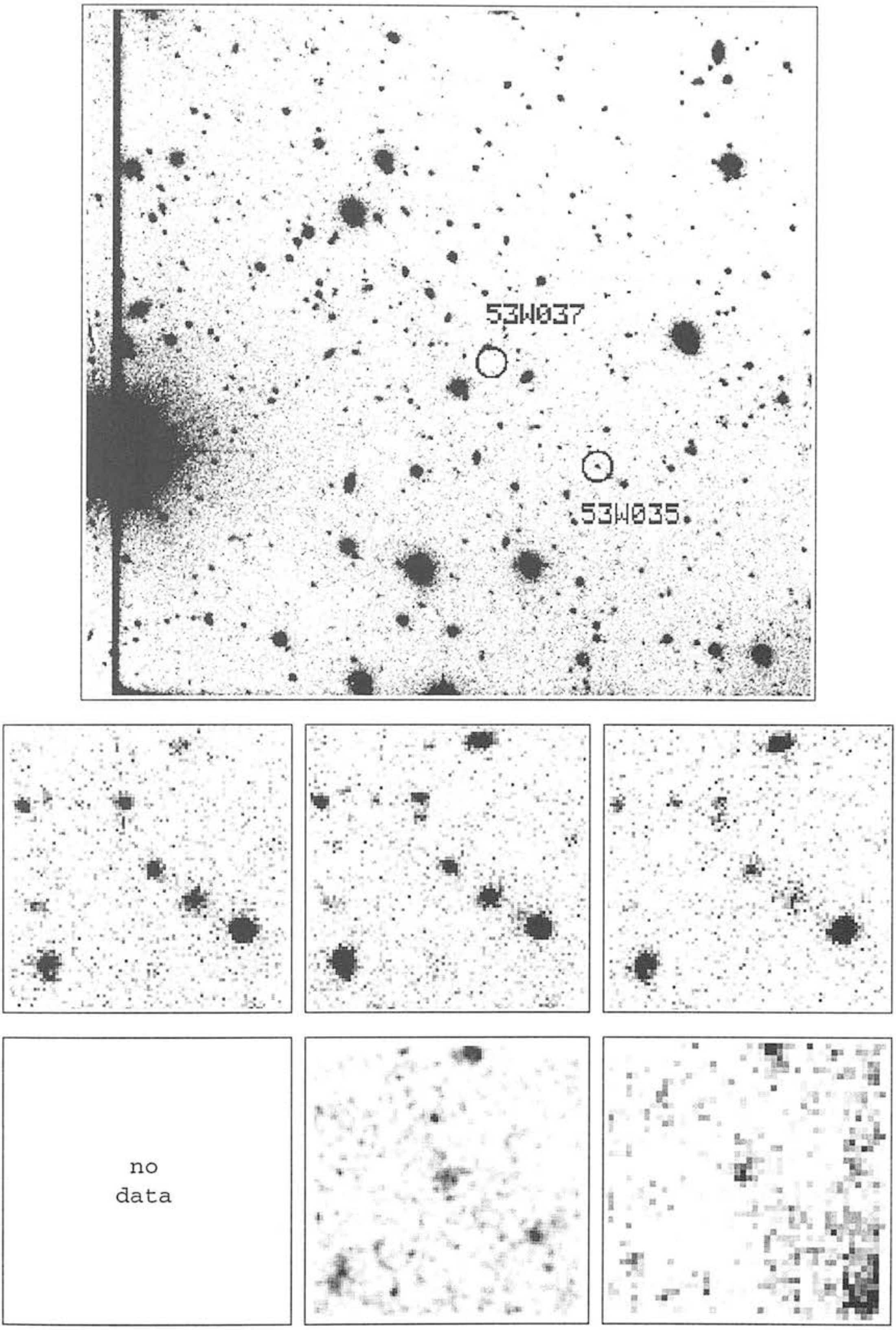

Figure 2.23 53W035

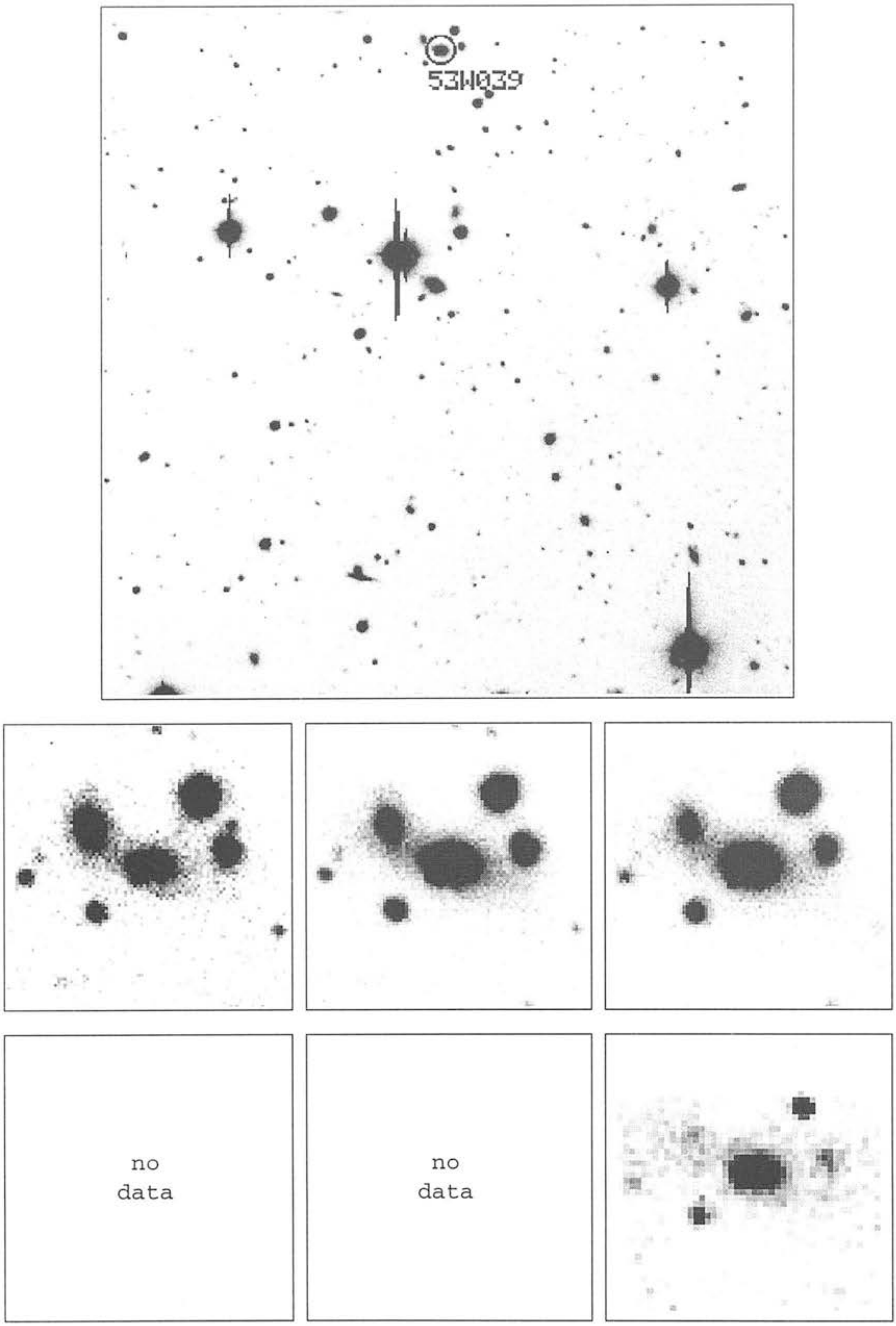

Figure 2.24 53W039

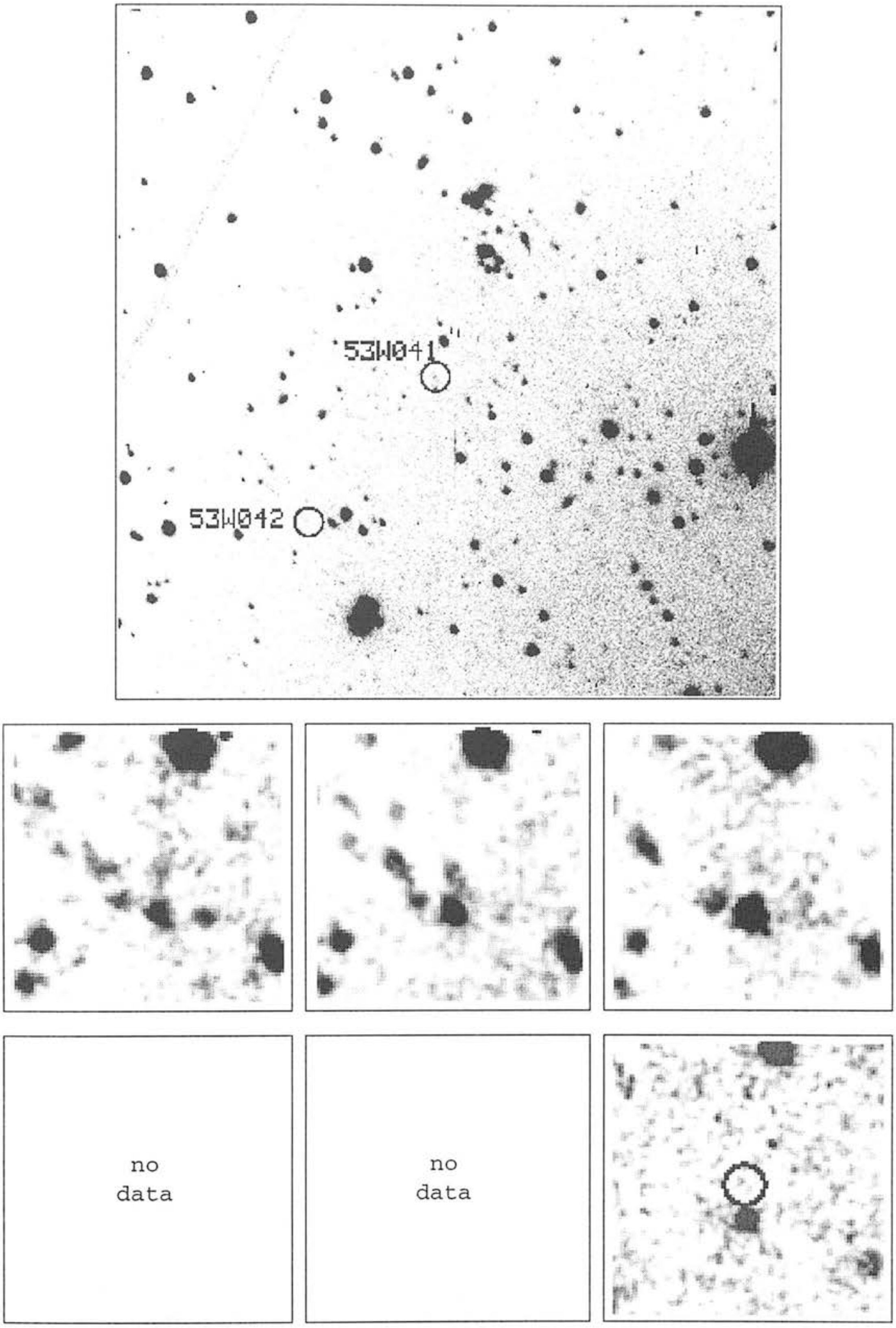

Figure 2.25 53W041

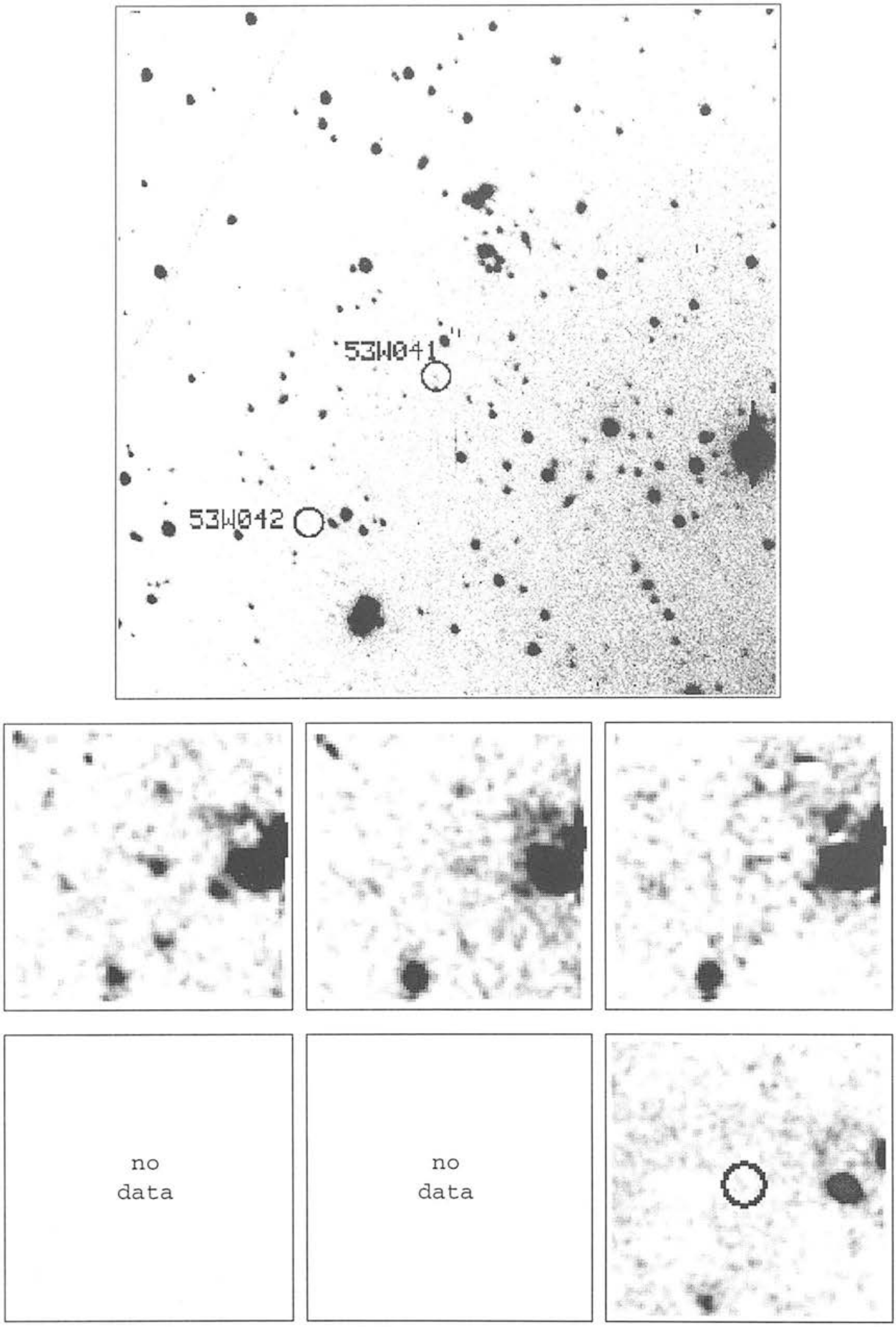

Figure 2.26 53W042

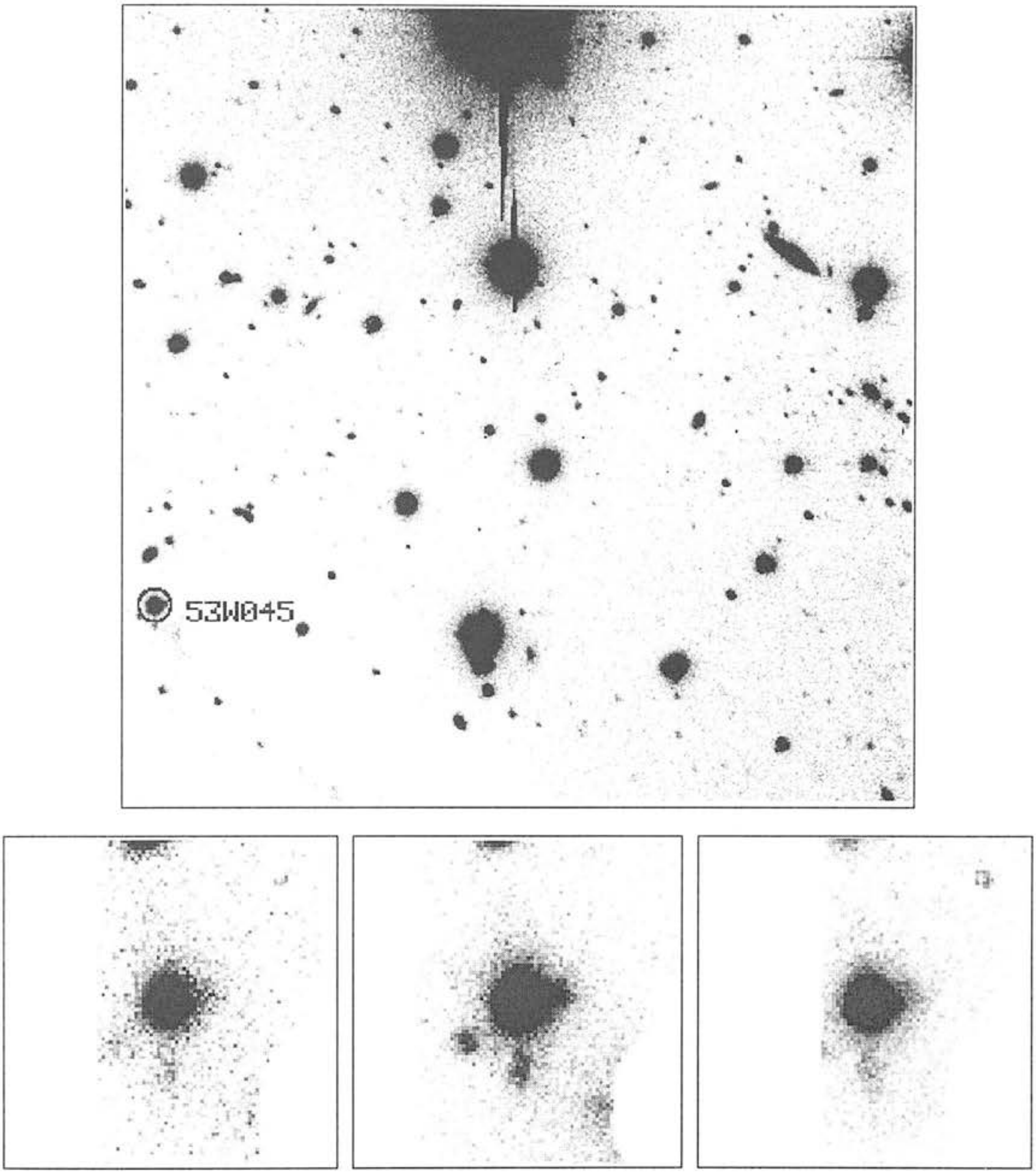

no
data

no
data

no
data

Figure 2.27 53W045

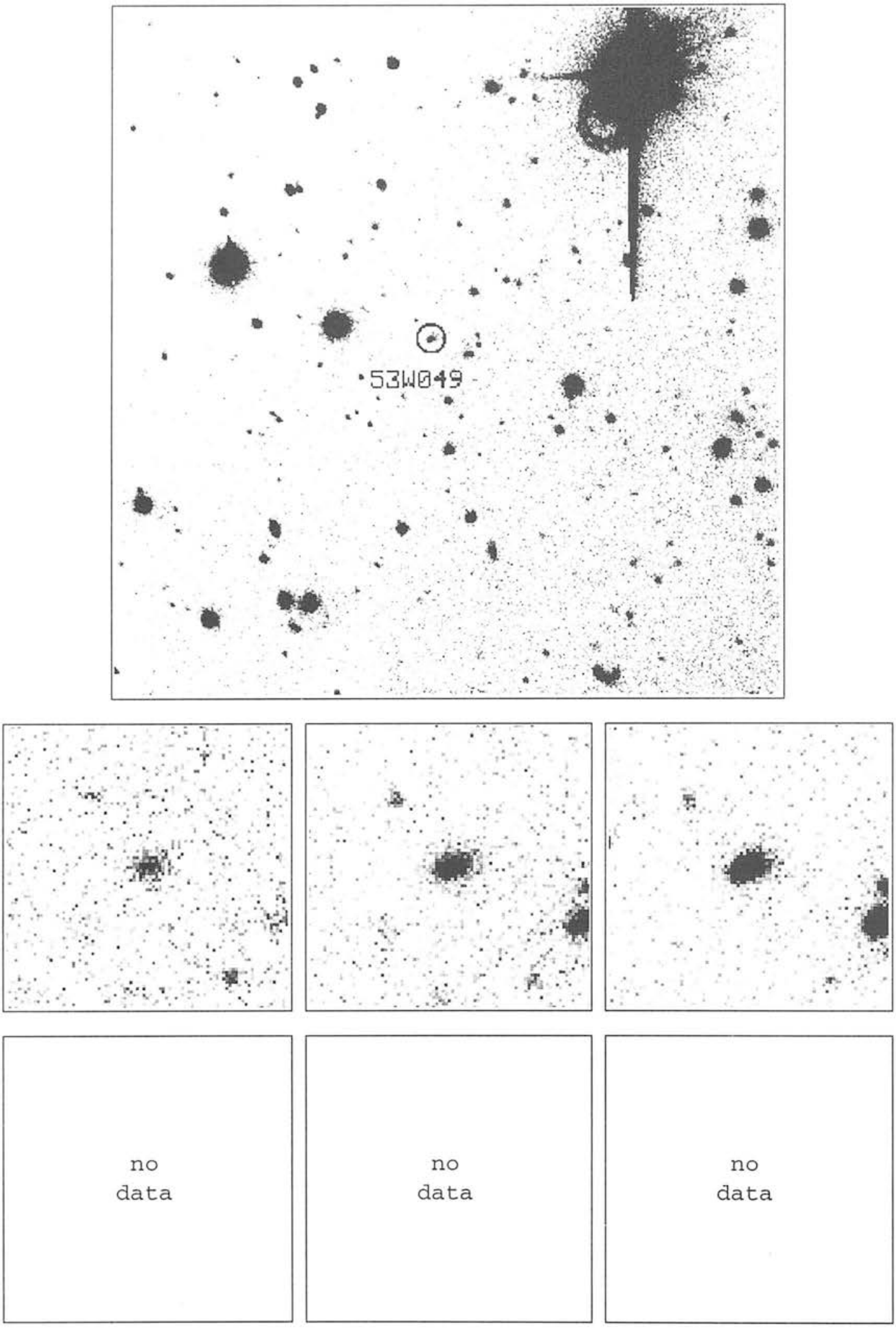

Figure 2.28 53W049

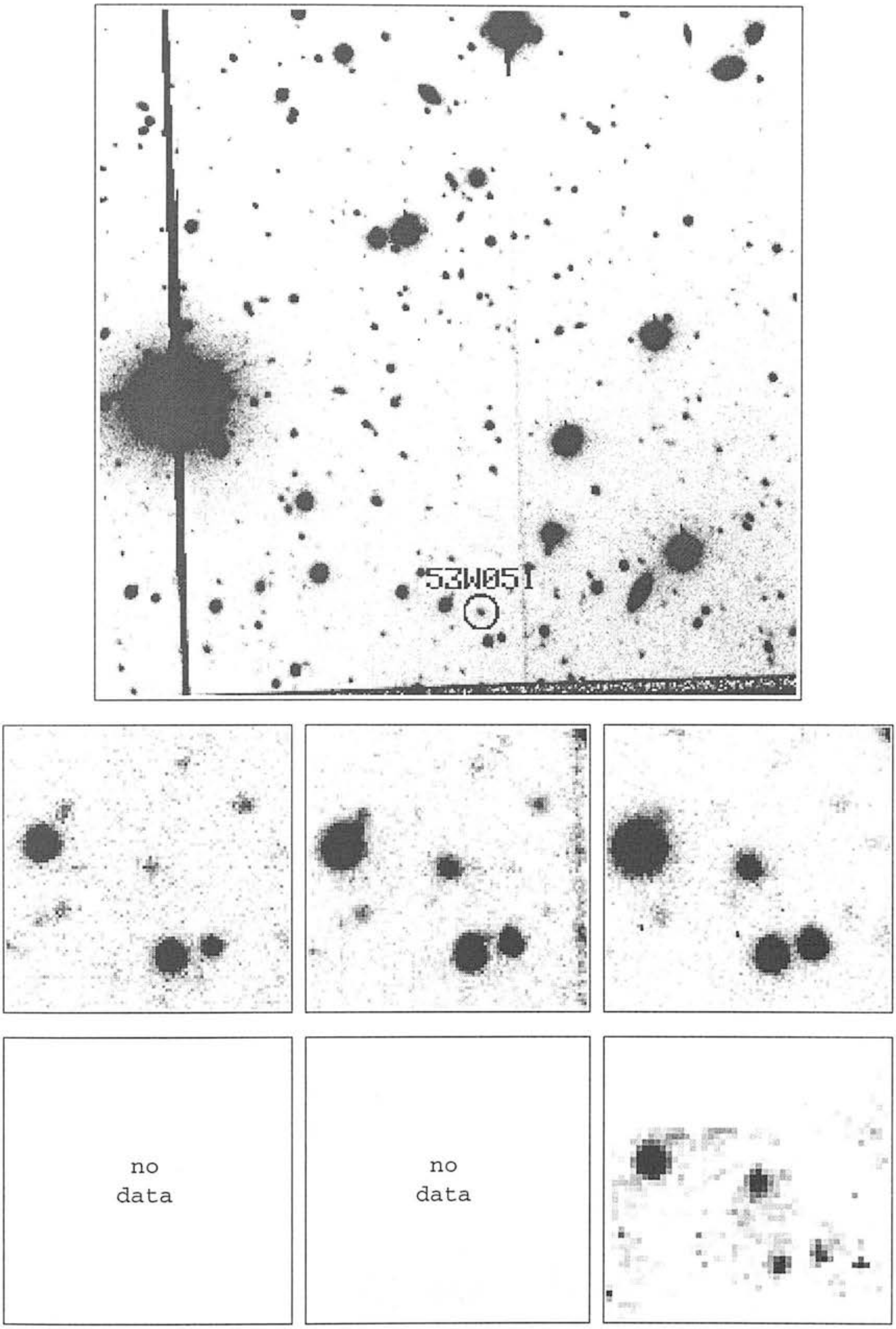

Figure 2.29 53W051

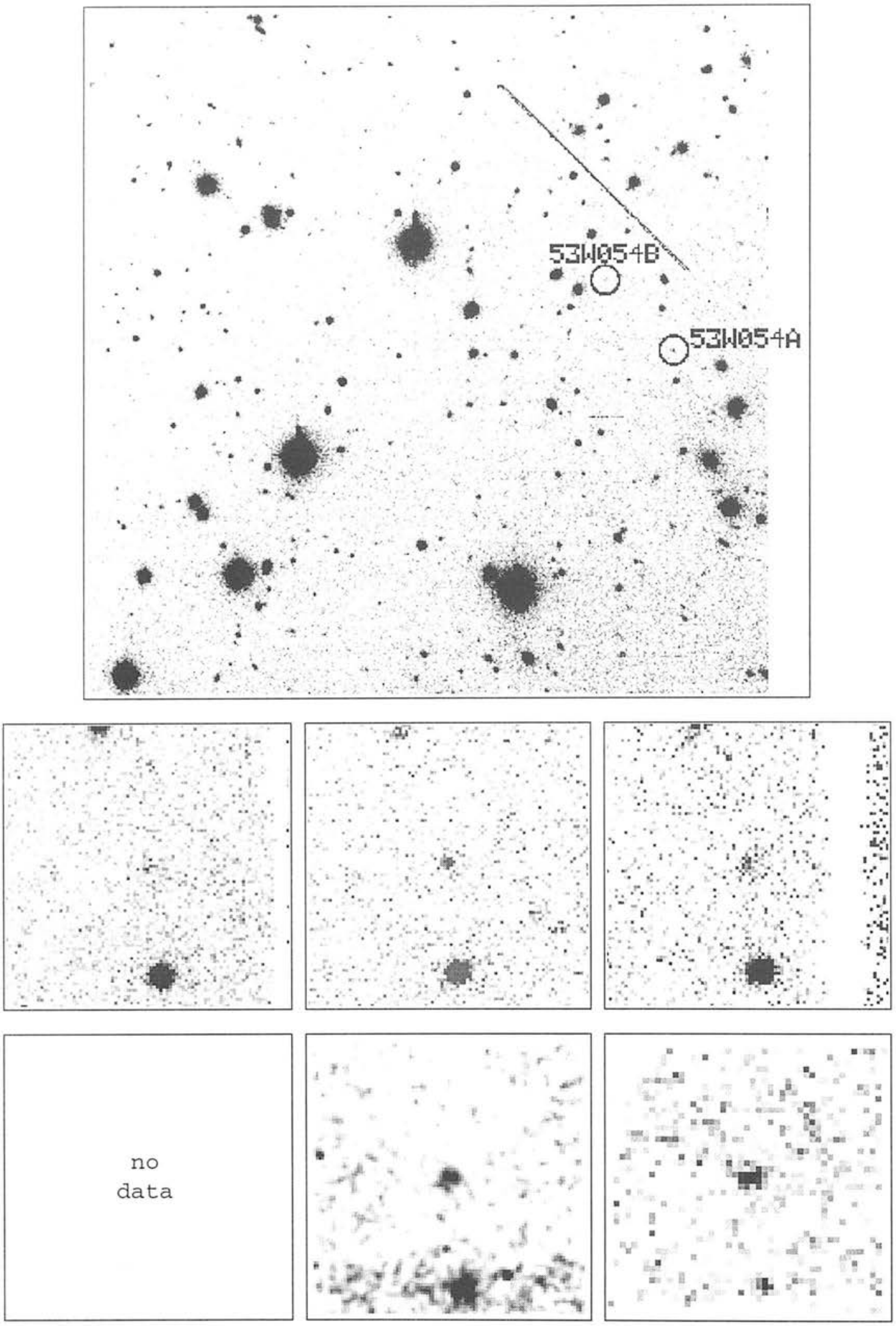

Figure 2.30 53W054A

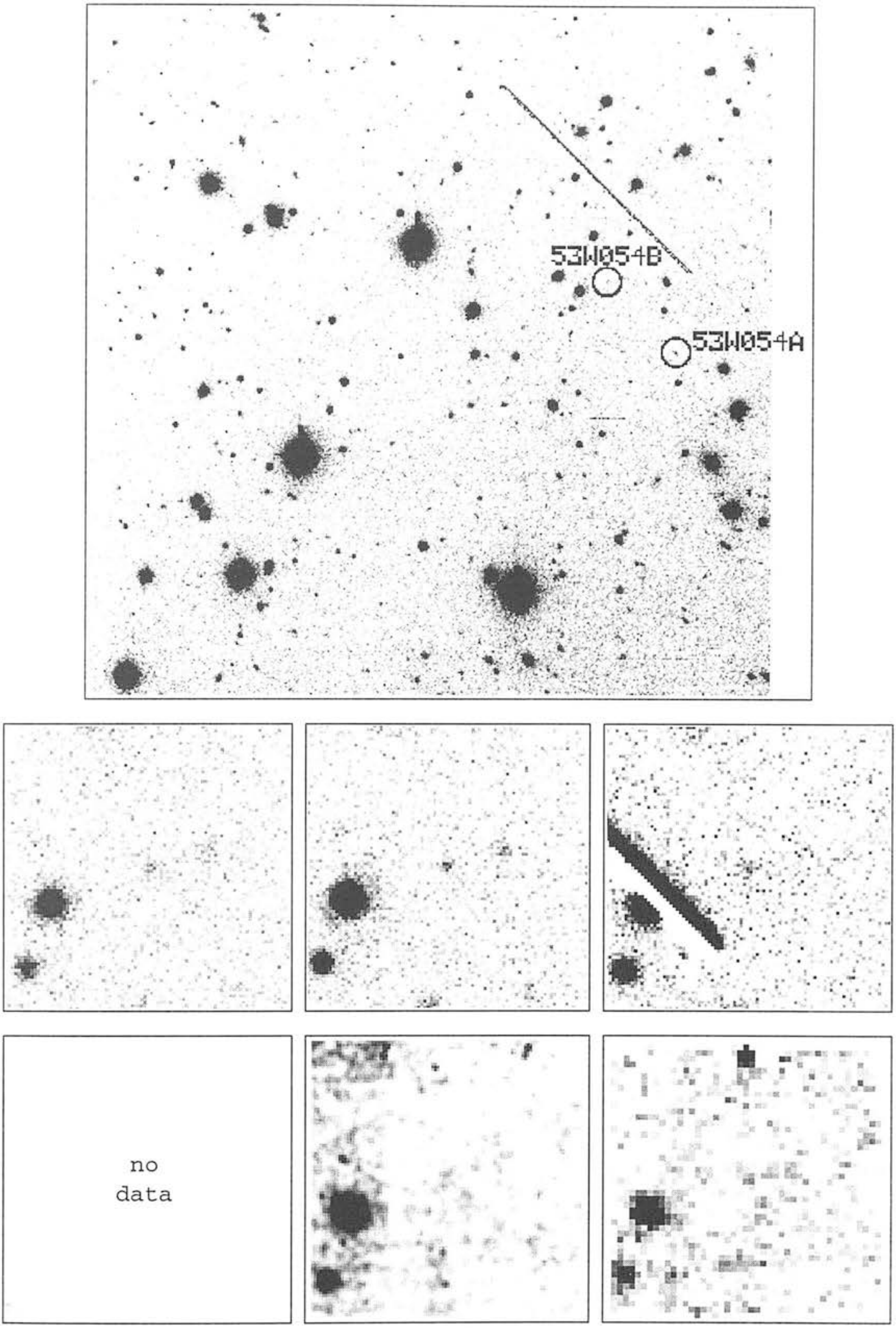

Figure 2.31 53W054B

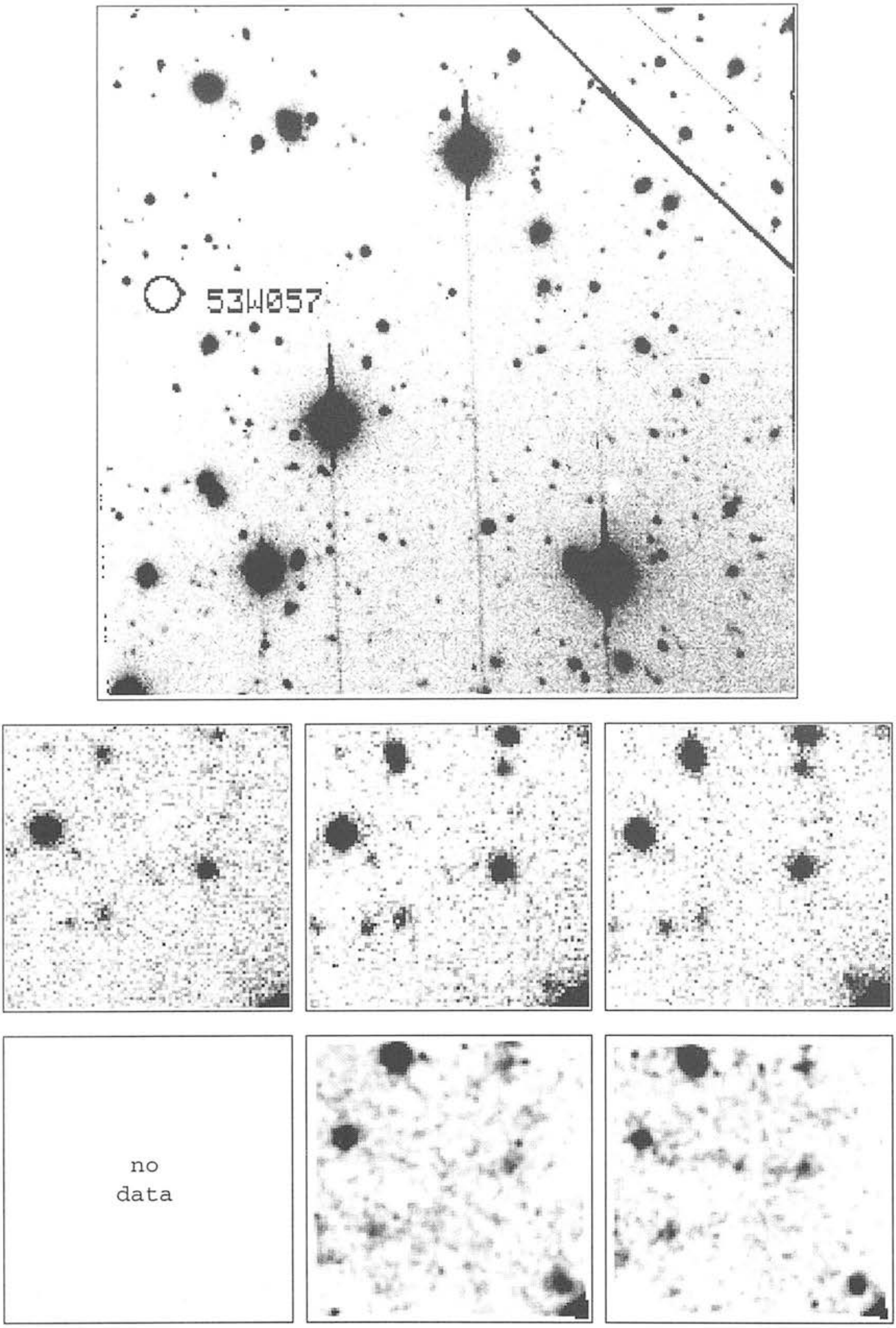

Figure 2.32 53W057

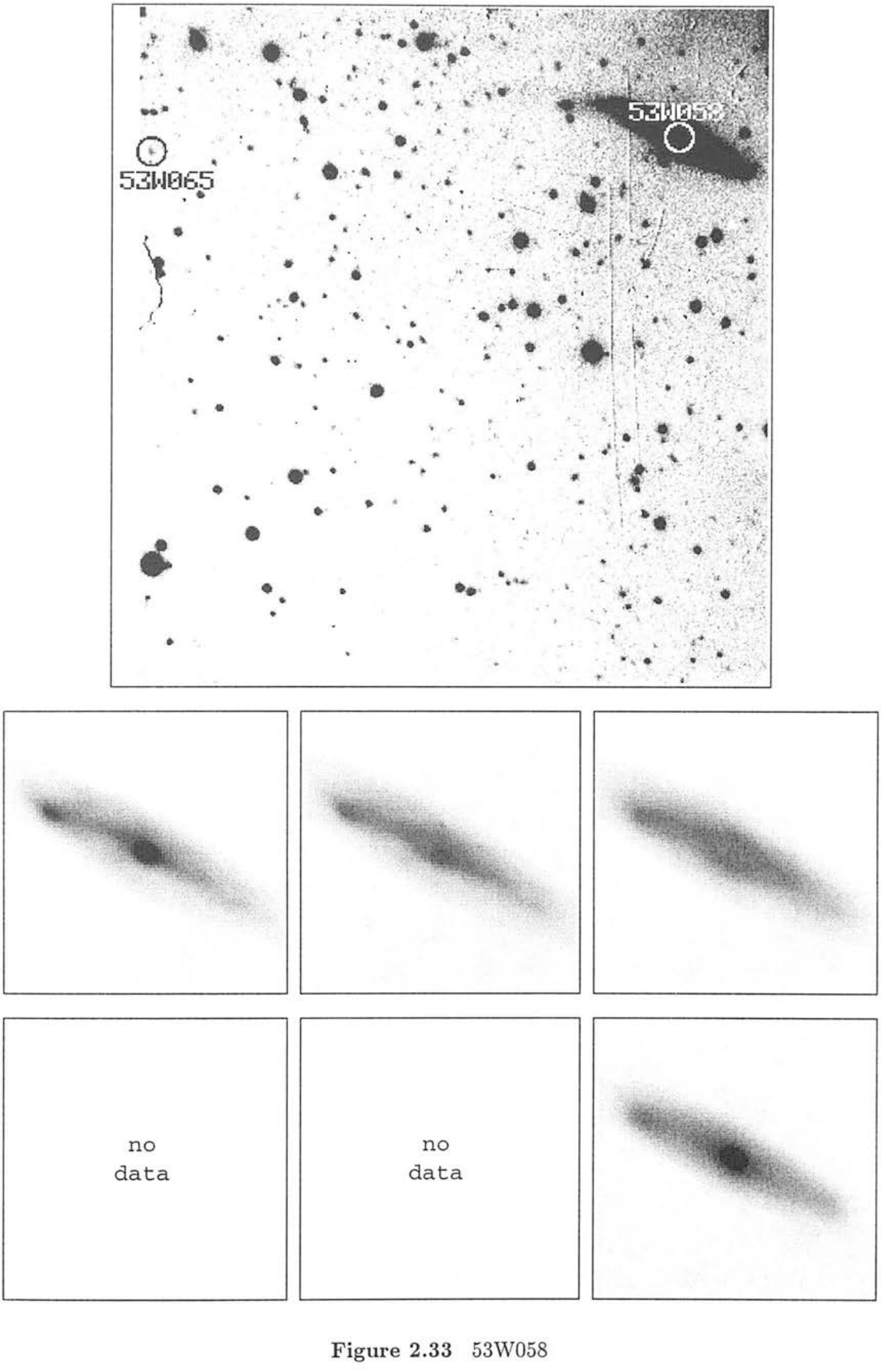

Figure 2.33 53W058

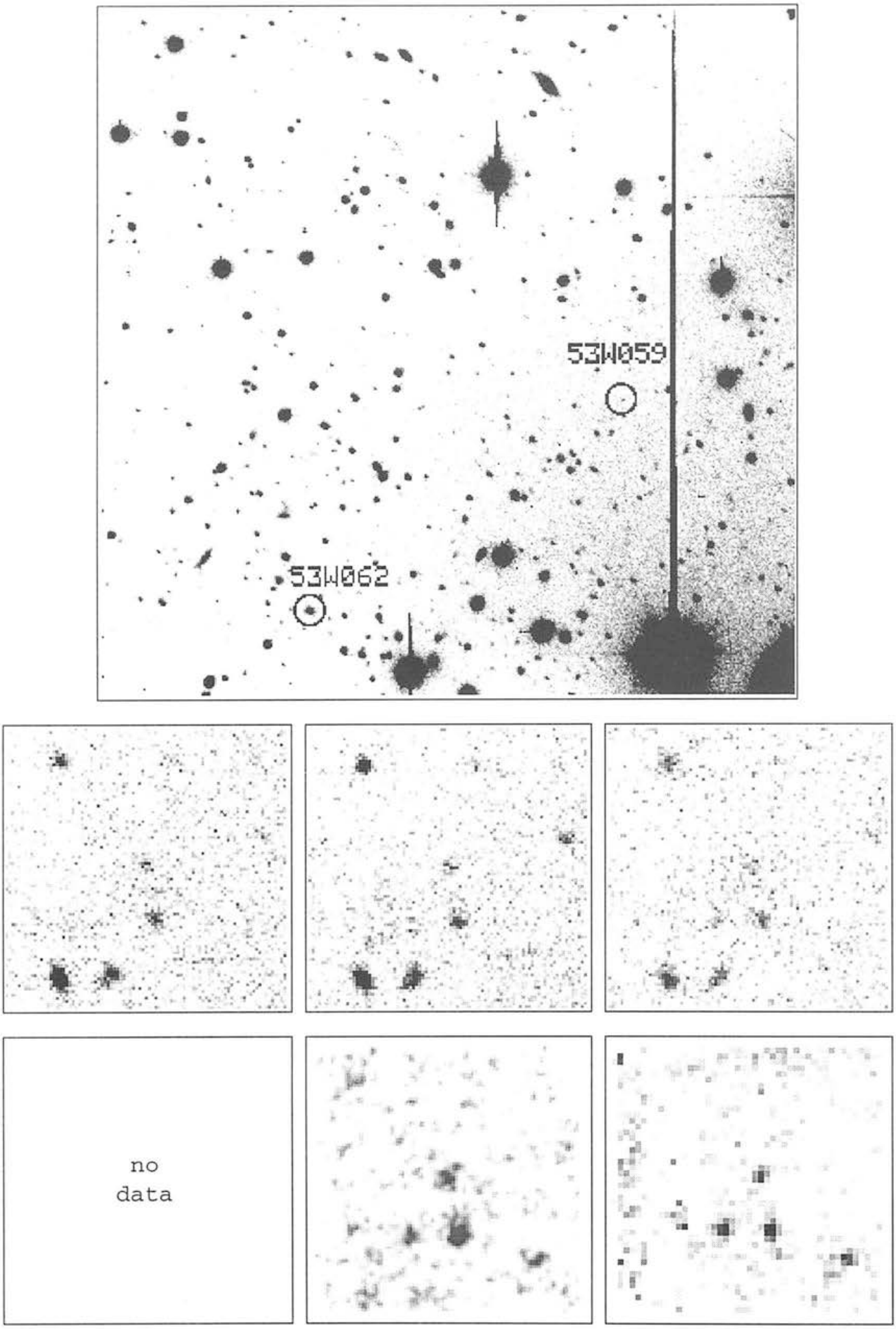

Figure 2.34 53W059

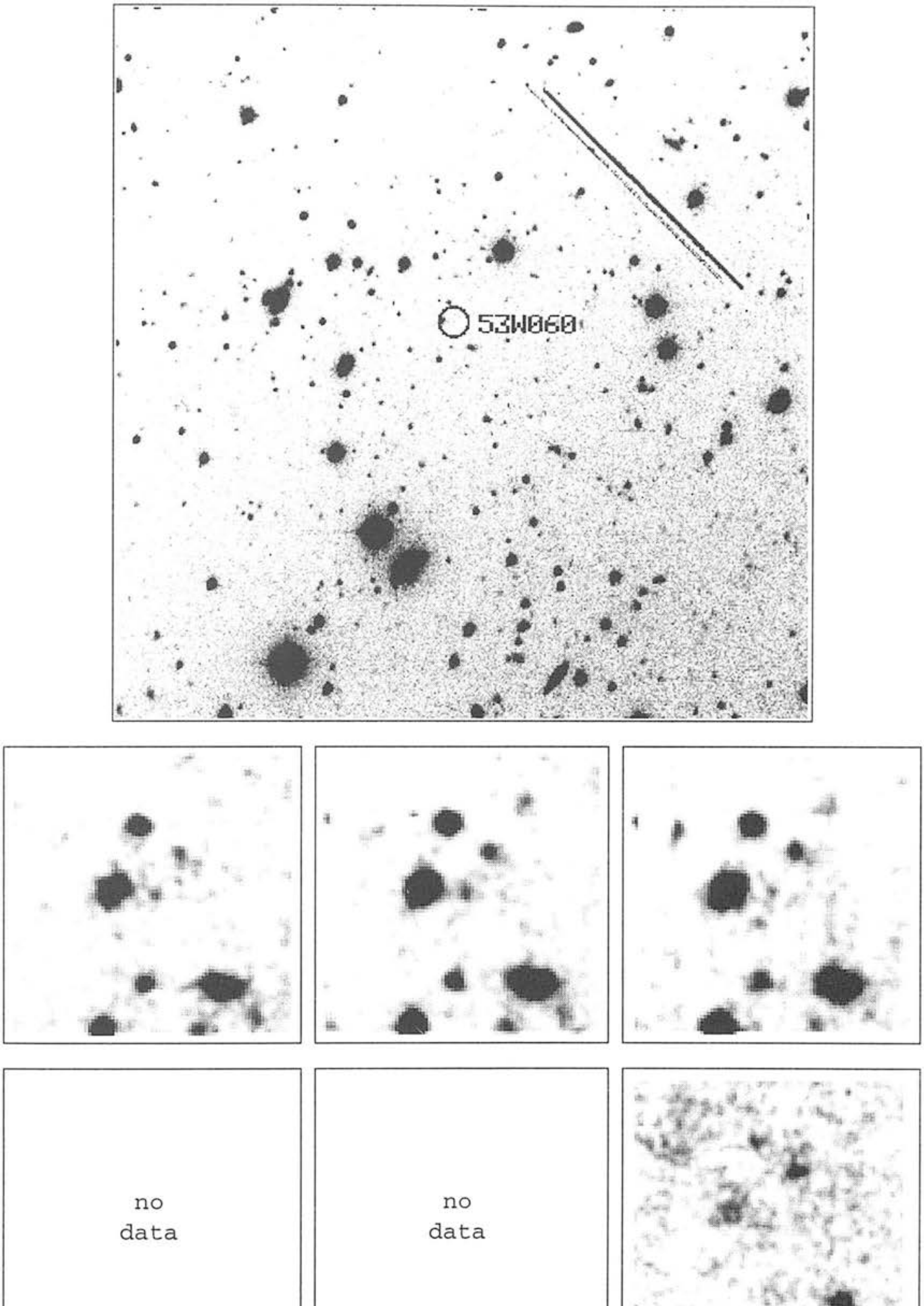

Figure 2.35 53W060

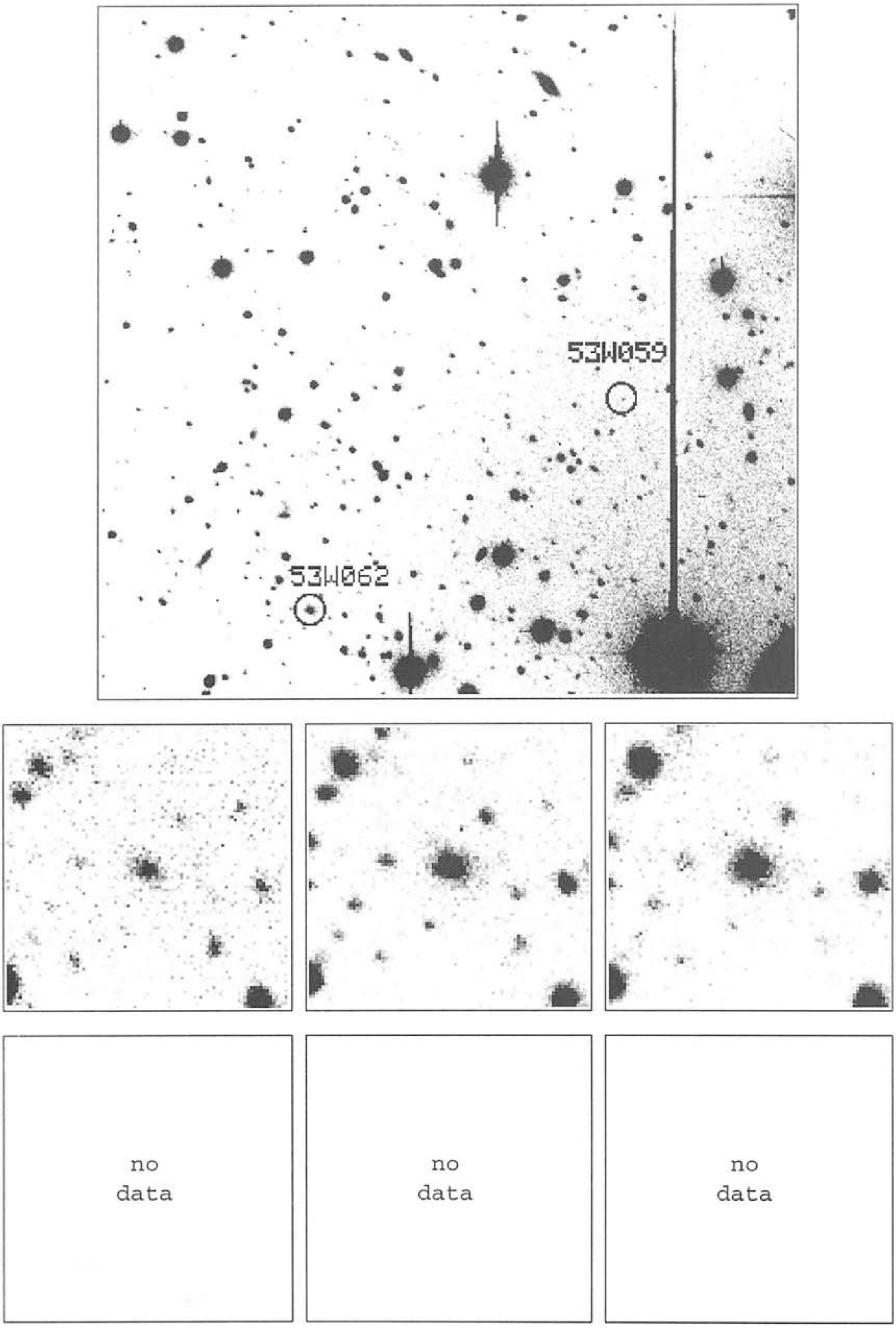

Figure 2.36 53W062

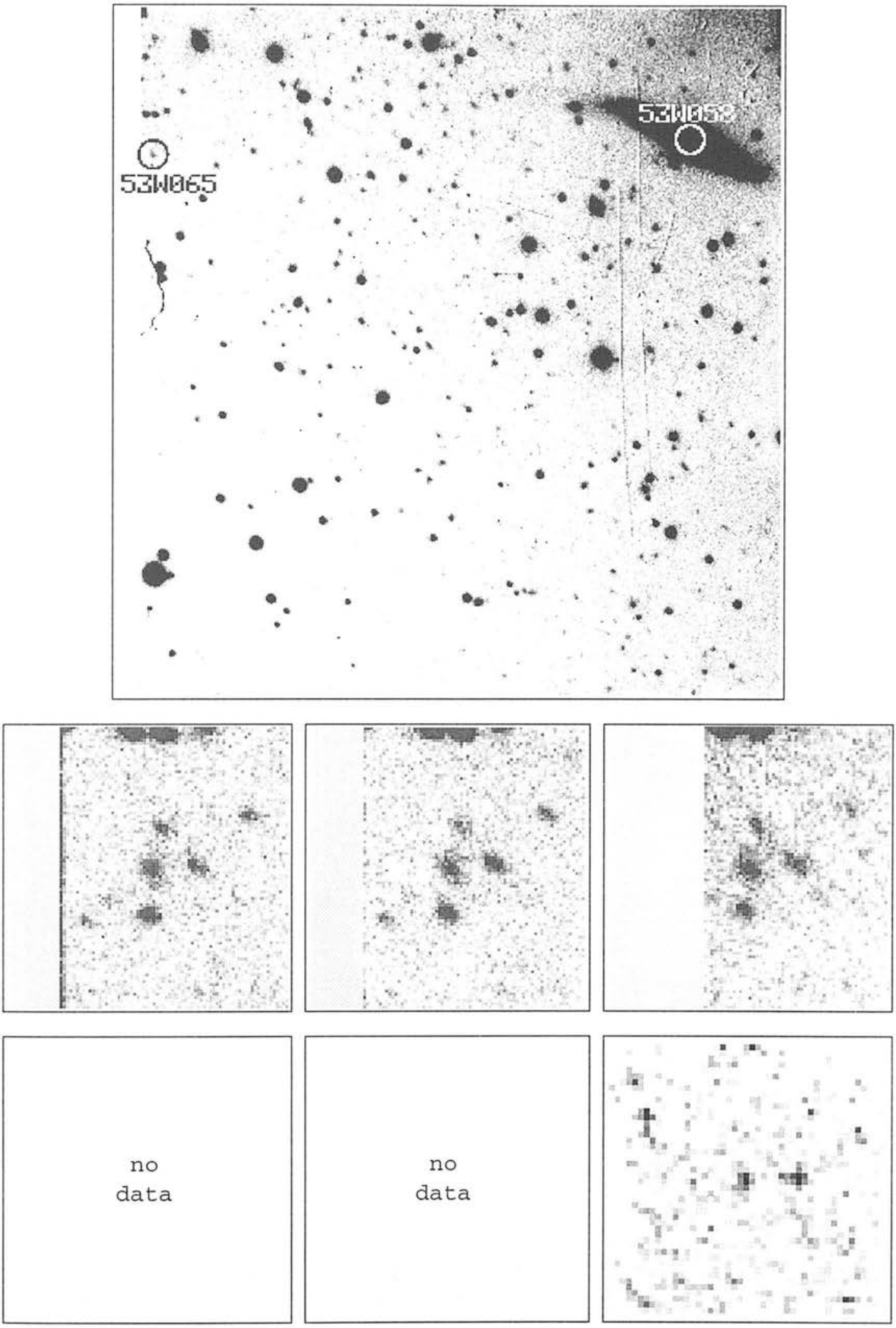

Figure 2.37 53W065

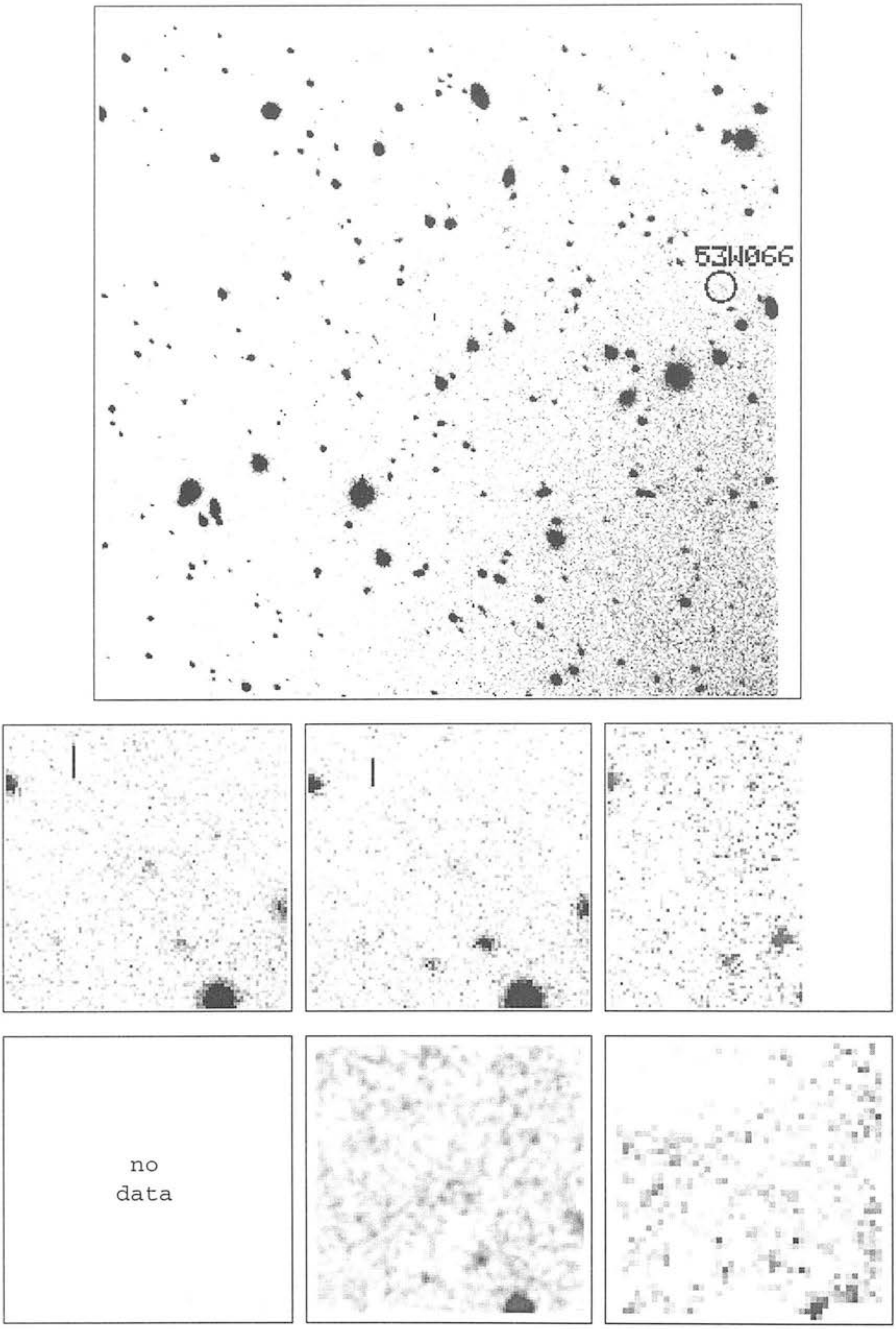

Figure 2.38 53W066

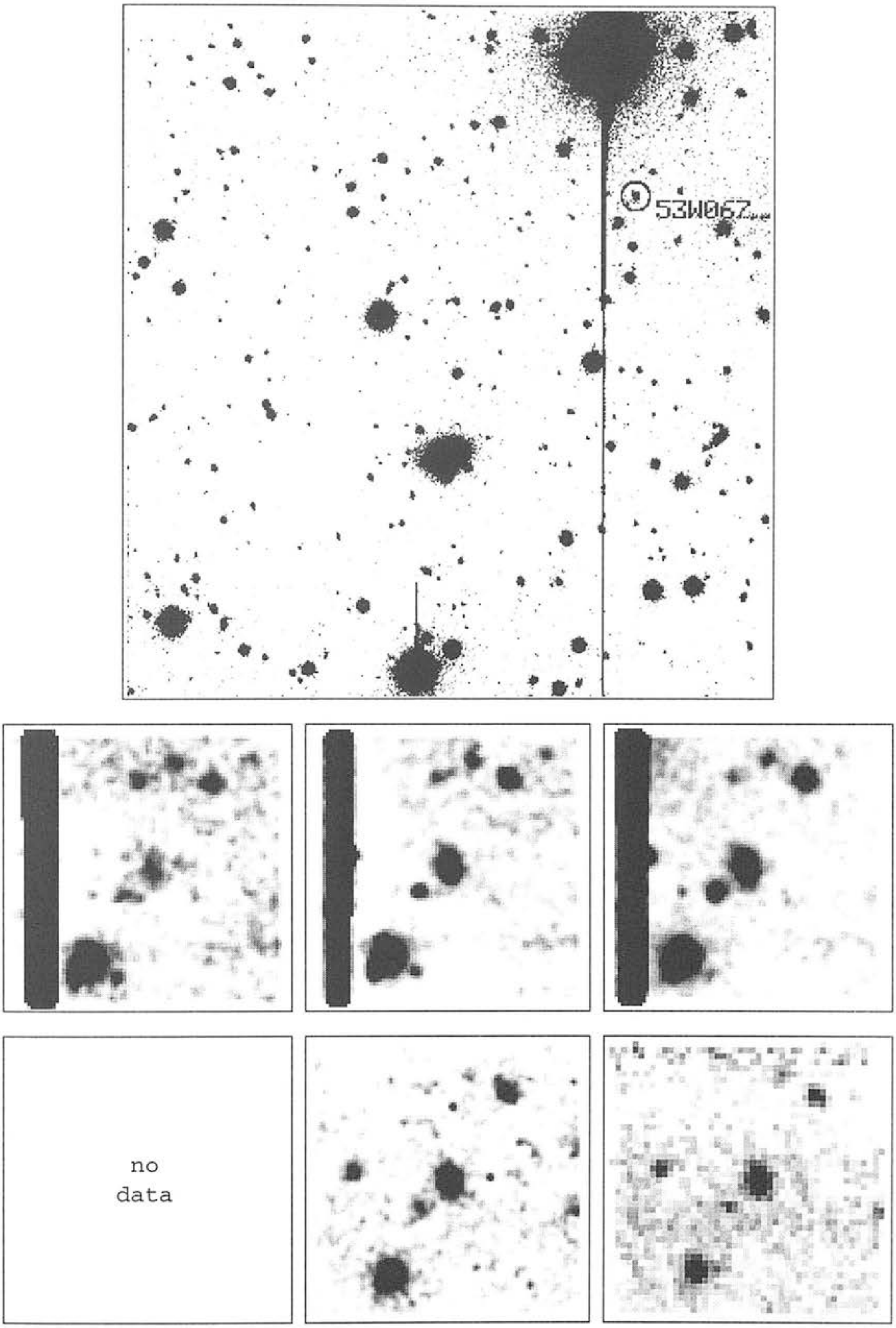

Figure 2.39 53W067

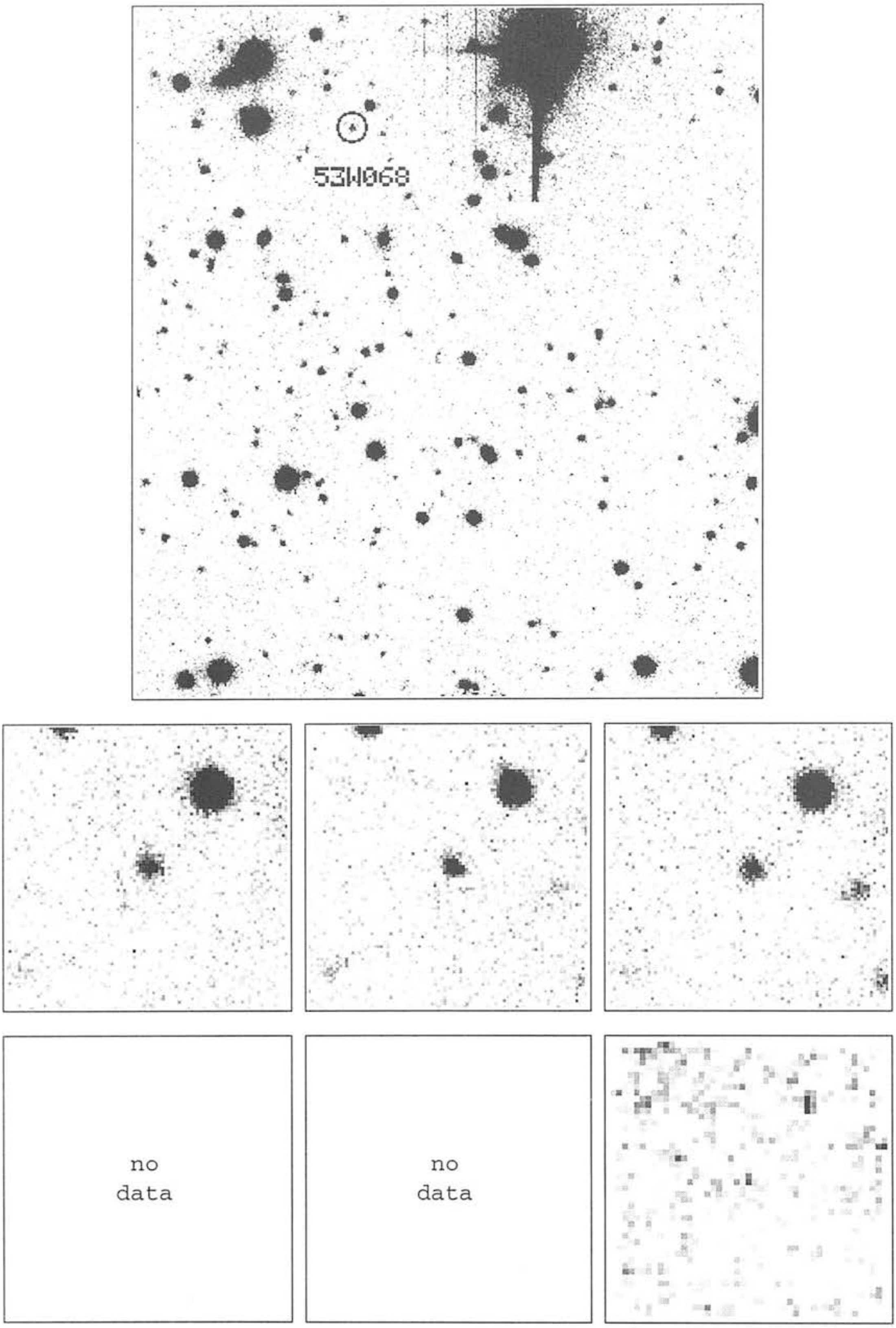

Figure 2.40 53W068

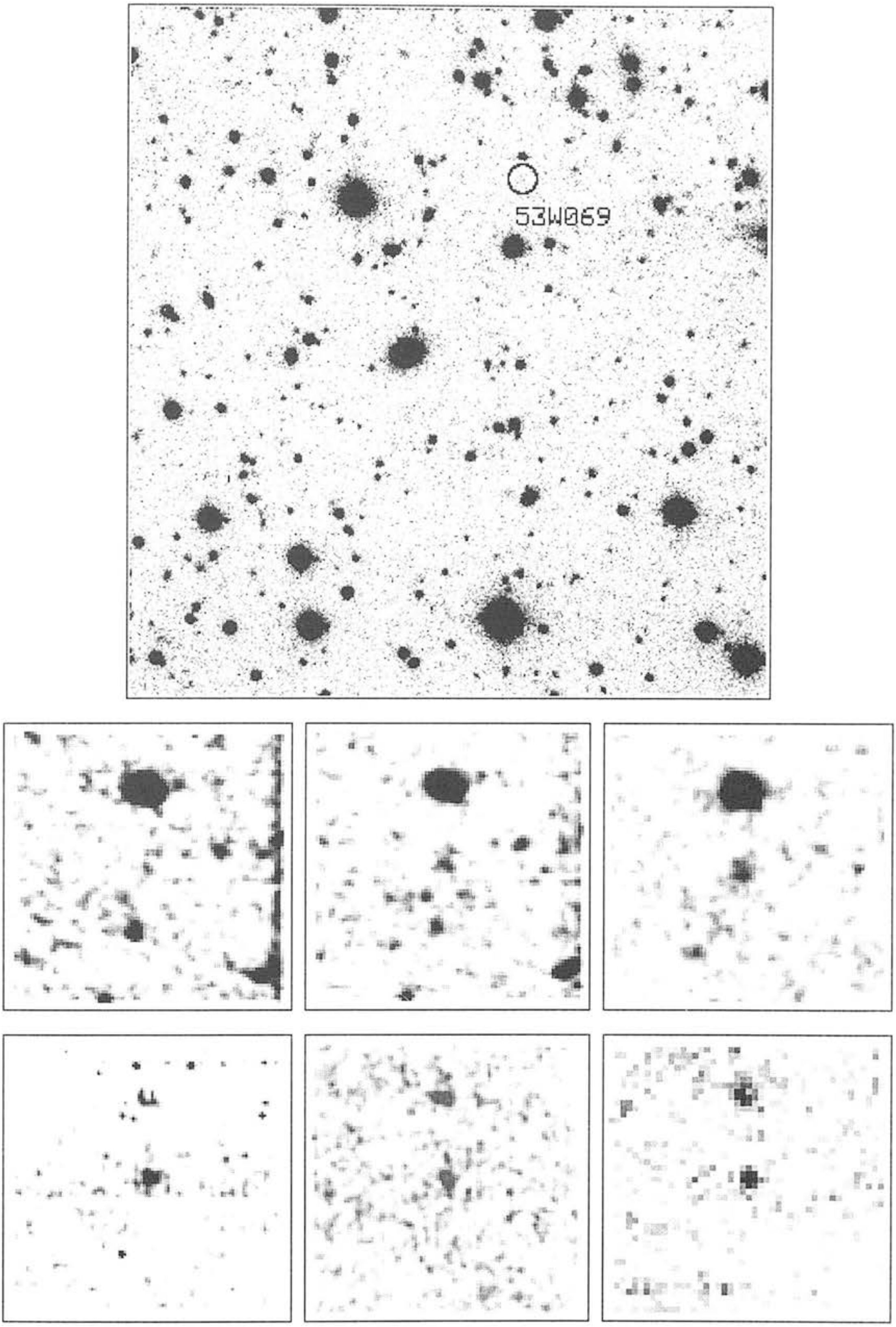

Figure 2.41 53W069

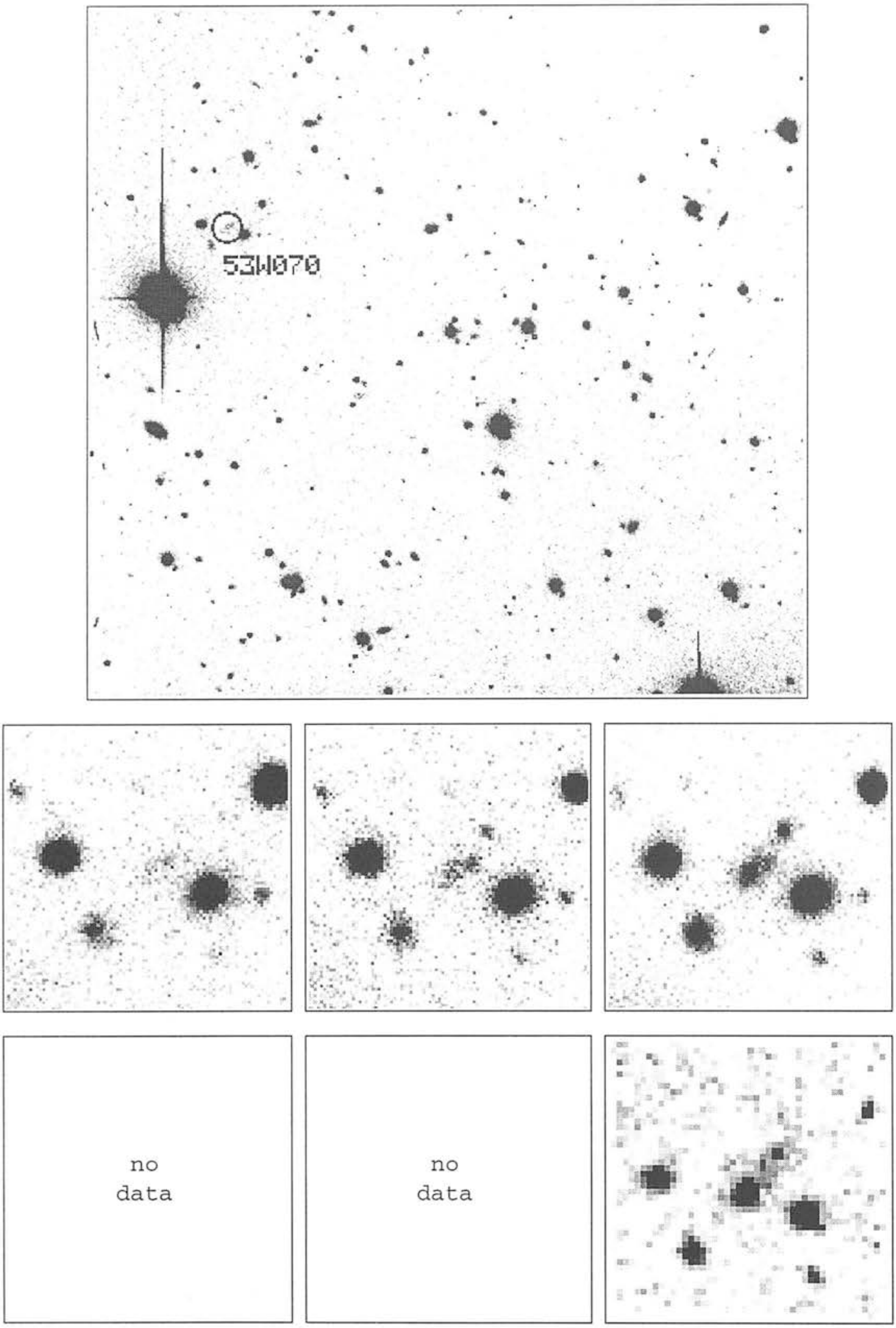

Figure 2.42 53W070

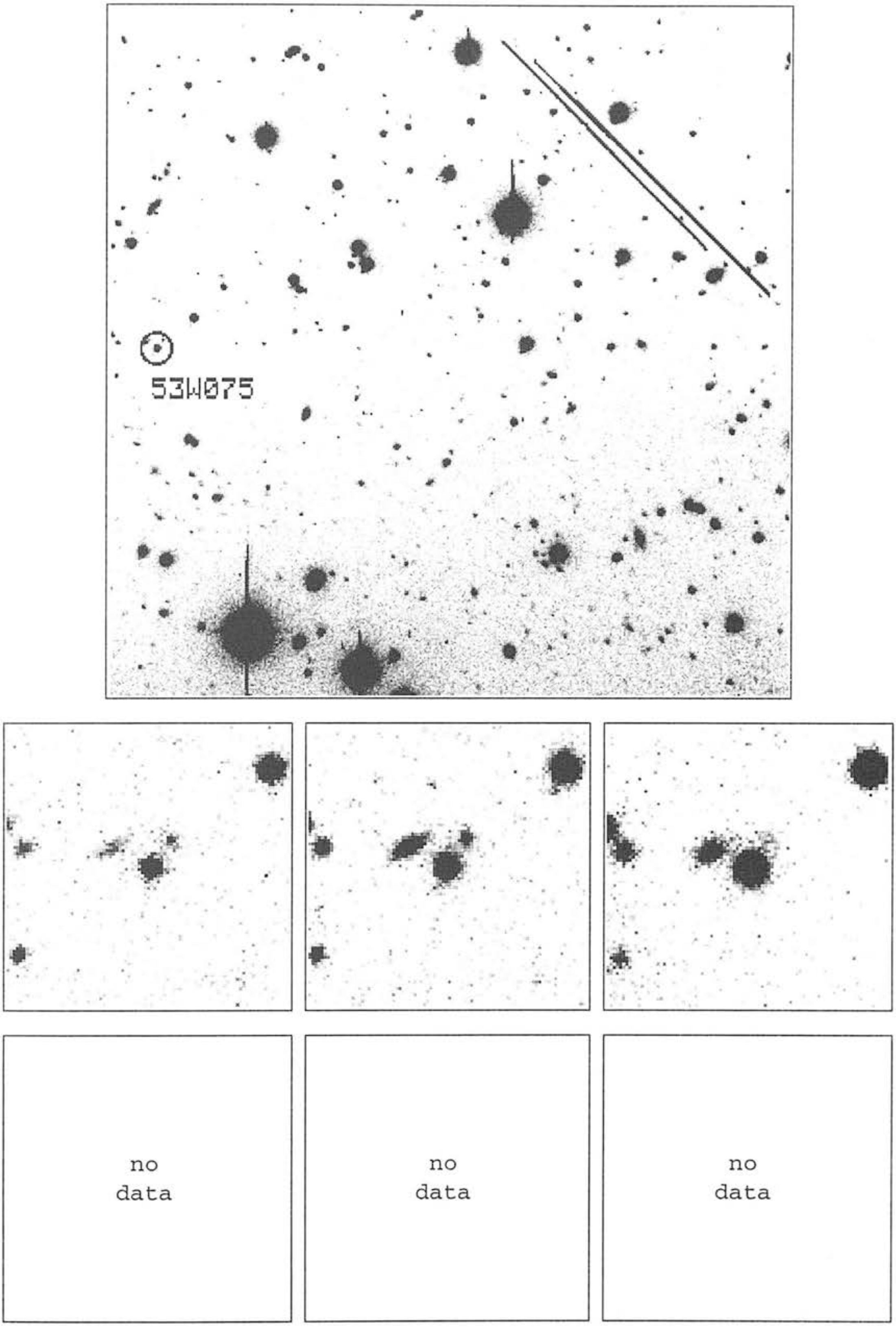

Figure 2.43 53W075

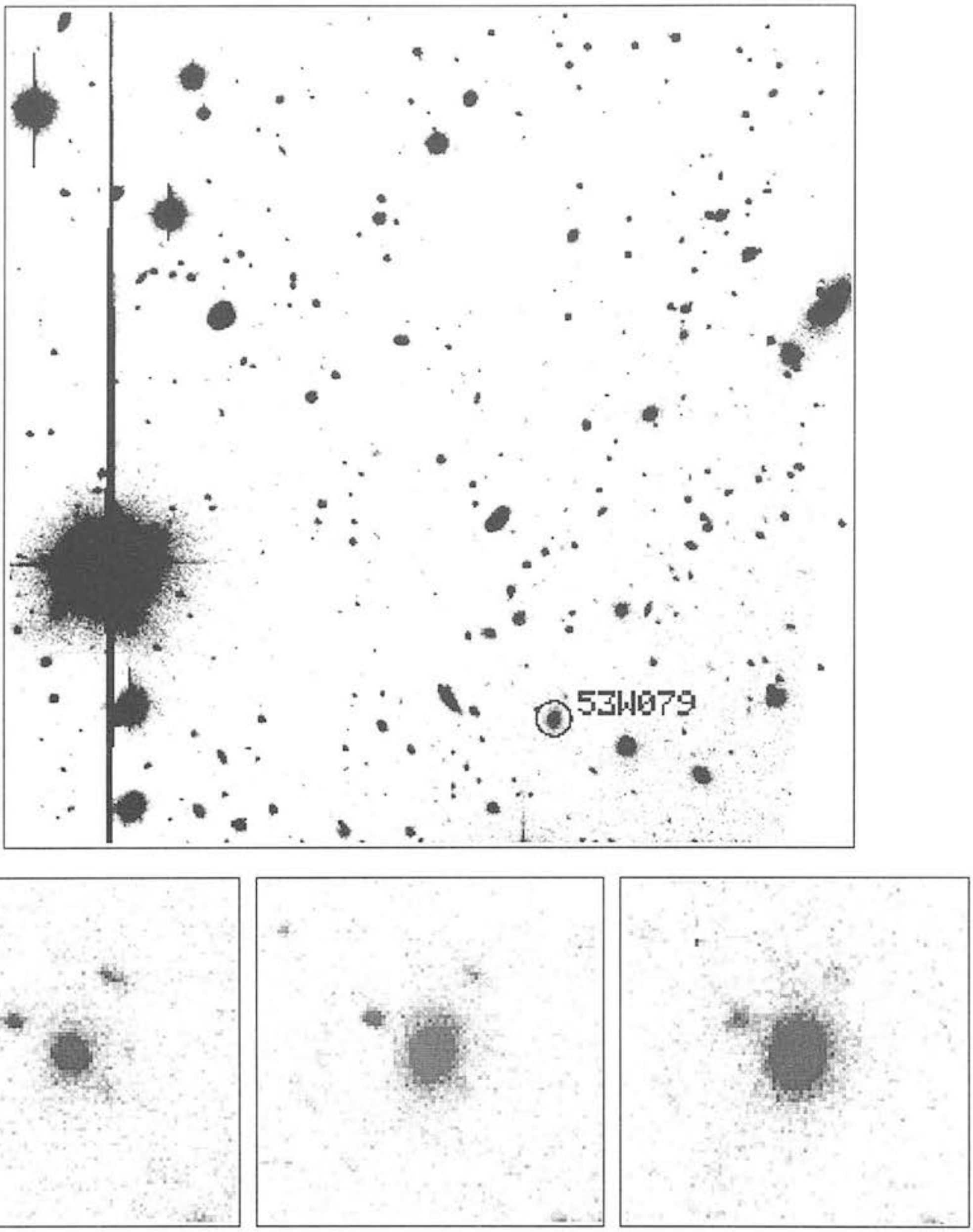

no
data

no
data

no
data

Figure 2.44 53W079

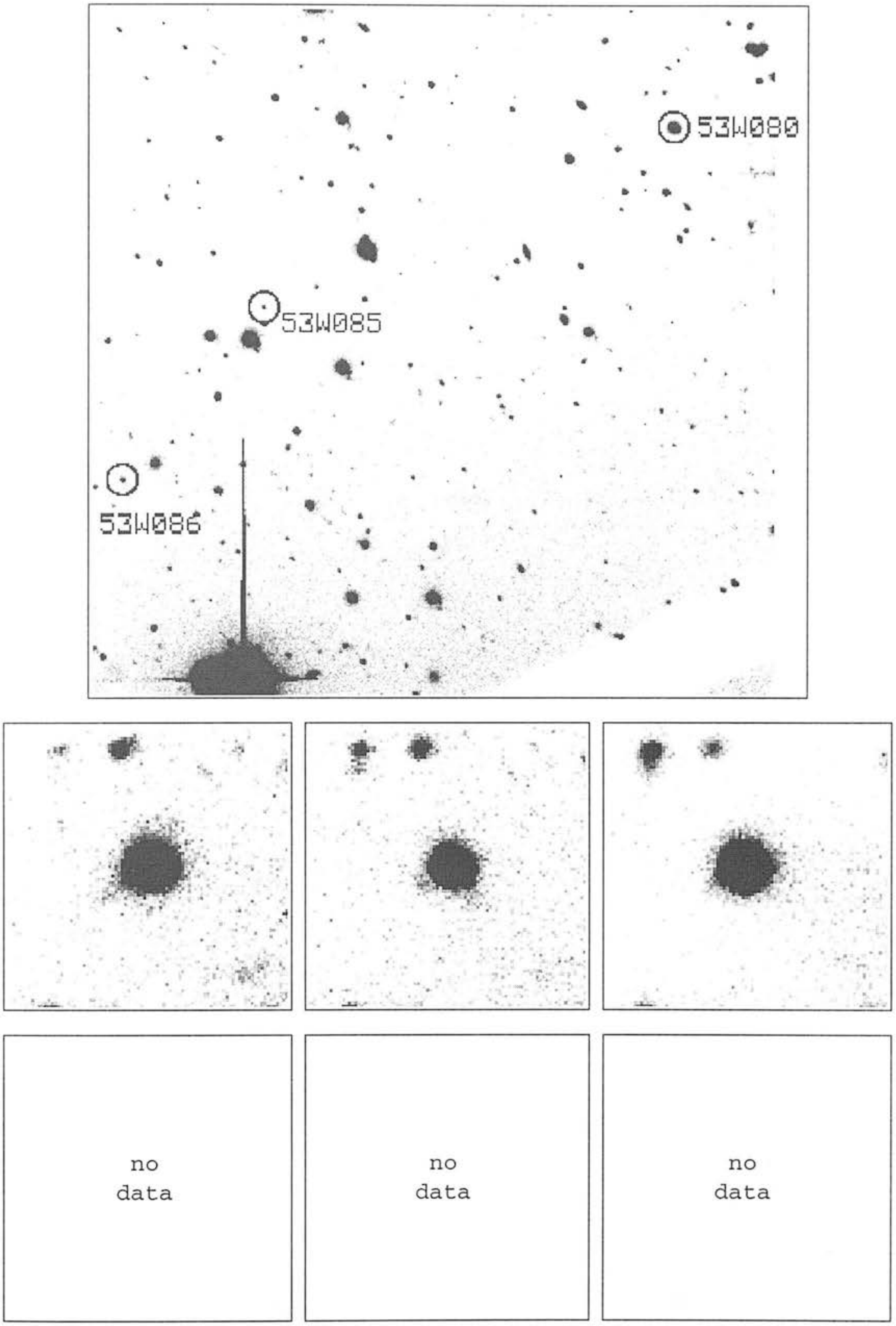

Figure 2.45 53W080

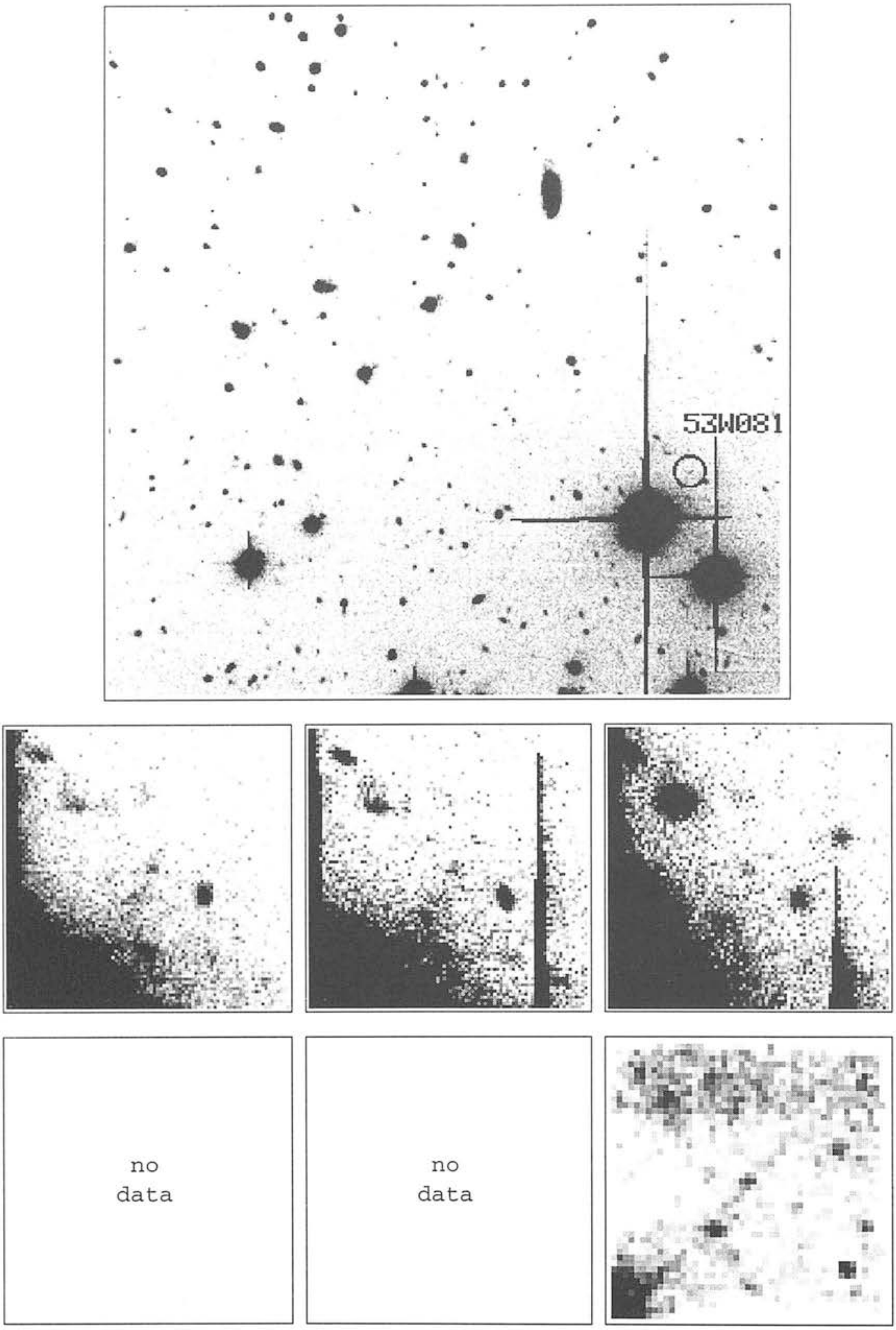

Figure 2.46 53W081

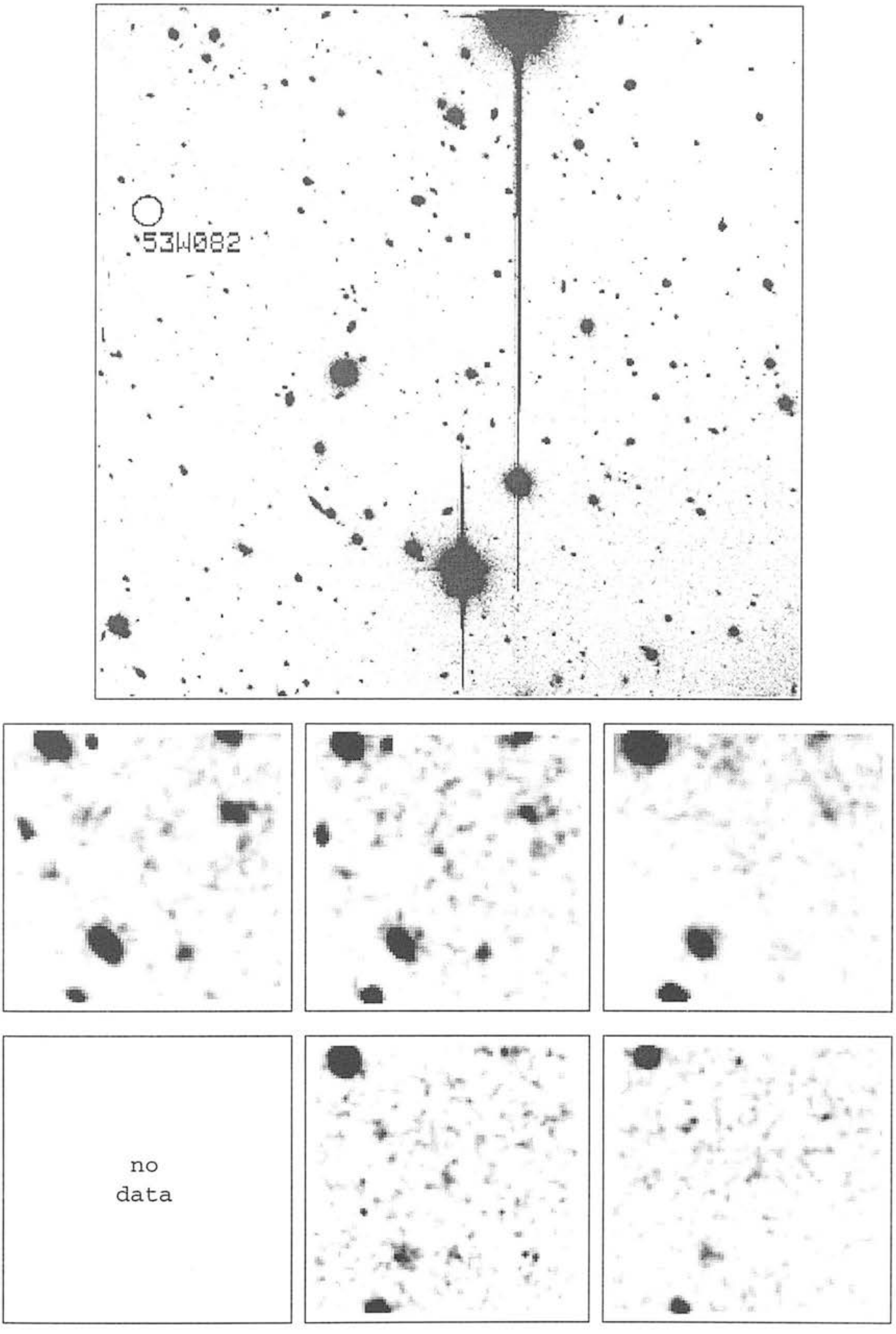

Figure 2.47 53W082

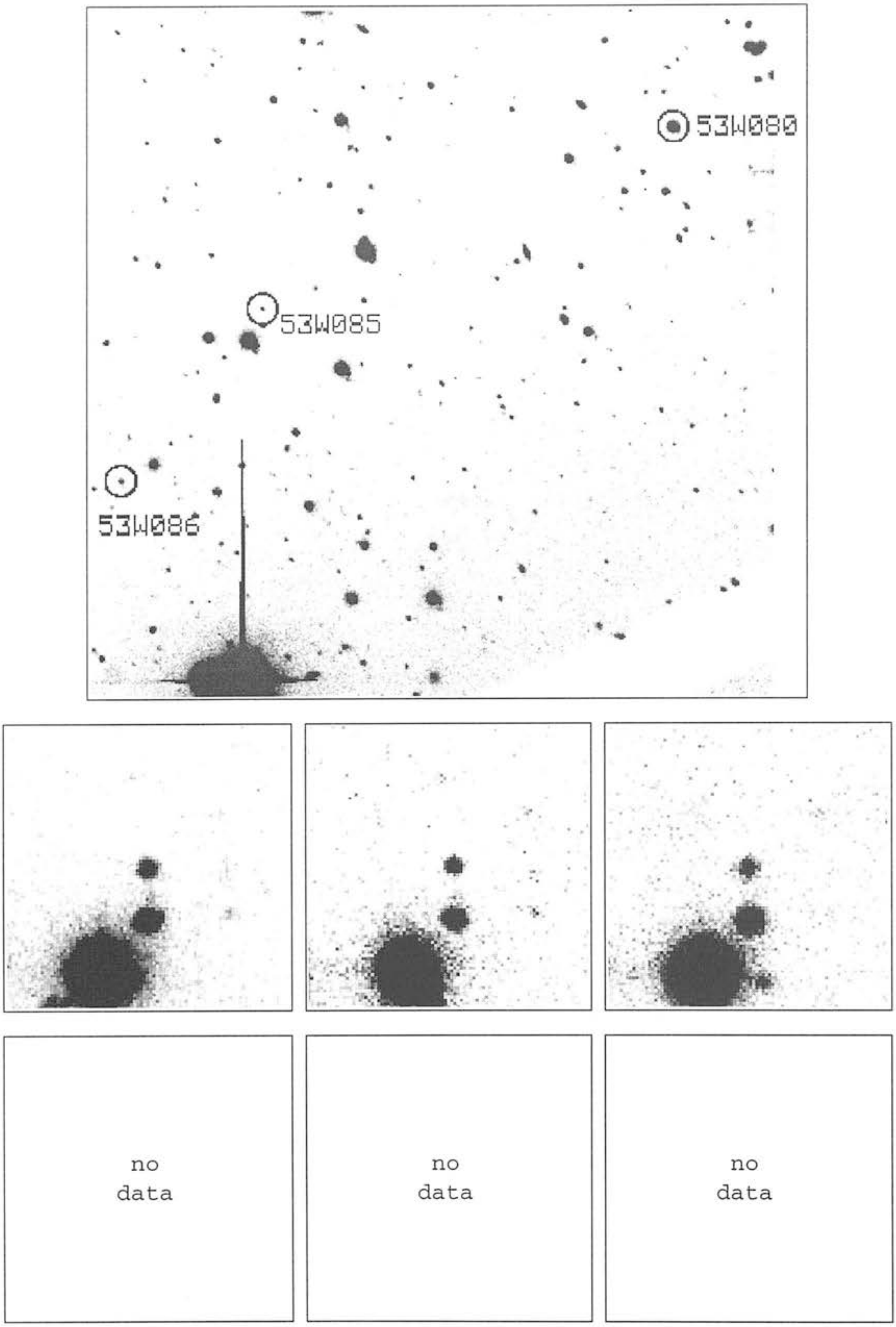

Figure 2.48 53W085

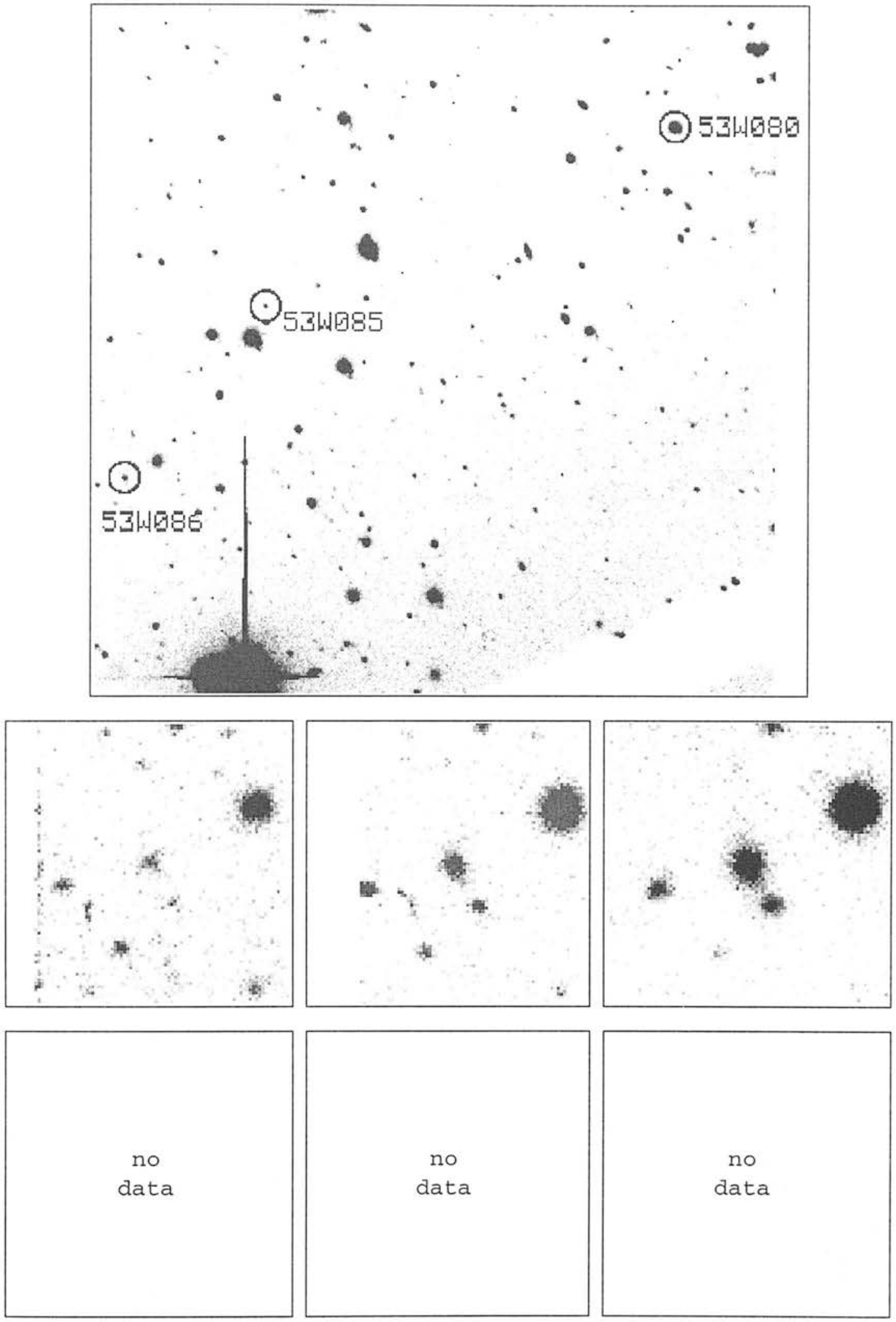

Figure 2.49 53W086

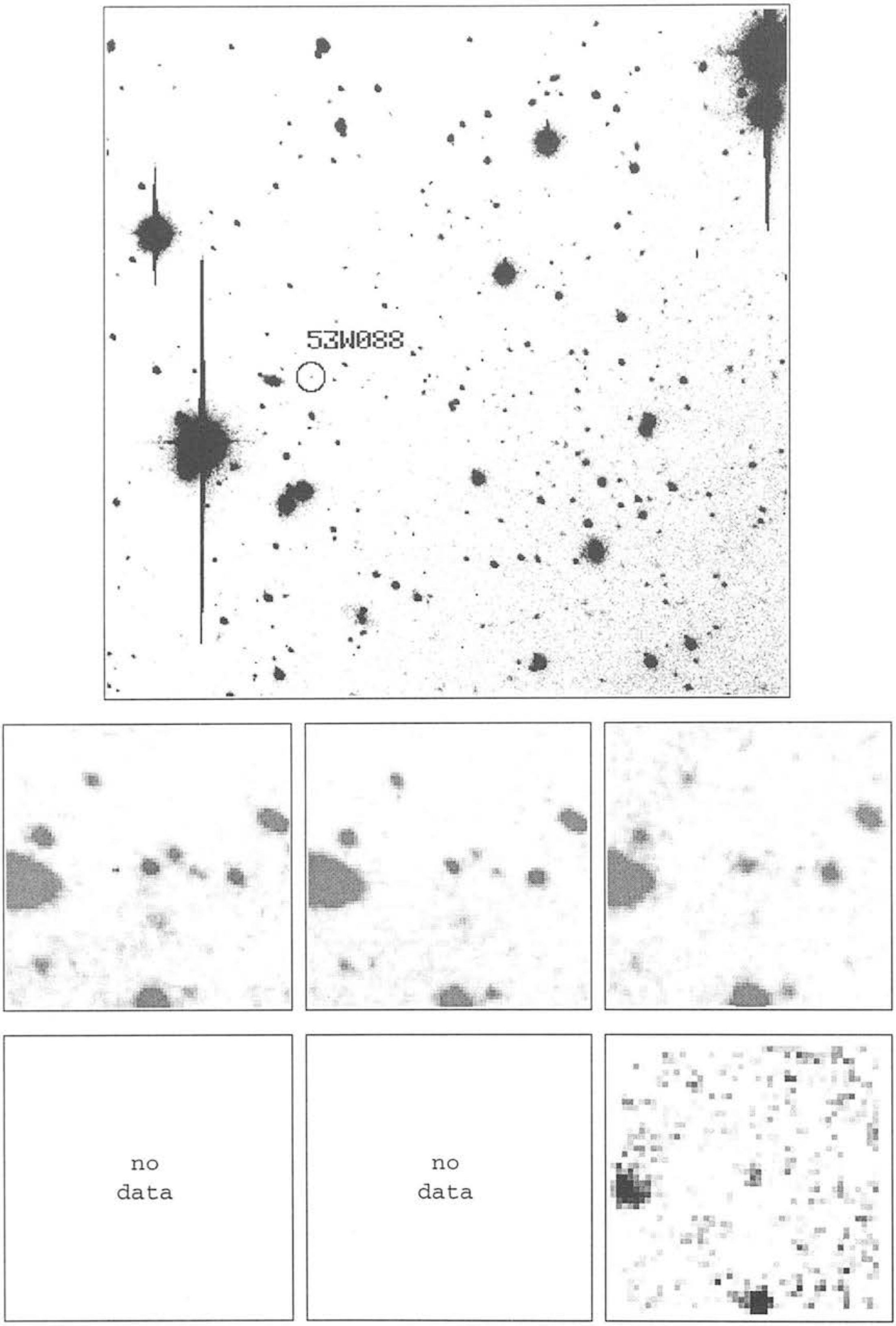

Figure 2.50 53W088

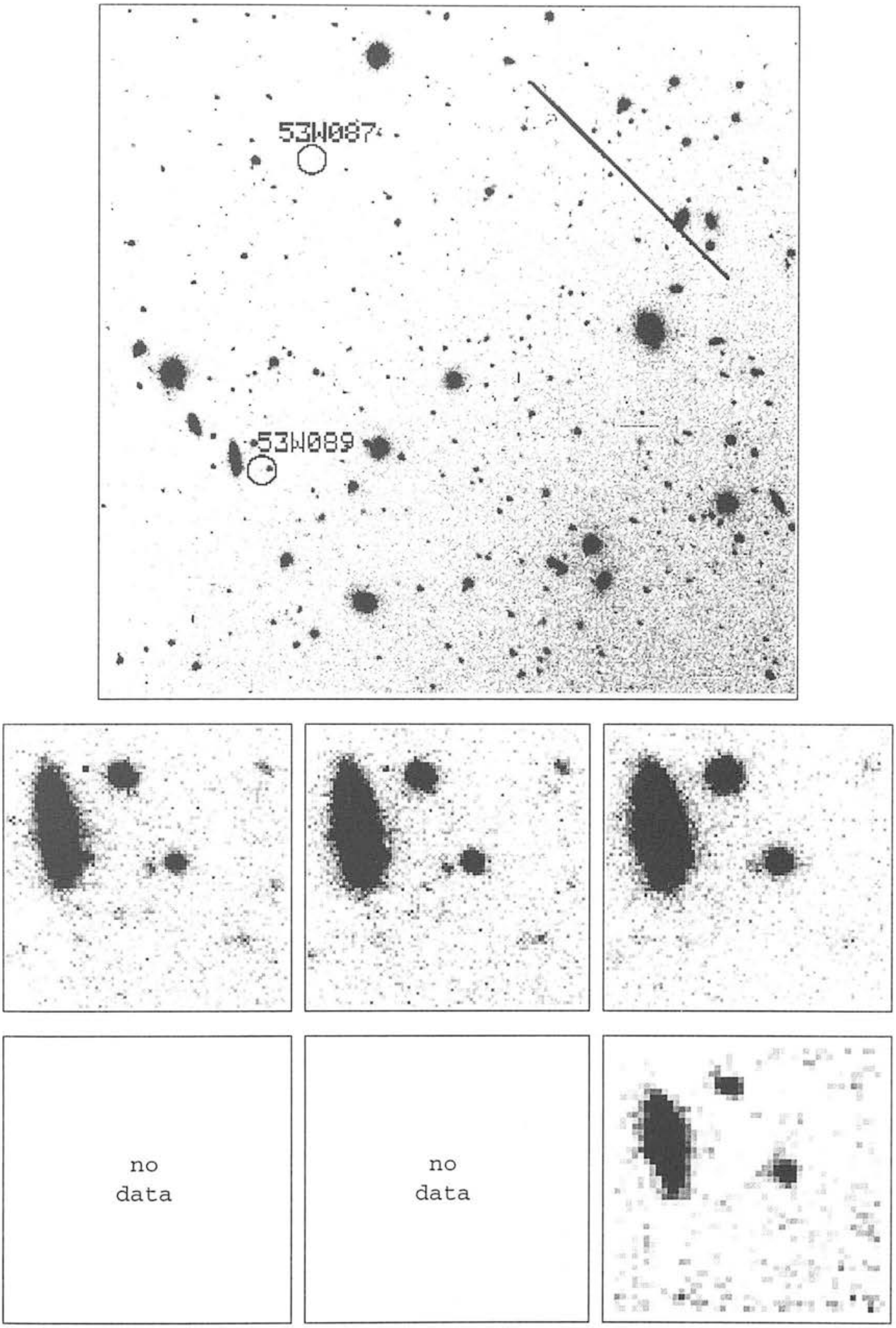

Figure 2.51 53W089

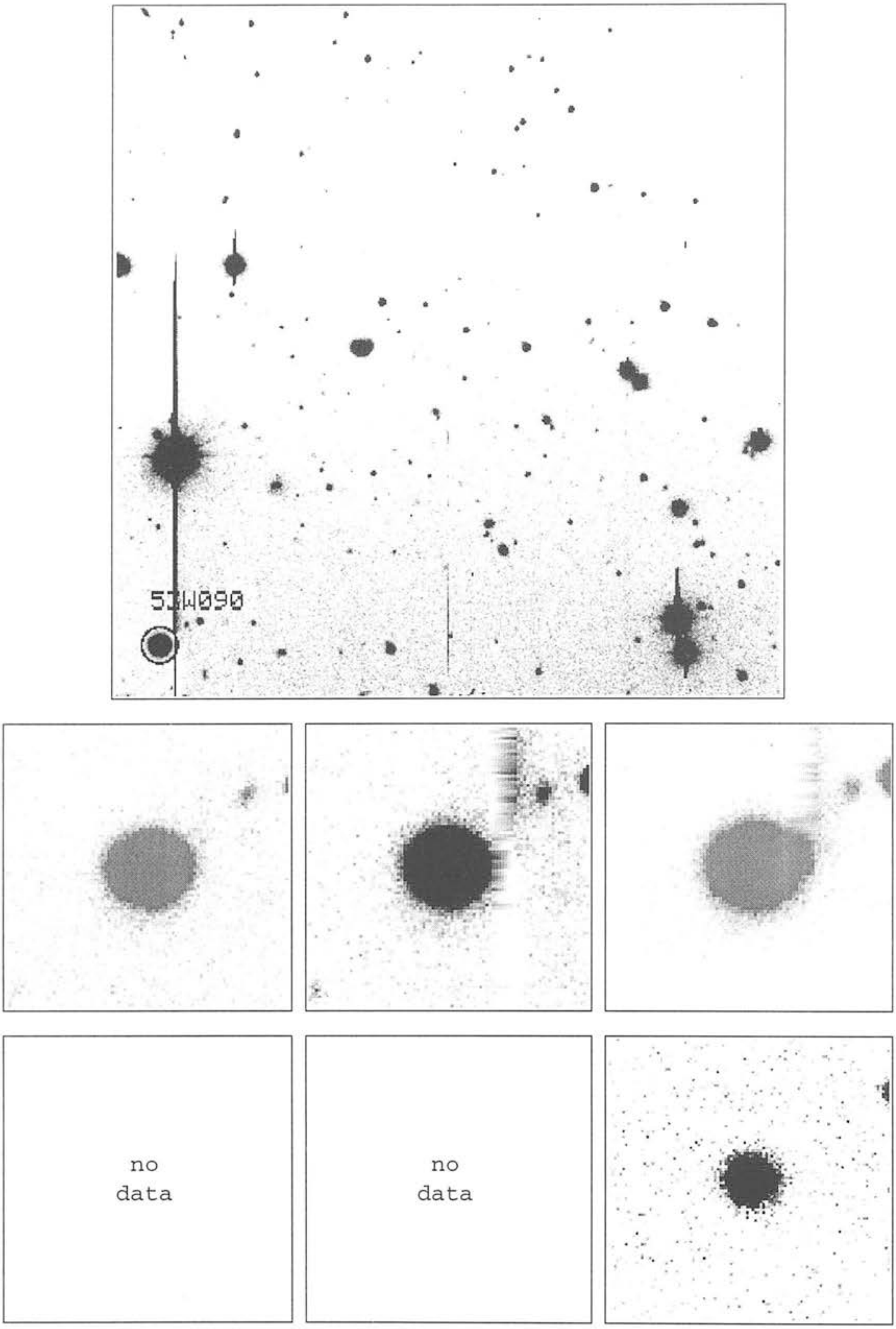

Figure 2.52 53W090

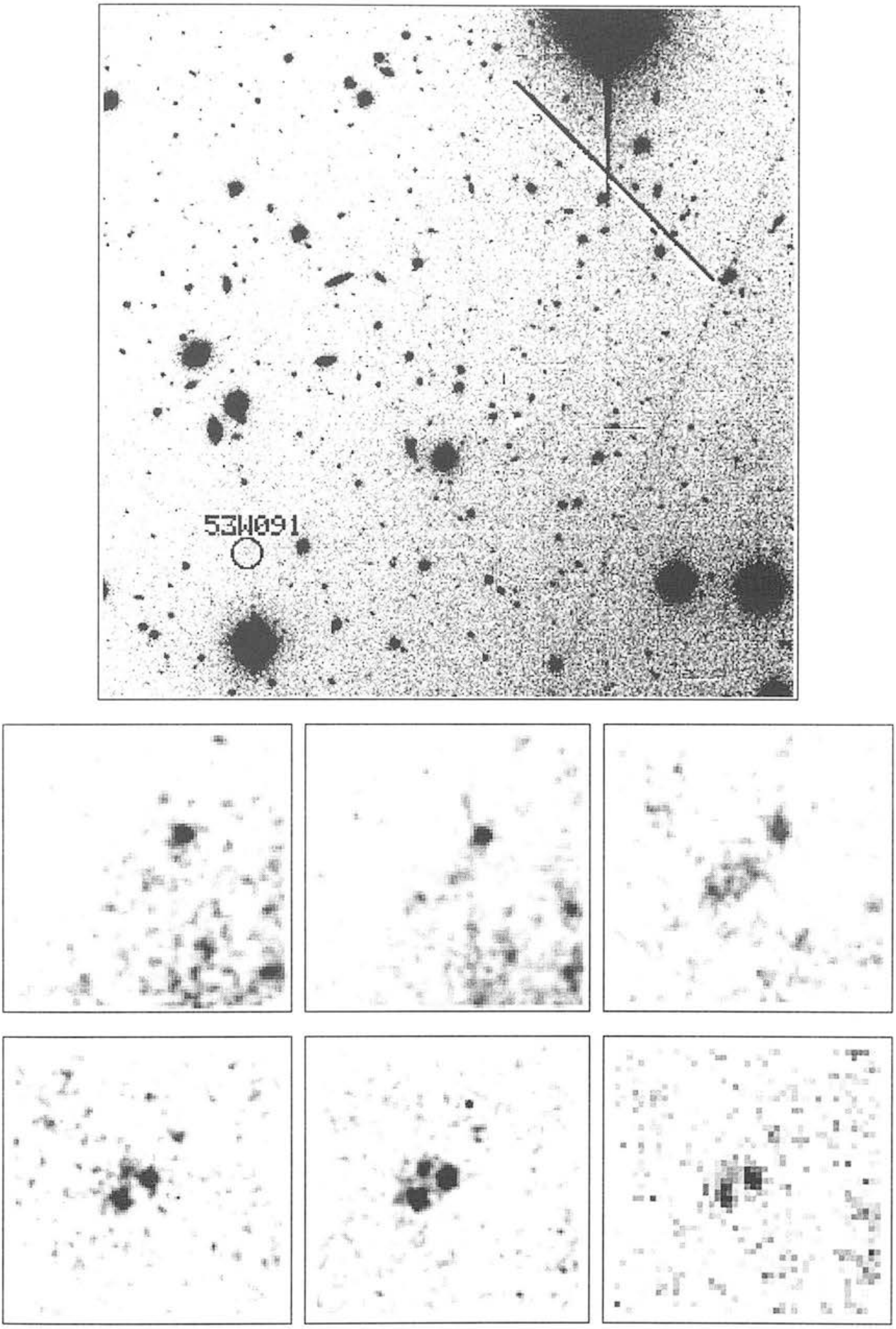

Figure 2.53 53W091

Chapter 3

Spectroscopy in the PSR and LBDS samples

The results of four observing runs to measure redshifts for sources in the Parkes Selected Regions and in the Leiden-Berkeley Deep Survey are reported. In the PSR, fifteen new redshifts have been determined, bringing the redshift content of this sample to 54%. Redshifts have also been measured for twelve sources in the LBDS, bringing the total to 67% of the sample. A comparison of the spectra shows that the LBDS sources are, in general, less active at rest-frame UV/optical wavelengths than the PSR sources.

3.1 Parkes Selected Regions

The purpose of this thesis is to investigate the cosmological evolution of galaxies, with particular emphasis on the luminosity function of radio sources. In order to do so, one needs to know the redshifts of the sources being investigated. This chapter will present the latest results of ongoing programmes to measure redshifts for sources in two radio surveys. This section describes observations of 38 sources in the Parkes Selected Regions (hereafter "PSR") and presents an update of the status of the sample. In the second half of the chapter (§§3.2 & 3.3) spectroscopic results from the Leiden–Berkeley Deep Survey ("LBDS") are reported.

3.1.1 Introduction

The Parkes Selected Regions is a complete sample of radio sources with $S_\nu \geq 0.1$ Jy at 2.7 GHz. Wall et al. (1971) found 188 sources with the Parkes 64 m telescope (HPBW of 8 arcmin), in six regions of the sky covering a total area of 0.075 sr (each region being $6^\circ\!.5 \times 6^\circ\!.5$). The co-ordinates of the field centres are given in table 3.1. Further observations were made at 1.5 GHz & 4.9 GHz with the VLA in A configuration (Downes et al. 1986). With a HPBW of $0''\!.5$ (at 4.9 GHz), these data provided accurate radio positions and morphologies for 178 of the sources, after rejecting ten sources from the sample because of confusion. Half the sources were also observed in C configuration (1.5 GHz & 4.9 GHz) in order to obtain reliable flux densities and to find large-scale emission. Optical counterparts were found for 100 sources on the Palomar Observatory Sky Survey and UK Schmidt plates, and 40 redshifts were measured.

A radio survey is most useful when the radio sources have been completely identified with optical/infrared counterparts. The optical identification programme of the PSR was essentially completed by Dunlop et al. (1989b), who used deep CCD images in B and R to identify a further 70 sources below the photographic plate limits. Only 8 sources remain unidentified following that work. Infrared K-band photometry was obtained for the majority of sources in four of the regions, with a limited number of observations in the remaining two ($12^{\rm h}$ and $13^{\rm h}$). Spectroscopic observations increased the number of redshifts to 82, corresponding to 46% of the sample (Dunlop et al. 1989b; Allington-Smith et al. 1991). The status of the sample as of 1989 is given in table 3.1.

The PSR was used for two studies in particular. First, the colour evolution of a sub-sample of the PSR was investigated by Dunlop et al. (1989a). Only those sources classified as galaxies (G & G?) in the four fields with nearly complete K-band photometry ($0^{\rm h}$, $1^{\rm h}$, $2^{\rm h}$ and $22^{\rm h}$) were selected to be in the sub-sample. This provided a "complete" sample in $S_{2.7}$, B, R and K at the expense of there being very few sources with measured redshifts. The redshifts

Table 3.1 Summary of the Parkes Selected Regions sample from Dunlop et al. (1989b).

Field centre (1950) RA	Dec	No. of sources	No. of IDs	No. of redshifts	No. of K mags
00 04 51	00 32	26	25	11	22
00 52 55	00 31	29	27	16	25
02 32 31	00 25	31	29	17	24
12 04 50	−00 31	25	24	10	11
13 40 48	−00 29	30	29	12	14
22 03 26	−18 50	37	36	16	32
	Total:	178	170 (96%)	82 (46%)	128 (72%)[1]

[1] For the four-region subsample ($0^{\rm h}$, $1^{\rm h}$, $2^{\rm h}$ and $22^{\rm h}$ fields), 84% had K photometry.

of these objects were therefore estimated from their K magnitudes using the empirical K–z relation (equation [1.10]) of Lilly et al. (1985). This estimation method was introduced in section 1.4 and will be discussed further in the next chapter (§4.1). Although the K–z relation is poorly known at high redshift, it is well-defined for $z \lesssim 1.7$. The main conclusions of Dunlop et al. (1989a) were not affected by the uncertainty at high-z, as they were based on the colours of galaxies at $z \sim 1$.

These conclusions were based on an updated version of the spectral evolution models of Guiderdoni and Rocca-Volmerange (1987) and were as follows: (i) All radio galaxies had evidence in $B - R$ for more activity than an old, passively-evolving burst model. (ii) The reddest $R - K$ colours could only be modelled by a galaxy that formed ~ 18 Gyr ago, placing limits on the Hubble constant ($H_0 \lesssim 50$ km s^{-1} Mpc^{-1} for $\Omega_0 = 0$) and the redshift of galaxy formation ($z_f \simeq 20$). (iii) The $B - R$ and $R - K$ colours could only be fit simultaneously by a two component model — an old stellar population plus a small fraction of recent star formation. (iv) The dispersion in the optical/infrared colours suggested that either the galaxies formed over a range of redshifts ($z_f \simeq 2$–20), or that they had different star-formation histories. Similar conclusions had been drawn from sources in the 3CR and 1-Jansky surveys, but the Dunlop et al. (1989a) investigation went 10–100 times fainter in radio flux.

The second study that made use of the PSR sample was the analysis of the radio luminosity function by Dunlop and Peacock (1990). This was introduced in chapter 1 and will be fully discussed in §4.1 below. Briefly, they constructed models of the luminosity function that were well-constrained where there were good data and then extrapolated them into those regions of the luminosity–redshift plane which lacked complete optical identifications or redshift information. Approximately half of the PSR sample had known redshifts and for the other sources the redshift had to be estimated. Once again this was done using Lilly's K–z relation (equation [1.10]), and in some cases the K magnitude itself had to be estimated from the B and R magnitudes.

The major result of Dunlop and Peacock (1990) was the discovery that both the steep-spectrum ($\alpha \geq 0.5$) and flat-spectrum sources showed a decline in comoving density at high redshift ($z \gtrsim 2$). However, this result depended critically on the accuracy of the redshift estimation and, as already noted, the K–z relation is poorly defined at $z \gtrsim 1.7$. If the estimates were too small and more of the sources were at high redshift than predicted, this could remove the necessity of a "cut-off" in the radio luminosity function. It was thus of interest to test the accuracy of the redshift estimates by measuring spectroscopic redshifts for as many of the high-z candidates as possible. In the remainder of this section, the results of a programme to do this are reported. Section 3.1.2 describes the observations and data reduction methods, and the results follow in §3.1.3. A discussion of the implications of the new results for the redshift cut-off are postponed until the next chapter (§4.2), following a detailed presentation of the model luminosity functions.

3.1.2 Observations and data reduction

The observations of 38 PSR sources were made over 8 nights (of which two were lost to bad weather) at the 3.9-m Anglo-Australian Telescope during two observing runs in April 1993 and July 1994, by J. S. Dunlop and S. Rawlings respectively. The instruments used were the Faint Object Red Spectrograph (FORS) in combination with the RGO Spectrograph (RGOS). After passing through the slit and dekker arrangement, the light beam is split at 5400 Å by a dichroic mirror with the red light being directed into FORS and the blue light continuing through RGOS. The FORS detector is a GEC CCD which is particularly sensitive to red wavelengths. The dispersion of the spectrograph is 10 Å pixel^{-1}, with a fixed wavelength coverage of 5200→10900 Å. The RGOS used with the Tek CCD (which is more sensitive to blue light than the GEC chip) and the 250B low dispersion grating, has a dispersion of 3.6 Å pixel^{-1} and a wavelength coverage of 3100→6800 Å. The two instruments together thus give a wide wavelength range of 3100→10900 Å with a low resolution, ideally suited for detecting faint emission line spectra.

The telescope was pointed at each target using the "blind offsetting" technique, as most of the sources were too faint to see directly. The relative position of a star near to the source

($\lesssim 1'$) was measured on the CCD, or a digital scan of the photographic plate, to sub-arcsecond accuracy. This star was centered in the spectrograph slit and a short exposure taken. The telescope was then offset to the source's position using the known separation of the star and source. This not only ensured that the source was centered in the slit but also showed which row/column of the CCD the source should be found in.

The raw spectrum usually consisted of two or more exposures for each detector (FORS and RGOS), typically of 1800 s duration. Flat-field exposures of both the twilight sky and the internal tungsten lamp were taken during the runs. Observations were made of spectrophotometric standard stars so that approximate flux calibrations could be made in order to join the FORS and RGOS halves of the spectra smoothly at 5400 Å, as well as to give information about the overall shape of the continuum. Featureless standard stars were also observed to aid in the removal of atmospheric absorption features at the red end of the spectrum.

Due to the faintness of these sources (typically $R \sim 22$–23) considerable time was spent on finding the best possible method to reduce the spectra, in particular how to flat-field and combine the raw exposures, and determining the best method of sky subtraction. For approximately half the sources, three or more exposures were made back-to-back, enabling these frames to be combined by taking the median of the separate frames in addition to the mean. It was found that although the theoretical signal-to-noise ratio should be a factor of $\sqrt{2}$ higher by taking the mean of the exposures compared to the median, in practice it made no detectable improvement, indicating that the noise was dominated by sky subtraction errors. Since taking the median simultaneously removed all the cosmic rays from the data, this method was used wherever possible. When only two exposures were obtained, they were simply combined by using the clipped mean of the two.

The flat-fields obtained with the internal tungsten lamp were found to suffer from significant vignetting and after investigation it was decided that the large-scale variations that they introduced caused more problems than the pixel-to-pixel variations that they corrected. It was decided to discard the tungsten flat-fields and only use the sky flats. The sky flats were produced by taking the median of ~10 twilight sky exposures, collapsing the resulting frame along the spectral direction (preserving the spatial information), and then growing back a two-dimensional flat-field with this spatial profile. The resulting sky flat successfully removed the vignetting across the slit and aided identification of the sources' position on the CCD.

The most important stage in the reduction procedure was the subtraction of the sky spectrum from the object spectrum, given that the number of counts in the object was typically 1% of the sky. In general, the sky flat-field resulted in a two-dimensional spectrum which was genuinely flat in the spatial direction. Attempts to fit a polynomial to the (small) spatial unevenness did not improve the flat-fielding. The best sky subtraction was obtained by producing a sky spectrum from the mean of ~5 columns from each side of the object, as close to the object as possible — in the cases where the object could not be seen its position was assumed to be the same as for the offset star or as in the previous or following exposures. This sky subtraction was the principal source of noise in the final spectra, and it was important to compare possible emission lines with the wavelengths of the sky emission lines which were not always removed completely.

The reduction procedure thus consisted of the following nine stages: (i) subtraction of a constant bias across the frame; (ii) division by the normalised sky flats; (iii) averaging of the exposures, using the median when possible and mean when not; (iv) identification and extraction of object and sky spectra; (v) subtraction of sky from object spectrum; (vi) division of the red spectrum by the normalised featureless standard to remove atmospheric absorption features; (vii) wavelength calibration and re-binning of the RGOS spectrum to the same dispersion as the FORS data; (viii) flux calibration from the spectro-photometric standard; and finally (ix) the blue and red spectra were spliced together after each was cut at 5400 Å. The basic steps in the method are illustrated in figure 3.3, with the exception that the tungsten flats were not used in this case.

Emission lines were identified from the spectra by looking for known patterns of prominent lines, and by comparison to spectra in the literature. In addition, an attempt was made to make the identification process more objective by writing a Fortran program that would try to fit all possible combinations of emission lines and redshifts, given a list of the wavelengths of observed emission line candidates. Although this program rarely produced a unique redshift and line list, it proved very useful for supplying a number of possible fits to the wavelengths and for confirming visual identifications. An attempt was also made to use a cross-correlation technique to fit a model spectrum to the observations using a routine in FIGARO (Shortridge et al. 1997), though this proved unsuccessful — perhaps due to the high noise in the observed spectra.

3.1.3 Results and discussion

Of the 38 radio sources observed, 15 have emission lines from which a redshift has been determined. A further 7 show weak/noisy features that have two or more possible identifications and no unambiguous redshift, and the remaining 16 sources show no evidence of emission lines. The 15 sources with new redshifts are listed in table 3.2, together with their identified spectral lines, and their spectra are presented in figure 3.1.

One interesting result of this work so far is the discovery that the radio galaxy 1339+015 lies at a redshift of 3.511, making it one of the most distant known at the time of discovery (1994). With an $R - K$ colour of 5.2, it is also one of the reddest galaxies known at $z > 3$. If this very red colour is due to an evolved 4000 Å-break, i.e. 1339+015 is an old galaxy, at such large lookback times this will have important implications for cosmology (at $z = 3.5$, the universe is only 1.4 Gyr old in an Einstein-de Sitter model with $H_0 = 50$ km s^{-1} Mpc^{-1}). However, the red colour may also be due to emission line contamination in the K-band — the Hβ and [O III] lines would be at 2.23 μm at that redshift. The strength of the emission lines in the optical spectrum suggests that the galaxy's optical/infrared emission may be dominated by the AGN, in which case the Hβ and [O III] lines could make a significant contribution to the K-band flux, thus making the galaxy younger than the colours alone suggest.

A few features can be noted about several of the other spectra in figure 3.1. The weak C III and [Ne III] emission lines in 1205+011 ($z = 0.495$) are very noisy, however the redshift is principally based on the stronger [O II] line and the rise of the spectrum into the red, following the 4000 Å-break. The rising blue continuum of 1212−007 ($z = 1.599$) is consistent with that expected in an active or young galaxy at that redshift. The redshift of 1331+004 ($z = 1.401$) is principally based on the identification of the broad line at 6726 Å with Mg II. The strong continuum blueward of this line is inconsistent with it being identified with Lyα, and if the line were [O II] 3727 or [O III] 5007 then either [O III] or [O II] respectively would also be visible in the spectrum. These are the only other reasonable identifications for such a significant emission line, thus it is concluded that Mg II is the correct ID — the very noisy C IV line at the edge of the spectrum also supports this conclusion. The redshift determinations for the other sources require little comment.

The emission lines detected in these fifteen PSR sources are typical of those found in previous PSR redshift programmes (Dunlop et al. 1989b; Allington-Smith et al. 1991). They are also typical of those seen in narrow emission-line radio galaxies (NLRGs) observed in the 3CR, 1-Jansky and similar samples (McCarthy 1993).

To summarise, 38 sources from the PSR survey with high estimated redshifts ($z \gtrsim 1$) have been observed with the AAT. Of these, emission line redshifts for 15 radio galaxies have been found over the wide range of $0.5 < z < 3.5$. This brings the total redshift content to 97 out of 178 sources (54%). A comparison of these results with their estimates will be presented in §4.2 below, together with a discussion of the implications for the cut-off in the radio luminosity function.

Table 3.2 The redshifts and line lists for the 15 sources in the Parkes Selected Regions subsample observed in 1993 & 1994.

Name	Type[1]	Mean Redshift[2]	$\lambda_{\rm obs}$ (Å)	Identification	z
1154−011	G	1.210 ± 0.001	4215	C III 1909	1.208
			7393	[Ne V] 3346	1.210
			7582	[Ne V] 3426	1.213
			8237	[O II] 3727	1.210
			8552	[Ne III] 3869	1.210
1154−019	G	0.862 ± 0.001	6947	[O II] 3727	0.864
			7206	[Ne III] 3869	0.862
			9042	Hβ 4861	0.860
			9236	[O III] 4959	0.862
			9324	[O III] 5007	0.862
1201−026	G?	1.429 ± 0.001	3766	C IV 1549	1.431
			3986	He II 1640	1.430
			4634	C III 1909	1.427
			6797	Mg II 2799	1.428
			7771	He II 3203	1.426
			9060	[O II] 3727	1.431
			9395	[Ne III] 3869	1.428
1205+011	G?	0.495 ± 0.001	3480	C II 2326	0.496
			5563	[O II] 3727	0.493
			5771	[Ne III] 3869	0.492
			5940	[Ne III] 3967	0.497
1212−007	G?	1.599 ± 0.005	4036	C IV 1549	1.606
			4963	C III 1909	1.600
			8646	[Ne V] 3346	1.584
			8929	[Ne V] 3426	1.606
1331+004	G?	1.401 ± 0.002	3714	C IV 1549	1.398
			6726	Mg II 2799	1.403
1339+015	?	3.511 ± 0.002	5481	Lyα 1216	3.507
			6989	C IV 1549	3.512
			8620	C III 1909	3.515

Table 3.2 *Continued.*

Name	Type[1]	Mean Redshift[2]	$\lambda_{\rm obs}$ (Å)	Identification	z
1345+008	G?	1.502 ± 0.001	3875	C IV 1549	1.502
			4105	He II 1640	1.503
			4168	[O III] 1663	1.506
			4768	C III 1909	1.498
			5810	C II 2326	1.498
			6053	Ne IV 2423	1.498
			8371	[Ne V] 3346	1.502
			8573	[Ne V] 3426	1.502
1346+018	G	0.648 ± 0.001	6140	[O II] 3727	0.647
			8013	Hβ 4861	0.648
			8176	[O III] 4959	0.649
			8256	[O III] 5007	0.649
1349−008	G	0.975 ± 0.001	3764	C III 1909	0.972
			4785	[Ne IV] 2423	0.975
			6609	[Ne V] 3346	0.975
			6765	[Ne V] 3426	0.975
			7362	[O II] 3727	0.975
			7641	[Ne III] 3869	0.975
			9598	Hβ 4861	0.974
			9795	[O III] 4959	0.975
			9887	[O III] 5007	0.975
2150−202	G?	1.326 ± 0.001	4440	C III 1909	1.326
			6512	Mg II 2799	1.327
			7974	[Ne V] 3426	1.327
			8667	[O II] 3727	1.325
			8998	[Ne III] 3869	1.326
			9235	[Ne III] 3967	1.328
			9466	[S II] 4072	1.325
2156−192	G	0.453 ± 0.001	5418	[O II] 3727	0.454
			5706	Ca K 3933	0.451
			5767	Ca H 3968	0.453
			7216	[O III] 4959	0.455
			7285	[O III] 5007	0.455
			7520	Mg b 5174	0.453
			8552	Na D 5893	0.451
			9531	Hα 6563	0.452

Table 3.2 *Continued.*

Name	Type[1]	Mean Redshift[2]	$\lambda_{\rm obs}$ (Å)	Identification	z
2158−160	G	1.236 ± 0.001	4265	C III 1909	1.234
			7465	[Ne V] 3346	1.231
			7659	[Ne V] 3426	1.236
			8342	[O II] 3727	1.238
			8656	[Ne III] 3869	1.237
			8883	[Ne III] 3967	1.239
2202−179	G?	1.351 ± 0.001	3643	C IV 1549	1.352
			4486	C III 1909	1.350
			6575	Mg II 2799	1.349
			8769	[O II] 3727	1.353
			9105	[Ne III] 3869	1.353
2215−185	G?	1.036 ± 0.002	4937	[Ne IV] 2423	1.038
			5017	O II 2470	1.031
			5684	Mg II 2799	1.031
			7594	[O II] 3727	1.038
			8016	Ca K 3933	1.038
			8085	Ca H 3968	1.038

[1] The optical classification of the source in Dunlop et al. (1989b), where 'G' is a galaxy, 'G?' is faint ID with colours suggesting it is a galaxy, and '?' is an uncertain optical classification. [2] Errors are the standard error on the mean of the individual line redshifts.

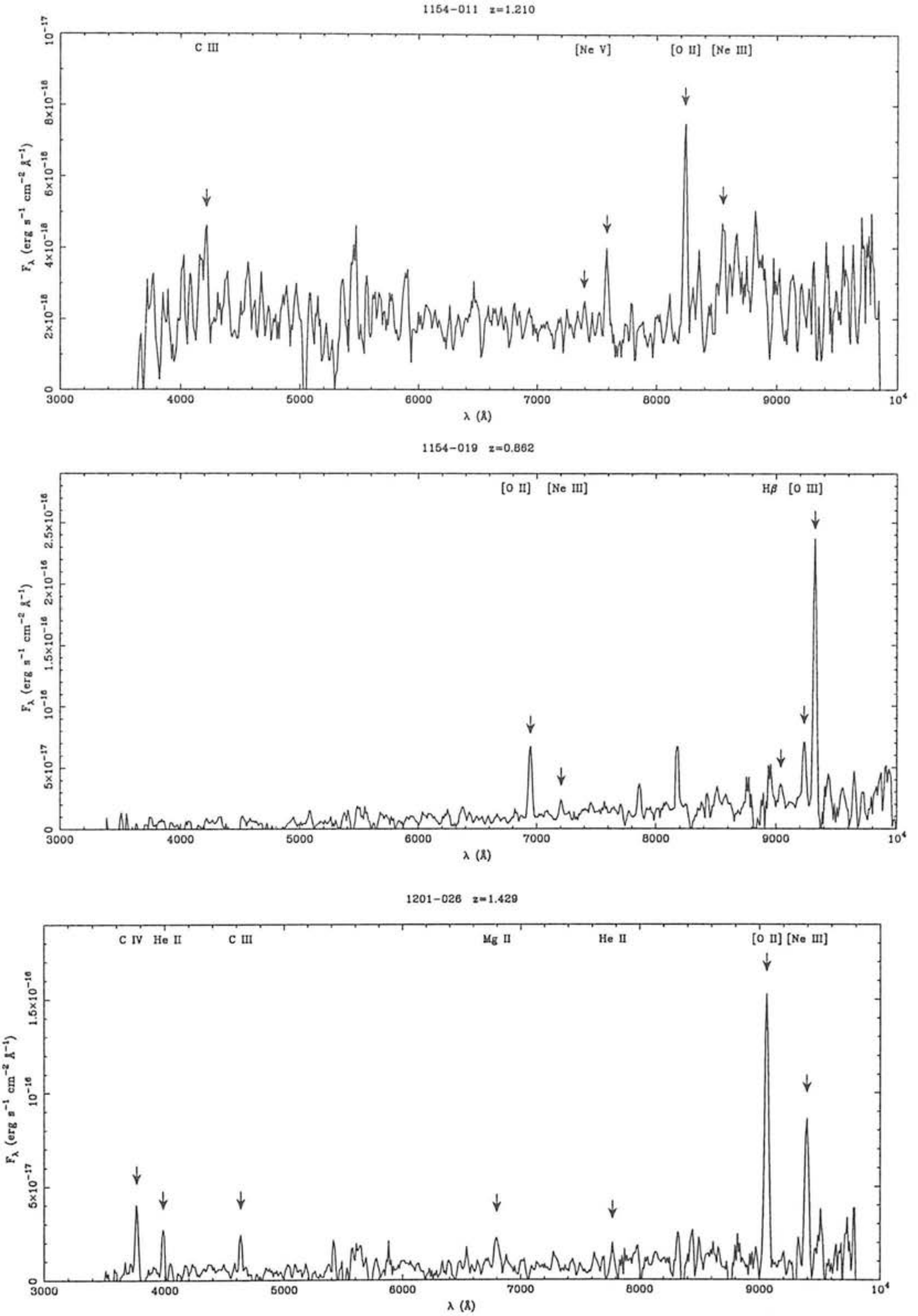

Figure 3.1 The spectra of the 15 sources in the Parkes Selected Regions for which new redshifts have been determined. The line identifications listed in table 3.2 are marked.

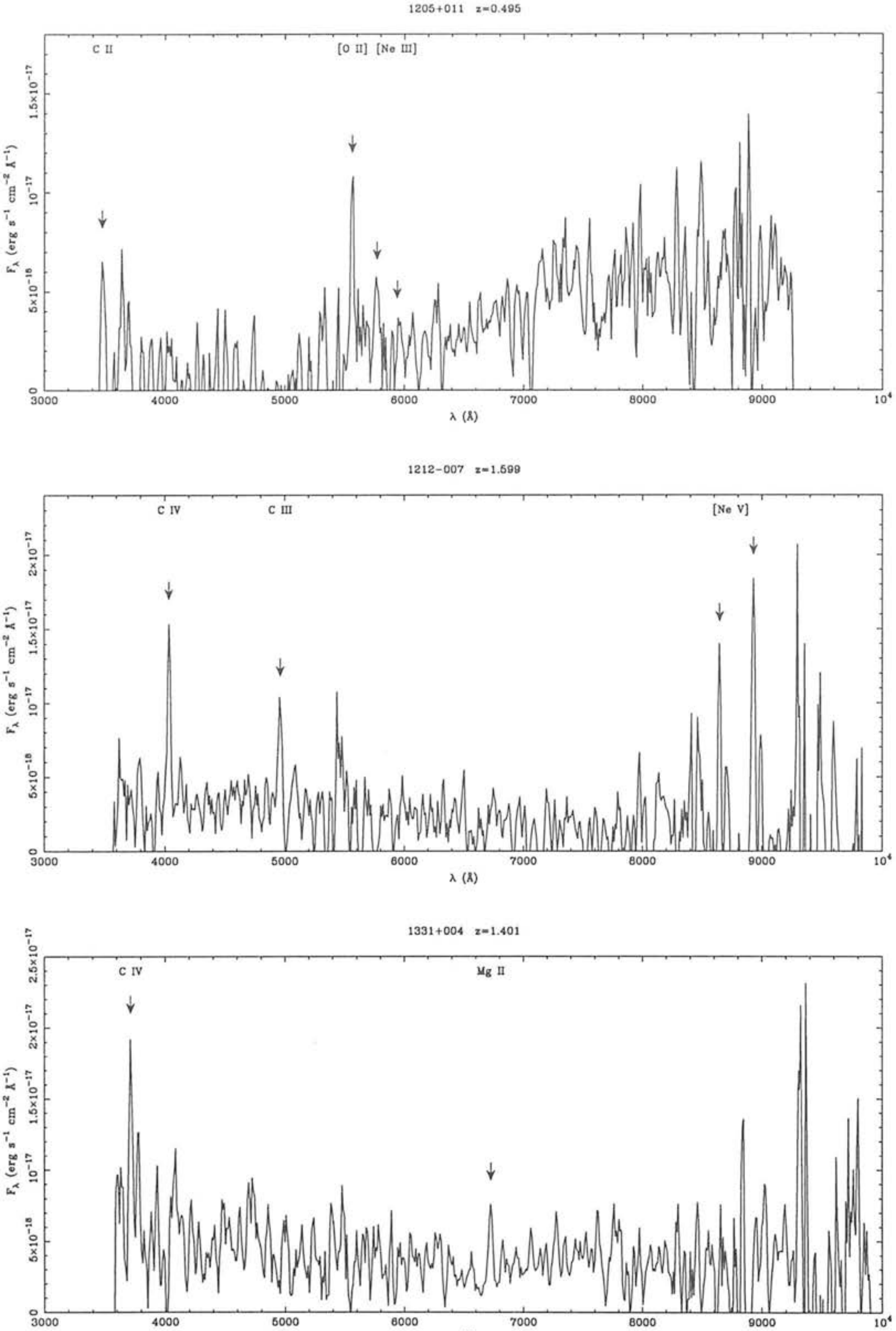

Figure 3.1 *Continued.*

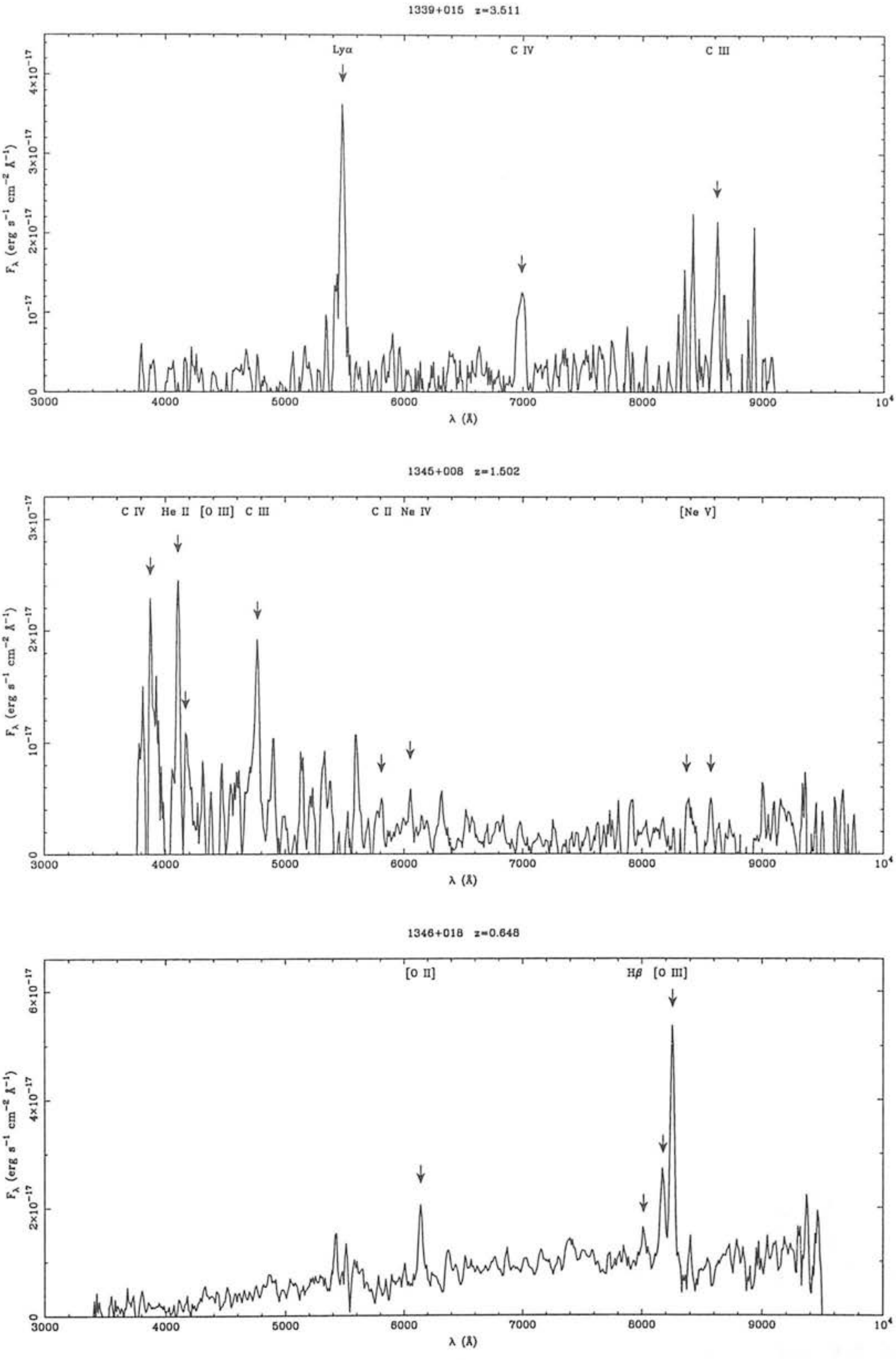

Figure 3.1 *Continued.*

1349-008 z=0.975

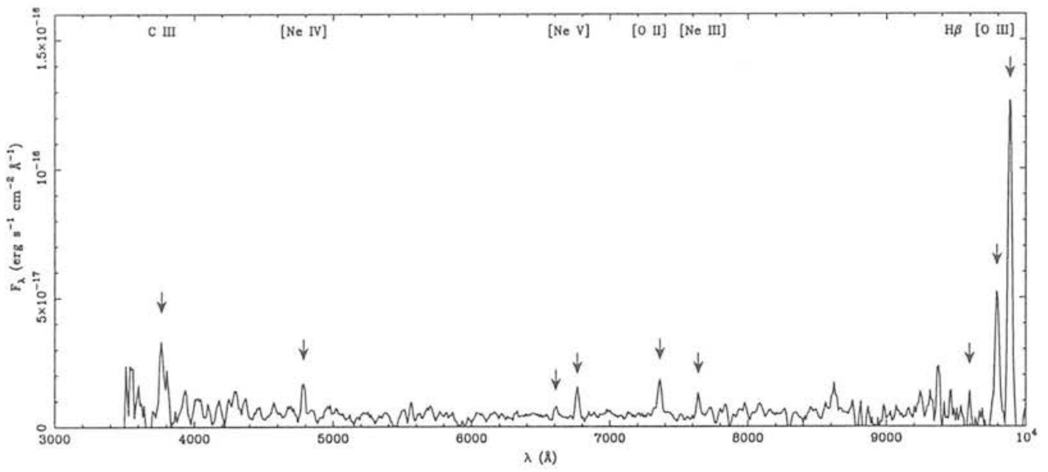

2150-202 z=1.326

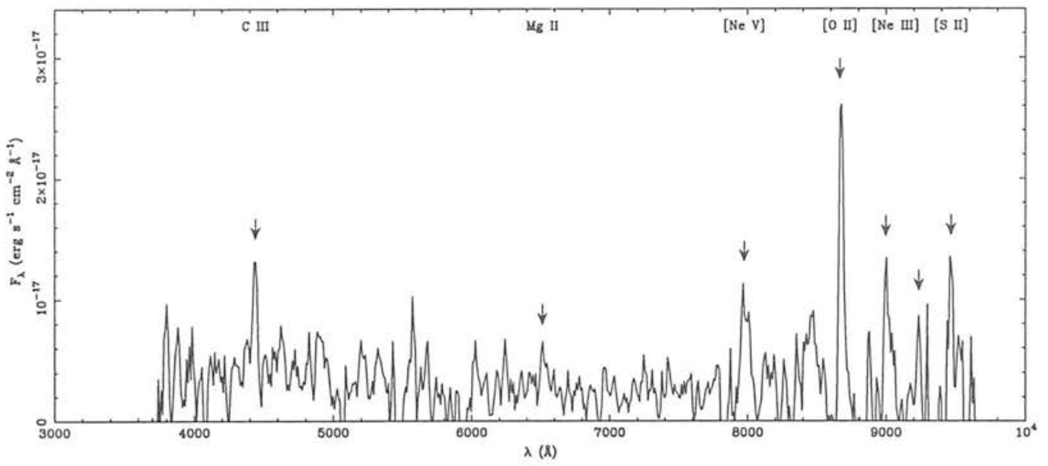

2156-192 z=0.451

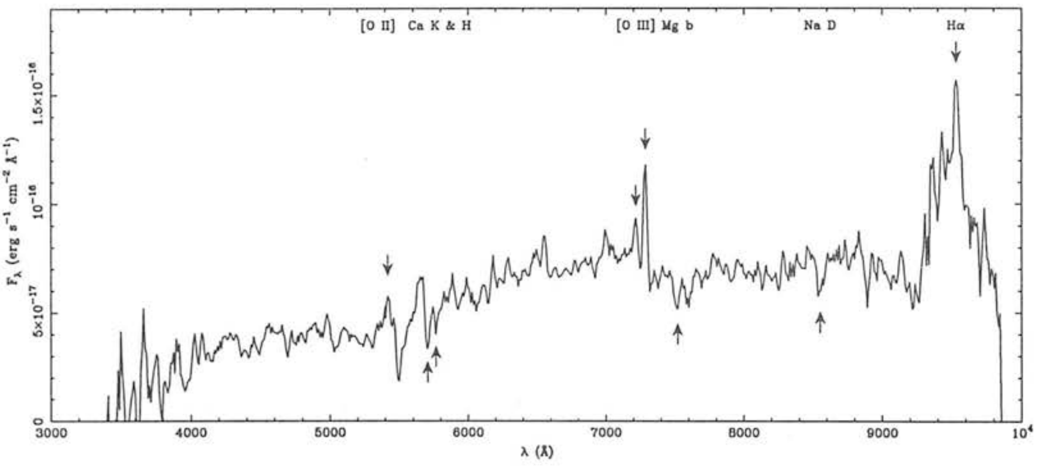

Figure 3.1 *Continued.*

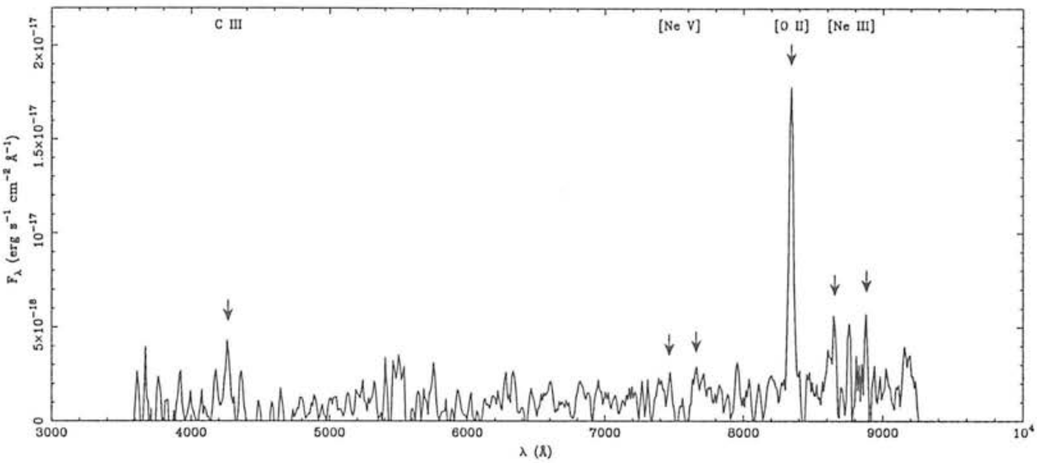
2158-160 z=1.236

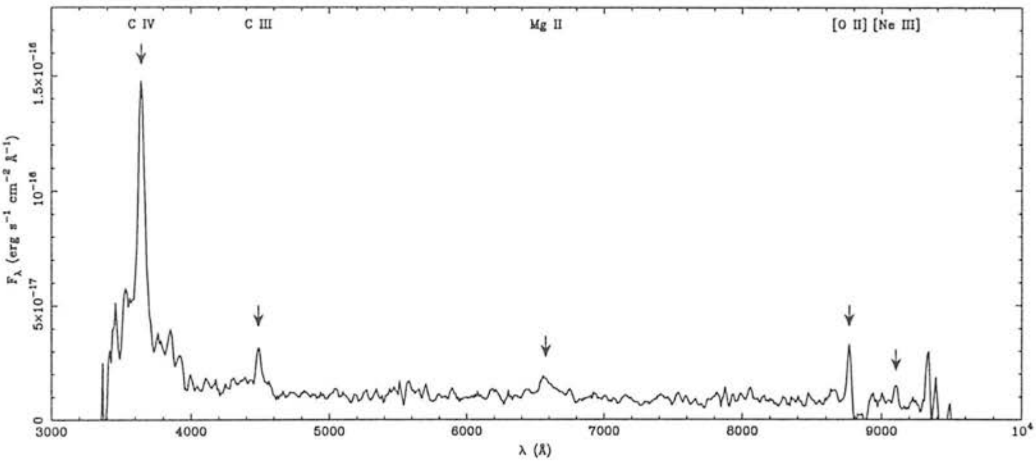
2202-179 z=1.351

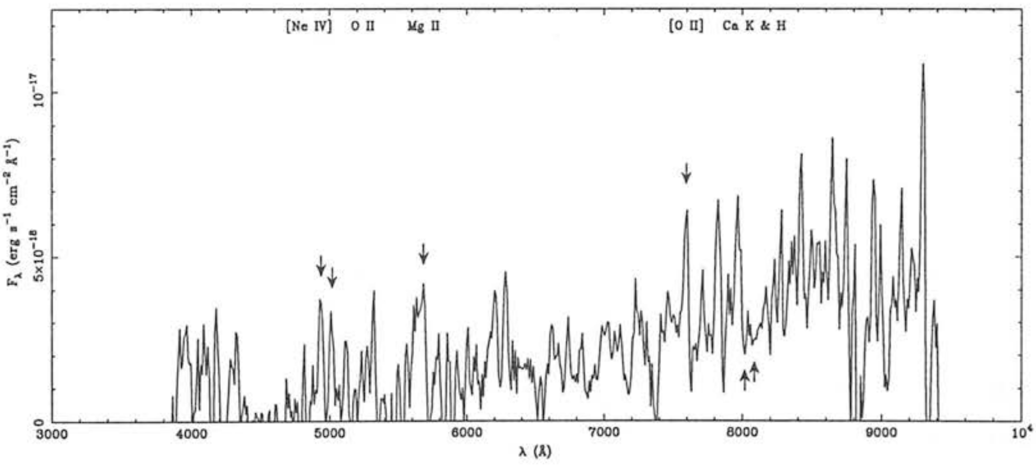
2215-185 z=1.035

Figure 3.1 *Continued.*

3.2 Leiden-Berkeley Deep Survey — I

Spectroscopic redshifts have been obtained for 175 of the sources in the LBDS survey and its deeper extensions, of which only three are at $z > 1$ (Windhorst et al. 1991). Until recently, only 16 of the sources in the complete 73-source LBDS Hercules sample had a published redshift, of which only one was at $z > 1$ (53W002 at $z = 2.390$). Another 22 redshifts had been measured by various observers (Windhorst, priv. comm.) and made available to the author. Thus half the sample was without redshift information. In order to be of maximum use in investigating the radio luminosity function and redshift cut-off, it was necessary to obtain spectra for as many of these remaining sources as possible.

In addition to the need to increase the overall redshift completeness of the sample, it can be seen from figure 2.9(f) that the Hercules field contains a number of faint red ($K > 17.5$, $r - K > 5$) galaxies. These sources are intrinsically interesting, as their K magnitudes imply a redshift $\gtrsim 1.5$ and their $(r - K)$ colours suggest they are galaxies with an old stellar population. At high redshifts in particular, important constraints can be put on the cosmological parameters (H_0, Ω_0, Λ) by determining the ages of the oldest (reddest) sources at any given redshift. This idea was introduced in chapter 1 and will be devolped further in chapter 5 below.

In order to address these two issues, a programme of spectroscopic observations was carried out over the past few years. In section 3.3 the results of observations designed to increase the total redshift content will be reported. In this section the investigation of the faint red galaxies is discussed.

3.2.1 Observations and data reduction

Observations of 7 faint red radio galaxies in the LBDS Hercules sample were obtained with the ISIS double-beam spectrograph at the 4.2-m William Herschel Telescope at the Observatorio del Roque de Los Muchachos, La Palma, on 21–24 June 1995 by M. J. Kukula and the author. ISIS operates in much the same way as the FORS/RGO Spectrograph described above (§3.1.2). Light from the slit is split at 6100 Å, with the blue and red light going into separate "arms" where the optical coatings and CCD detectors are sensitised to blue and red wavelengths respectively. The total wavelength coverage was 3160→9060 Å with a dispersion of 2.9 Å pixel^{-1}.

Each observation consisted of 4–6 exposures of 30 minutes each on the radio galaxy, with spectro-photometric standard stars and featureless continuum stars observed each night. Given the faintness of the targets ($r > 23$), the acquisition procedure consisted of pointing the telescope on a nearby star and then performing a blind offset to the galaxy co-ordinates. A short (~100 s) exposure of the offset star enabled the expected position of the target on the CCD to be determined for each source individually. Flat-field exposures of both the internal tungsten lamp and the twilight sky were taken during the run.

As with the PSR data discussed in the previous section, a lot of time was spent investigating the best method of reducing the observations. For the flat-fields it was found that the best results were obtained by using both the tungsten flat-field to remove the pixel-to-pixel sensitivities, and the sky flat-field (processed as in §3.1.2) to remove the vignetting effects of the slit. After attempts to perform the same sequence of reduction steps as used for the PSR data, it was found that such a method produced spectra with very poor signal-to-noise. After various investigations into fitting polynomials to the sky background and optimal extraction techniques, it was decided to use a two-dimensional sky subtraction on the exposures. The POLYSKY application in FIGARO (Shortridge et al. 1997) was used to fit a first order polynomial to each column of the CCD individually before subtracting a mean sky spectrum obtained from rows on each side of the source position. The resulting frame was examined in two dimensions allowing a detection to be claimed for 5 of the 7 sources. The only information obtained by extracting a one-dimensional spectrum at this stage was the overall shape of the continuum.

The (partial) reduction procedure was thus: (i) subtraction of a constant bias across the frame; (ii) median averaging of the individual exposures; (iii) flat-fielding by tungsten and sky flats; and (iv) subtraction of the sky spectrum with POLYSKY fitting.

3.2.2 Results and discussion

The observed spectra were too faint to successfully extract a one-dimensional spectrum from any of the sources. Investigation of the sky-subtracted two-dimensional images revealed that five of the sources had been detected, but there were no features visible in two of the spectra: 53W087 and 53W091. The first of these (53W087) does not have an optical or infrared counterpart, so it is perhaps not too surprising that nothing was detected. Observations of 53W091 with the 10-m Keck telescope will be discussed in chapter 5.

Of the five sources that were detected, two were continuum detections and the others were line detections. Continuum emission from 53W042 was detected thoughout the blue arm but very little was visible in the red, consistent with the blue optical colour $(g - r) \simeq -0.9$. This limits the location of the 912 Å Lyman-limit break to be at a shorter wavelength than the blue end of the spectrum, and thus places an upper limit on the redshift of $z \lesssim 2.5$. The second source that was detected in continuum emission was 53W069. For this source, the spectrum was only visible for wavelengths $\lambda > 7200$ Å, giving the not very significant redshift limit of

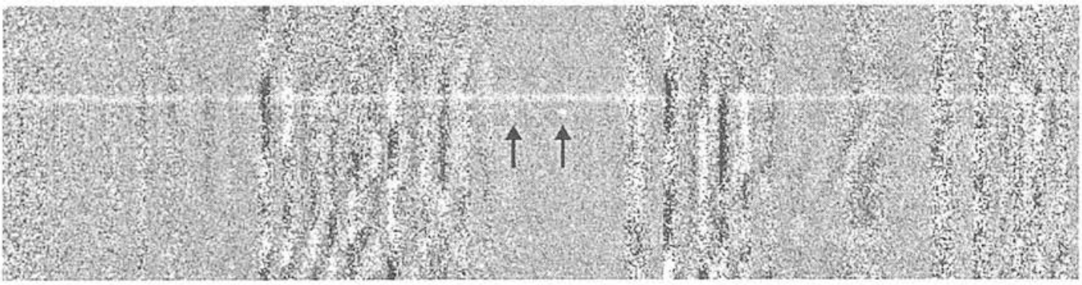

Figure 3.2 Spectrum of 53W089 showing the [O III] 4959 Å and 5007 Å emission lines at $z = 0.633$. The wavelength range is 7300–9000 Å and the spatial extent of the figure is $\sim 50''$. The strong continuum emission is from an un-associated object $3''$ to the west of the radio source.

Table 3.3 Line identifications for 53W089.

Name	Mean Redshift[1]	λ_{obs} (Å)	Identification	z
53W089	0.634 ± 0.001	6093	[O II] 3727	0.635
		8097	[O III] 4959	0.633
		8178	[O III] 5007	0.633

[1] Error is the standard error on the mean of the individual line redshifts.

$z \lesssim 6.9$ (again from the location of the Lyman-limit). This galaxy was observed with the Keck telescope the following year, and will be also discussed in chapter 5.

The only source for which multiple emission lines were detected was 53W089, yielding a redshift of 0.634. The [O III] lines at 4959 Å and 5007 Å are clearly visible in the two-dimensional spectrum (figure 3.2). An [O II] emission line was also marginally detected in the image — the line identifications and individual redshifts are given in table 3.3. The expected position of Hβ (usually associated with [O III]) is in a region of the spectrum that is dominated by fringing effects and was not detected. Such a low redshift for this object was suprising as it was not detected in the infrared ($K > 19.2$), giving an estimated (K–z) redshift of $z \gtrsim 3.8$. It thus appears to be a low-luminosity galaxy and emphasises the need to obtain spectroscopic redshifts for a representative sample of the LBDS high-redshift candidates. It is necessary to determine whether 53W089 is an unusual source or whether the faint sources in the sample are in fact a population of low-luminosity sources at low redshift.

The final two sources (53W037 and 53W060) both yielded a possible detection of a single emission line in their two-dimensional spectra. Whilst a redshift is not claimed for either source, one can speculate that the lines may be due to either Lyα or [O II] 3727 as they are the strongest lines normally observed in AGN. The line at 4452 Å in 53W060 could be either [O II] at $z = 0.2$ or Lyα at $z = 2.7$. For 53W037, the 8662 Å line may be [O II] at $z = 1.3$ or even Lyα at $z = 6.1$. This line, however, is at the red end of the spectrum where the fringing (due to strong night sky lines) is particularly bad. Further observations of this source in 1997 (see §3.3) failed to detect this object, so this emission line is probably not real.

While these results have done little to increase the redshift content of the LBDS sample, the results are important for the study of weak radio galaxies, in that they show that these sources are not in general dominated by strong emission lines. These galaxies are not very active in the (rest-frame) UV/optical and are thus closer to normal elliptical galaxies in their properties than the powerful radio galaxies in the 3CR survey, for example. Recall that this was one of the motivations behind studying radio galaxies of lower power than the 3CR, 1-Jansky and PSR samples.

To summarize, these observations have shown that one has reached the limit of what can be done with a 4 m telescope, in regards to faint galaxy spectrometry — all these sources have optical magnitudes of $25 < r < 26$. Insufficient information could be extracted from these spectra to pursue the aim of this section, i.e. to investigate the spectral properties of the oldest galaxies in the Hercules sample. However, pursuit of this topic will continue later in chapter 5, from a somewhat different perspective.

3.3 Leiden-Berkeley Deep Survey — II

Whilst the reddest sources are, in many ways, the most exciting objects to study from a cosmological point of view, they are also the hardest to observe — as the results of the previous section have shown. With respect to completing the redshift content of the LBDS Hercules sample, however, the bluer sources are more amenable to optical spectroscopy — their colours suggest more AGN/star-formation activity, implying stronger emission lines and thus making them easier to observe. This section will describe a second observing run at the WHT, in which we concentrated on these blue sources.

3.3.1 Observations and data reduction

Observations of 22 sources in the LBDS Hercules field were obtained at the 4.2-m William Herschel Telescope at the Observatorio del Roque de Los Muchachos, La Palma, on 30 June – 3 July 1997 by J. S. Dunlop. Once again the ISIS double-beam spectrograph was used with the R158B/R gratings and the 6100 Å dichroic (§3.2.1).

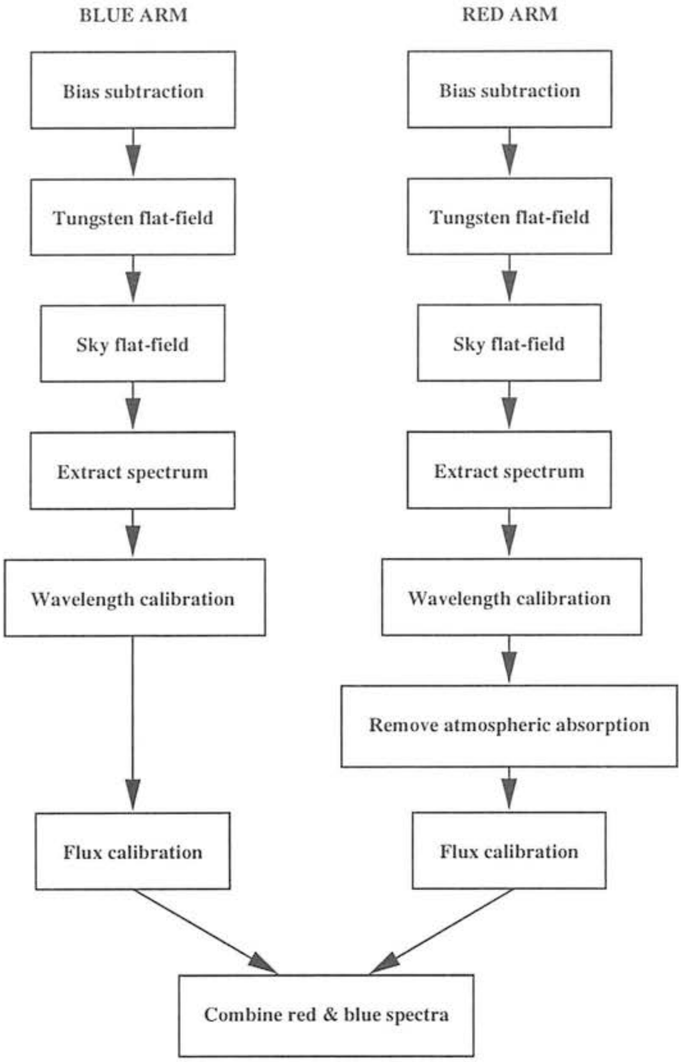

Figure 3.3 Stages in the reduction of spectroscopic data.

Each observation consisted of between one and four exposures of 1800 s each, giving a total exposure of 0.5–2 hours per target. The spectra were reduced online throughout the night, enabling the observer to move to the next target as soon as sufficient signal was obtained to determine a redshift. No more than two hours were spent on a target, even if it was only a marginal detection. The targets were acquired by blind-offsetting from a nearby star, which was also used to determine the expected position of the source in the CCD. Spectro-photometric standards were observed at the start of each night. Arc spectra, tungsten flat-fields and twilight sky flat-fields were taken at the start and end of each night.

The data were reduced using the NOAO spectroscopy packages ONEDSPEC, APEXTRACT and LONGSLIT in IRAF. Although the required steps were the same as for the previous AAT and WHT spectroscopy programmes (§§3.1, 3.2, figure 3.3), the procedures used were somewhat different and are described here in full.

1) A constant bias was subtracted from every image, calculated from the mean of the bias-strip in each exposure.
2) For each night, a tungsten flat-field was made from the median of the tungsten lamp exposures taken at the start and end of observing. The flats were normalised by fitting a high-order (14–20) cubic spline to the dispersion axis, and dividing the flat by the fit — this preserves the pixel-to-pixel sensitivity variations whilst removing the spectral signature of the lamp.
3) Sky flat-fields were constructed for each night from observations of the twilight sky at dusk and dawn. The exposures were bias subtracted, divided by the tungsten flat, then the median of the exposures was calculated. The image was binned into 100-pixel-wide bins and a low-order (5–8) cubic spline fitted to the surface. This fit was then used as the sky flat to correct for spatial variations in the illumination of the slit.
4) After bias subtraction and flat fielding, the one-dimensional spectrum was extracted with APEXTRACT. The two-dimensional image was binned along the dispersion axis and the strongest part of the spectrum was used to determine the spatial profile of the source. An aperture of $3''$ was usually sufficient to contain the object, whilst keeping the sky to a minimum. Sky apertures of $5''$–$9''$ width were defined on each side of the object aperture and separated from it by $1''$–$2''$. For strong continuum sources, the object aperture could be traced along the full length of the dispersion axis with a low-order (1–3) polynomial, and this trace was used to extract the spectrum. For sources with poor continuum signal, an adjacent observation of an offset or standard star was used to define the trace. At each point along the dispersion axis, a third order polynomial was fitted to the sky apertures to define the background level beneath the object, which was then subtracted. Sigma-clipping was used in the fit to prevent deviant pixels (e.g. cosmic rays) from distorting the background. The one-dimensional spectrum was then extracted using two methods: (a) standard extraction, where the pixels are simply added in the spatial direction at each dispersion co-ordinate; and (b) optimal extraction, where the pixels are weighted by their variance, as computed from the spatial profile and a noise model for the CCD (cosmic rays can be automatically rejected as a consequence of this method). After comparison with a Keck spectrum of one of the targets (53W067), it was discovered that the optimal extraction technique

produces a spurious signal for faint sources that are not detected along the whole length of the dispersion axis. This was a problem for approximately half of the observations — in these cases the standard extraction was used, otherwise the optimal technique gave the better spectrum. Cosmic rays were removed by hand at this stage, when the standard extraction was used.

5) Wavelength calibration of the extracted spectrum was performed using a copper–argon arc lamp exposure taken at either the start or end of the night. The arc spectrum was extracted from the same rows as the object, and fitted by a quadratic polynomial. The spectra were then re-binned to a linear scale, with a dispersion of 2.90 Å and a range of 3167.8→6134.5 Å for the blue and 6091.0→9057.7 Å for the red.
6) Removal of the atmospheric absorption features in the red arm of the spectrum was performed using observations of the early-type star G138−31a. A spectrum of this star was extracted for each night and wavelength calibrated. The continuum was interpolated across the Hα absorption line to remove it. A continuum fit was then made to the spectrum, using a 30$^{\mathrm{th}}$-order polynomial, and excluding the strong night-sky absorption features at 6880 Å, 7240 Å, 7610 Å and 8200 Å. The spectrum was replaced by the fit at all points except for the four bands, and finally normalized by dividing by the fit. All red-arm spectra were subsequently divided by this normalized smooth star to remove the strongest atmospheric absorption.
7) The spectrophotometric standard star BD+33°2642 was observed at the start of each night. A spectrum was extracted, wavelength calibrated and the red arm divided by the smooth star. It was then resampled into 49 Å bins (blue) and 98 Å bins (red), for comparison with the catalogued standard fluxes. A sensitivity function was calculated as the ratio of standard flux to observed flux at each sampled wavelength, which was then interpolated to a smooth function using a high-order (12–16) cubic spline. The function had to be extrapolated beyond 8500 Å due to the lack of catalogue information at longer wavelengths, so must be considered uncertain in this regime. The order of the spline was chosen so that the function is well-behaved at the edges of the spectrum, whilst still fitting variations on a scale of a few hundred ångstroms. Each object spectrum was then calibrated by first correcting for extinction (using a table provided by the observatory), and then multiplying by this sensitivity function.
8) Finally, the calibrated blue and red spectra were combined by taking the average of the 11-pixel (32 Å) overlap region. The calibrations were tested at this stage by applying them to both the standard and smooth star observations, and examining the quality of the join at 6100 Å. The "self-calibration" of the standard star produced a result

indistinguishable from the catalogue values (as it should), though there was a small step of about 8% in the blue and red flux across the join of the smooth star. This level of photometric accuracy was quite sufficient for this project which was concerned with measuring redshifts rather than accurate fluxes.

The resulting spectra were compared both with previous observations in this thesis and in the literature, in order to identify emission and/or absorption features that could be used to determine a redshift.

3.3.2 Results and discussion

Of the twenty-two sources observed, eleven have yielded a redshift, seven were detected in continuum emission but no definite redshift could be determined, and four were not detected. Table 3.4 gives the redshifts and line lists for the eleven sources whose redshift has been determined, and the spectra are plotted in figure 3.4. Several of these sources deserve comment.

The redshift of 53W026 has been determined from the location of the 4000-Å break — the precise location of the break is uncertain as it falls within the noisy part of the spectrum where the blue and red halves were joined, and the large error ($\Delta z = 0.05$) reflects this. The [O II] emission line in 53W065 is the basis for its redshift of 1.185, as this is the only strong feature in the spectrum. There is an absorption feature at 6110 Å consistent with it being Mg II at the same redshift, but this is right on the join between the two halves of the spectrum and its reality is thus suspect. 53W083 has a very clear 4000-Å break at 6510 Å putting it at $z = 0.628$, but no other features could be identified in the spectrum.

The redshift of 53W068 ($z = 0.048$) is very low and is potentially incorrect. The good agreement between the redshifts of the three identified lines ([O II] in emission, Ca H and Ca K in absorption) would seem unlikely to occur randomly, and the overall shape of the continuum is consistent with these identifications, thus it is included in table 3.4. However, with an r magnitude of 22.5 and K of 19.4, this source would be *very* underluminous if it really is at $z = 0.048$. The possibility that one of the broad absorption/emission features around 3900–4300 Å is Lyα at $z \sim 2.4$ was also considered. This would be more consistent with its optical/infrared magnitudes, however none of the other features in the spectrum can be identified with emission or absorption lines at that redshift.

Seven sources have sufficient continuum flux to enable a strong upper limit to be placed on the wavelength of the 912 Å Lyman-limit break. (Below 912 Å there is essentially no flux in a galaxy's spectrum due to absorption of the ionizing radiation.) This enables upper limits to be placed on the redshifts of these sources, which are listed in table 3.5. Their spectra are

Table 3.4 Redshifts and line identifications for LBDS Hercules sources observed in June 1997.

Name	Mean Redshift[1]	$\lambda_{\rm obs}$ (Å)	Identification	z
53W012	1.328 ± 0.001	3814	He II 1640	1.326
		4440	C III 1909	1.326
		5641	Ne IV 2423	1.328
		7981	[Ne V] 3426	1.330
		8682	[O II] 3727	1.330
53W019	0.5415 ± 0.0005	6056	Ca K 3933	0.5400
		6117	Ca H 3968	0.5416
		7979	Mg b 5174	0.5421
		7722	[O III] 5007	0.5422
53W022	0.5279 ± 0.0001	5694	[O II] 3727	0.5278
		7428	Hβ 4861	0.5281
		7577	[O III] 4959	0.5279
		7650	[O III] 5007	0.5279
53W026	0.55 ± 0.05[2]	~6200	4000-Å break	0.55
53W027	0.4027 ± 0.0002	4803	[Ne V] 3426	0.4019
		5227	[O II] 3727	0.4025
		6822	Hβ 4861	0.4034
		6956	[O III] 4959	0.4027
		7024	[O III] 5007	0.4028
53W034	0.2809 ± 0.0001	4775	[O II] 3727	0.2812
		6226	Hβ 4861	0.2808
		6353	[O III] 4959	0.2811
		6411	[O III] 5007	0.2804
		8389	[N II] 6548	0.2812
		8406	Hα 6563	0.2808
		8432	[N II] 6583	0.2809
53W048	0.6755 ± 0.0003	6587	Ca K 3933	0.6748
		6649	Ca H 3968	0.6756
		7208	G-band 4300	0.6763
		8668	Mg b 5174	0.6753
53W065	1.185 ± 0.001	8151	[O II] 3727	1.187
		6110	Mg II 2799	1.183

Table 3.4 *Continued*

Name	Mean Redshift[1]	$\lambda_{\rm obs}$ (Å)	Identification	z
53W067	0.759 ± 0.001	6551	[O II] 3727	0.758
		6927	Ca K 3933	0.761
		6983	Ca H 3968	0.760
		7550	G-band 4300	0.756
53W068[3]	0.048 ± 0.002	3897	[O II] 3727	0.046
		4125	Ca K 3933	0.049
		4166	Ca H 3968	0.050
53W083	0.628 ± 0.003[2]	6510	4000 Å-break	0.628

[1] Errors are the standard error on the mean of the individual line redshifts. [2] Error derived from the uncertainty in the exact location of the 4000 Å-break. [3] Uncertain redshift — see text for a discussion.

presented in figure 3.5 for reference. Two sources (53W013 and 53W021) are barely detected, whilst most of these objects are reasonable detections. 53W036 has a quite substantial flux (7×10^{-18} erg s^{-1} cm^{-2} Å^{-1} across most of the spectrum) compared with the other sources discussed in this section. Nevertheless, none of these seven objects have any lines or breaks that could be succesfully identified with known spectral features.

Four of the twenty-two sources were not detected: 53W004, 53W037, 53W054A and 53W054B. The failure to detect any emission line in 53W037 at 8662 Å suggests that the feature seen in the 1995 observations (§3.2.2) was not real.

This observing run, focussing on the 'blue' sources in the sample, was far more succesful than the 1995 run discussed in the previous section which focussed on the faint red sources. As expected, the blue objects were more active than the red ones, in terms of having more emission lines, and thus redshifts were easier to measure for them. Comparing these spectra with those of the PSR galaxies observed in §3.1, it can be seen that even the blue LBDS galaxies do not in general have emission lines that are as strong as the PSR sources. Only about one-quarter of the LBDS sources with new redshifts have spectra dominated by emission lines, compared with two-thirds of the PSR sample. All the spectroscopic evidence available points to the weaker radio sources being less active in the UV/optical than the objects found in the brighter radio surveys such as the PSR, 1-Jansky and 3CR samples. These sources in the LBDS are likely to be more representative of the general galaxy population than the powerful radio galaxies.

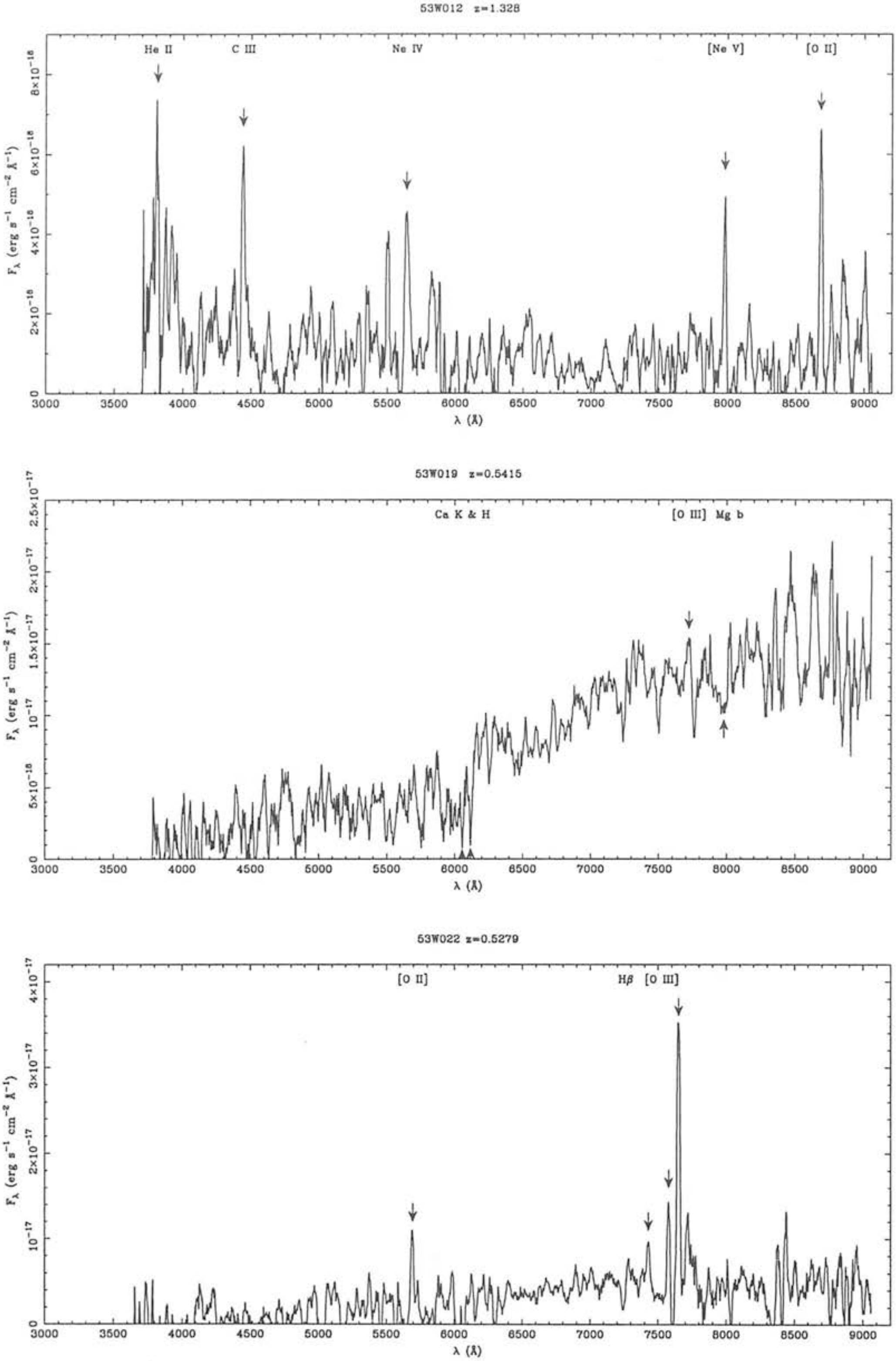

Figure 3.4 WHT spectra of 'blue' sources in the LBDS Hercules field with a definite or probable redshift. Smoothed by 32 Å (11 pixels). 'S' denotes a residual night sky line.

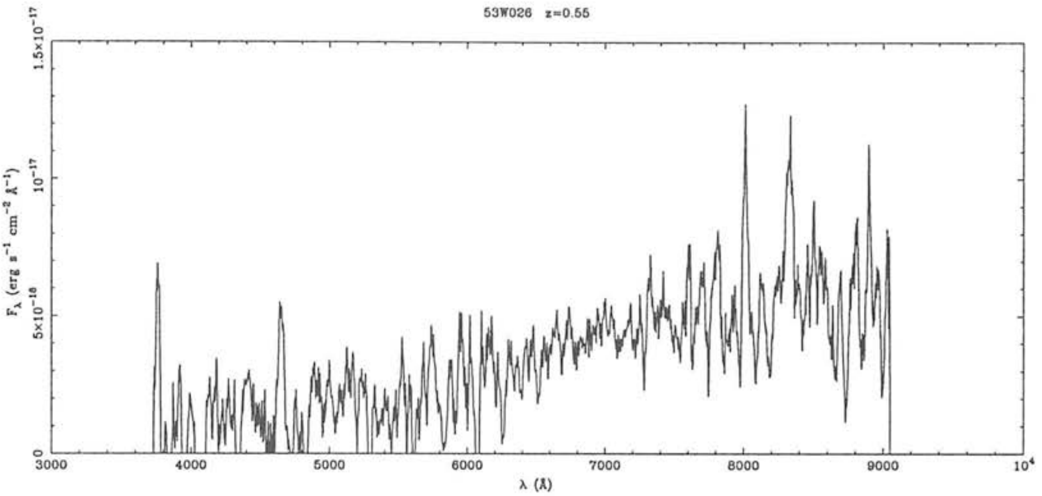

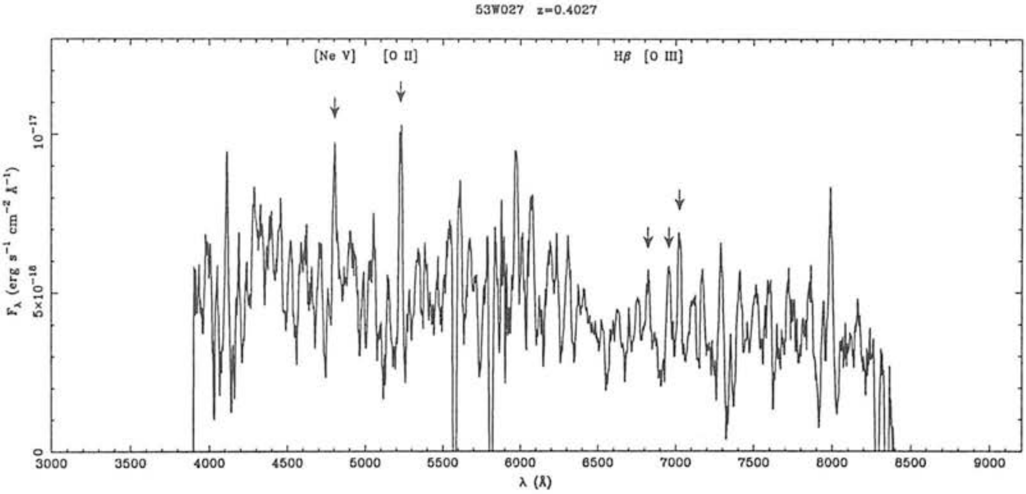

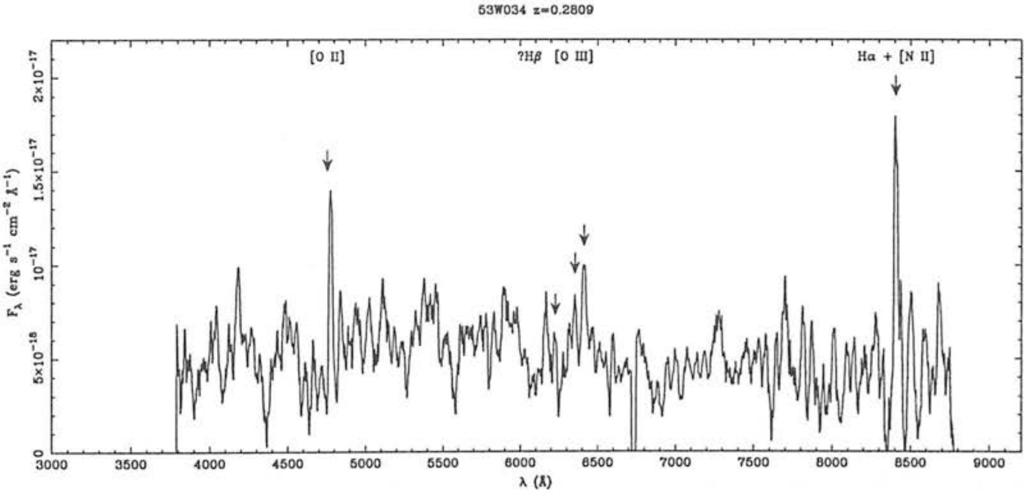

Figure 3.4 *Continued.*

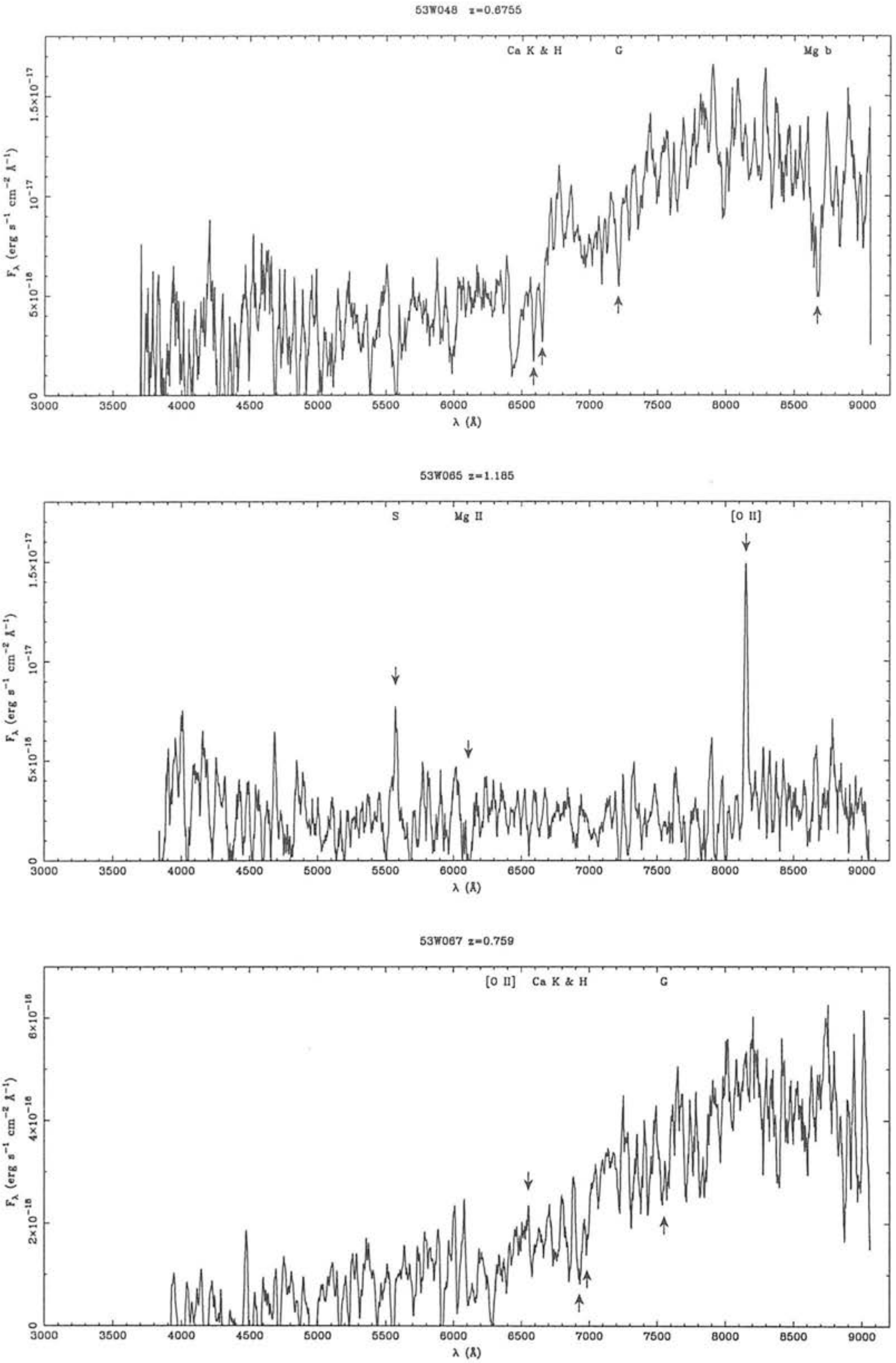

Figure 3.4 *Continued.*

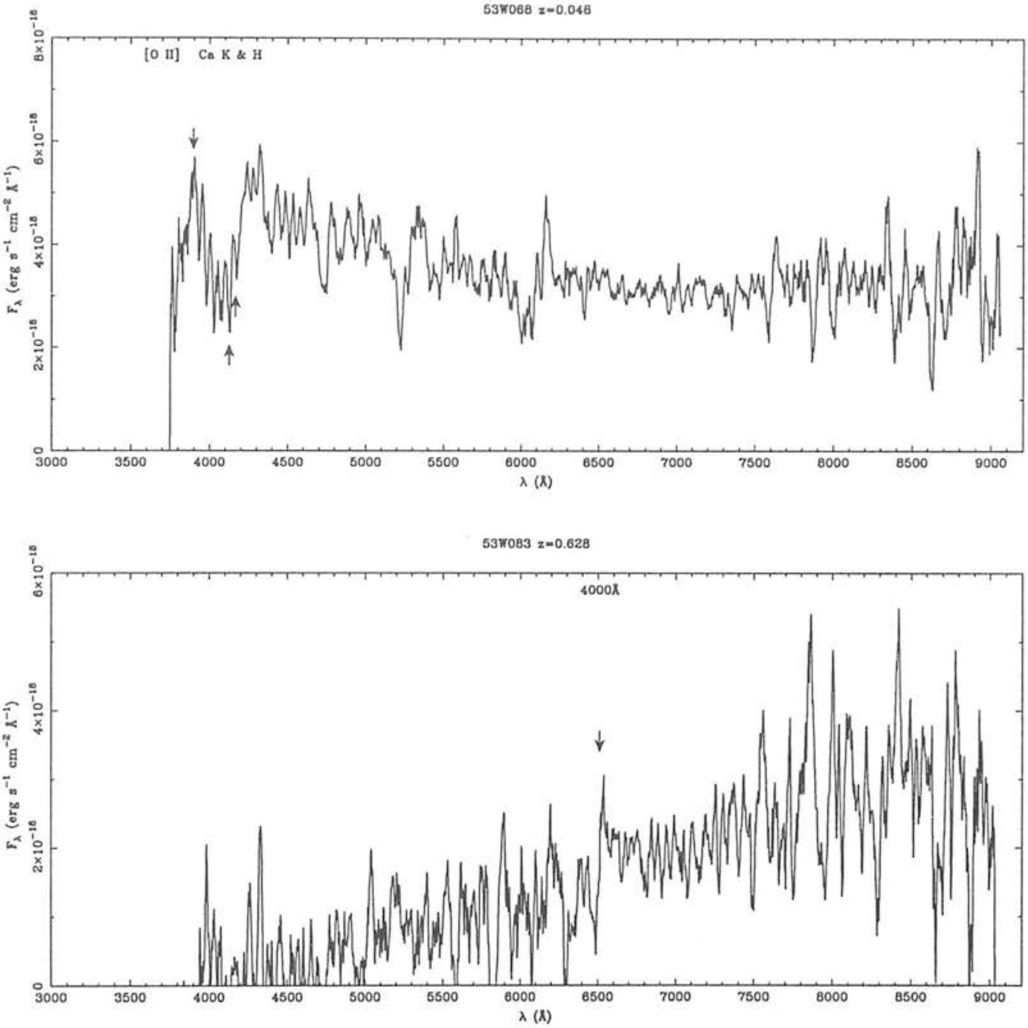

Figure 3.4 *Continued.*

Table 3.5 Upper limits on the redshifts of LBDS Hercules sources.

Name	Redshift	λ_{obs} (Å)[1]	Name	Redshift	λ_{obs} (Å)[1]
53W013	$\lesssim 3.2$	3860	53W035	$\lesssim 3.6$	4200
53W014	$\lesssim 3.1$	3740	53W036	$\lesssim 3.2$	3800
53W021	$\lesssim 5.6$	6000	53W070	$\lesssim 3.1$	3750
53W029	$\lesssim 3.9$	4500			

[1] Shortest wavelength at which flux is detected.

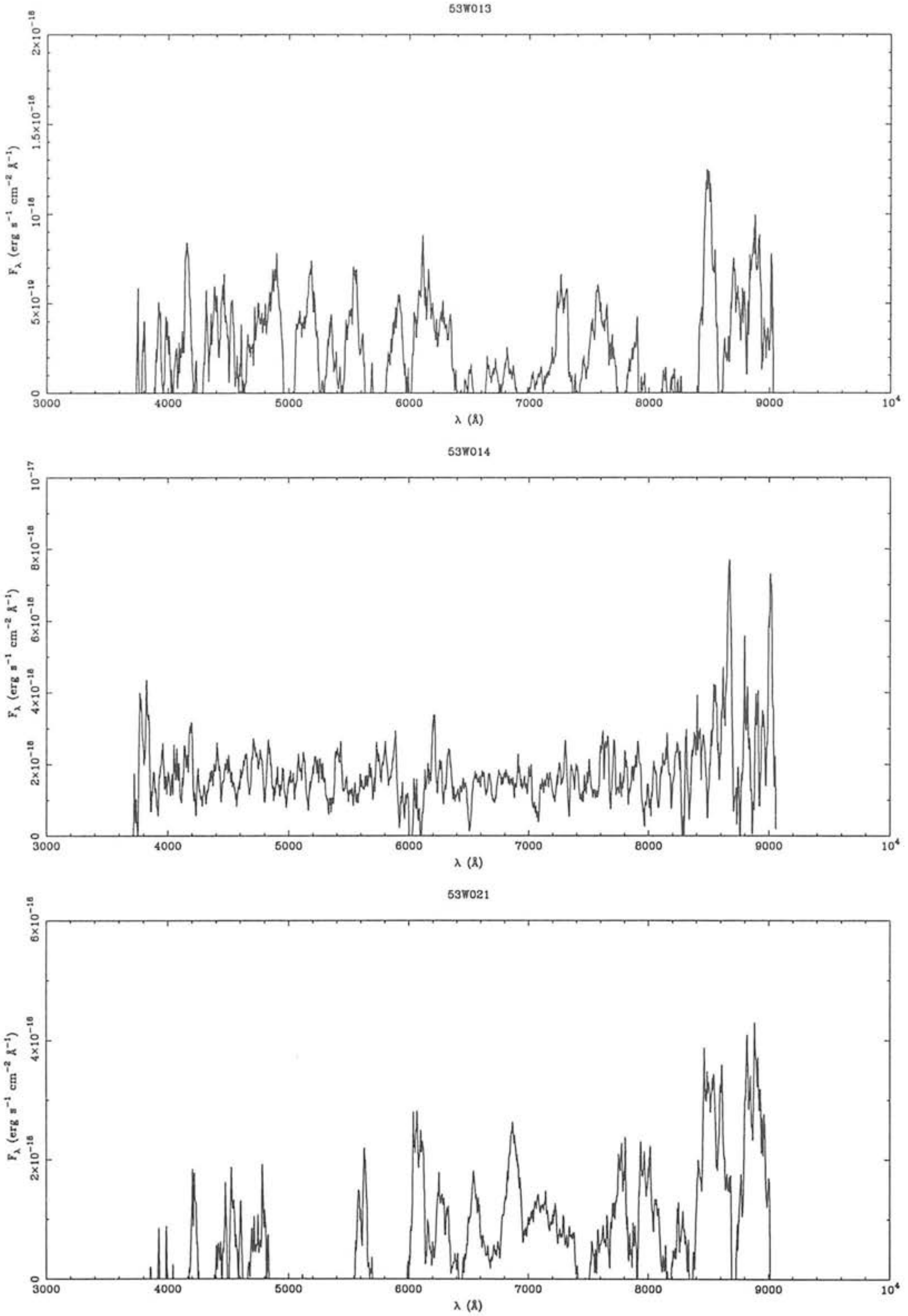

Figure 3.5 WHT spectra of 'blue' sources in the LBDS with a detection of continuum, but no redshift determined. Smoothed by 32 Å (11 pixels), except for 53W013 and 53W021 which are smoothed by 102 Å (35 pixels).

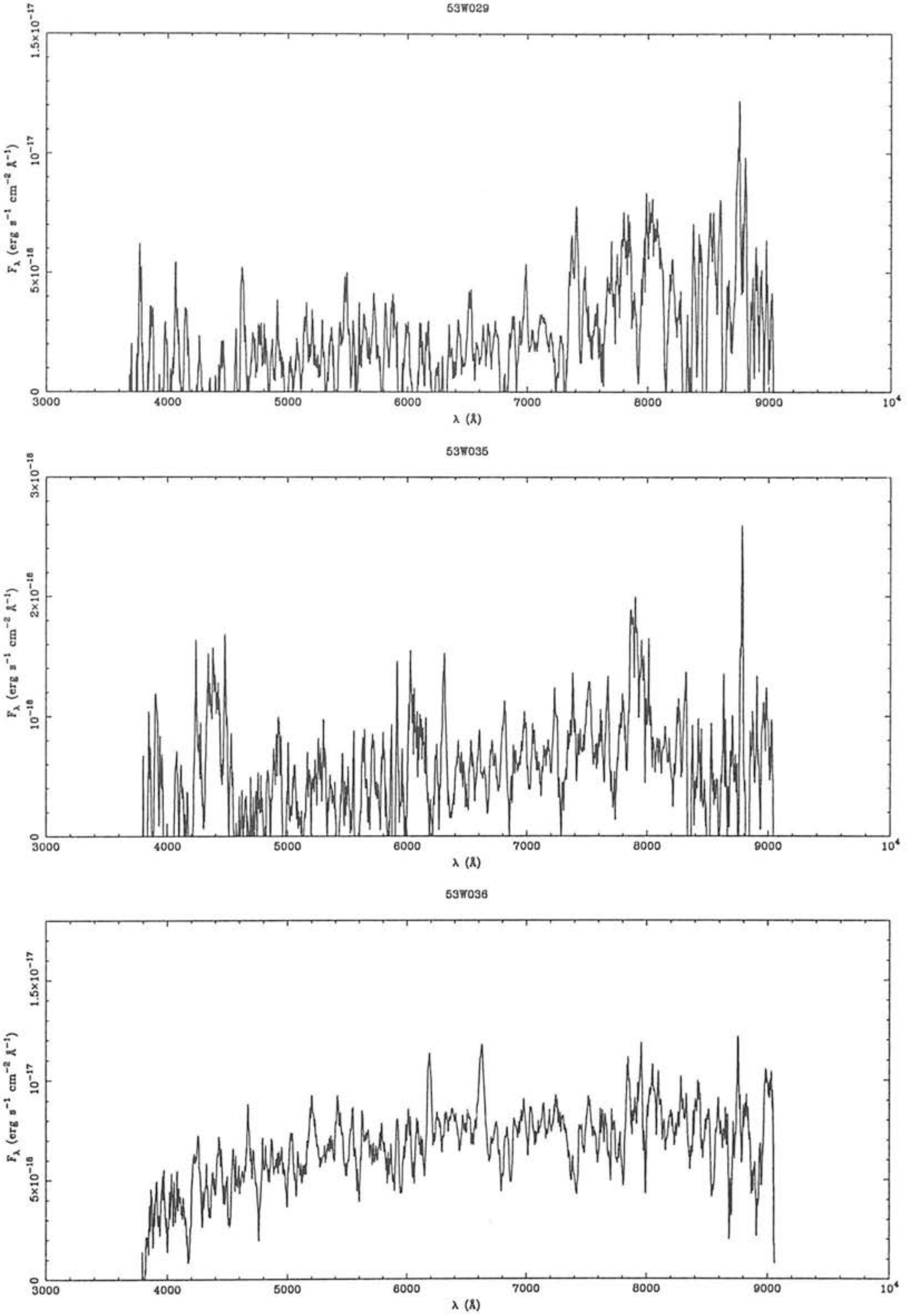

Figure 3.5 *Continued.*

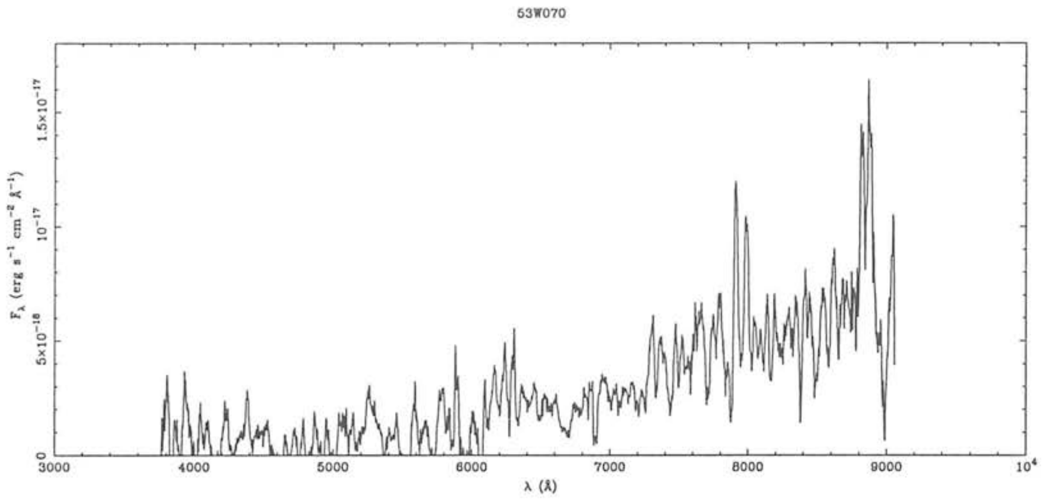

Figure 3.5 *Continued.*

Compared with this milli-Jansky survey, even the sources found in the PSR are "powerful".

The results presented in this section and the last have now brought the total number of redshifts in the LBDS Hercules sample to 49 out of 73 sources (67%). For the 2-mJy subsample, 41 of 64 sources (64%) have redshifts. It is seen that the redshift content of the sample is far from being complete. In order to use the Hercules data to investigate the radio luminosity function and redshift cut-off, it is essential to have full redshift information — the redshifts of the remaining sources must be estimated. This is the topic of §4.3, and a discussion of the redshift distribution of the complete sample will be postponed until after that.

Chapter 4

Evolution of the radio luminosity function

The cosmological evolution of the radio luminosity function (RLF) is investigated, with particular emphasis on the possible high-redshift cut-off. The PSR and LBDS Hercules samples together cover eight orders of magnitude in luminosity and probe powerful sources with $\log_{10} P_{2.7} \gtrsim 25$ out to redshifts of $z \gtrsim 5$. The implications of new redshift measurements in the PSR are discussed, and a method of estimating redshifts for the LBDS sources is developed. These results are then compared with the model RLFs of Dunlop and Peacock (1990). It is confirmed that the most luminous objects decline in number at $z \gtrsim 2$, in agreement with these models. The lower luminosity population ($\log_{10} P_{2.7} \lesssim 26$) sampled by the LBDS is found to be more numerous at $0.2 \lesssim z \lesssim 1$ than the models predict. The observed RLF for these sources shows evidence for a cut-off at lower redshifts ($z \sim 0.5$–1.5) than for the more powerful objects, as first suggested by Windhorst (1984).

4.1 The evolving radio luminosity function

One of the primary aims of this thesis is to confirm or refute the existence of a decline in the radio source population at high redshift (the "redshift cut-off"). It is well established that the radio luminosity function (RLF) rises with redshift out to $z \simeq 2$, but beyond that its behaviour is more uncertain. The flat-spectrum population ($\nu < 0.5$, where $S_\nu \propto \nu^{-\alpha}$) shows a decline at higher redshifts. The steep-spectrum population was reported by Dunlop and Peacock (1990; hereafter "DP90") to show a similar decline, but their conclusion depended critically upon the accuracy of the redshift estimates that they used to model the RLF. This work was introduced in section 1.4 and will now be reviewed in some detail. The remainder of this chapter will reassess the high-redshift behaviour of the RLF in the light of new data, as follows. Section 4.2 presents a discussion of how the new PSR redshifts from chapter 3 affect the conclusions of DP90. The photometric redshift estimates needed to complete the redshift content of the LBDS Hercules field are detailed in section 4.3. In the final section (§4.4) the RLF observed in the LBDS is compared with the results of DP90.

4.1.1 Review of Dunlop and Peacock (1990)

The aim of this paper was to investigate the evolution of the radio luminosity function, with the emphasis being to determine the behaviour of the RLF at high redshift. It was an extension of work begun by Peacock and Gull (1981) and Peacock (1985). The basic idea is to find a model (or rather, an ensemble of models) of the luminosity function $\rho(P, z)$, that is consistent with all the available data. In those regions of the (P, z) plane where the redshift content of the data is high, generally corresponding to the higher flux densities, the model will be well defined. The model can then be extrapolated across the rest of the (P, z) plane, subject to the constraints of less direct data such as source counts. By choosing an ensemble of smooth functions, it is hoped that they will span all the possible extrapolations of the existing data, predicting the form of the luminosity function in those regions that are incomplete. Of course, it is known that the real universe is not smooth on all scales, so the models will only be approximations to the actual form of the RLF.

The data were drawn from four complete samples at a frequency of 2.7 GHz, together with source counts at fainter flux limits and measurements of the local RLF. Three of the samples were the same as used by Peacock (1985), with flux densities $S_{2.7} > 0.5$, 1.5 & 2.0 Jy and containing 40, 171 & 235 sources respectively. The redshift content of these samples was $\sim$80%. The fourth complete sample, and the greatest advance in this paper over earlier work, was the Parkes Selected Regions (see §3.1). This sample has a flux density limit of 0.1 Jy and contains 178 sources, with a higher proportion of steep-spectrum sources (principally radio galaxies) than the other samples. The weakness of the PSR, however, was that only 46% of the sources had redshifts — dividing the sample according to spectral index showed that only one-third of the steep-spectrum sources had redshifts, whilst the redshifts of two-thirds of the flat-spectrum population were known.

Being the deepest sample, the PSR provided the strongest probe of high-redshift space and thus good estimates were needed for those sources without redshifts. As was introduced in section 1.3, Lilly et al. (1985) found that the infrared Hubble diagram for 3CR and 1-Jansky radio galaxies can be described by the empirical relation $\log_{10} z = -5.368 + 0.384K - 0.00385K^2$ (equation [1.10]). The majority of PSR sources had K magnitudes, allowing DP90 to add those with redshifts to the Hubble diagram (their figure 3), from which they concluded that the PSR sources were consistent with the empirical relation of Lilly et al. They then used this equation to estimate the redshifts of the remaining 54% of the PSR data. To test the reliability of the estimates they first added a random scatter to the estimates, consistent with the observed scatter in the K–z diagram, and found that the resulting redshift distribution was statistically unchanged. Secondly, they modified equation [1.10] so as to produce systematically larger estimated redshifts at faint K magnitudes. They performed their analysis using both the empirical K–z estimates (denoted the "MEAN-z" distribution) and the modified estimates (the "HIGH-z" distribution).

The ensemble of RLFs consisted of five different models that were found to be consistent with the data. They are described as "free-form" models, in the sense that their dependence on P and z was not defined *a priori* to be of any particular form, simply that they are smooth functions that can be described by a series expansion. Separate models were constructed for the steep- and flat-spectrum sources:

$$\log_{10} \rho = \sum_{i=0}^{5} \sum_{j=0}^{5-i} A_{ij} x^i(P) y^j(z) + A_{60} x^6(P) \qquad \text{for} \quad \alpha \geq 0.5 \qquad [4.1]$$

$$\log_{10} \rho = \sum_{i=0}^{4} \sum_{j=0}^{4-i} A_{ij} x^i(P) y^j(z) \qquad \text{for} \quad \alpha < 0.5 \qquad [4.2]$$

where x and y are transformed axes of the P–z plane:

$$x(P) = 0.1(\log_{10} P - 20) \qquad \text{and} \qquad y(z) = 0.1z \qquad [4.3]$$

The sixth-order term in equation [4.1] was included to assist in fitting the local RLF. Integration of the RLF is carried out over the redshift range $z = 0 - 10$ and the luminosity range $P_{2.7} =$

$10^{18} - 10^{30}$ W Hz^{-1} sr^{-1}. This is the first model, FF-1. The other four free-form models modify various aspects of this:

- FF-2: an exponential cut-off is enforced at high luminosity: $\rho \rightarrow \rho \exp(-P/P_c)$, where $P_c = 10^{28}$ W Hz^{-1} sr^{-1};
- FF-3: the redshift co-ordinate used is $y(z) = \log_{10}(1+z)$;
- FF-4: integration of the RLF is terminated at $z = 5$;
- FF-5: a cut-off at high redshift is enforced such that the RLF decays sinusoidally from $z = 2$ to a value of zero at $z > 5$, i.e. for $2 < z < 5$, $\rho \rightarrow \rho \cdot (1 + \cos\phi)/2$, where $\phi = (z-2)\pi/3$, and for $z \geq 5$, $\rho = 0$.

Each of these models was derived twice, using the MEAN-z and HIGH-z redshift estimates. The parameters A_{ij} are given in Appendix C of DP90. All the models were derived for a Hubble constant of $H_0 = 50$ km s^{-1} Mpc^{-1} and a density parameter of $\Omega_0 = 1$. The results are illustrated in figure 4.1 for the flat-spectrum population and figures 4.2–4.3 for the steep-spectrum sources, all for the MEAN-z data only.

For the flat-spectrum population, figure 4.1, a decline in the RLF at high redshift is required by the models for all luminosities where the complete sample database has good coverage of the P–z plane (figures 4.1(a)–(c)). The strength of this result is due to the nearly complete redshift data for the flat-spectrum population — notice how narrow a range of RLFs is permitted. For the steep-spectrum sources, it can be seen from figure 4.2 that the cut-off is only *required* for the most luminous objects ($\log_{10} P_{2.7} \geq 27$), although it is *consistent* with the data at all luminosities. Note that the apparently strong cut-off at the lowest luminosities is totally unconstrained by the complete sample data, whose flux-density limit corresponds to $\log_{10} P_{2.7} \simeq 23.5$ at $z = 0.1$ (see the arrows in these figures). Dunlop and Peacock (1990) concluded that these models demonstrate the need for a cut-off in the radio luminosity functions at high redshift ($z \gtrsim 2$), the first time that this had been quantified in the steep-spectrum population (although it had also been suggested by the observations of Windhorst (1984), using the LBDS survey).

In addition to the free-form models discussed thus far, DP90 also attempted to fit the data with two simple parametric models: pure luminosity evolution (PLE) and a combination of luminosity and density evolution (LDE). The PLE luminosity function was considered to be the sum of a high-power evolving component and a low-power non-evolving component:

$$\rho(P,z) = \rho_l(P) + \rho_h(P,z) \qquad [4.4]$$

where

$$\log_{10} \rho_l = \sum_{i=0}^{6} b_i x^i(P) \qquad \text{with} \qquad x^i(P) = 0.1(\log_{10} P - 20) \tag{4.5}$$

and

$$\rho_h = \rho_0 \left[\left(\frac{P}{P_c(z)} \right)^{\alpha} + \left(\frac{P}{P_c(z)} \right)^{\beta} \right]^{-1} \tag{4.6}$$

in analogy to the optical quasar luminosity function. $P_c(z)$ is the 'break' luminosity between the two power-laws and was parameterized as

$$\log_{10} P_c = a_0 + a_1 z + a_2 z^2 \tag{4.7}$$

Using a quadratic expansion allows the possibility of negative luminosity evolution at high redshift, i.e. a cut-off in the RLF.

An acceptable fit to the data was found for the MEAN-z redshift distribution and a critical universe ($\Omega_0 = 1$), but this model failed for $\Omega_0 = 0$, and when the HIGH-z distribution was used. The low-power component ρ_l was found to be unnecessary for the flat-spectrum sources, and was attributed to the emission from star formation in spiral/irregular galaxies. Note, however, that more recent studies of spiral and starburst galaxies at μJy flux levels have shown them to have flat, or inverted ($\alpha < 0$), spectra (Windhorst et al. 1993), thus casting some doubt on DP90's interpretation of ρ_l.

To investigate the possibility that the cut-off was due to negative density evolution whilst the positive luminosity evolution continued at $z \gtrsim 2$, the PLE model was modified to allow ρ_0 to vary with redshift:

$$\log_{10} \rho_0 = \sum_{i=0}^{5} c_i y^i(z) \qquad \text{with} \qquad y(z) = 0.1z \tag{4.8}$$

This LDE model was found to require a milder evolution of the break luminosity than the PLE:

$$\log_{10} P_c = a_0 + \frac{a_1}{\eta} \left[1 - (1+z)^{-\eta} \right] \tag{4.9}$$

Taking the cosmological density to be $\Omega_0 = 1$, LDE was successfully fitted to both the MEAN-z and HIGH-z data. The best-fit parameters for PLE and LDE are given in Appendix C of DP90, and the luminosity functions are illustrated in figures 4.1 & 4.2 alongside the free-form models.

Having shown that both the free-form models and the PLE/LDE parametric models require a decline in the RLF at high redshifts, DP90 also performed a model-independent test of the cut-off using the $V/V_{\max}$ test (Schmidt 1968; Rowan-Robinson 1968). Here, V is the cosmological volume enclosed by an object and $V_{\max}$ is the volume that would be enclosed by

(a) Flat-spectrum

(b) Flat-spectrum

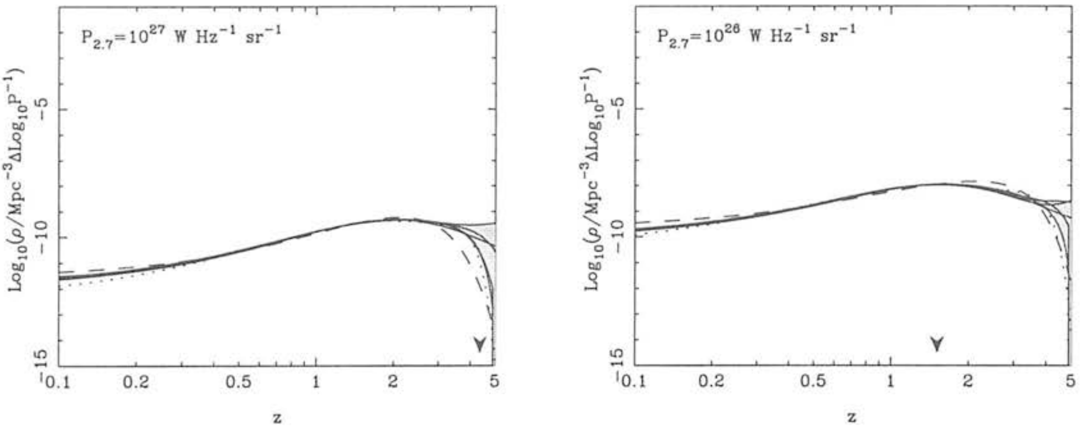

(c) Flat-spectrum

(d) Flat-spectrum

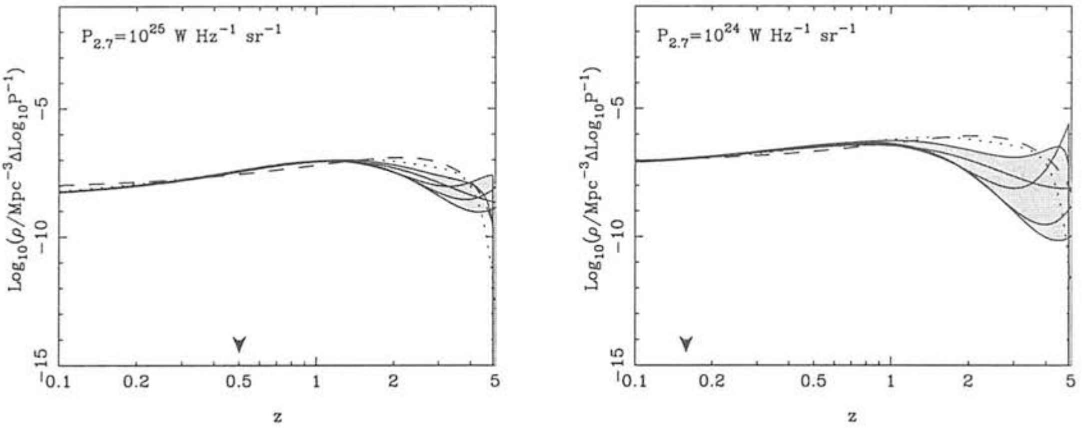

(e) Flat-spectrum

(f) Flat-spectrum

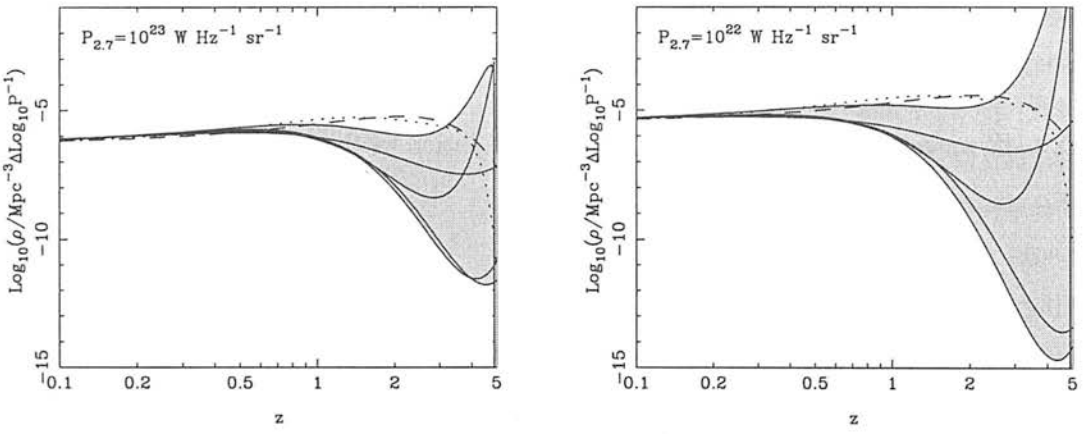

Figure 4.1 The RLFs of Dunlop and Peacock (1990) for flat-spectrum sources, in steps of $\Delta \log_{10} P_{2.7} = 1$. Shaded areas show the range of $\rho(P, z)$ for the free-form models. Dashed line is PLE; dotted line is LDE. Arrows denote the redshift of a source at the flux-density limit of the PSR sample — in (e) & (f) the flux-density limit corresponds to $z < 0.1$.

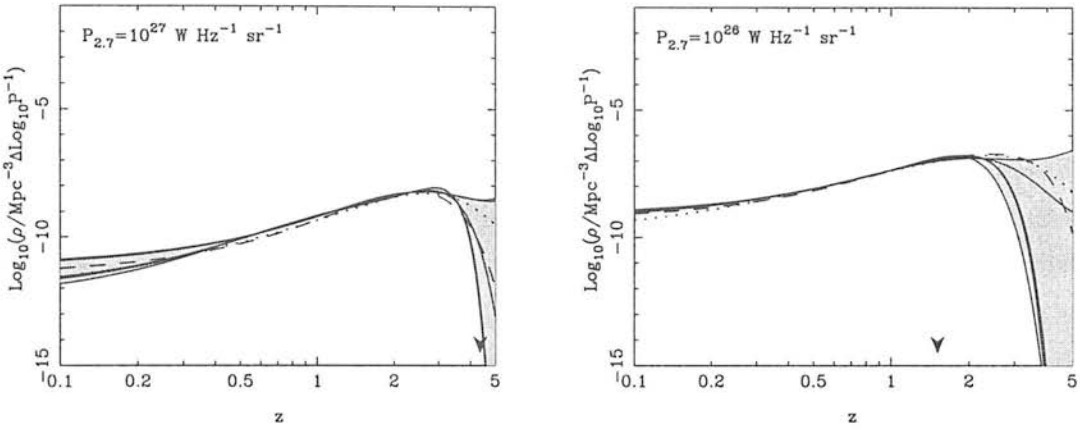

(a) Steep-spectrum

(b) Steep-spectrum

(c) Steep-spectrum

(d) Steep-spectrum

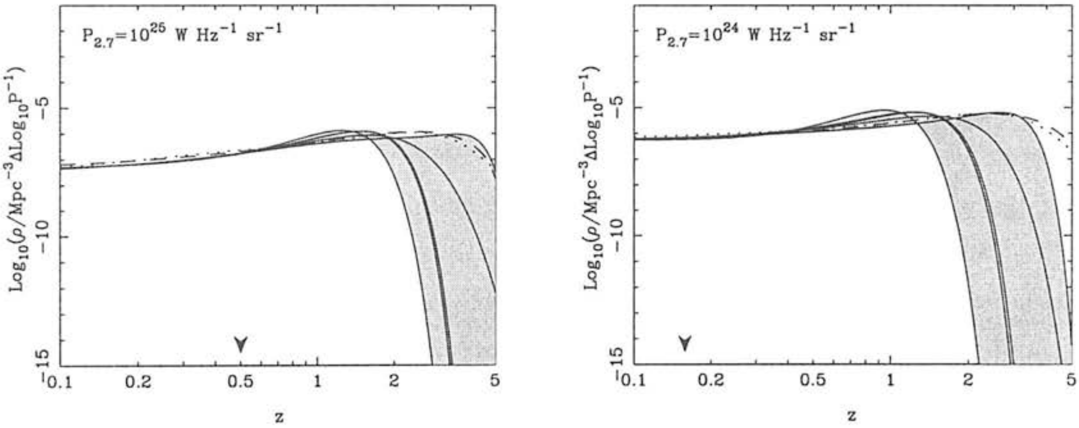

(e) Steep-spectrum

(f) Steep-spectrum

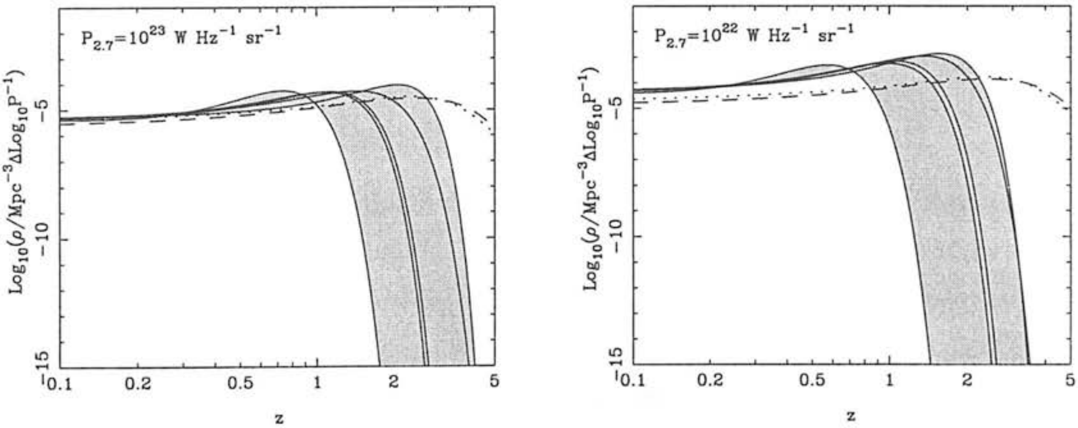

Figure 4.2 The RLFs of Dunlop and Peacock (1990) for steep-spectrum sources, in steps of $\Delta \log_{10} P_{2.7} = 1$. Shaded areas show the range of $\rho(P, z)$ for the free-form models. Dashed line is PLE; dotted line is LDE. Arrows denote the redshift of a source at the flux-density limit of the PSR sample — in (e) & (f) the flux-density limit corresponds to $z < 0.1$.

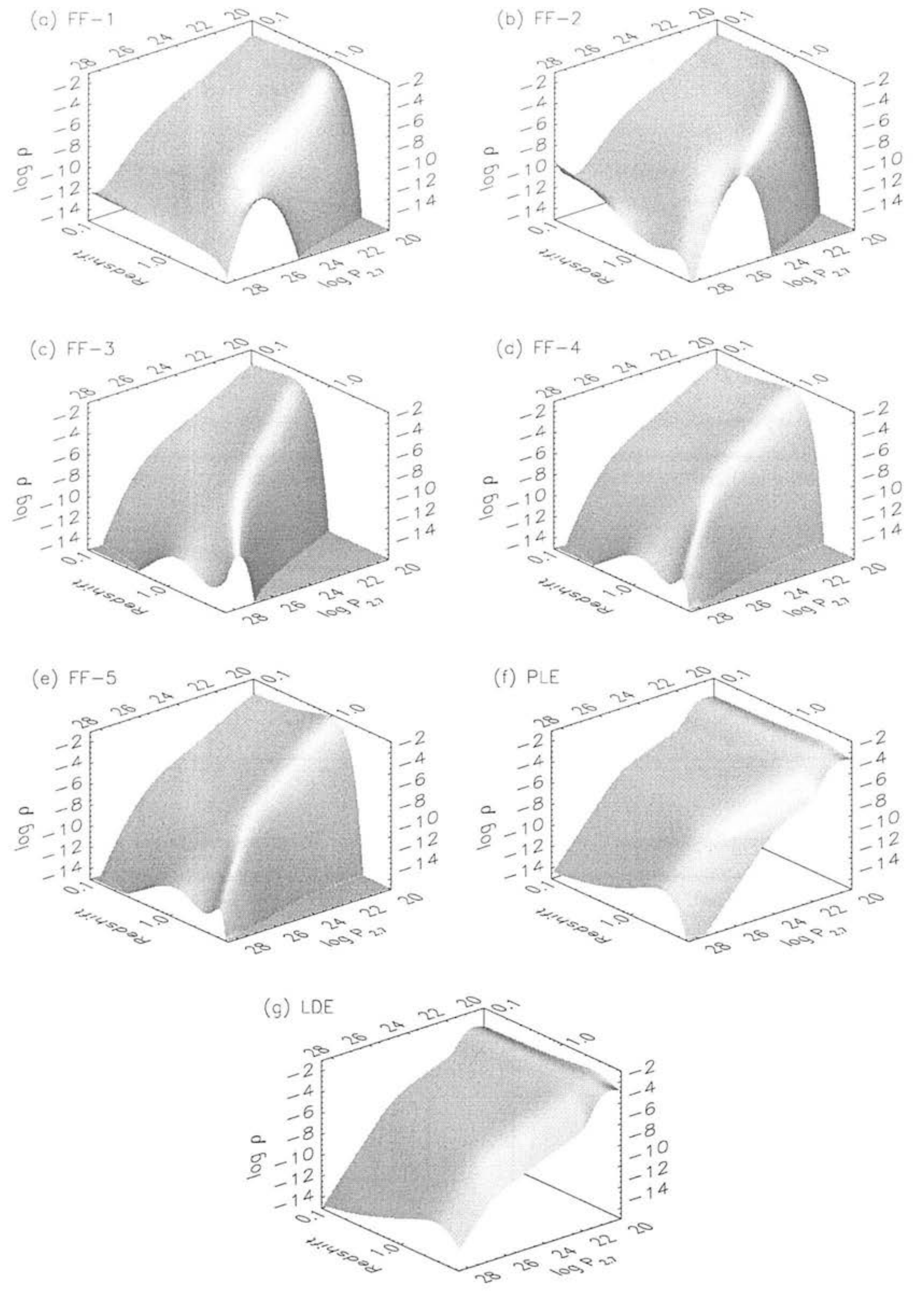

Figure 4.3 Three-dimensional representation of the steep-spectrum radio luminosity functions of Dunlop and Peacock (1990). The luminosity $P_{2.7}$ is in W Hz^{-1} sr^{-1} and the space density ρ is in $\mathrm{Mpc}^{-3}\ \Delta\log_{10} P^{-1}$. The redshift axis runs from 0.1 to 5.

the same object if it were at the flux-density limit of the sample. For a uniform distribution of objects in space, the mean $\langle V/V_{\max}\rangle$ should be 0.5. Values $\langle V/V_{\max}\rangle > 0.5$ indicate an increase in comoving density with redshift, while $\langle V/V_{\max}\rangle < 0.5$ indicates a deficit of high-redshift objects. This classical test was modified in two ways. First, it was generalised such that the volumes depend on the survey depth as a function of sky area, in order that the four complete samples (of different flux-density limits) could be combined into a single test (Avni and Bahcall 1980). Second, a banded version of the test was required (Osmer and Smith 1980; Avni and Schiller 1983). This replaces the volumes (V, $V_{\max}$) by $V - V_0$, where V_0 is the cosmological volume enclosed by a redshift z_0. The banded $V/V_{\max}$ test is then a function of redshift and enables any high-redshift negative evolution to be separated from the strong, positive evolution at lower redshifts.

Applying this test to the complete sample database gave values $\langle V/V_{\max}\rangle < 0.5$, on average, for the flat-spectrum sources at $z \gtrsim 1$ and for the steep-spectrum sources at $z \gtrsim 1.5$. The errors on $\langle V/V_{\max}\rangle$ were sufficiently large to make this a marginal result, however the conclusions were not particularly sensitive to the choice of cosmology, nor to the choice of MEAN-z or HIGH-z redshift distributions so long as the luminosity was restricted to $\log_{10} P = 26 - 27$ where the data is most complete (in terms of P–z coverage). At lower redshifts, values of $\langle V/V_{\max}\rangle > 0.5$ clearly demonstrated the strong positive evolution of both the steep- and flat-spectrum populations at $z \lesssim 1$.

In conclusion, Dunlop and Peacock (1990) found evidence that the comoving density of both flat- and steep-spectrum sources suffers a decline at redshifts between $z = 2$ and 4. This conclusion was drawn from the behaviour of both free-form and simple parametric modeling (PLE/LDE), and the model-independent, banded $V/V_{\max}$ test.

4.1.2 Testing the reality of the redshift cut-off

It was noted above that one of the disadvantages of using the Parkes Selected Regions in the determination of the RLF at high redshifts is the low redshift completeness (46%) of the sample. Dunlop and Peacock (1990) emphasized throughout their paper how the redshift cut-off in the models was dependent upon the estimated redshifts of half the PSR sample. The plots of their RLFs in figures 4.1 & 4.2 show how the upper limits to the possible luminosity functions are consistent with *no* cut-off. In particular, at high redshifts ($z \gtrsim 2$ say) it only requires a handful of sources to change the density significantly, given the relatively small volume elements. It is therefore necessary to test the models with more data. This can be done in two possible ways.

First, one can remove the uncertainty in the PSR redshift distribution by measuring the redshifts of the remaining 54% of the sample. It has been seen above how narrow the possible

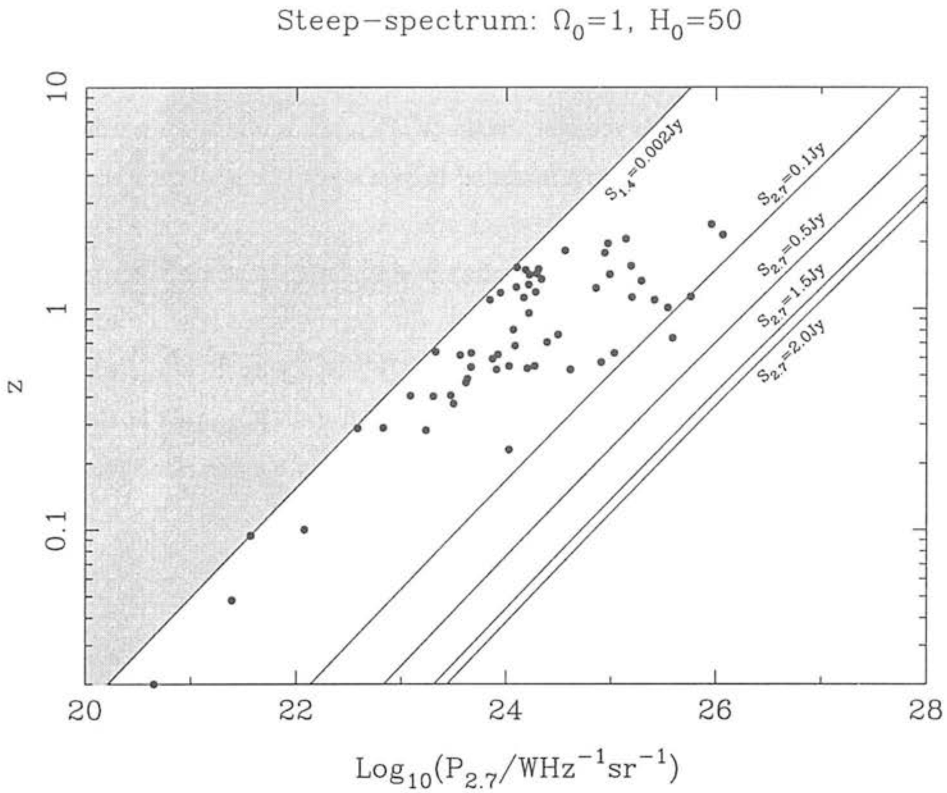

Figure 4.4 The parameter space that is probed for surveys of different flux-density limits: $S_{2.7} = 0.1$ (PSR), 0.5, 1.5 & 2.0 Jy are the survey limits corresponding to the complete samples used in DP90; $S_{1.4} = 0.002$ Jy is the limit of the 2-mJy LBDS Hercules sample. (Limits are plotted for steep-spectrum sources $\langle\alpha\rangle \simeq 0.8$; compare figure 9 of DP90 for the flat-spectrum case.) The symbols are the 60 sources in the 2-mJy Hercules sample with optical identifications and either spectroscopic or photometric redshifts (see §4.3).

range of RLF models is, when there is complete redshift data available. At $z \lesssim 1$ the models are tightly constrained — it is at higher redshifts that the spectroscopic data is lacking, in exactly the region of the P–z plane that is crucial for testing the cut-off. This was the motivation behind the spectroscopic observations described in section 3.1. The next section (§4.2) will discuss the implications of these spectroscopic results.

The second way to test the high-redshift behaviour of the RLF is to use a sample with a lower flux-density limit. Figure 4.4 shows how much more of the P–z plane is made accessible by the LBDS Hercules sample which, with a flux-density limit of $S_{1.4} = 2$ mJy, is ~100 times fainter than the PSR. In the PSR sample only the most powerful ($\log_{10} P_{2.7} > 26$) steep-spectrum sources are detectable at $z > 1.5$. The LBDS can detect sources at the same redshift which have luminosities of $\log_{10} P_{2.7} \simeq 23.5$ — such sources are below the flux-density limit of the PSR for any redshift $z > 0.1$. If there is not a high-redshift cut-off in the RLF, then there will be a significant fraction of sources in the LBDS at high redshifts. For example, figure 14(b) of DP90 predicts the cumulative redshift distribution for the whole LBDS sample based on the ensemble of free-form models. As many as 10% of the sources may have redshifts greater than 3, although the predicted distribution is rather poorly constrained beyond $z \gtrsim 0.7$.

The ability of the LBDS to confirm or refute the cut-off was one of the motivations to complete the optical identification of the LBDS and to obtain redshift measurements for as many sources as possible. As reported in the previous two chapters, this has been done for the two Hercules fields in the sample and it is these results that will be used in section 4.4 to test the reality of the redshift cut-off.

4.2 Implications of the updated PSR sample

Prior to the current work, 46% of the Parkes Selected Regions sources had redshifts: 26 of 38 flat-spectrum sources (68%) and 56 of 140 steep-spectrum sources (40%). The results of the spectroscopy reported in §3.1 have added one flat-spectrum source to this list and a further 14 steep-spectrum sources, bringing the redshift content to 71% and 50% respectively. Whilst this is only a small step closer to redshift completeness, it is nevertheless useful to consider how these results affect the conclusions of Dunlop and Peacock (1990).

4.2.1 Accuracy of the redshift estimation

The estimated redshifts $z_{\rm est}$ of these fifteen sources were calculated from Lilly's K–z relation (equation [1.10]) and are listed in table 4.1. The K magnitudes were taken from the literature (Dunlop et al. 1989b; Dunlop and Peacock 1990; Dunlop and Peacock 1993), with four exceptions. For 1339+015 a new measurement of $K = 19.1$ was used (Dunlop, priv. comm.). For 1349−008, 2150−202 & 2215−185 the K magnitude itself was estimated from the optical colour, based on a relation between the $(B - R)$ colours and K magnitudes of the PSR radio galaxies: $K = -1.1\,(B - R) + 18.3$ (Dunlop et al. 1989b). Although this relation is very broad (at $B - R = 2$, $K = 17.5 \pm 0.5$ and the corresponding uncertainty in z is ± 0.5), it allows an approximate redshift to be calculated. The estimates are compared with the spectroscopic redshifts in figure 4.5.

It is seen from the figure, that the estimated redshifts have a tendency to be larger than the spectroscopic ones. The median difference between estimated and spectroscopic redshifts is $\langle \Delta z \rangle_{\rm med} = \langle z_{\rm est} - z_{\rm spec} \rangle_{\rm med} = 0.18$, with a standard deviation about the median of $\sigma_{\rm med} = 0.35$.

With the exception of the only flat-spectrum source in the subsample (1205+011), the estimated redshifts for sources with $z_{\rm spec} \lesssim 1$ are correct. Most of the disagreement between

Table 4.1 K magnitudes and redshift estimates for the fifteen PSR sources with newly measured redshifts.

Source	K	z_{est}	z_{spec}
1154−011	17.10 ± 0.30	1.2	1.21
1154−019	16.81 ± 0.05	1.0	0.86
1201−026	18.17	2.2	1.43
1205+011	17.20 ± 0.20	1.3	0.50
1212−007	17.87 ± 0.19	1.8	1.60
1339+015	19.1 ± 0.2	3.6	3.51
1331+004	17.81	1.8	1.40
1345+008	18.20	2.2	1.50
1346+018	16.29 ± 0.09	0.7	0.65
1349−008	(16.9)[1]	1.0	0.98
2150−202	(17.7)[1]	1.7	1.33
2156−192	14.96 ± 0.06	0.3	0.45
2158−160	17.39 ± 0.12	1.4	1.24
2202−179	16.79 ± 0.10	1.0	1.35
2215−185	($\lesssim 17.8$)[1]	$\lesssim 1.7$	1.04

[1] Estimated from $B - R$.

z_{spec} and z_{est} occurs at $z > 1$. This is consistent with the K–z diagram of DP90 (their figure 3), where the Parkes sources were shown to follow the same relation as the brighter 3CR and 1-Jansky sources, noting that there are only two PSR sources with $z > 1$ on that diagram. Looking at the trend of points in figure 4.5, it suggests that at higher redshifts there is a *systematic* over-estimation of z_{est}. This would correspond to a steepening of the K–z relation at $z > 1$ — in the sense that at any given redshift the PSR sources are optically less luminous than the 3CR/1-Jy sources. This was also suggested by the K-band magnitude distributions of figure 2.8, where the PSR galaxies were seen to be, on average, a magnitude fainter than the 3CR galaxies.

Contrary to the general trend, the highest redshift source (1339+015) actually lies almost exactly on Lilly's K–z relation, with the difference between estimated and spectroscopic redshifts being only $\Delta z = 0.1$. Perhaps this is showing that there is a mixed population of sources in the PSR — some "standard candle" sources that follow the K–z relation at all redshifts, and a population of optically less luminous sources at lower redshifts.

Finally, it is interesting to note how these results compare with the work of Eales et al. (1997) on the K–z diagram for their B2/6C sample (§1.3). They found that at $z > 0.6$

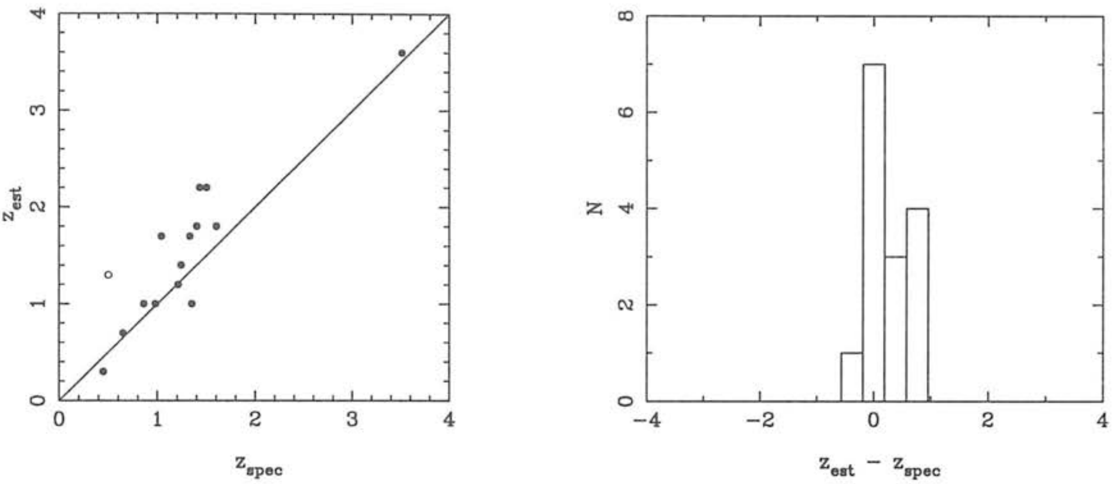

Figure 4.5 A comparison of the estimated redshifts (z_{est}) from the K–z relation, and the spectroscopic redshifts (z_{spec}) for the 15 source PSR subsample. *Left:* The solid line denotes the locus of $z_{\mathrm{est}} = z$. Filled circles are steep-spectrum sources, the hollow circle is the only flat-spectrum source in the subsample. *Right:* The same data plotted as the difference between estimated and measured redshift.

the fainter radio sources in their sample were $\sim$ 0.6 magnitudes fainter at K than the 3C sources. A comparable effect is seen (indirectly) in the PSR data in figure 4.5, although it is not until $z \gtrsim 1.2$ that the discrepancy with the 3C data becomes as large as was observed by Eales et al.

4.2.2 Implications for the redshift cut-off

In calculating their radio luminosity functions, Dunlop and Peacock (1990) used two different estimated redshift distributions. Recall that the MEAN-z distribution used Lilly's K–z relation to predict the redshift from the K magnitude, and the HIGH-z distribution modified these estimates, such that the estimated redshifts were systematically increased at faint K magnitudes. The first conclusion that can be drawn from the results shown in figure 4.5 is that the HIGH-z redshift distribution must be a poor representation of the data. Indeed, the MEAN-z esimates (as used in this figure) are themselves higher on average than the spectroscopic redshifts, so even larger estimates are certainly unrealistic. Thus the results derived from the modified redshift distribution, the HIGH-z luminosity functions of DP90, can be rejected and will not be considered further.

The effect of a 20% random scatter in the estimated redshifts was shown by DP90 to produce a redshift distribution that was statistically indistinguishable from the MEAN-z distribution. Although the scatter in the new redshifts is somewhat larger ($\sim$30%) than considered by DP90 it is not unreasonable to assume that this will not change the *distribution* of redshifts significantly. Thus if figure 4.5 is to be interpreted as an increased scatter about the K–z relation at high redshift, then these new results will have little effect on the conclusions of DP90.

The more interesting possibility is that the MEAN-z redshift estimates used by DP90 were systematically too large at $z \gtrsim 1$. The effect of this is best illustrated with reference to figure 9 of DP90 (the P–z plane; cf. figure 4.4 here). If the true redshift of a source is less than its estimated redshift, then its true luminosity will also be less than its estimated luminosity — it will move towards the lower-left of the P–z plane, on a locus parallel to the flux-density limit lines in these figures. The effect will be to de-populate the high-P, high-z corner of the P–z plane thus strengthening the conclusions of DP90 that there is a cut-off in the RLF *for the most powerful sources,* $\log_{10} P > 27$.

The effect that a systematic over-estimation of z would have at lower radio luminosities is rather different. For $z \lesssim 1$, the K–z estimates are in agreement with the data, so the RLFs will be unaffected at luminosities $\log_{10} P \lesssim 25.5$ (corresponding to the flux-density limit at $z \simeq 1$). The key luminosities of interest are then $25.5 < \log_{10} P < 27$. Within this area of the P–z plane there will be an *increase* in the number of sources compared with the distribution used by DP90 — sources with high estimated luminosities will move into this area at lower redshifts and luminosities. The effect will be to produce a net increase in the number of high redshift sources per $\Delta \log_{10} P$, particularly at the high-P end of this luminosity range. The quantative changes expected in the model RLFs cannot be predicted easily without deriving fits to the new data. Although $\rho(P, z)$ would increase at $z = 3$ say (as $z_{\rm est} = 4$ sources move to $z_{\rm est} = 3$), thus decreasing the evidence for a cut-off, $\rho(P, z)$ would also increase at $z = 2$ (as $z_{\rm est} = 3$ sources move to $z_{\rm est} = 2$), tending to increase the evidence for a cut-off. The relative importance of these two effects will determine whether or not the cut-off is enhanced or removed. It can be seen from figure 4.2 that it would not require many more sources at $z = 2 - 3$ to remove the (already marginal) necessity for a decline in the high-redshift RLF.

In summary, the new redshifts of PSR sources measured in §3.1 allow the HIGH-z luminosity functions of DP90 to be rejected; they strengthen the conclusion of DP90 that there is a cut-off in the steep-spectrum population, but only at high luminosities; at lower luminosities, $\log_{10} P \lesssim 27$, there remains considerable uncertainty in the form of the RLF.

To resolve this uncertainty would require more spectroscopic redshifts — at least enough to determine: (i) whether a steeper K–z relation is needed for the PSR at $z \gtrsim 1$; or (ii) if the discrepancies in figure 4.5 are just the effect of an increased scatter in Lilly's K–z relation. The observing effort required to get the redshift content of the PSR to the necessary completeness is considerable. The fifteen redshifts discussed here are the result of six nights of telescope time, for which the success rate (number of redshifts per source observed) was less than 50% (see §3.1). To increase the redshift completeness to even 70% say, would require another two weeks' observing on a 4-m class telescope. Since it is generally the faintest sources that do not have redshifts, the success rate can only decrease further. Even as larger telescopes are becoming operational, it is still unrealistic to expect the redshift content of the PSR sample to increase sufficiently to resolve the uncertainty in the cut-off. The following sections will address the issue from the complementary perspective of a sample with a lower flux-density limit — the LBDS.

4.3 Photometric redshifts in the LBDS

Prior to the start of the current work, only 16 of the 73 sources in the LBDS Hercules fields had redshifts published in the literature. Chapter 3 reports measurements of 12 more obtained by the author. Another 21 redshifts have been measured by various observers and made available, bringing the total to 49 out of 73 sources (67%). Separating these according to spectral index gives 40 out of 52 (77%) steep-spectrum sources, and 9 out of 21 (43%) flat-spectrum sources with redshifts. See table 2.5 for the details and corresponding references.

In order to make best use of the LBDS to examine the evidence for a cut-off in the radio luminosity function, it is necessary to have complete redshift information for the sample. It was seen in chapter 3 how difficult it is to get good spectroscopy on these milli-Jansky sources, even more so than for the PSR sample, and so once again the unknown redshifts must be estimated. It will be seen from the infrared Hubble diagram for the LBDS Hercules field (chapter 5) that Lilly's K–z relation cannot be used to reliably estimate z — for these sources there is significant scatter about the relation for $z \lesssim 1$, and at higher redshifts the sources are systematically fainter than the 3CR/1-Jansky sources that define the K–z relation. A more sophisticated redshift estimation method was needed that used all the available photometry. In this section, the background to photometric redshift estimation is presented, followed by a discussion of the technique that was found to work best for the LBDS. The resulting redshift distributions are given in §4.3.4.

4.3.1 Introduction

The idea of using broadband photometry to estimate redshifts was first proposed thirty-six years ago by Baum (1962) who used nine photometric bands to essentially locate the 4000-Å break in elliptical galaxies. Loh and Spillar (1986) used six medium-band filters to estimate the redshifts of ~200 cluster and field galaxies, finding good agreement with the limited number of spectroscopic redshifts available to them. Koo (1985) used the photographic bands $U^+J^+F^+N^+$ together with the models of Bruzual (1983) to trace the locus of a galaxy across colour–colour plots, as a function of redshift. Comparison with the spectroscopic redshifts of ~100 galaxies yielded an accuracy of $|\Delta z| = |z_{\rm spec} - z_{\rm phot}| \leq 0.04$ for two-thirds of the sources at $z_{spec} < 0.35$ and $|\Delta z| \leq 0.06$ for $0.35 < z_{\rm spec} < 0.6$.

Although these methods were successful for low redshift galaxies, they were not applied to sources at $z \gtrsim 0.6$ due to the small number of spectroscopic redshifts available at higher z in their samples. As has been noted before, radio galaxies were for many years the only galaxies known in great numbers at high redshift, and methods for estimating their redshifts arose along different lines. The infrared Hubble diagram for radio galaxies provided an empirical relationship between the K-band magnitude and the redshift of a radio galaxy (see §1.4 & equation [1.10]). After finding this relationship, Lilly et al. (1985) used it to estimate the redshifts of the remaining galaxies in their sample from their K magnitudes. In a later paper, Lilly (1989) showed that the broadband spectral energy distributions of 1-Jansky radio sources could be modelled by a combination of an "old" (>2 Gyr) and a "young" (<1 Gyr) stellar population. Using the spectral synthesis models of Bruzual (1983) he fitted the observed SEDs, varying the redshift and the fraction of the young component at 5000 Å (denoted f_{5000}). Although the main purpose was to measure the star-formation activity in the sample (via f_{5000}), he also used this method to estimate the redshifts of ~10 sources. Two of these had spectroscopic redshifts, giving $|\Delta z| = 0.02$ and 0.33 for $z = 3.40$ and 2.17 respectively. All estimates had K magnitudes consistent with the K–z diagram, suggesting they were unlikely to be significantly in error.

As discussed in §4.1 above, Dunlop and Peacock (1990) used the K–z relationship of Lilly et al. to estimate the redshifts of half the sources in the Parkes Selected Regions, in order to investigate the radio luminosity function. In Dunlop and Peacock (1993) they used a modified version of Lilly's "old"+"young" model to predict photometric redshifts for a subsample of the PSR. For the "young" or "blue" component they used a power-law spectrum ($f_\nu \propto \nu^{-\alpha}$, with $\alpha = 0.2$) instead of a young stellar population, chosen to reproduce the flat f_ν UV–optical continuum observed in high-redshift radio galaxies. Comparison of the estimates with the eight galaxies at $z > 0.5$ which had spectroscopic redshifts gave an accuracy of $\langle z_{\rm phot}/z_{\rm spec}\rangle = 0.97 \pm 0.11$. These colour-estimated redshifts were, on average, a factor of $\sim$0.8 smaller than the corresponding K–z redshift estimates for this subsample.

Recent interest in photometric redshift estimation was aroused by the need to obtain redshifts in the Hubble Deep Field (HDF; Williams et al. 1996). The faintness of the galaxies in the HDF makes obtaining complete spectroscopic redshifts an impractical option — a more efficient approach was to develop the methods of estimating redshifts from the photometry. The methods fall into two basic categories: (i) fitting the data to either *observed* or *model* SED templates; and (ii) generating an empirical fit to the photometry. A review of the techniques and results is given by Hogg et al. (1998).

The first method consists of calculating the observed colours that a template spectrum would have at a given redshift, through a given set of filters, and then comparing that simulation with the data. The redshift is determined from the best fitting simulation by minimizing χ^2. The various groups using this method differ essentially in their choice of template spectra. Lanzetta et al. (1996), Fernández-Soto et al. (1999) and Sawicki et al. (1997) used observed spectra of four Hubble types (E/S0, Sbc, Scd, Irr), extended into the UV and the IR using the models of Bruzual and Charlot (1993). Gwyn and Hartwick (1996) used the evolving model spectra of Bruzual and Charlot (1993), while Mobasher et al. (1996) used the models of Yoshii and Takahara (1988). The effects of inter-galactic absorption short-ward of Lyman-α and of dust absorption within the galaxy were modelled in various ways. The second method is that of Connolly et al. (1995). Using a "training set" of galaxies with known redshifts, they fit a low-order polynomial to the magnitudes and colours of the galaxies, giving an empirical relationship between the photometric properties and the redshift. This technique has been applied to both the HDF (Connolly et al. 1997) and a region coinciding with the Canada-France Redshift Survey (Brunner et al. 1997).

When the photometric predictions are compared with known spectroscopic redshifts, the agreement at low redshifts ($z \lesssim 1$–1.5) is very good with 68% of sources having $|\Delta z| = |z_{\rm phot} - z_{\rm spec}| < 0.1$ and almost all sources agreeing within $|\Delta z| < 0.3$ (Hogg et al. 1998). At higher redshifts, the photometric estimates are more uncertain. For example, Fernández-Soto et al. (1999) find that $\Delta_{rms} z = 0.45$ for $z > 1.5$. It is also interesting to note a systematic error that appears in plots of $z_{\rm phot}$ against $z_{\rm spec}$. Trails of points running parallel to each axis are found — these are sources with either low $z_{\rm spec}$ predicted to have a much larger $z_{\rm phot}$ or vice versa (see figure 9 of Ellis (1997) and figures 3 & 4 of Lanzetta et al. (1996)). The possible origin of this error will be addressed below, as it is also apparent in the current work.

An important point to recall when comparing the results of photometric redshift estimates in the HDF with estimates based on other data, is the very high quality of the HDF observations. This is particularly apparent for comparisons with ground-based data, such as that presented here. The HDF observations have a resolution of $0\farcs1$, exposure times of 1–1.5×10^5 seconds per filter, with very low background. Typical ground-based observations have $\sim$10× poorer resolution, $\sim$10× shorter exposures and a background that is 1–3 magnitudes brighter.

The next sub-section describes the method used to estimate the redshifts of sources in the LBDS Hercules field. Section 4.2.3 then compares the estimates with the known spectroscopic redshifts, and the basic properties of the resulting redshift distributions are discussed in section 4.2.4.

4.3.2 Estimation methods

In order to develop the best possible method of calculating photometric redshifts, the ideas of several of the above authors were combined and investigated. Galaxy spectra from the new spectral synthesis models of Jimenez et al. (1999) (see §1.5) were used to compute the template SEDs. The observed magnitudes were compared with the model predictions using the χ^2 statistic, for a broad range of redshift, model age and fraction of "young" component (for both a young stellar population and a power-law). The best-fit parameters were then determined by minimizing χ^2 over a restricted subset of the parameter values.

The spectral models consist of an array of flux densities for wavelengths 90 Å–100 μm (with variable wavelength sampling), at ages of 0.01–14 Gyr, for five different metalicities and two different initial mass functions (IMFs). They are described in detail in §1.5. The models with Miller-Scalo IMF and solar metalicity ($Z = 0.02$) were used — the estimated redshifts were not sensitive to the choice of IMF or Z. A template spectrum was computed by first selecting the spectrum of the required age $F_\lambda^{\rm old}$, then adding to that a "young" component $F_\lambda^{\rm young}$ scaled such that this component is a fraction f_{5000} of the total flux at 5000 Å, i.e. $f_{5000} = F_\lambda^{\rm young}(5000\ \text{Å})\ /\ F_\lambda(5000\ \text{Å})$, where $F_\lambda = F_\lambda^{\rm old} + F_\lambda^{\rm young}$. Three forms for the "young" component were tested: a young stellar population of age 0.03 Gyr, one of age 0.1 Gyr (following Lilly 1989), and a power-law $F_\lambda^{\rm young} \propto (\lambda/5000)^{-2+\alpha}$ with $\alpha = 0.2$ (following Dunlop and Peacock 1993).

Inter-galactic absorption due to hydrogen systems along the line of sight was modelled as a damping of the flux at wavelengths shorter than Lyα, such that $F_\lambda(\lambda < 1216\ \text{Å}) \rightarrow F_\lambda \cdot e^{-\tau}$, with $\tau = ((1+z)/5.3)^3$ (Gunn and Peterson 1965). The Lyman-limit discontinuity, due to the weak stellar emission and strong interstellar H I absorption shortward of 912 Å, was modelled by a cut-off of the form $F_\lambda(\lambda < 912\ \text{Å}) = 0$. (The Jimenez et al. models do, in fact, successfully reproduce the Lyman-limit discontinuity but this additional step was retained for compatability with older spectral synthesis models.) The effects of possible dust absorption within the galaxy were not considered — the additional parameters necessary could not be easily accommodated, given that each source had on average only four magnitudes with which to compare the models. Finally the spectrum is redshifted: $\lambda \rightarrow \lambda \cdot (1+z)$.

The synthetic flux in a given filter is computed by convolving the model spectrum $F_\lambda(\lambda)$ with the appropriate filter response function $T_f(\lambda)$

$$F = \int_{\lambda_1}^{\lambda_2} F_\lambda(\lambda) \cdot T_f(\lambda) \cdot \mathrm{d}\lambda \qquad [4.10]$$

where $(\lambda_1 \colon \lambda_2)$ is the wavelength region for which T_f is non-zero. The response function T_f has been computed from the filter transmission, the atmospheric extinction and (for the optical filters) the quantum efficiency of the CCD detector, and was obtained from databases at the telescopes (Palomar and UKIRT). The synthetic magnitude is then

$$m_f^{\mathrm{syn}} = -2.5 \, \log_{10} \left(\frac{F}{F_f^{\mathrm{std}}} \right) \qquad [4.11]$$

where F_f^{std} is the flux that a standard star has in the same filter. The standard stars are BD+17°4708 for the gri filters and Vega (α Lyrae) for the U^+JHK filters. The fluxes F_f^{std} are computed from tabulated flux density measurements of the standard stars using equation [4.10].

The set of synthetic magnitudes (m_f^{syn} for filters $f = U^+griJHK$) are compared with the data (m_f) using the χ^2 statistic:

$$\chi^2 = \sum_f \left[\frac{m_f - (m_f^{\mathrm{syn}} + \Delta m^{\mathrm{syn}})}{\sigma_f} \right]^2 \qquad [4.12]$$

which is then minimized with respect to the normalization Δm^{syn}. This normalization simply scales the model spectrum by a constant so that the synthetic magnitudes fit the data (physically, it is the combination of the absolute bolometric magnitude of the source plus the $1/r^2$ dimming.)

This process of generating synthetic magnitudes and determining the normalization is repeated for redshifts $0 \leq z \leq 5$ in steps of 0.1, "young" component fractions $0 < f_{5000} < 1$ in steps of 0.02, and the twenty galaxy ages (0.01, 0.03, 0.07, 0.1, 0.3, 0.7, 1, 2, 3, 4, 5, 6, 7, 8, 9, 10, 11, 12, 13, 14 Gyr). Equation [4.12] is evaluated for each combination of the parameters z, f_{5000}, age (Δm^{syn} having been determined already), yielding an array of values of $\chi^2(z, f_{5000}, \mathrm{age})$ for each of the three different "young" components. When m_f is an upper limit, the term contributing to the summation is defined to be an exponential with value $\simeq 1$

when the model magnitude ($m_f^{\rm syn} + \Delta m^{\rm syn}$) equals the 1-$\sigma$ limit, increasing exponentially when the model is brighter than the data, and making an exponentially decreasing contribution to χ^2 when the model is fainter than the data.

An approximation to the best-fitting parameters was determined by finding the minimum value of χ^2 in the coarse three-dimensional array. This approximation was refined and errors on the parameters determined by using the minimization technique described in §15.5 of Press et al. (1992). Defining $\mathbf{a} = (z, f_{5000}, {\rm age})$, the minimizing parameters $\mathbf{a}_{\rm min}$ are computed from the approximate parameter set $\mathbf{a}_{\rm app}$ following equation 15.5.1 of Press et al.:

$$\mathbf{a}_{\rm min} = \mathbf{a}_{\rm app} + \mathbf{D}^{-1} \cdot [-\nabla\chi^2(\mathbf{a}_{\rm app})] \qquad [4.13]$$

where $\mathbf{D}$ is the second derivative (Hessian) matrix of χ^2. The derivatives of χ^2 are evaluated from a 5×5×5 grid of points centered on $\mathbf{a}_{\rm app}$. Errors on the parameters ($\boldsymbol{\sigma}$) are determined from the diagonal elements of $\mathbf{D}^{-1}$ and, to the extent that the measurement errors are normally distributed, $\boldsymbol{\sigma}$ are the 68% confidence limits on each parameter separately.

4.3.3 Comparison with spectroscopic redshifts

Two-thirds of the Hercules sample have spectroscopic redshifts ($z_{\rm spec}$), so the best-fit photometric redshift ($z_{\rm phot}$) could be compared with the true redshift for these sources. This was done first of all visually by plotting $z_{\rm phot}$ against $z_{\rm spec}$ to see how well the points followed the locus of $z_{\rm phot} = z_{\rm spec}$. Secondly, the median, $\langle\Delta z\rangle_{\rm med}$, of $\Delta z = z_{\rm phot} - z_{\rm spec}$ was computed, together with the standard deviation about the median $\sigma_{\rm med} = \sqrt{\sum(\Delta z - \langle\Delta z\rangle_{\rm med})^2/N}$. Any sources with $\Delta z > 2.5\,\sigma_{\rm med}$ were rejected and $\sigma_{\rm med}$ was recomputed. Each redshift estimation method was assessed on the basis of the values of $\langle\Delta z\rangle_{\rm med}$ and $\sigma_{\rm med}$, the number of points rejected (N_{rej}) in the second iteration of $\sigma_{\rm med}$, and the proportion of redshifts that were underestimated (since it is the underestimated redshifts that would affect the subsequent analysis of the redshift cut-off most severely).

It rapidly became clear from these comparisons that minimizing χ^2 over the whole of the parameter ranges produced a very poor result, $\Delta z > 0.5$ for almost all sources. The next stage in the analysis was to determine which *restricted* set of parameters produced the best redshift estimates. Several methods were tested: (i) In order to approximate the methods of the HDF groups (e.g. Lanzetta et al. 1996; Sawicki et al. 1997), the number of spectral templates was limited to three, corresponding to E/S0, Sabc & Sd/Irr galaxies. This was done by fixing f_{5000}=0, and using ages of 14, 1 & 0.1 Gyr to approximately represent the increasing UV flux of early- to late-type galaxies. (ii) Following Lilly (1989) the "old" component was fixed at ages of either 5, 10, 12 or 14 Gyr, and χ^2 minimized with respect to z and f_{5000}. This

Table 4.2 Accuracy of the photometric redshifts for the two component model.

"Young" component	$\langle \Delta z \rangle_{\rm med}$	$\sigma_{\rm med}$	N_{rej}
0.1 Gyr stellar population	0.12	0.28	3
0.03 Gyr stellar population	0.09	0.35	5
Power-law $f_\nu \propto \nu^{-0.2}$	0.05	0.43	4

was done for two stellar "young" component models of ages 0.03 & 0.1 Gyr, and for the power-law component of Dunlop and Peacock (1993). (iii) The age parameter at each redshift was limited such that it was less than the age of the universe at that z, then χ^2 was minimized with respect to all three parameters. (iv) The "young" spectral component was restricted to values of $f_{5000} < 0.67$, < 0.5 and $f_{5000} = 0$, with the minimization performed over the remaining parameter ranges.

Of these methods, it was the second one that produced the most accurate results — fixing the age of the "old" component and fitting to z and f_{5000}. Using the maximum possible age for the "old" stellar population (14 Gyr) gave $\langle \Delta z \rangle_{\rm med} \simeq 0.1$ and $\sigma_{\rm med} \simeq 0.3$, compared with $\langle \Delta z \rangle_{\rm med} \simeq 0.3$ and $\sigma_{\rm med} \simeq 0.4$ for a 5 Gyr-old population. As shown in figure 4.6, varying the form of the "young" component had the effect of improving $\langle \Delta z \rangle_{\rm med}$ at the cost of making $\sigma_{\rm med}$ broader. The values of these diagnostics are given in table 4.2. The 0.1 Gyr stellar population was chosen as the best "young" component overall — it has the narrowest error distribution and the least number of very deviant points, whilst the median difference between photometric and spectroscopic redshifts remains well within the error distribution.

It can be seen in figure 4.6 that there are several sources with small spectroscopic redshifts ($z_{\rm spec} \lesssim 0.5$) that are assigned significantly larger photometric redshifts. This effect can also be seen in the work of Lanzetta et al. (1996) and Ellis (1997). In the case of 53W090 at $z_{\rm spec} = 0.094$, this is probably due to poor photometry — it is a bright galaxy that extends well beyond the apertures used in both the optical and IR images, and the difference in seeing between the two may be sufficient to distort the true colours. For the other sources (note that it is generally the same sources in each plot that show this disagreement), there appear to be two effects: (i) for $z_{\rm phot} \sim 2$ the location of the 4000-Å break can be anywhere from 1 μm to 2 μm due the lack of infrared data at J & H; and (ii) for $z_{\rm phot} \sim 3$ the 4000-Å break is being mis-interpreted as the Lyman-limit break at 912 Å. In virtually all cases a second minimum in χ^2 is found close to the spectroscopic redshift. Figure 4.7 illustrates this for 53W019 and 53W034, the only two spectroscopic sources which show this effect when a 0.1 Gyr stellar

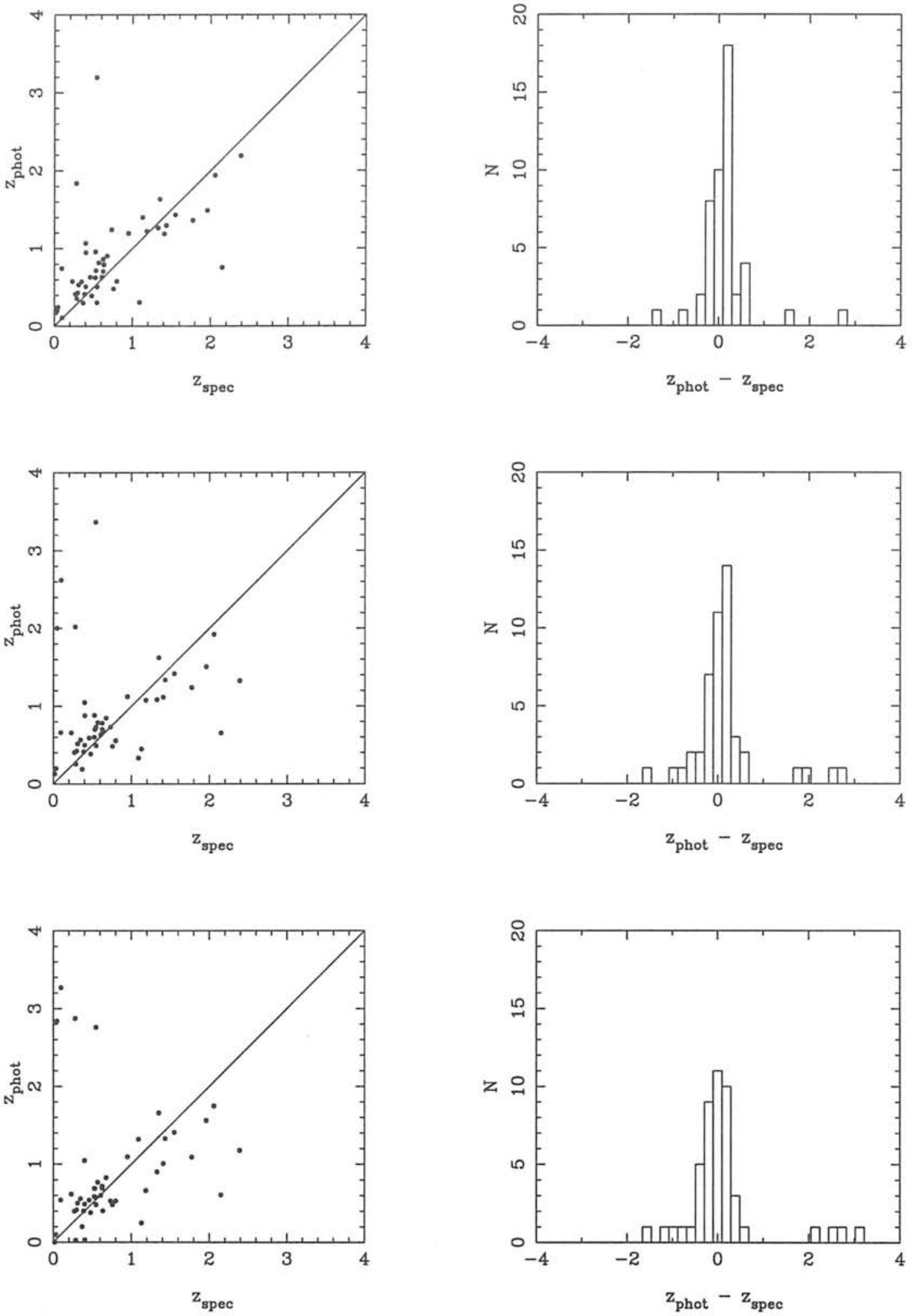

Figure 4.6 Comparison of the photometric and spectroscopic redshifts for a 14 Gyr-old stellar population plus a blue component consisting of: (a, *top*) a 0.1 Gyr stellar population; (b, *middle*) a 0.03 Gyr stellar population; (c, *bottom*) a power-law $f_\nu \propto \nu^{-0.2}$.

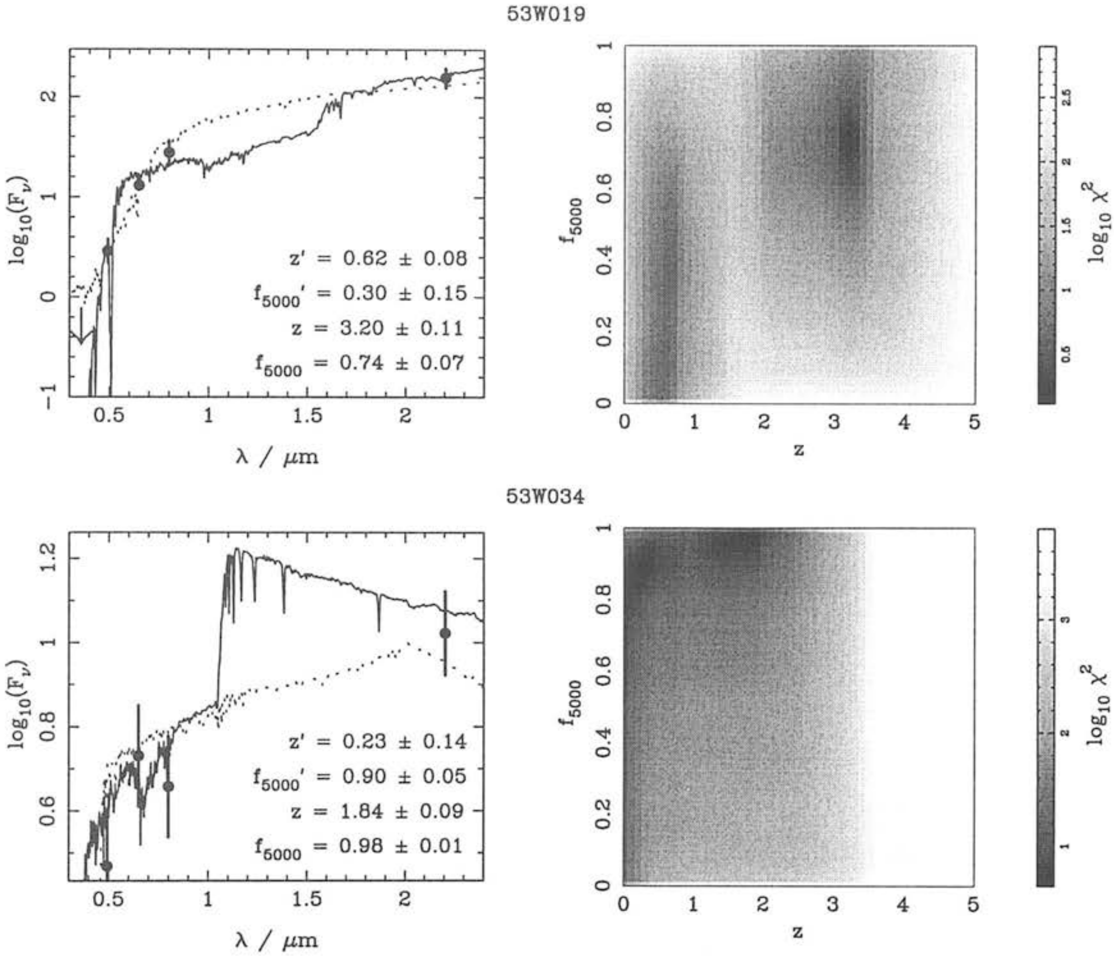

Figure 4.7 Redshift estimates for 53W019 (*top*) and 53W034 (*bottom*). Solid lines denote the best-fit photometric redshift (z), dotted lines denote the redshift (z') corresponding to the secondary minimum in χ^2. The spectroscopic redshifts are 0.542 and 0.281 respectively.

population is used as the blue component.

The two sources that have photometric redshifts that are significantly underestimated by this two component method are 53W009 ($z_{\rm spec} = 1.090$) and 53W075 ($z_{\rm spec} = 2.150$). Both are classified as quasars and it is perhaps not too surprising that their SEDs are not successfully modelled by a galaxy spectrum. Note, however, that the redshifts of the other quasars in the sample are correctly estimated.

4.3.4 Results

The best-fitting model SEDs and χ^2 functions for the twenty-one sources without spectroscopic redshifts are presented in figure 4.8. For those sources which have an upper limit to the redshift based on a continuum detection in the spectrum (table 3.5), this limit has been taken into account in determining $z_{\rm phot}$ and the errors, however the plots of χ^2 are presented *before* this additional constraint was applied. In fact, the spectroscopic continuum limits affect the predicted redshift of only one source — 53W070 — ruling out the high-z minimum in χ^2 at $z_{\rm phot} \simeq 3.7$.

Figure 4.9 presents the likelihood functions $L(z)$ for these sources, normalized to a peak value of unity. The likelihood is defined as $L(z) \propto \exp(\ -\chi^2(z)/2\ )$, where χ^2 has been minimized with respect to f_{5000} (i.e. $\chi^2(z) = \chi^2(z, f_{\rm min})$ where $f_{\rm min}(z)$ is the value of f_{5000} for which χ^2 is a minimum at each fixed z). Table 4.3 lists the best-fit photometric redshifts, together with the one-sigma errors δz, which measure the width of the primary peak in $L(z)$, and the 99% confidence limits $z_{\rm low}$, $z_{\rm high}$, which measure the lowest and highest reasonable redshift, taking into account the multi-peaked nature of the likelihood functions. It can be seen from figure 4.9 that about half the sources have peaks at two distinct redshifts, often of comparable likelihood. Thus the width of the primary peak (δz) is, in general, a poor measure of the uncertainty in $z_{\rm phot}$ and the 99% confidence limits are preferred. Indeed, these limits roughly correspond to the maximum and minimum redshifts at which $L(z)$ is distinct from zero in these plots.

In the remainder of this chapter, results will often be quoted for the "best", "low" and "high" redshift distributions, meaning that the photometric redshifts of these twenty-one sources are taken to be the values of $z_{\rm phot}$, $z_{\rm low}$ & $z_{\rm high}$ in table 4.3 respectively. The redshifts of the other forty-eight sources are, of course, taken to be their true spectroscopic values. The three distributions are presented in figure 4.10 for the full LBDS Hercules sample, and figure 4.11 shows just those sources in the 2-mJy sample. The high-z and low-z distributions are somewhat artificial as they assume that *all* the sources simultaneously lie at the extremes of their ±99% error bounds, but they bracket the realistic redshift distributions allowed by the data.

Recall that there are four sources in the sample that are unidentified and therefore do not appear in the redshift distributions (all four sources have $S_{1.4} > 2$ mJy). 53W043 was obscured by a bright star ($V \simeq 12$) in the Four-shooter CCD observations, but a lower limit of $F^+ \gtrsim 22.5$ was obtained from the photographic plates (unlike the CCDs, the star was not saturated on the plates). This places a limit on the redshift of 53W043 of $z \gtrsim 0.5$. The other three unidentified sources (53W006, 53W0037, 53W0087) all have $r \gtrsim 25$ placing them at $z \gtrsim 1$–2.

The full 73-source sample is considered first: for the best-z distribution, the median redshift is 0.61; for the low-z distribution it is 0.46; and for the high-z case the median is 0.63. The median redshift for the best-z distribution of sources in the 2-mJy sample is 0.68, little

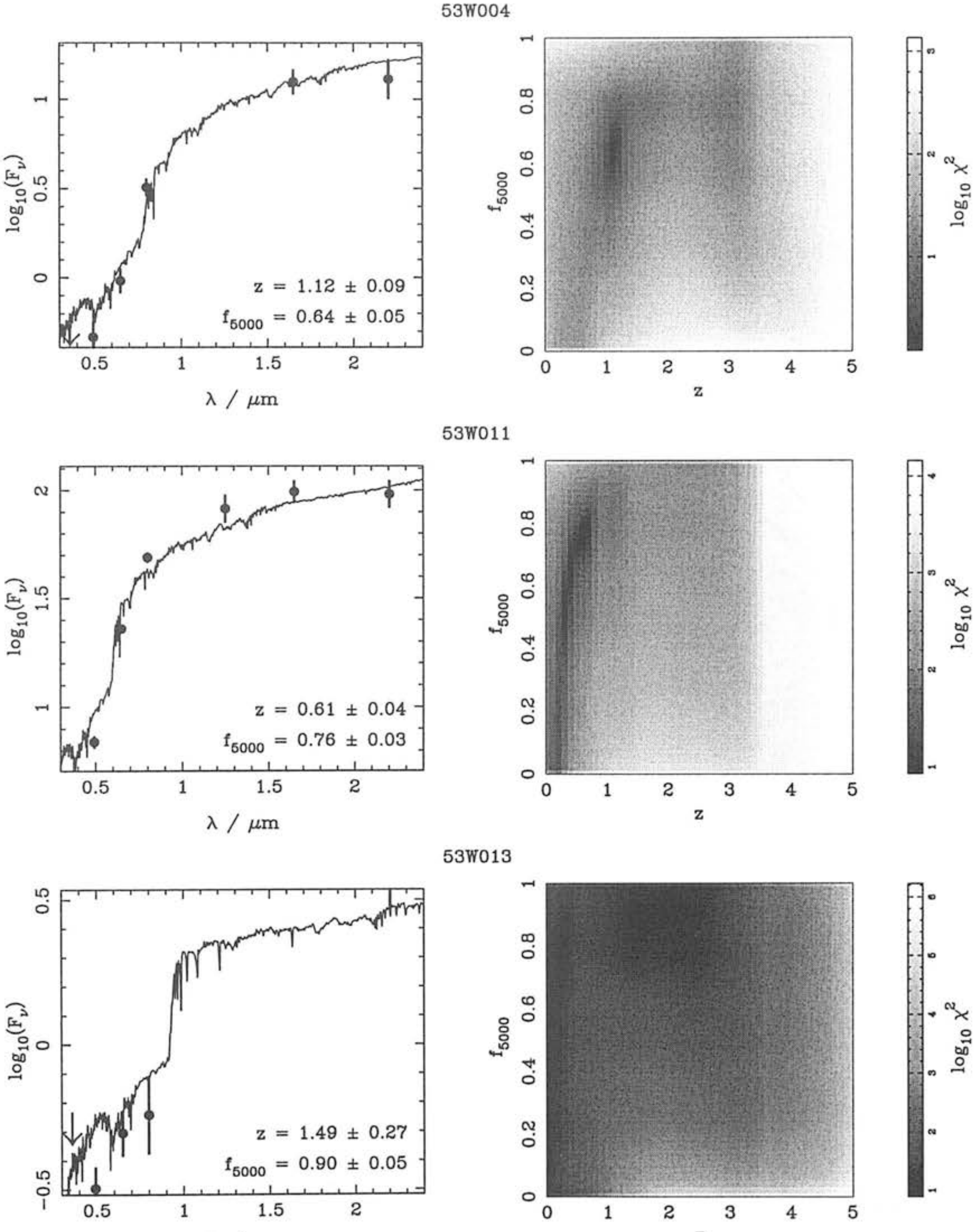

Figure 4.8 SEDs and χ^2 functions for the twenty-one sources in the Hercules sample for which photometric redshifts are required.

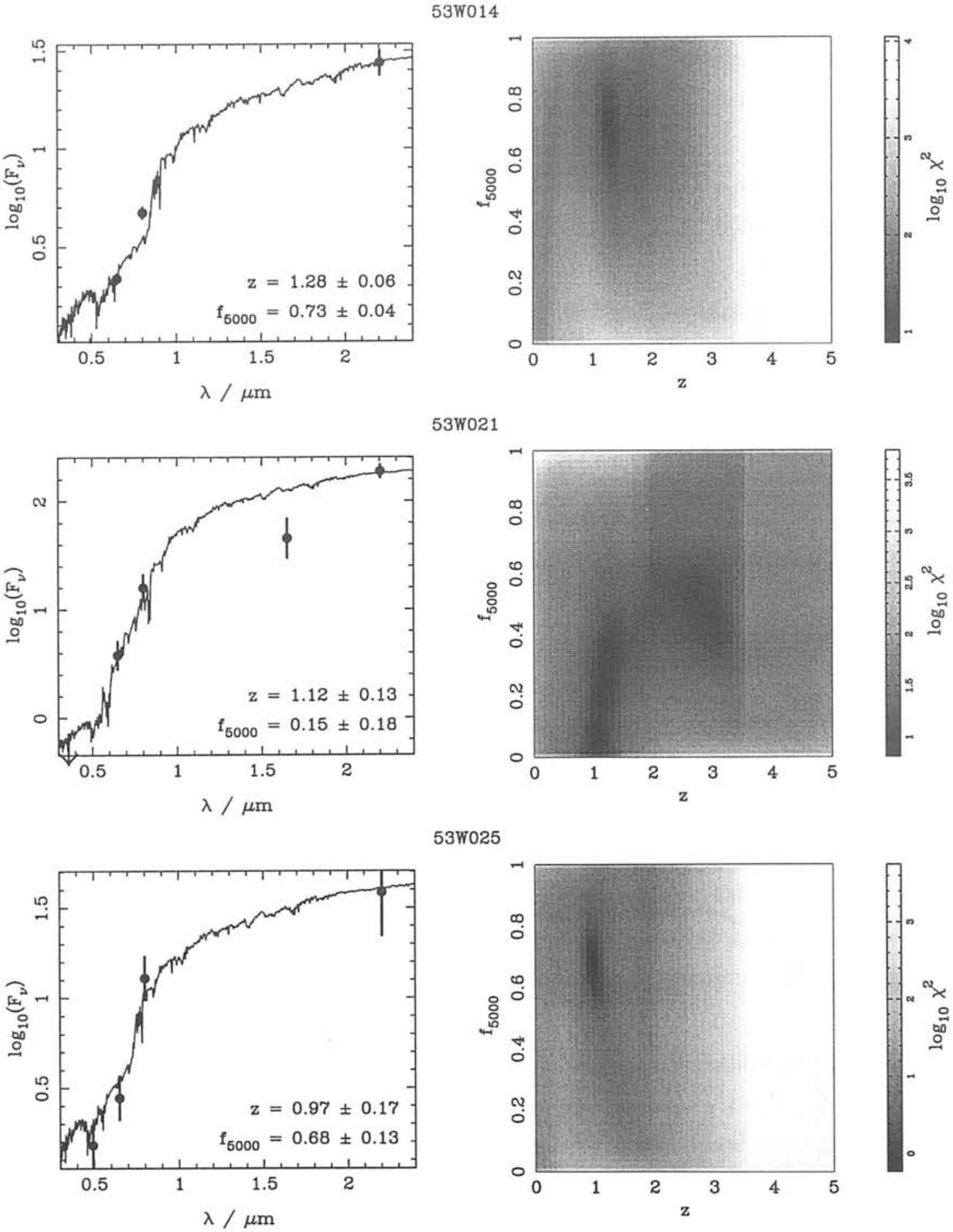

Figure 4.8 *Continued.*

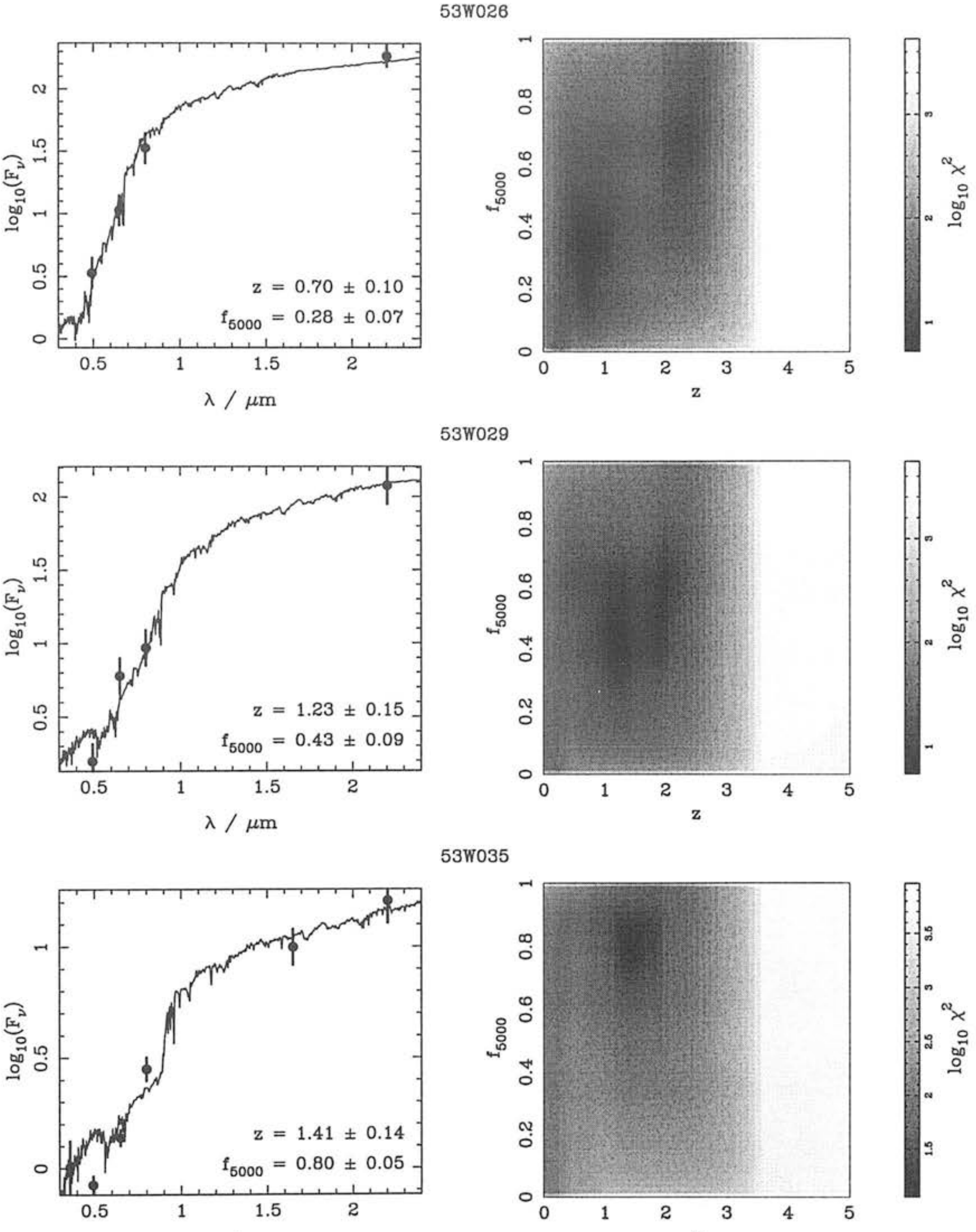

Figure 4.8 *Continued.*

53W036

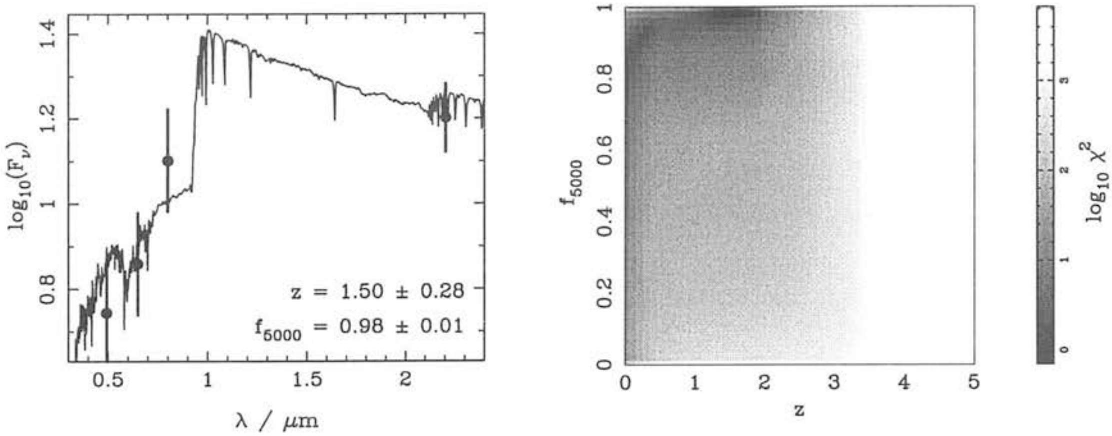

53W041

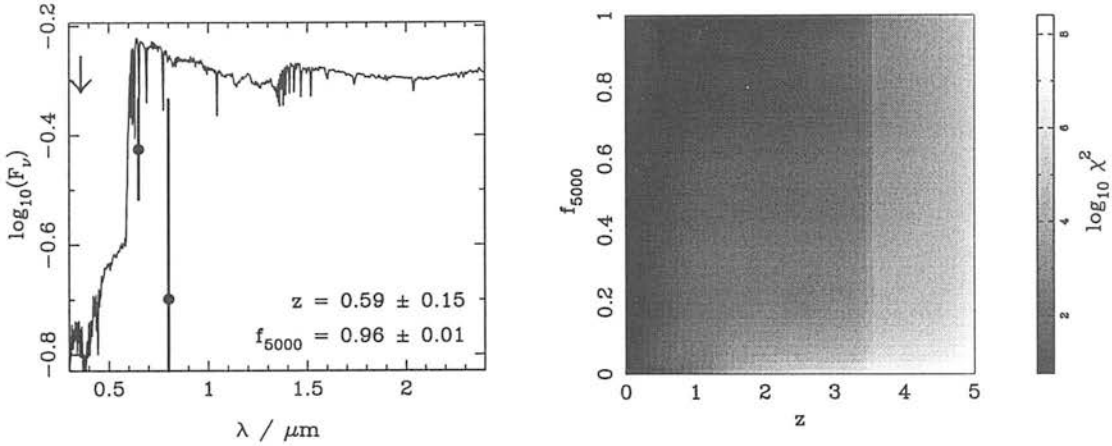

53W042

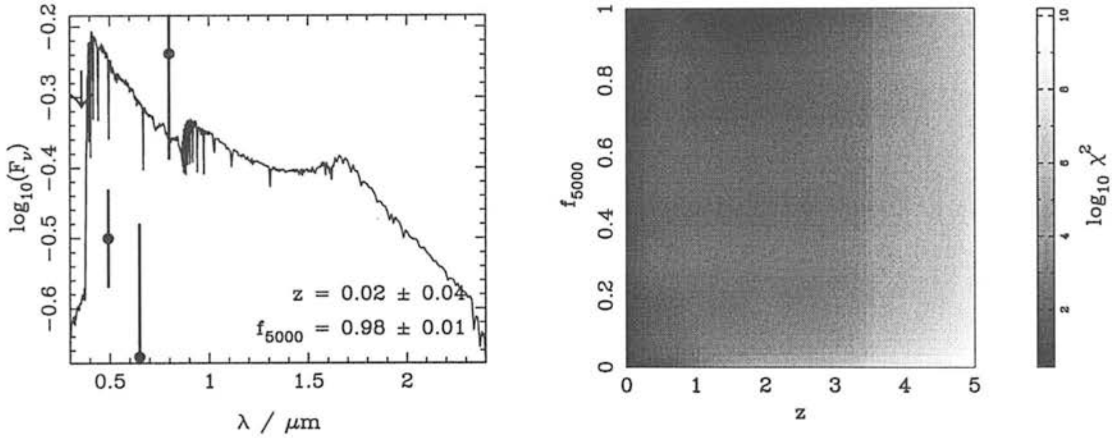

Figure 4.8 *Continued.*

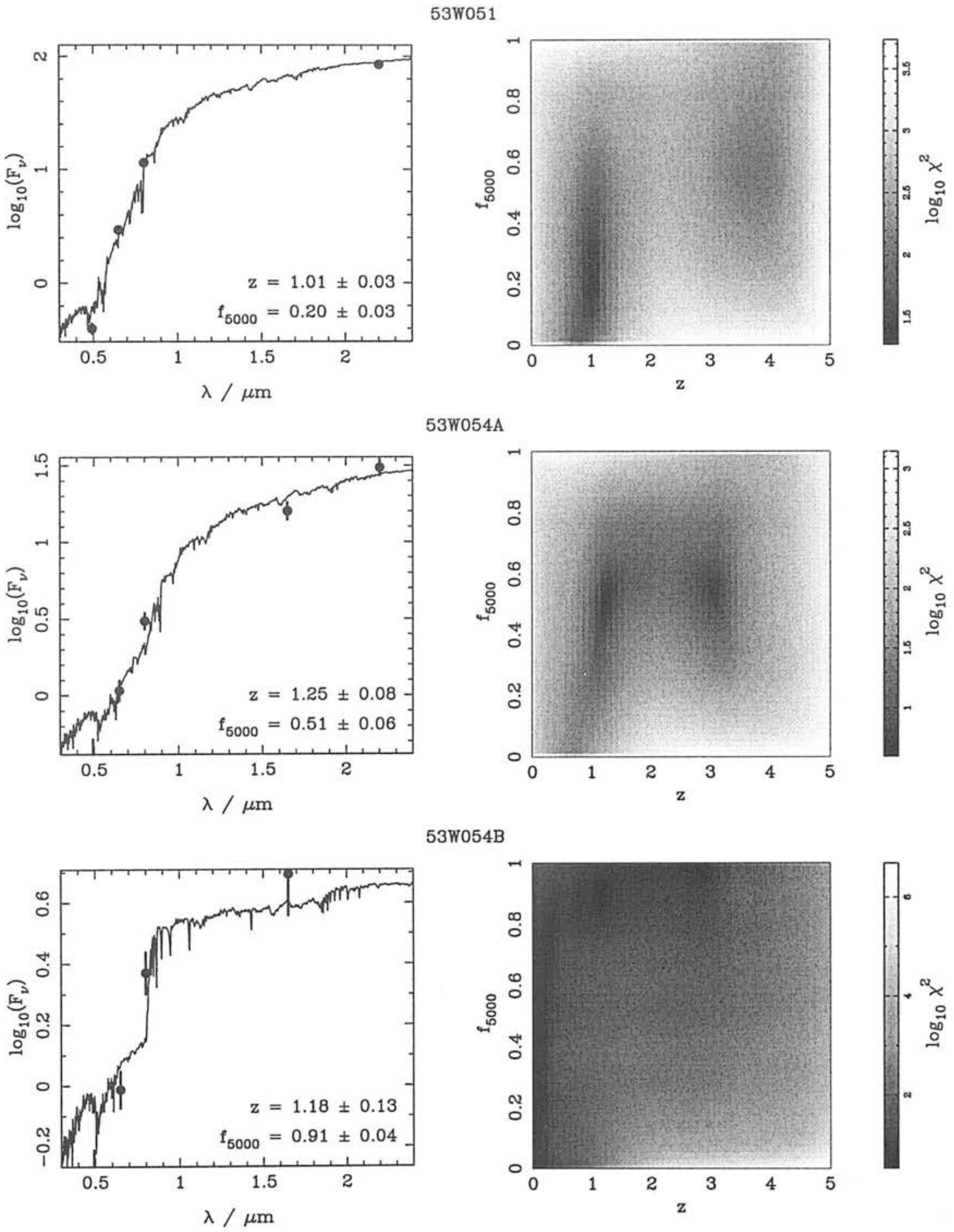

53W051

53W054A

53W054B

Figure 4.8 *Continued.*

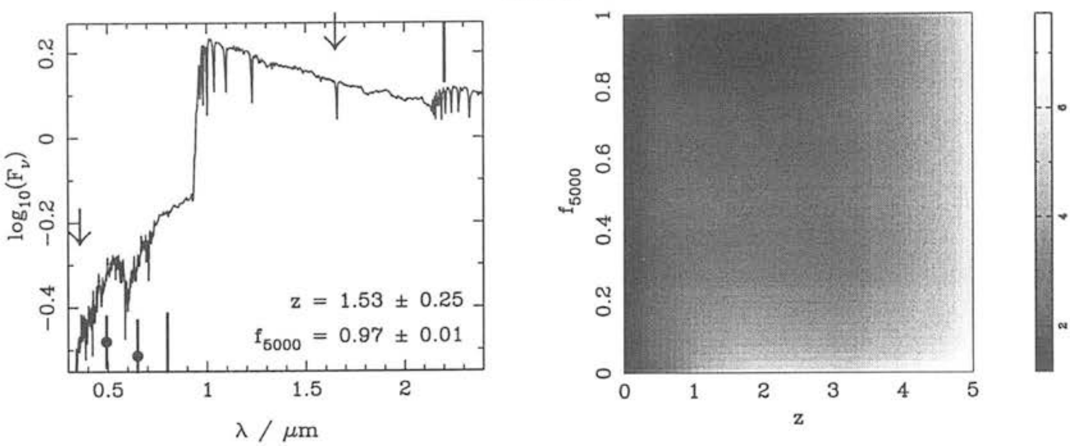
53W057

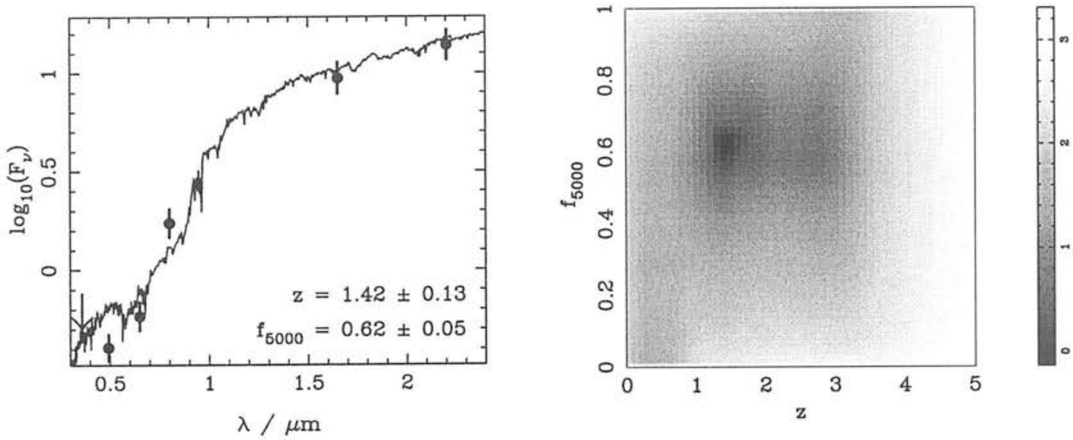
53W059

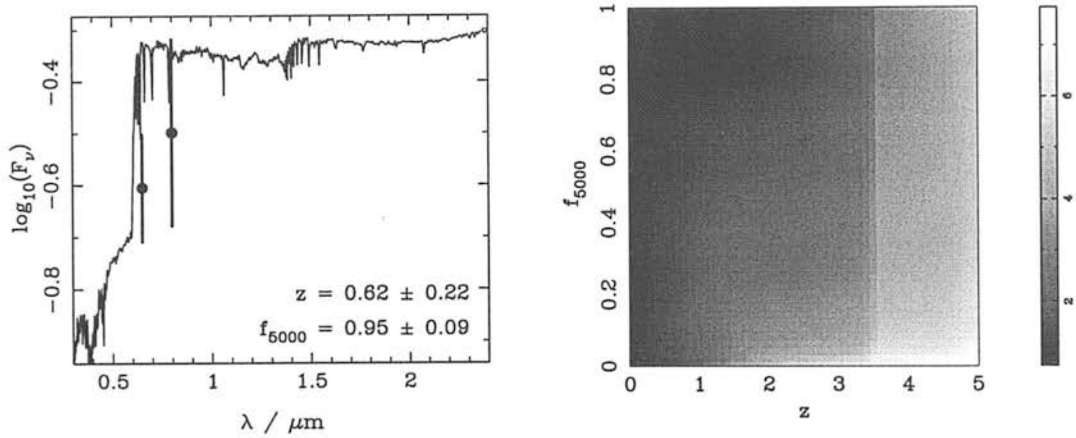
53W060

Figure 4.8 *Continued.*

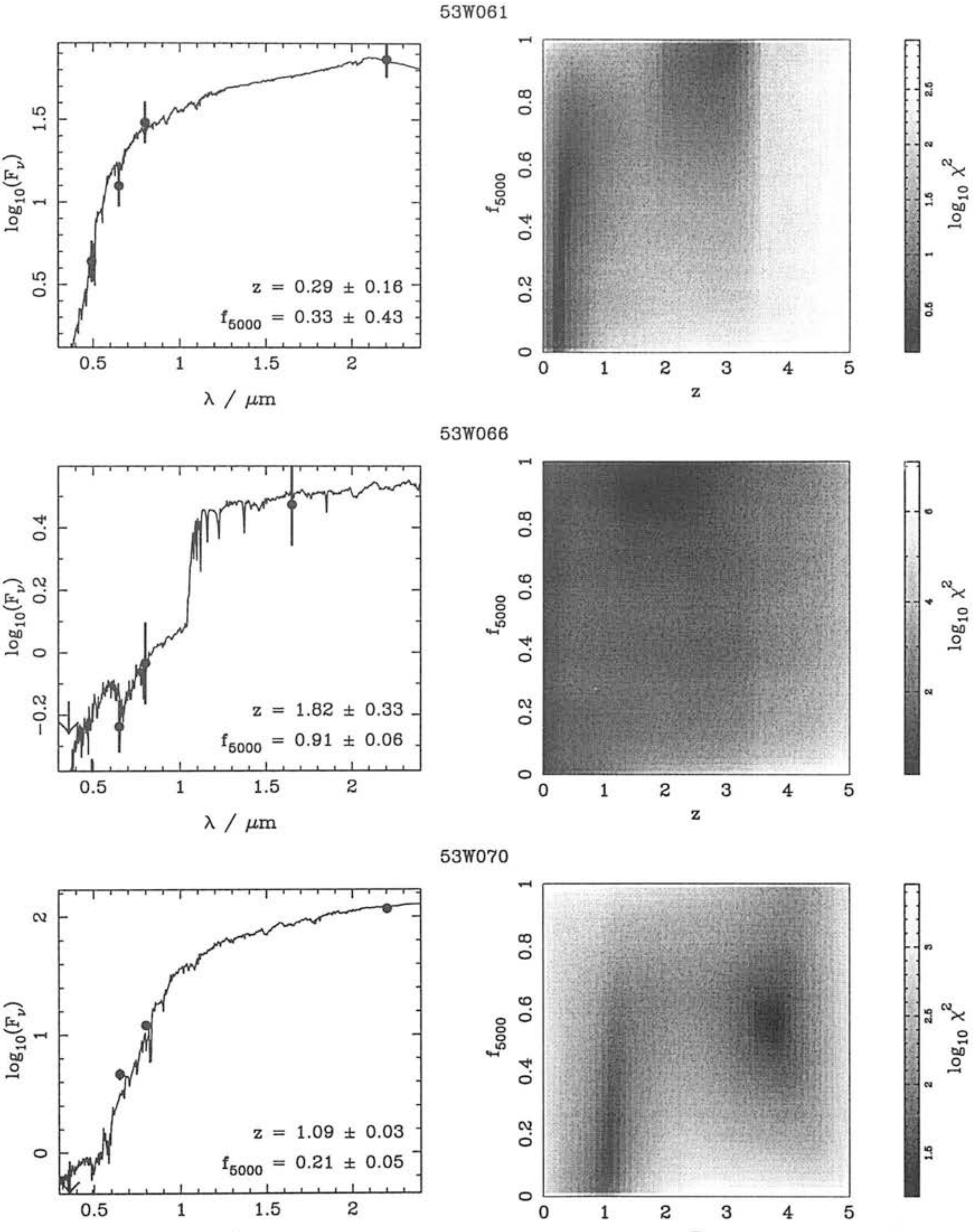

Figure 4.8 *Continued.*

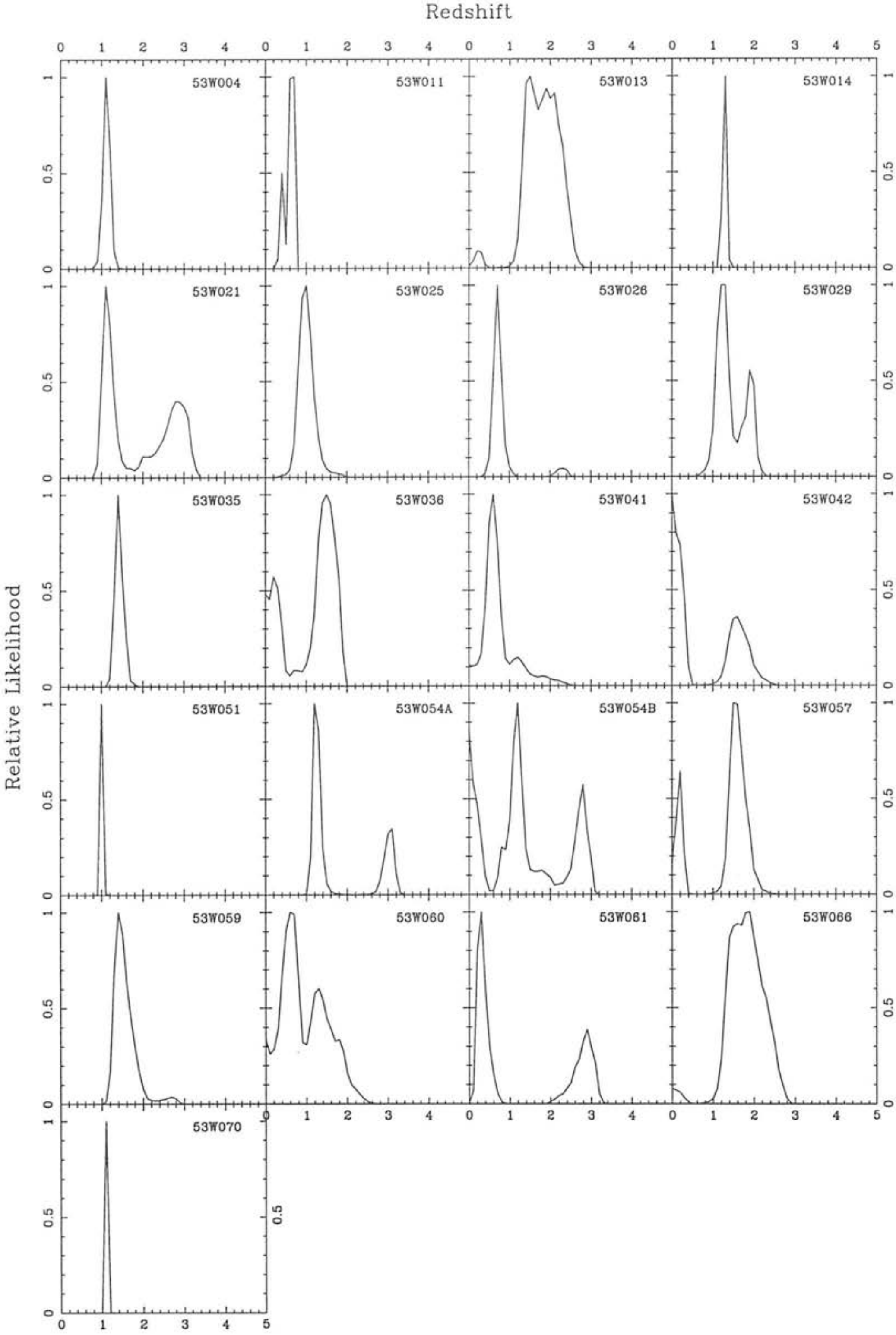

Figure 4.9 Likelihood functions for the twenty-one sources in the LBDS Hercules sample with photometric redshifts. $L(z)$ is normalized to a peak of unity.

Table 4.3 Photometric redshifts and errors for those twenty-one sources without spectroscopic redshifts. The one-sigma error on $z_{\rm phot}$ is δz, and $z_{\rm low}$, $z_{\rm high}$ are the 99% confidence limits.

Source	$z_{\rm phot}$	δz	$z_{\rm low}$	$z_{\rm high}$	Source	$z_{\rm phot}$	δz	$z_{\rm low}$	$z_{\rm high}$
53W004	1.12	0.09	0.8	1.4	53W042	0.02	0.04	0.0	2.4
53W011	0.61	0.05	0.1	0.9	53W051	1.01	0.03	0.8	1.2
53W013	1.49	0.27	0.0	2.8	53W054A	1.25	0.08	1.0	3.3
53W014	1.28	0.06	1.1	1.5	53W054B	1.18	0.13	0.0	3.1
53W021	1.12	0.13	0.8	3.4	53W057	1.53	0.25	0.0	2.2
53W025	0.97	0.17	0.5	1.6	53W059	1.42	0.13	1.1	2.8
53W026	0.70	0.10	0.4	2.5	53W060	0.62	0.22	0.0	2.4
53W029	1.23	0.15	0.7	2.3	53W061	0.29	0.16	0.0	3.3
53W035	1.41	0.14	1.1	1.8	53W066	1.82	0.33	0.0	2.8
53W036	1.50	0.28	0.0	2.0	53W070	1.09	0.03	0.9	1.3
53W041	0.59	0.15	0.0	2.3					

changed from the full sample. The low-z distribution has a median of 0.53 and for the high-z case it is 1.09. The four unidentified sources have a total weight of 6.1 and will change the median redshifts very little if they are included — they will simply increase the high-redshift tail of each distribution.

Comparing these results with fainter radio surveys at sub-mJy and μJy flux limits, it is seen that the redshift distribution changes very little over more than two orders of magnitude in radio flux (Windhorst and Waddington 1999). In particular, radio observations of the HDF down to 9 μJy result in a very similar distribution to figures 4.10(b) and 4.11(b), with a mean redshift of ~0.8 (Richards et al. 1998).

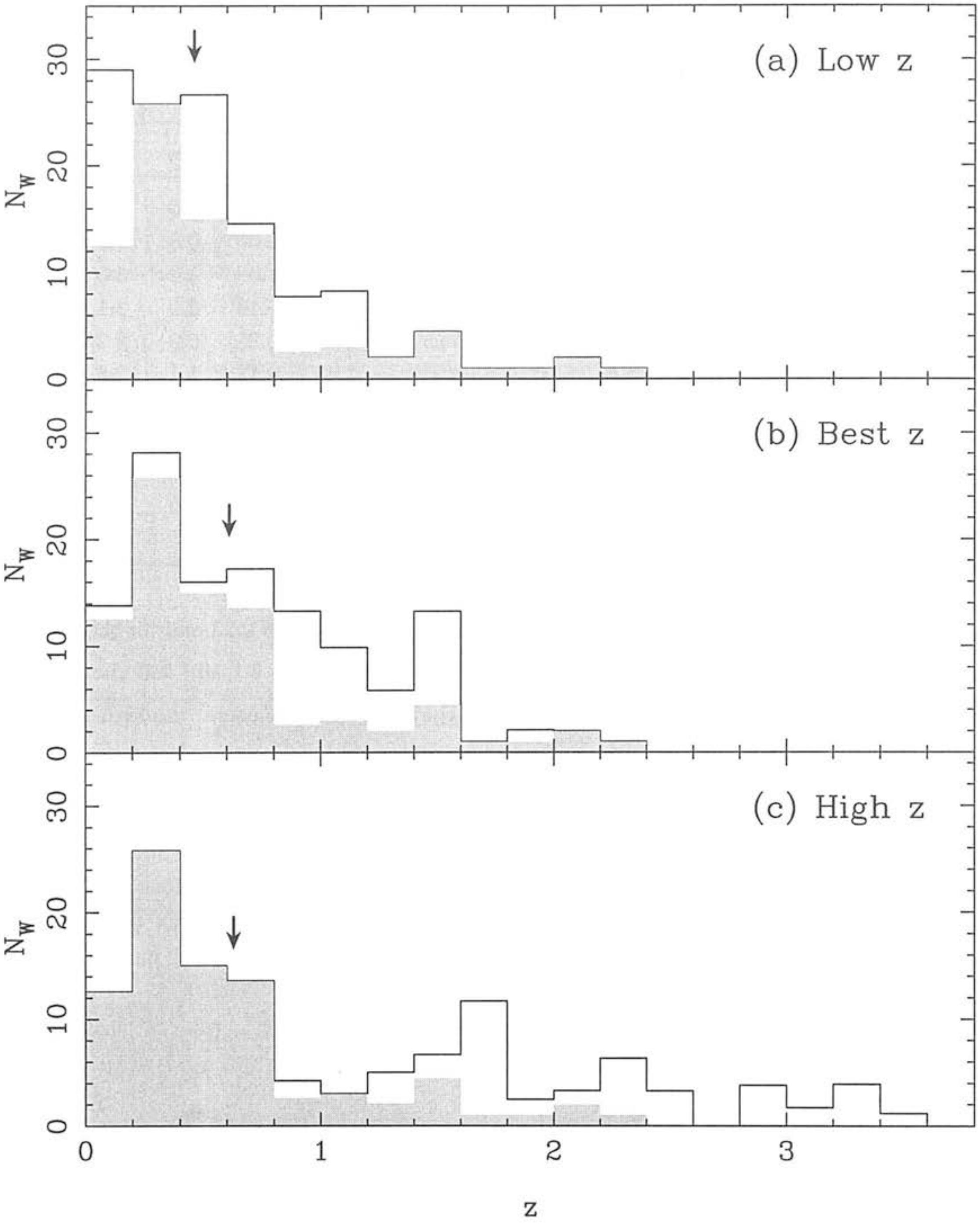

Figure 4.10 Redshifts of sources in the LBDS Hercules sample, for the three photometric redshift distributions: (a) the 99% lower confidence limits $z_{\rm low}$; (b) the best-fitting redshifts $z_{\rm phot}$; and (c) the 99% upper confidence limits $z_{\rm high}$. Filled histograms are the sources with spectroscopic redshifts, outlined histograms are the sources with photometric redshifts. An arrow denotes the median redshift of each distribution. Note that the ordinate is the weighted number of sources — i.e. corrected for primary-beam attenuation and resolution bias.

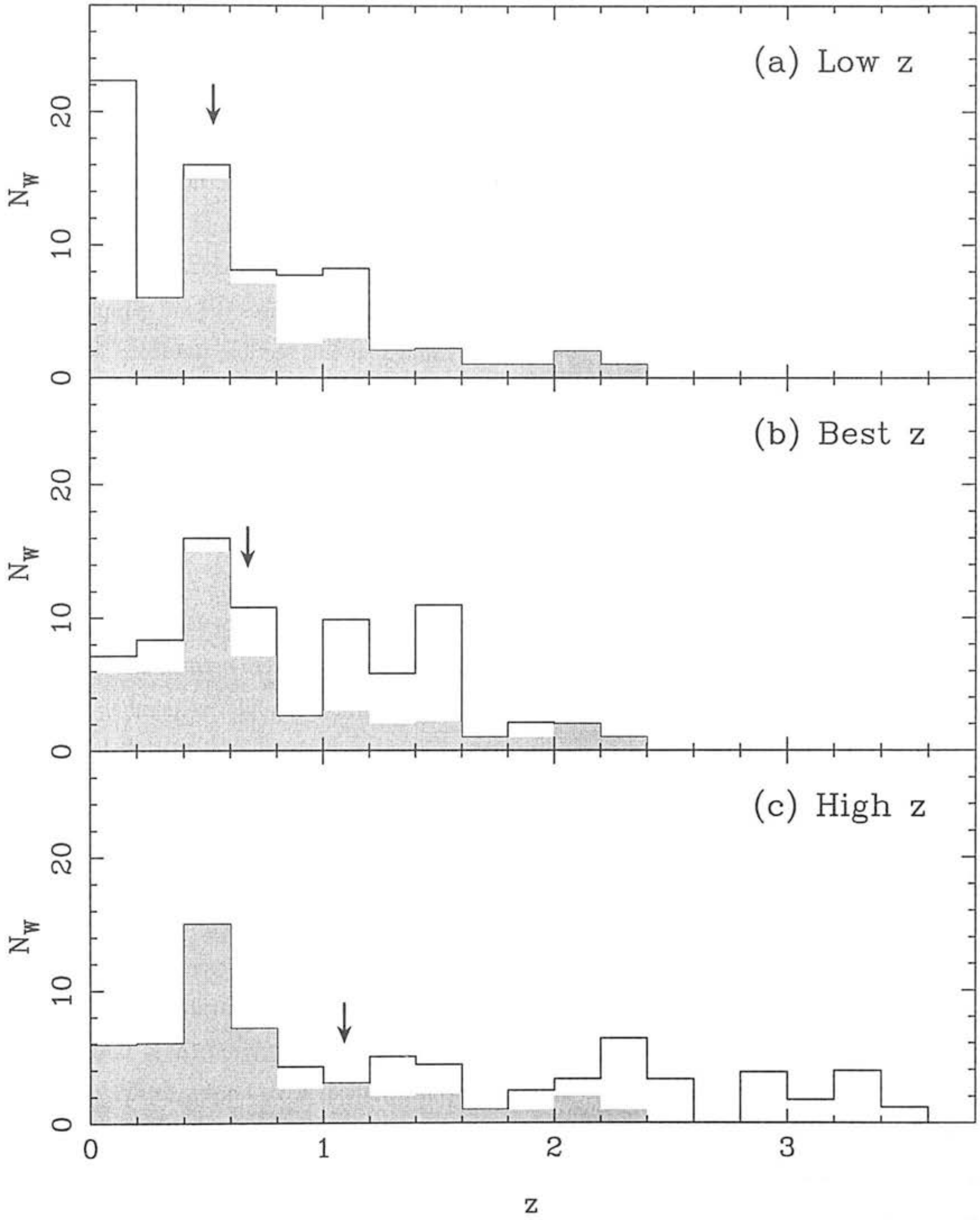

Figure 4.11 Redshifts of sources in the 2-mJy Hercules sample, for the three photometric redshift distributions. See figure 4.10 for full caption.

4.4 The LBDS radio luminosity function and the redshift cut-off

The previous section detailed the photometric redshift estimates that have been used to "complete" the redshift content of the LBDS Hercules sample. The sample is now in a position to be used to investigate the radio luminosity function in some detail, and in particular to examine the evidence for a redshift cut-off in the radio population. As was discussed in chapter 2, the large weights of the nine sources with $1 \leq S_{1.4} < 2$ mJy causes the full sample to be biassed towards these low signal-to-noise objects. Throughout this section, therefore, only the 64 sources in the 2-mJy sample will be considered. A cosmology of $H_0 = 50$ km s^{-1} Mpc^{-1}, $\Omega_0 = 1$ and $\Lambda = 0$ will be used for consistency with DP90.

4.4.1 Comparison with the RLF models of Dunlop and Peacock (1990)

Two approaches have been used in order to compare the predictions of Dunlop and Peacock (1990) with the Hercules data. First, the luminosity functions were used to calculate the expected redshift distribution in the Hercules field, in the form of cumulative number counts. Second, the space density of sources in the sample was calculated as a function of radio luminosity and redshift, to compare directly with the models. This second method has the advantage that the luminosity dependence can be investigated directly, but with only 64 sources in the sample (of which four have no optical counterpart) the sampling and statistics are quite poor. The first method allows more robust conclusions to be drawn, but at the expense of losing the luminosity information.

Dunlop and Peacock (1990) divided their data according to spectral index, and calculated model RLFs for the steep-spectrum ($\alpha \geq 0.5$) and flat-spectrum ($\alpha < 0.5$) populations separately. For their complete samples, spectral indices were known for all sources. However, the data from the fainter samples were generally restricted to source counts, with no spectral index information available. To separate the faint number counts into steep- and flat-spectrum sources, they approximated the flat-spectrum contribution by a model, $\mathrm{d}n_{\mathrm{flat}}/\mathrm{d}S = 45\, S^{-2.5} \exp[-(\ln S)^2/8]$ Jy^{-1} sr^{-1}, which was then subtracted off the data to give the steep-spectrum counts. These number counts were incorporated into the respective RLF models of the two populations.

It rapidly became apparent that the number of steep-spectrum sources in the Hercules data was significantly lower than the models predicted, and conversely there were more flat-spectrum sources in the data than in the models. The predicted *total* number of sources (steep plus flat) agreed with the data, as it should, thus demonstrating that the spectral index separation used by DP90 was incorrect. In particular, their model for $\mathrm{d}n_{\mathrm{flat}}/\mathrm{d}S$ predicts that there should be 5–10 flat-spectrum sources in the 2-mJy sample, where there are in fact 31 of them (after applying the weights for incompleteness). Indeed, the ratio of steep-spectrum to flat-spectrum sources is the same in both the PSR and 2-mJy Hercules samples, at $2:1$.

Two methods of dealing with this inconsistency between the data and models were considered. First, the flat-spectrum and steep-spectrum models could each be scaled so that they predicted the observed number of sources in the 2-mJy sample. The problem with this method is that the fraction of flat-spectrum sources in the models is a function of flux density, and thus a complicated function of redshift and luminosity (the variables in the model). Simply scaling the model by a constant would not correct for this in any reasonable manner.

The second method, and the one that will be adopted, is to remove the distinction between flat-spectrum and steep-spectrum sources altogether. The data will be considered as a single population, and the models will simply be added together. Mathematically, this is possible as the RLF models are essentially just the number of sources observed in the survey, which can of course be summed. Physically, this is justified by the work of several authors. One of the main conclusions of DP90 was that both populations behave very similarly and may therefore come from a single population. Padovani and Urry (1992) demonstrated that steep- and flat-spectrum radio quasars and FR-II radio galaxies were consistent with being the same physical objects, viewed at different angles and with a range of relativistic beaming parameters (see also Urry and Padovani 1995). Thus the remainder of the chapter will consider a single radio luminosity function for sources of all spectral indices.

The cumulative number counts are calculated for each of the RLFs: five free-form models, PLE and LDE. The number of sources at redshifts less than z is:

$$N(<z) = \int_0^z \left[\int_{\log P_1}^{28.0} \rho(P,z) \cdot \mathrm{d}P \right] \cdot \left(\frac{\mathrm{d}V}{\mathrm{d}z} \right) \mathrm{d}z \qquad [4.14]$$

where P_1 is the luminosity of a source at redshift z whose flux density would be equal to the detection limit of $S_{2.7} = 1.2$ mJy. The projected flux density limit at 2.7 GHz is derived from the flux density limit of the survey at 1.4 GHz ($S_{1.4} = 2$ mJy) using the median spectral index of sources in the sample $\langle\alpha\rangle = 0.79$. P_1 is calculated from $S_{2.7}$ using equation [1.6]. Equation [4.14] is evaluated numerically in steps of $\Delta \log_{10} P = 0.025$ and $\Delta z = 0.01$. The volume element is $\mathrm{d}V \simeq \Delta V = \Psi \cdot (V(z+\Delta z) - V(z))$, where the volume of the universe (in $\mathrm{Mpc}^3\ \mathrm{sr}^{-1}$) out to redshift z is $V(z)$, given by equation [1.9], and $\Psi = 3.78 \times 10^{-4}$ sr (1.22 sq. deg.) is the solid angle of the radio sample. The observed cumulative redshift distribution is computed by summing the weights of the sources from $z = 0$ to the redshift of

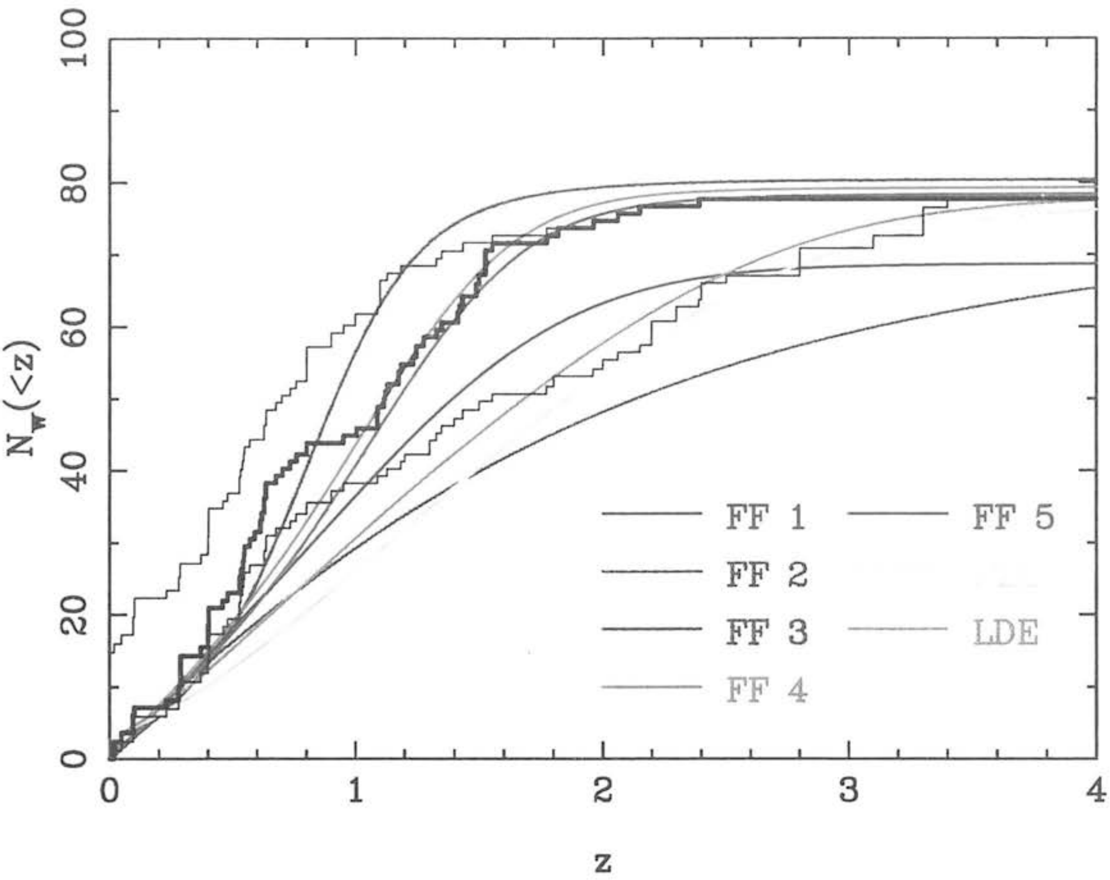

Figure 4.12 The cumulative redshift distribution of all sources in the 2-mJy Hercules sample. N_W is the *weighted* number of sources with redshifts less than z. The bold histogram is computed from the best redshift distribution, the lighter histograms correspond to the low and high redshift distributions. Coloured lines are the luminosity functions of Dunlop and Peacock (1990): free-form (FF) models 1–5, pure luminosity evolution (PLE) and luminosity/density evolution (LDE). A cosmology of $\Omega_0 = 1$ and $H_0 = 50$ km s^{-1} Mpc^{-1} is assumed.

each source in turn. The results are presented in figure 4.12.

The first comment to make about this figure, is that five of the models correctly predict the total number of sources in the sample to within 5%. The weighted number of sources is 83.7, of which 6.1 are unidentified and do not appear in the figure, and the models predict $N_{\rm total} \simeq 79$. The other two models (FF-1 and FF-2) converge to $N_{\rm total} \simeq 73$ by $z = 8$. All the models fit the data at low redshifts $z \lesssim 0.4$, where they were relatively well-constrained by the local RLF. It can be seen that the second free-form model (FF-2) fails to fit the data at all higher redshifts $z \gtrsim 0.4$. The first of the free-form models (FF-1) approximately follows the high-z redshift distribution at all redshifts, however the total number of sources is ~10% too few.

The pure luminosity evolution (PLE) and luminosity/density evolution (LDE) models produce an excellent match to the high-z distribution at $z \gtrsim 2$, although there are many more sources at $z \simeq 0.6$ than predicted. This agreement between the PLE and LDE models and the data at large redshifts was also found by Dunlop (1997), using an earlier version of this sample without the photometric redshifts. The PLE and LDE models, however, are only consistent with the *high-z* distribution and fail to fit the most likely redshift distribution at any $z \gtrsim 0.4$. Recall that the high-z distribution assumes that all the sources are simultaneously at the 99% upper confidence limits of their possible photometric redshifts, and thus represents the *most extreme* limit of the distribution.

The third of the free-form models (FF-3) is in reasonable agreement with the best-z and high-z data for redshifts $z \lesssim 0.6$–0.8, but then continues to rise steeply. It predicts that there should be only five sources at $z > 1.5$, somewhat inconsistent with the data — there are already 10 sources with spectroscopic redshifts greater than this. The best fits to the data are free-form models FF-4 and FF-5. At $z < 0.4$ and $z > 1$ they match the best-z distribution flawlessly. The only disagreement occurs over the range $0.4 \lesssim z \lesssim 1$, where the observed redshift distribution rises more rapidly than the models. This rise is due to two sharp peaks in the observed redshift distribution — there are 7 sources at $z = 0.54 \pm 0.02$ and 5 sources at $z = 0.62 \pm 0.01$ in the 2-mJy sample (plus another source at $z = 0.61$ with $S_{1.4} = 1.7$ mJy). These two peaks are evidence for (super-) clusters along the line-of-sight, statistical variations that the RLF models could not possibly predict. With these exceptions, the FF-4 and FF-5 models of DP90 fit the observed redshift data well, and FF-3 is also approximately consistent within the uncertainties of the photometric redshifts.

Figure 4.12 has shown which models correctly predict the overall redshift dependence of the radio luminosity function, but it says nothing about the luminosity dependence. To investigate this, an attempt has been made to calculate the observed RLF to compare directly with the models. This was done by redshift and luminosity binning of the 2-mJy Hercules data. The luminosity of each source at 2.7 GHz was calculated from the total flux (at 1.4 GHz) and the 21–50 cm spectral index, using equation [1.6]. Eight luminosity bins were used, from $\log_{10} P_{2.7} = 20$ to 28 in steps of $\Delta \log_{10} P_{2.7} = 1$. Five redshift bins were used, from $z = 0$ to 4, centered on $z = 0.1$, 0.5, 1.1, 1.7 and 3.0. These redshifts approximately correspond to ages of 90%, 50%, 33%, 25% and 10% of the current age of the universe (for Einstein-de Sitter cosmology, $(1 + z) \propto t^{-2/3}$). The bins were chosen so as to contain enough sources to be statistically useful, whilst being sufficiently narrow to resolve the redshift dependence of the RLF. The weighted number of sources in each (P, z) bin was calculated, and converted to a space density $\rho_{\rm obs}$ by dividing by the volume of the bin.

Given the relatively large width of the redshift bins, an additional weight had to be applied to each source to correct for the fact that the weakest sources could not have been detected at all redshifts within the bin. Specifically, each weight was modified thus: $w_i \rightarrow w_i \cdot V/V_{lim}$, where $V = V(z_2) - V(z_1)$ is the volume of universe enclosed by the bin extending from redshift z_1 to z_2, and $V_{lim} = V(z_{lim}) - V(z_1)$ is the volume enclosed from z_1 to the redshift z_{lim} at which the source would fall below the radio flux-density limit of the sample. $V(z)$ is given by equation [1.9]. If $z_{lim} \geq z_2$ then the source could have been detected at any redshift within the bin and w_i was not changed. The assumption required to make this correction is simply that $\rho(P, z)$ does not change significantly within $z_1 \rightarrow z_2$. It is seen that the data points from successive bins are consistent within 1–2-σ, verifying that this is a reasonable assumption. Errors are assigned to each bin on the basis of Poisson counting statistics, i.e. $\delta\rho = \sqrt{\sum w_i}$, applied to the raw weights *before* correcting for the flux-density-limit bias. Given that the sample is almost completely identified in the optical (to 93%), it is not necessary to similarly weight the sources with respect to the optical detection limits.

The binned luminosity function is presented in figure 4.13 for each of the three photometric redshift distributions. The rather poor sampling of the (P, z) parameter space is apparent from these diagrams, not only from the size of the error bars but also the absence of data at high luminosities (the small area of the sample is insufficient to contain large numbers of the luminous, and thus rare, sources). Whilst the small number of sources is the weakness of this method of analysing the data, its strength lies in the accuracy with which the luminosities are known, given the nearly complete redshift information for the sample.

The first point to note is that the observed RLF does not change significantly with redshift, in those luminosity bins that are sampled at more than one redshift. This is particularly apparent at $\log_{10} P = 24.5$, where the RLF is unchanged, within the 1-σ errors, over $z \simeq 0.4$–1.8. This is somewhat due to the small number of objects in each bin and hence the relatively large error bars, but the low-power ($< P^*$) RLF clearly evolves more slowly than at the higher luminosities studied by DP90.

Looking in detail at the luminosity function derived from the best photometric redshift estimates (figure 4.13b), there is good evidence for a luminosity-dependent turnover in the RLF at $z \simeq 1.1$–1.7. At $\log_{10} P = 23.5$, the density of sources at $z = 0.8$–1.4 is lower by an order of magnitude than it is in the lower redshift bin. There is no evidence for a turnover in the next luminosity bin, but at $\log_{10} P = 25.5$ the RLF at $z \simeq 1.8$ is significantly lower than at $z \simeq 1.1$ and is marginally lower still in the highest redshift bin. The turnover or "cut-off" redshift appears to increase with increasing 2.7 GHz radio luminosity.

This trend is even more dramatic when the low-z photometric redshifts are considered

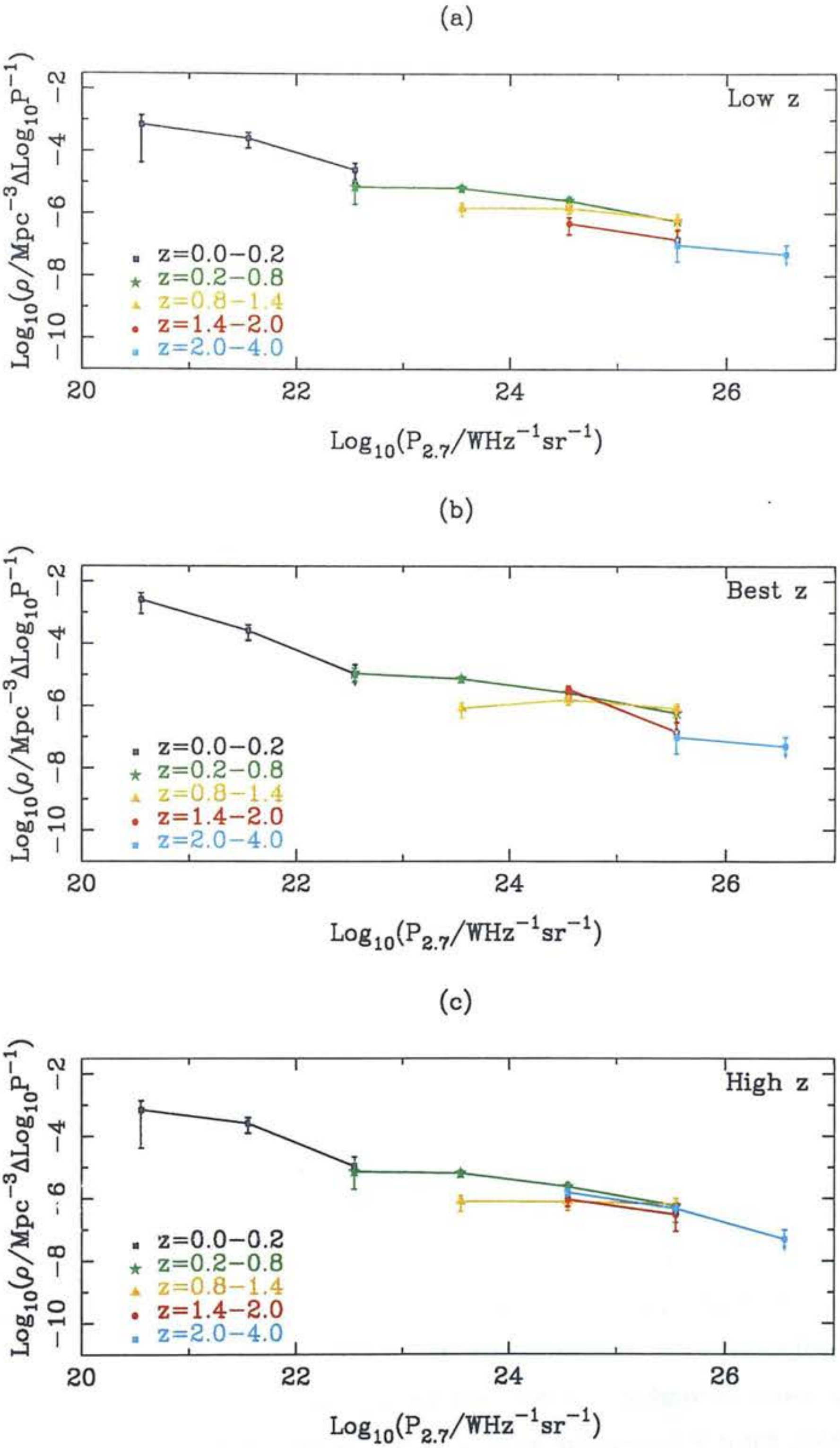

Figure 4.13 The observed radio luminosity function for the 2-mJy Hercules sample, for each of the three photometric redshift distributions: (a) low-z; (b) best-z; and (c) high-z.

(figure 4.13a). At a redshift of 0.5, the $\log_{10} P = 22.5$ sources have a lower density than at $z \simeq 0.1$. The $\log_{10} P = 23.5$ sources turnover around $z \simeq 0.8$, the $\log_{10} P = 24.5$ sources perhaps nearer to $z \simeq 1.1$ and the $\log_{10} P = 25$–26 objects begin to decline in density at $z \sim 1.5$. The high-z redshift distribution produces an RLF that behaves somewhat differently. At luminosities below $\log_{10} P = 24$ it is essentially the same as the best-z case, but at higher luminosities the RLF does not change significantly within the error bars. There is no convincing evidence for a cut-off at these luminosities.

The binned luminosity function ρ_{obs} is compared with the model RLFs of Dunlop and Peacock (1990) in figures 4.14–4.16, for each of the three redshift distributions. The preceding discussion concentrated upon the properties of the observed luminosity function and its dependence on the photometric redshifts, without reference to the models. It is now appropriate to investigate how the models compare with the data, and to try to determine whether the fits seen in the cumulative counts of figure 4.12 are consitent with the *luminosity* dependence of the models as well as the redshift dependence.

The first point to be noted is that all the models are consistent with the data in the first redshift bin $0 \leq z < 0.2$, as was seen in the cumulative distribution. The PLE and LDE models show how the non-evolving low-power component (ρ_l) fits the data particularly well at $\log_{10} P \simeq 20 - 22$. Each model will now be considered in turn and compared with the data derived using the three photometric redshift distributions.

The first free-form model (FF-1) fits the data in the two highest redshift bins of the best-z data, but at redshifts of $z = 0.2$–1.4 it fails — it predicts too many lower luminosity sources and too few higher luminosity ones. Although this model fits the high-z cumulative counts reasonably well, it is seen from figure 4.16(a) that the luminosity dependence of the model is very different from the data.

It was seen above that the second of the free-form models (FF-2) gave the worst fit to the cumulative counts. The cause of this is seen in figures 4.14(b) and 4.16(b) — the model predicts too few $\log_{10} P = 24$–26 sources at $z \simeq 0.5$; although at $z \gtrsim 0.8$ and $\log_{10} P > 24$ the model fits the high-z data very well.

Once again, too many lower luminosity and too few higher luminosity sources are predicted by free-form model FF-3, at intermediate redshifts ($0.2 < z < 1.4$). The high-redshift behaviour of this model is roughly consistent with the low-z distribution of photometric redshifts (figure 4.15c), but it is inconsistent with the high-z distribution at all $z \gtrsim 0.2$.

Recall that RLF models FF-4 and FF-5 produced the best fit to the cumulative number counts, being in excellent agreement with the best-z data for $z \gtrsim 1$. Figures 4.14(d)–(e) show the luminosity dependence of these models. At $z \simeq 0.5$ the models predict too many

(a) FF 1

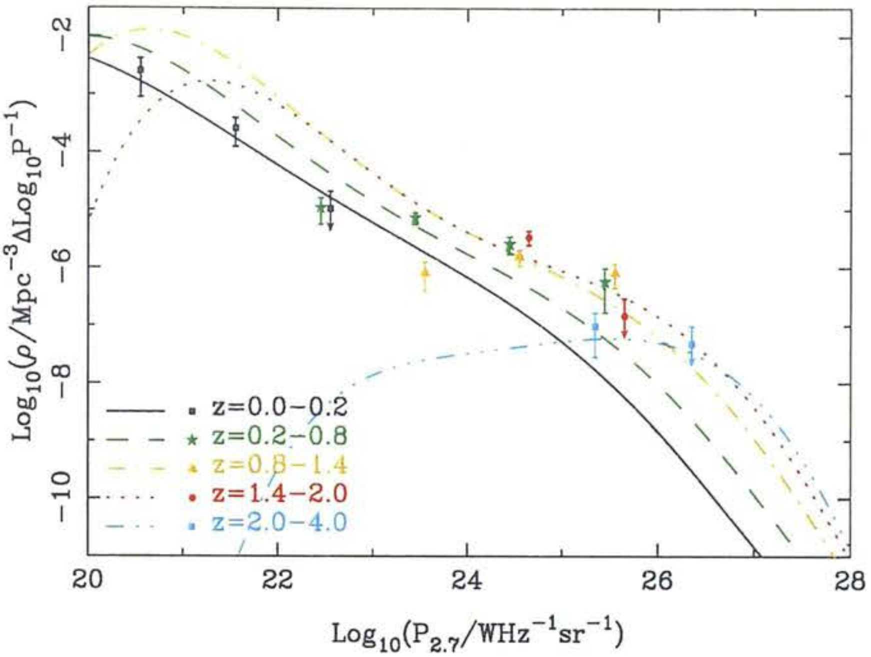

(b) FF 2

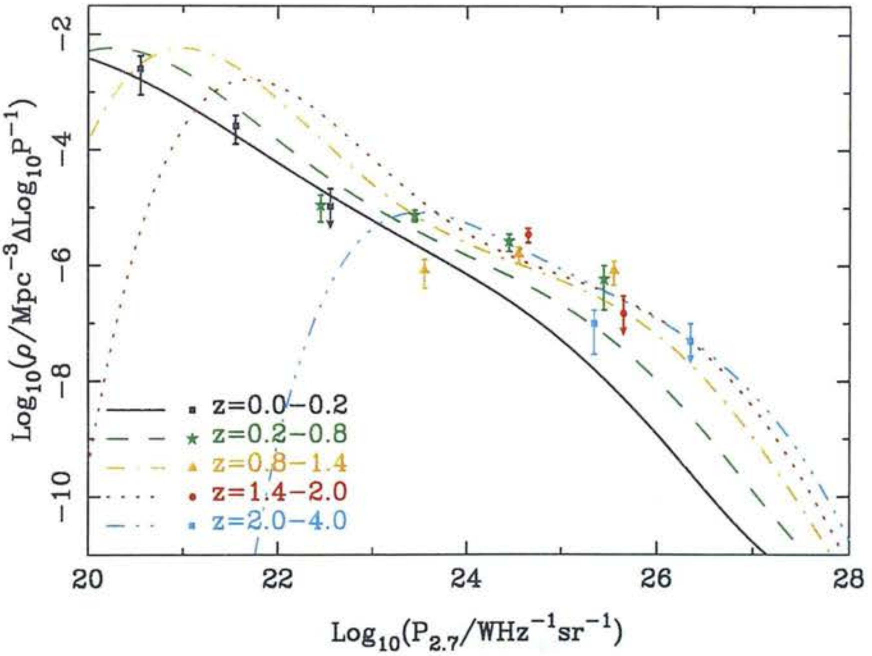

Figure 4.14 The observed radio luminosity function (data points), using the best-z photometric redshifts, compared with the models of Dunlop and Peacock (1990). The models are plotted for redshifts $z = 0.1$, 0.5, 1.1, 1.7 and 3.0 corresponding to the center of each bin. The data is offset along the abscissa to add clarity to the points.

(c) FF 3

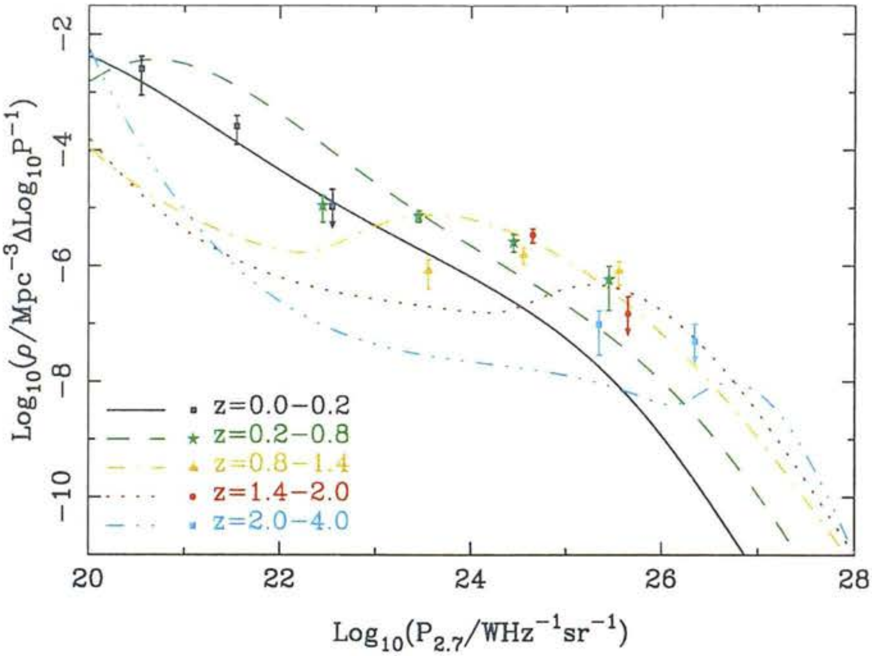

(d) FF 4

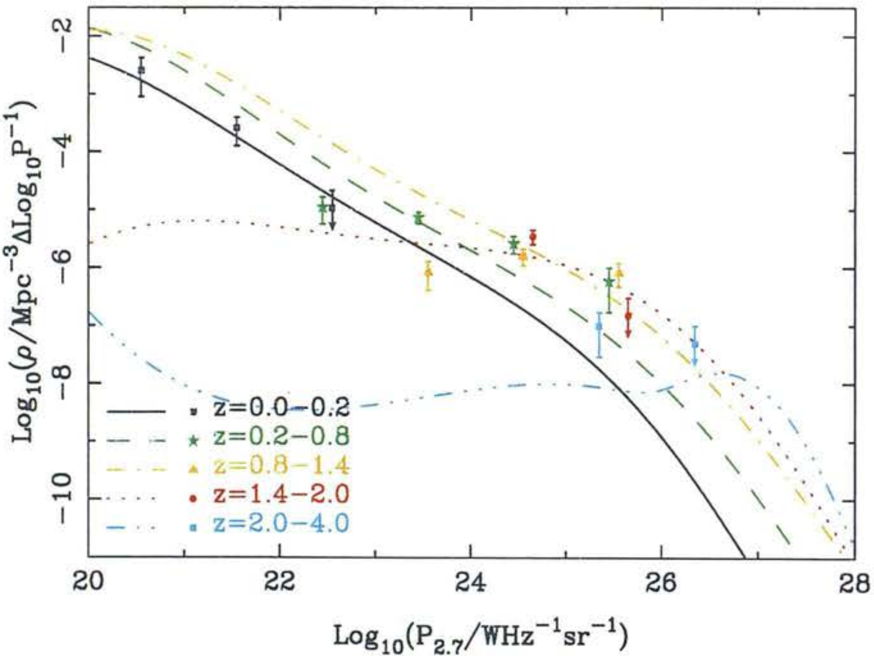

Figure 4.14 *Continued.*

(e) FF 5

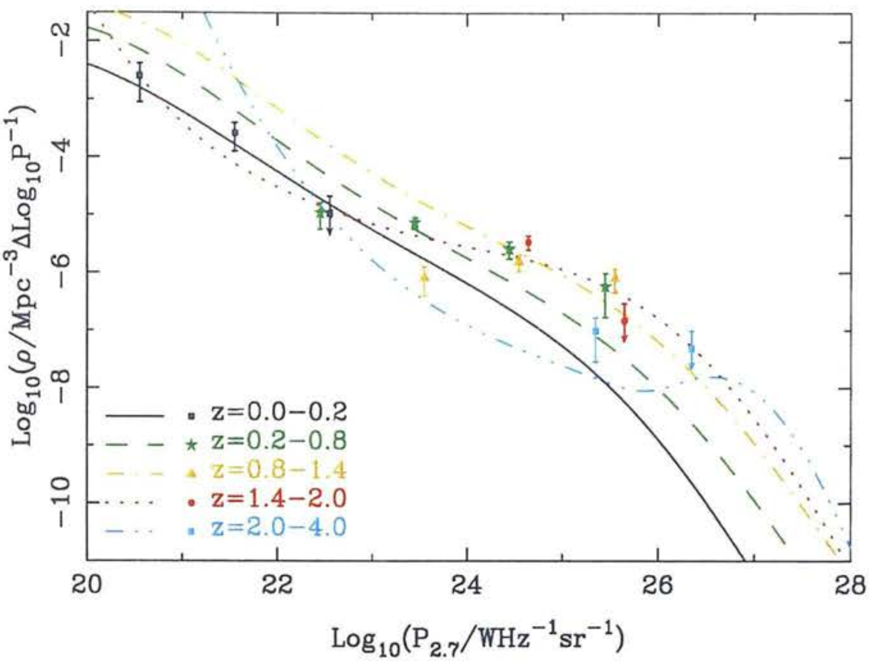

(f) PLE

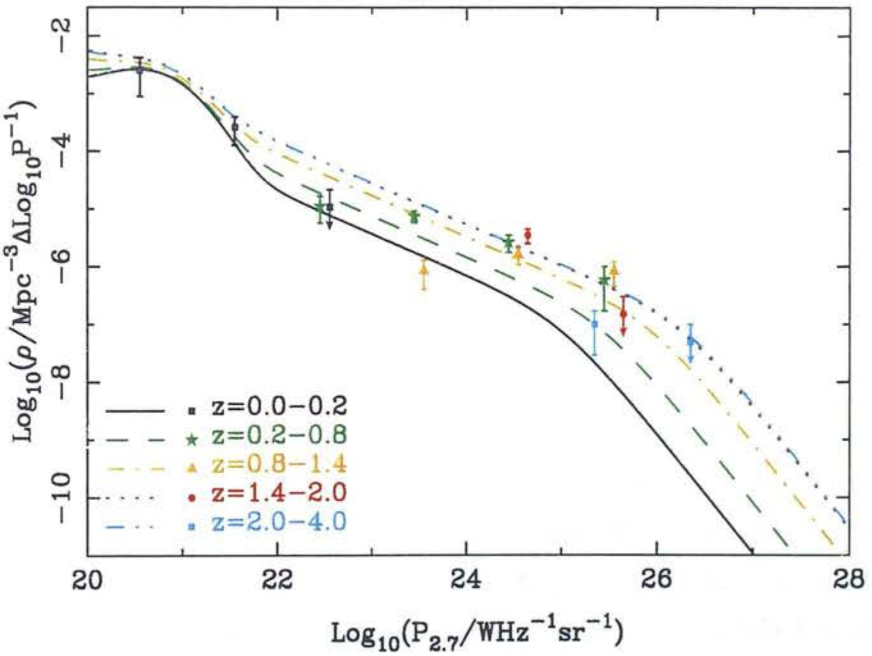

Figure 4.14 *Continued.*

(g) LDE

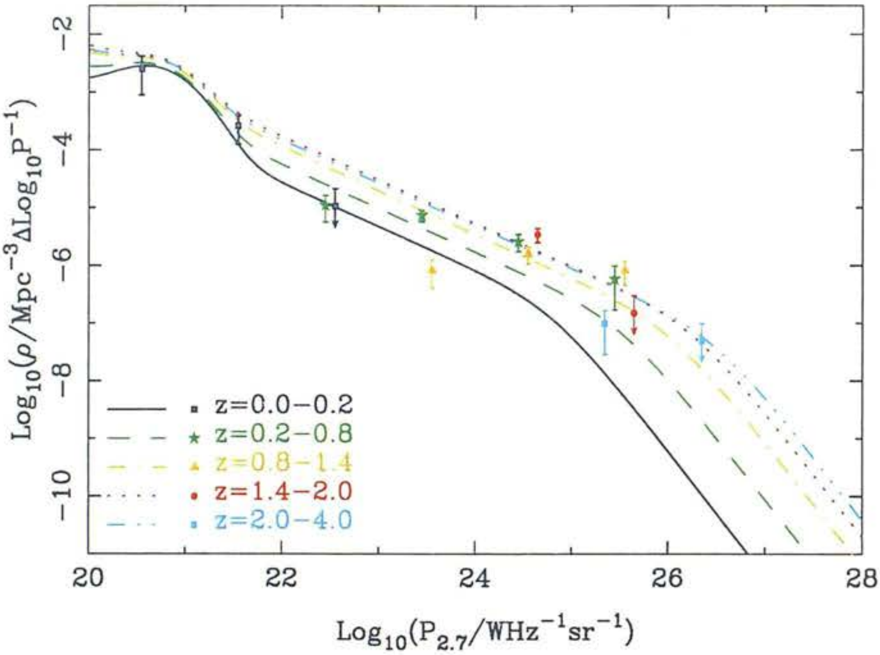

Figure 4.14 *Continued.*

$\log_{10} P = 22.5$ sources and too few at $\log_{10} P = 24$–26. In the next redshift bin ($0.8 \leq z < 1.4$), there are once again too many lower luminosity sources predicted, but the $\log_{10} P = 24$–26 sources match the data. In the two highest redshift bins, the models and data are in reasonable agreement. Thus it is seen that although the redshift dependence of these two models matches the data, the accuracy of the luminosity dependence is not nearly as good.

Finally, the two parametric models (PLE and LDE) are shown in figures 4.14–4.16(f)–(g). Recall that these two models provided a good fit to the high-z cumulative redshift distribution at $z \gtrsim 2$. The luminosity dependence of these two models in the two highest redshift bins (z = 1.4–2 and 2–4) fits the high-z data relatively well. At lower redshifts, the same behaviour is observed as in the other models — too many lower power sources and not enough higher power sources are predicted. The models do not fit the low-z or best-z distributions.

To summarize, *none* of the luminosity functions of Dunlop and Peacock (1990) provide a good description of both the redshift and luminosity dependence of the data at milli-Jansky levels. In general, the models predict too many $\log_{10} P = 22$–24 sources and too few $\log_{10} P = 24$–26 sources at intermediate redshifts ($0.2 \lesssim z \lesssim 1.4$). If there are two (super-) clusters in the Hercules field, this would explain why the models predict too few sources at $z \sim 0.6$, but it would not explain why there are fewer sources observed at lower luminosities, nor why there

(a) FF 1

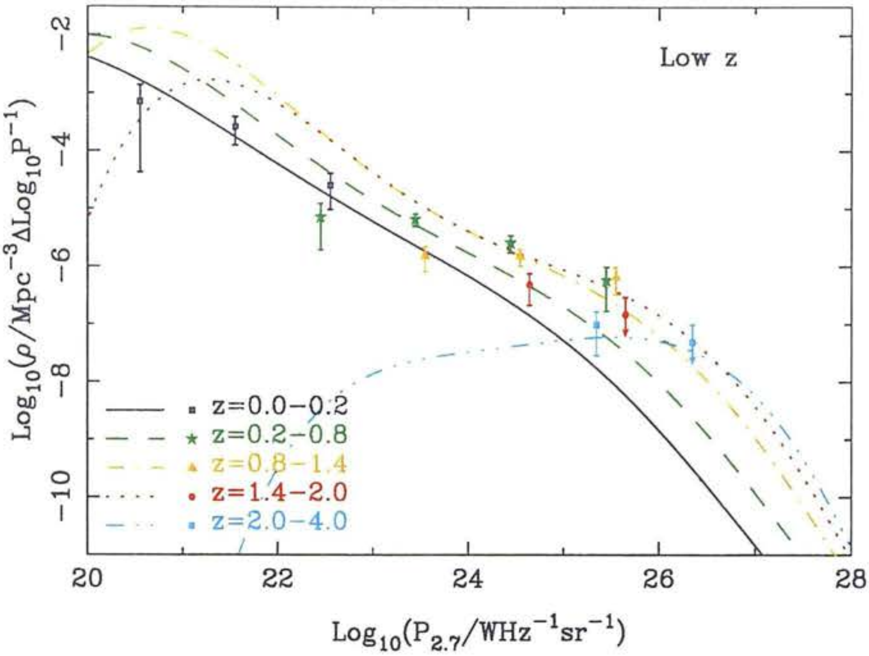

(b) FF 2

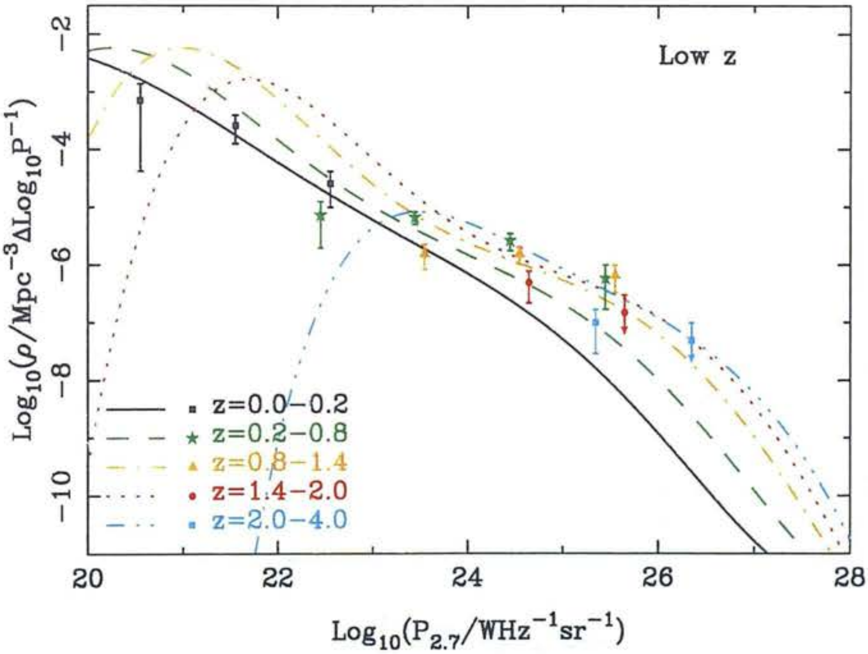

Figure 4.15 The observed radio luminosity function (data points), using the low-*z* photometric redshifts, compared with the models of Dunlop and Peacock (1990). See caption to figure 4.14.

(c) FF 3

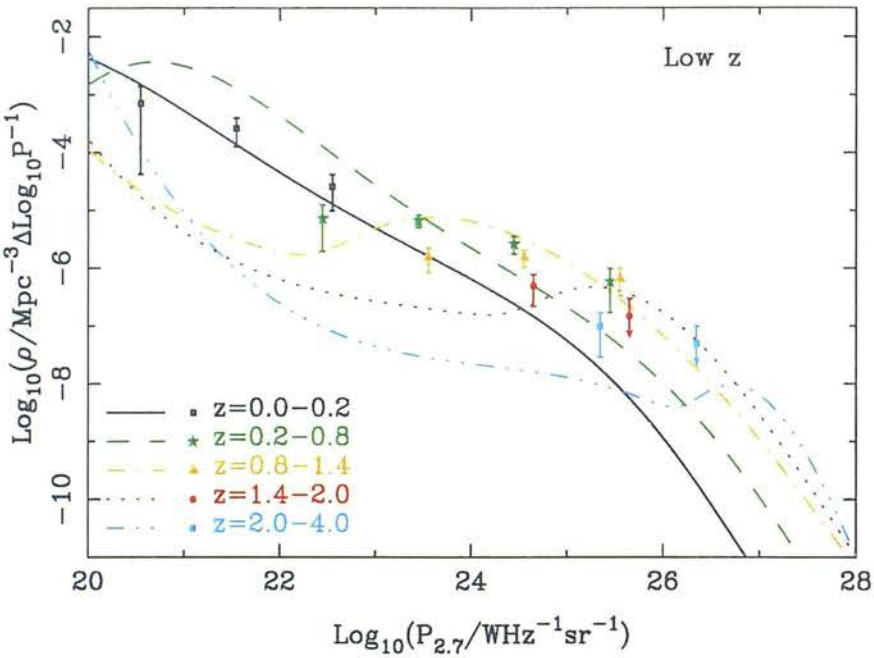

(d) FF 4

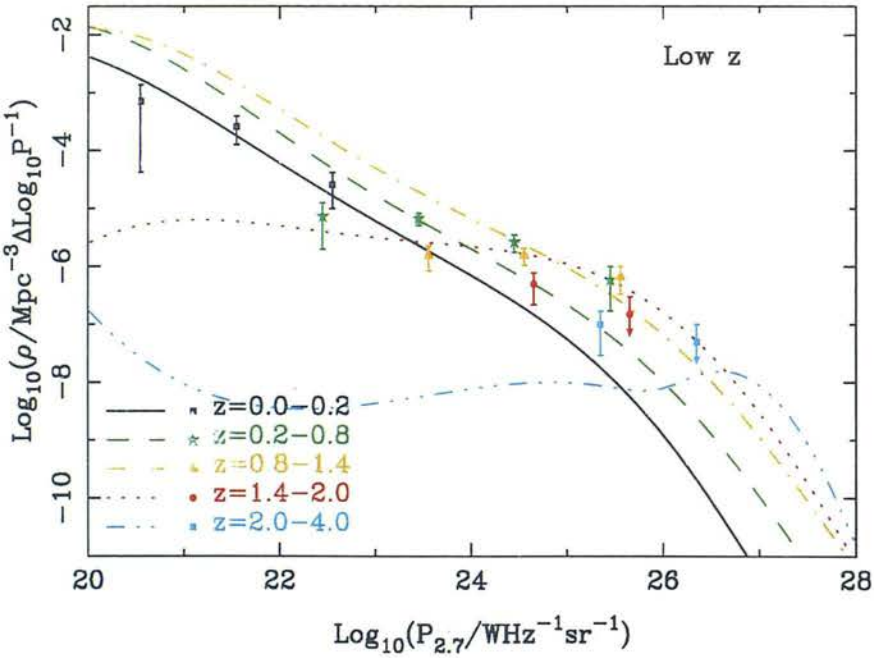

Figure 4.15 *Continued.*

(e) FF 5

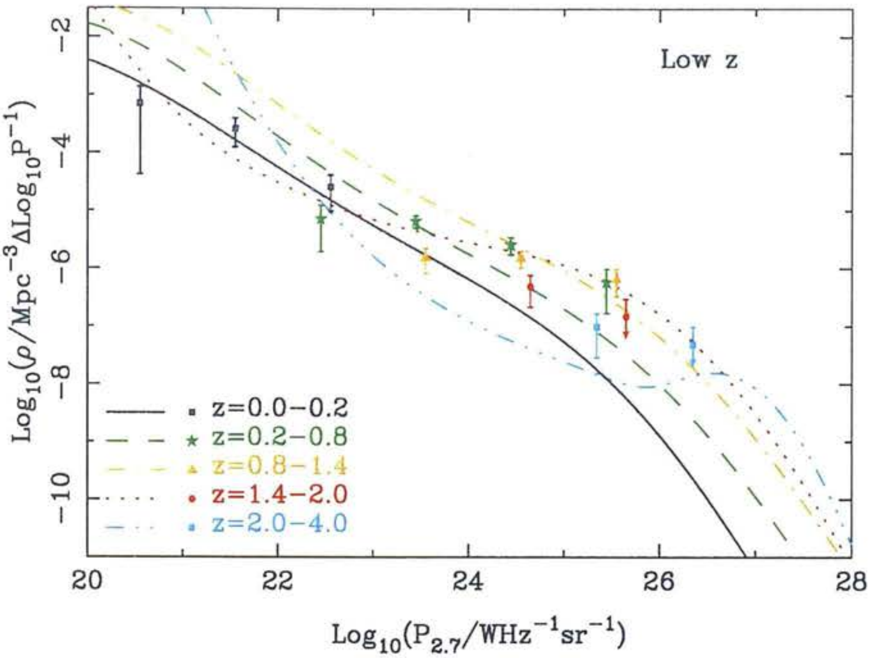

(f) PLE

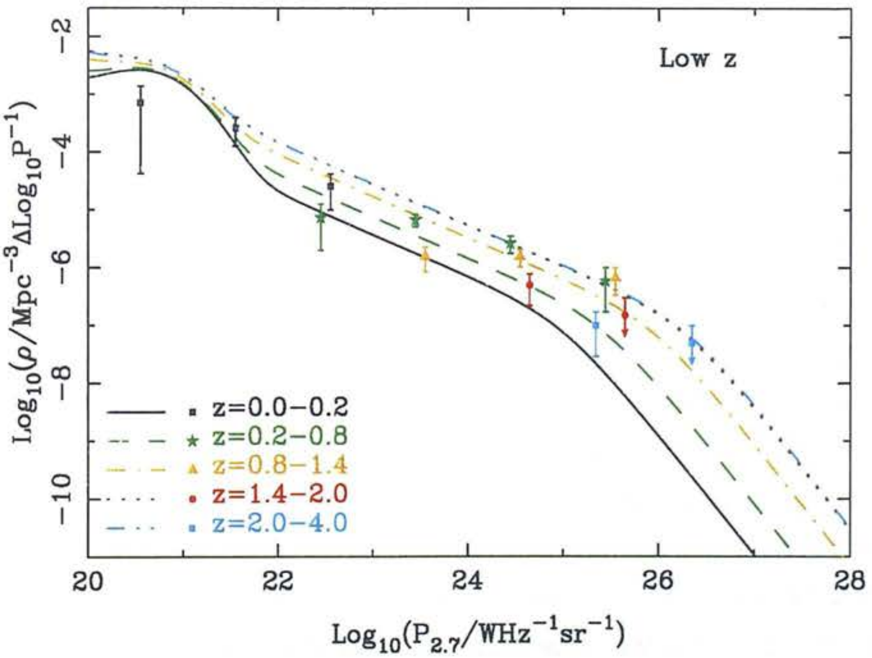

Figure 4.15 *Continued.*

(g) LDE

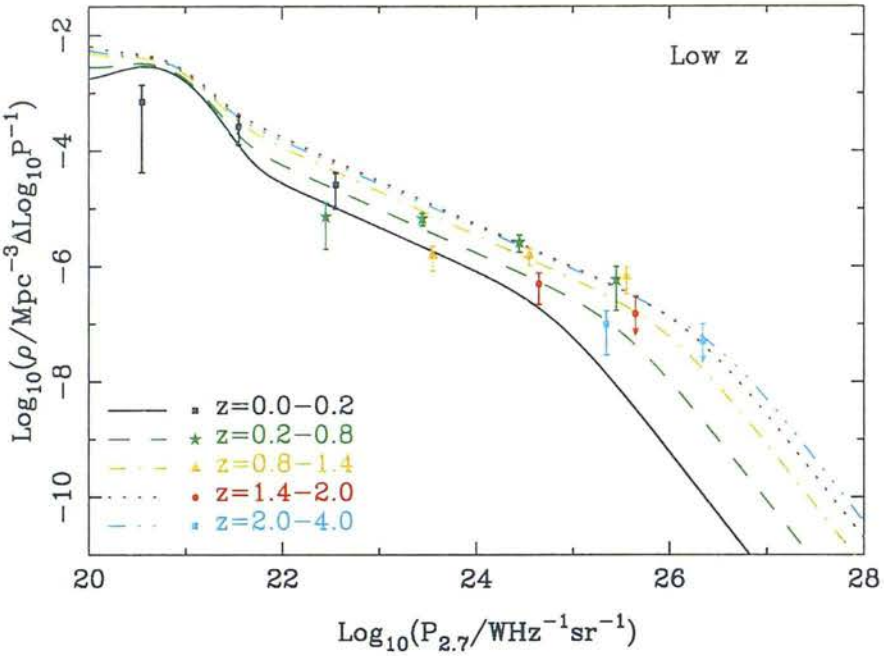

Figure 4.15 *Continued.*

are more observed at $z \sim 1.1$.

4.4.2 The redshift cut-off revisited

Having found that none of the RLF models fit both the P- and z-dependence of the data, is there still any evidence to confirm or refute the existence of a decline in the RLF at high redshift? The most reliable comparisons between the new data and the models should be made in that region of the P–z plane where the two datasets (DP90 and LBDS Hercules) overlap. The DP90 sample is restricted to $24 < \log_{10} P < 28$ with the majority of sources having $\log_{10} P \gtrsim 25$. The LBDS Hercules sample essentially covers the luminosity range $20 < \log_{10} P < 26$ (with a single source at $\log_{10} P \sim 26.5$). Thus, not only is there very little overlap between the two samples, but there is only a *single* source in the LBDS Hercules sample that coincides with the luminosity range over which the model RLFs show an unambiguous cut-off ($26 < \log_{10} P < 28$). Even the upper limits to the high-luminosity sources in Hercules are too high to place any useful restriction on the majority of the RLFs — the 3.78×10^{-4} sr area of the two Hercules fields is simply too small to contain a statistically useful number of high-z sources. The high-P/high-z area of the P–z plane which is crucial for determining the robustness of the redshift cut-off is too sparsely covered by the LBDS Hercules sample to be

(a) FF 1

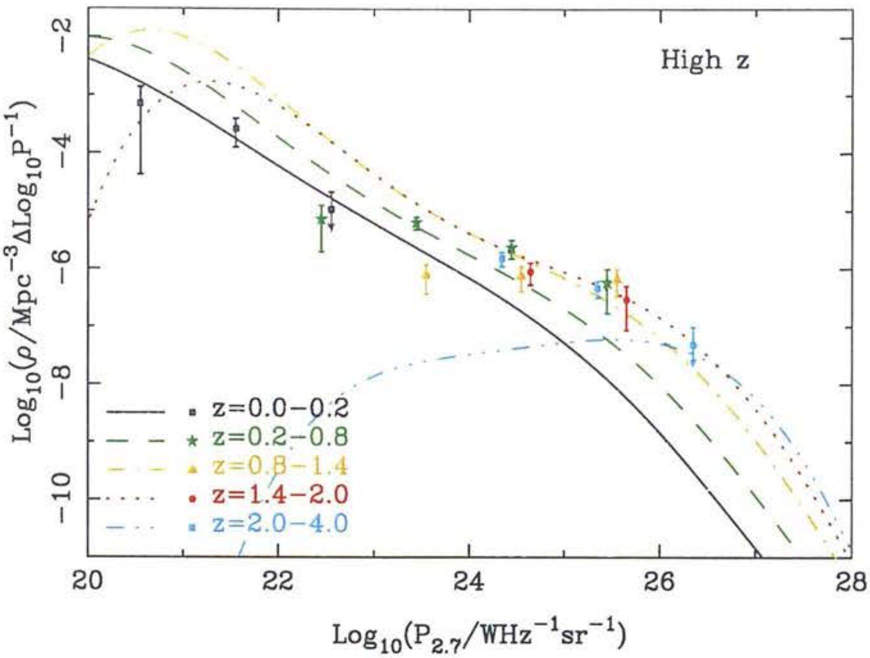

(b) FF 2

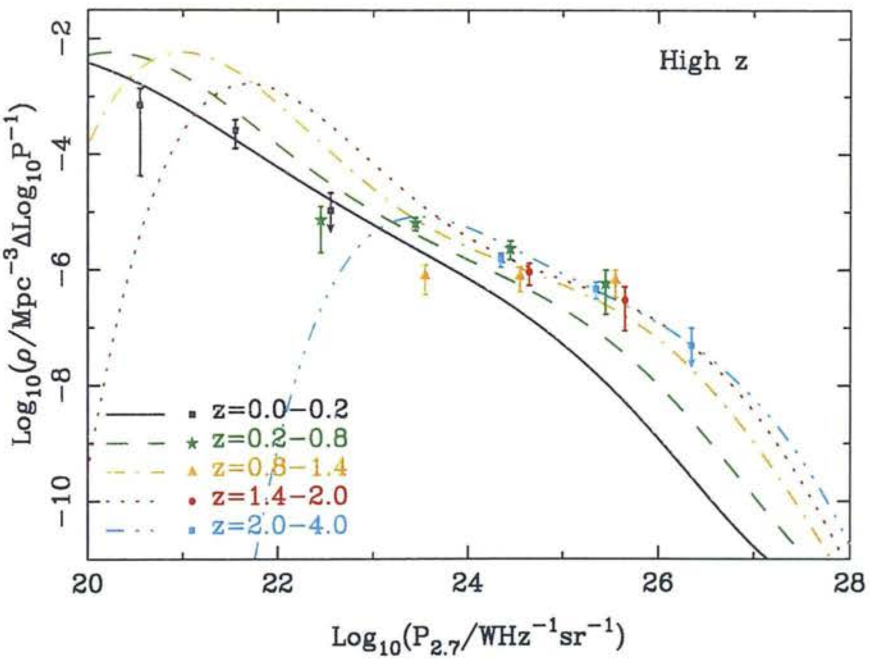

Figure 4.16 The observed radio luminosity function (data points), using the high-z photometric redshifts, compared with the models of Dunlop and Peacock (1990). See caption to figure 4.14.

(c) FF 3

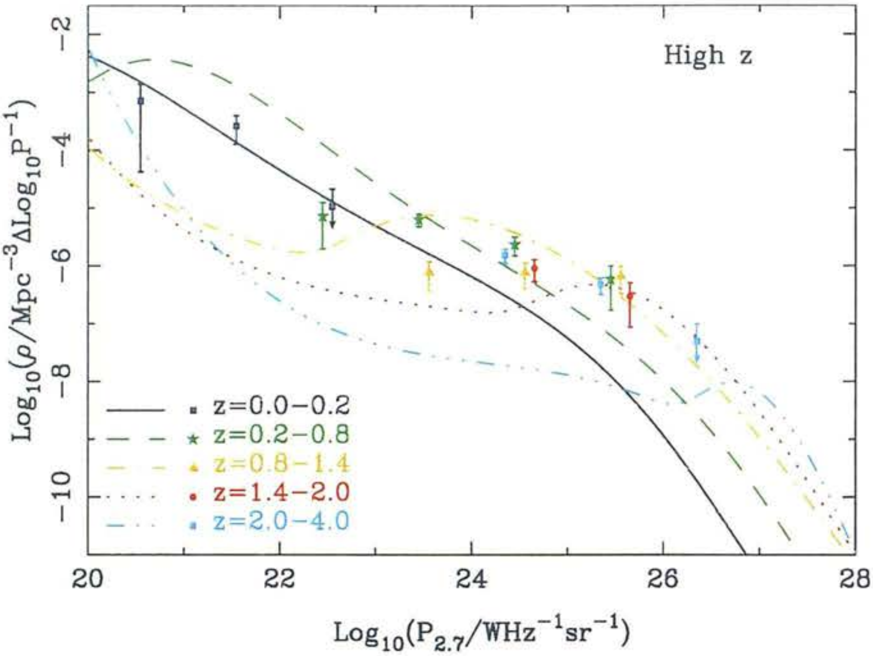

(d) FF 4

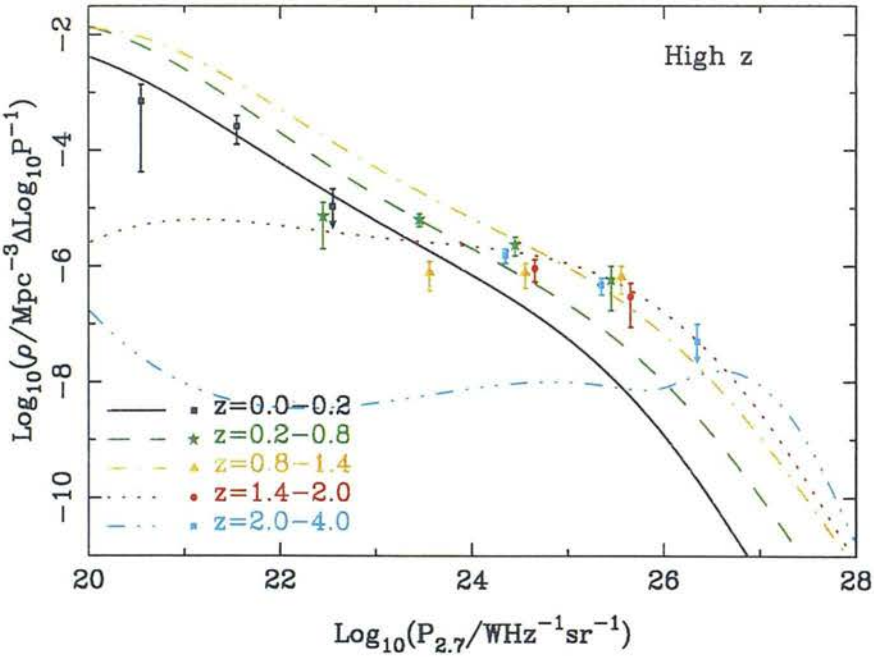

Figure 4.16 *Continued.*

(e) FF 5

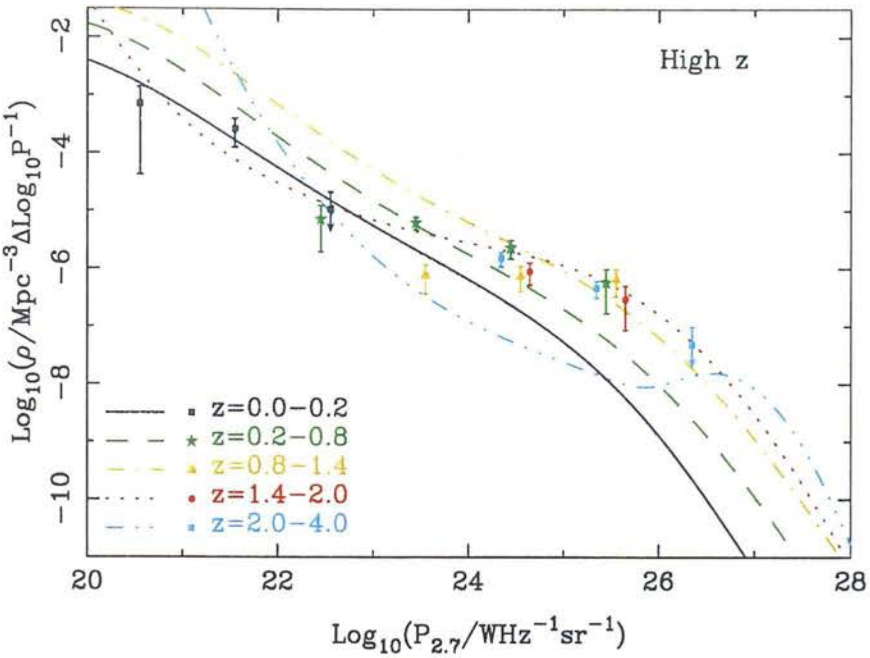

(f) PLE

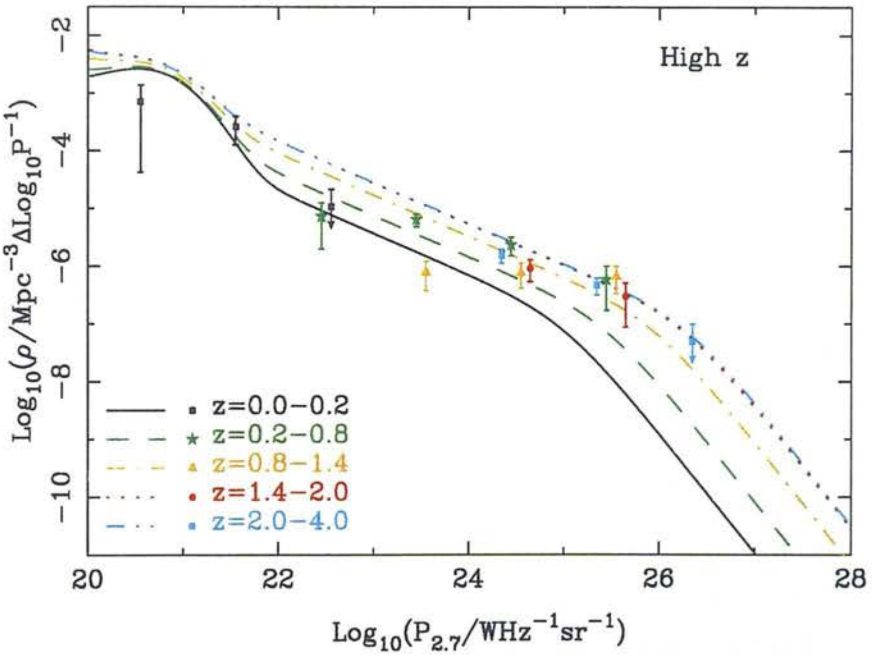

Figure 4.16 *Continued.*

(g) LDE

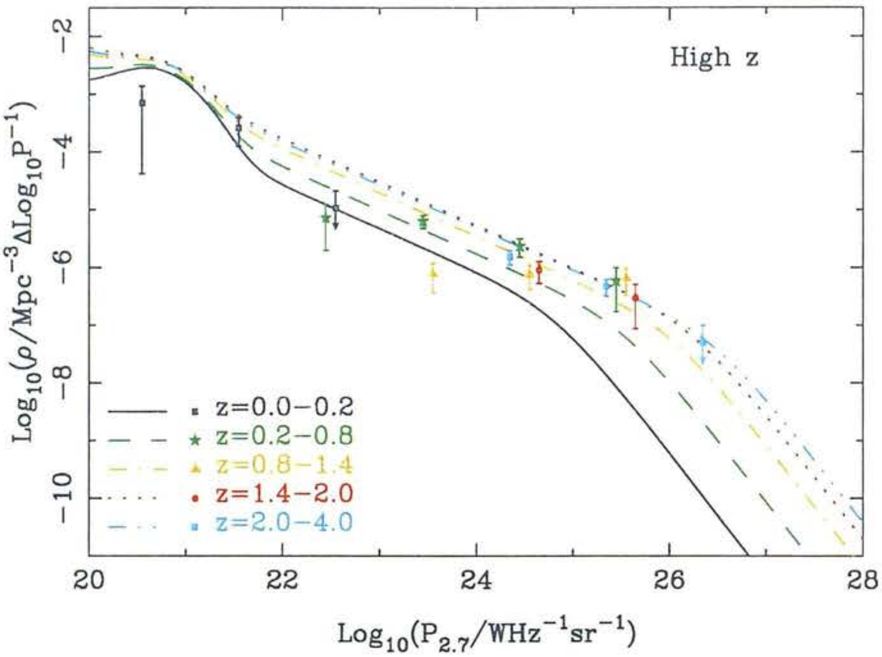

Figure 4.16 *Continued.*

of any use in directly testing the results of DP90.

If the RLF models are rejected as being a poor fit to the data, is there any evidence *within the data themselves* for a cut-off in the luminosity function? It was pointed out in the previous sub-section that there is marginal evidence that the RLF turns over at $z = 0.5$–2 and that the redshift at which this occurs is a function of the luminosity. If the redshift binning is done more coarsely such that the highest-z bin is $z = 1.5 - 3.0$, then this turnover is significant at the 2–3-sigma level at $\log_{10} P \simeq 24.5$, and marginal (< 1-σ) at $\log_{10} P \simeq 25.5$. Thus there is some evidence for a cut-off in the RLF, but at a lower redshifts than DP90 found. Qualitatively, this trend is consistent with the free-form RLF models, where the redshift at which the RLF turns over decreases with decreasing luminosity (see figure 4.3).

In order to confirm these tentative results, the P–z plane must be more fully sampled. This can be achieved from three complementary directions. First, the current 2-mJy Hercules sample can be added to the brighter complete samples used by Dunlop and Peacock (1990). This will produce a sample with virtually continuous coverage of the luminosity over eight orders of magnitude, $20 < \log_{10} P < 28$. Second, using the photometric redshift estimation technique developed in §4.3, together with the new spectroscopy results in the PSR (§3.1), the redshift content of the DP90 sample could be significantly improved. Third, although this thesis has concentrated on the two Hercules fields from the LBDS, the full survey covers ~ 4× the area of the current sample. Essentially complete optical identifications are available for the whole LBDS, although the redshift content of the other fields is poor ($\lesssim 50\%$) and the infrared data is even more limited. Nevertheless, the much larger area will contain correspondingly more $\log_{10} P = 25$–27 sources that will bridge the gap between the PSR and Hercules samples.

With these additions to the database of DP90, it will be possible to re-calculate their models with much tighter constraints at the low-luminosity end of the RLF, and test the reality of the redshift cut-off below the "break" in the luminosity function at $\log_{10} P^* = 25$.

4.5 Summary

The main results of this chapter can be summarized as follows:

- Comparison of the newest redshifts in the Parkes Selected Regions with their K–z estimates showed that at $z \gtrsim 1$, either (i) there is an increased scatter in the K–z diagram; or (ii) the PSR sources are systematically fainter at K than the 3C and 1-Jy sources.
- If (ii) is correct, these new redshifts have confirmed the existence of a decline in the RLF at high luminosities ($\log_{10} P \geq 27$).
- Photometric redshifts were derived for the twenty-one sources in the LBDS Hercules sample without spectroscopic redshifts. The estimation method that produced the best results was one in which the galaxy SEDs are represented as the sum of two model spectra with ages of 14 Gyr and 0.1 Gyr. The SEDs are fitted to the data by varying the redshift and the ratio of young to old stellar populations.
- The resulting complete redshift distribution of the 2-mJy sample has a median of $z = 0.68$, and is very similar to the distribution of μJy sources in the HDF, two orders of magnitude fainter in flux.
- The RLFs of Dunlop and Peacock (1990) do not fit the LBDS data particularly well. The models predict too many $\log_{10} P = 22$–24 sources and too few $\log_{10} P = 24$–26 sources at intermediate redshifts ($0.2 \lesssim z \lesssim 1.4$). However, the overall redshift dependence is reasonably matched by free-form models FF-4 and FF-5.
- There is a suggestion in the data that a redshift cut-off *is* required for sources with $\log_{10} P \lesssim 26$, and that the redshift at which the RLF declines is a function of luminosity. However, the small area of the LBDS Hercules sample is inadequate to conclusively confirm or refute the reality of the redshift cut-off at all luminosities.

Chapter 5

Spectral evolution of the LBDS radio galaxies

The optical and infrared Hubble diagrams for the LBDS Hercules radio sources are investigated. It is found that passive evolution of the population synthesis models of Jimenez et al. (1999) successfully traces the evolution of the bright radio galaxies, with the exception of the K-band magnitude at high redshifts. The $r-K$ colours of the galaxies are compared with the models in order to trace the evolution of the red envelope. The reddest galaxies at intermediate redshifts require a universe of age $\gtrsim 12$ Gyr in order to evolve their red colours. The two reddest galaxies in the sample are found to be ~ 4 Gyr-old at $z \simeq 1.5$, placing strong constraints on the age of the universe at high-z. For a Hubble constant of 65 km s^{-1} Mpc^{-1}, the data either require a low density, $\Omega_0 \lesssim 0.2$, or for a critical universe a cosmological constant with $\Omega_\Lambda \gtrsim 0.6$ is necessary.

5.1 Introduction

The purpose of this thesis is to study the cosmological evolution of galaxies from two directions. The first is to investigate the evolution of the radio luminosity function, particularly the high-redshift decline in the radio source population. This was the subject of the last chapter. The second aim of the thesis is to trace the evolving stellar populations of the host galaxies of these radio sources, which will be addressed in this chapter.

One of the key aims in the early studies of radio sources was the desire to observe galaxies at large redshifts, and thus at an early stage in their evolution. There are two motivations behind this. At low redshifts, luminous radio galaxies are almost exclusively giant ellipticals. Although the mechanism that triggers the powerful radio emission in some galaxies rather than others is not fully understood, it is reasonable to suppose that the same mechanism would occur throughout the universe and that radio galaxies at high redshifts are also associated with giant ellipticals. Second, by using radio selection to pick out high-redshift sources, the optical/infrared properties of the objects should be unbiassed. At high flux densities, however, this is generally not the case as the AGN can severely alter the properties of the host — e.g. via the alignment effect (McCarthy et al. 1987), or emission-line contamination of the broadband colours (Eales et al. 1993). In surveys with a lower flux density limit, less active sources can be observed and the influence of the AGN on the host galaxy is significantly reduced (Dunlop and Peacock 1993).

The 1 mJy flux limit of the Leiden-Berkeley Deep Survey is a factor of 10^3–10^4 fainter than the 1-Jansky and 3CR surveys in which AGN contamination of the host is prevalent, and $\sim$100 times fainter than the galaxies in the Parkes Selected Regions which show no alignment effect in the infrared at $z \simeq 1$ (Dunlop and Peacock 1993). Thus it is suggested that the optical/infrared properties of the LBDS host galaxies are essentially unaffected by their AGN, and that they are a fair representation of the general elliptical galaxy population out to redshifts $z \gtrsim 5$. This is not necessarily true in all cases, for example, the LBDS source 53W002 has been shown to have Lyα and CO emission aligned with the radio continuum (Windhorst et al. 1998), however this is likely to be an exceptional rather than a representative case as it is one of the most luminous galaxies in the LBDS.

It was seen in chapter 3 that the typical line emission of the LBDS sources is much weaker than for the PSR sources. Indeed, a number of the sources observed during this thesis have no emission lines at all. This is consistent with known correlations between radio luminosity and Lyα or [O II] equivalent widths, for example (McCarthy 1993). The spectra of the two $z \simeq 1.5$ LBDS sources discussed below (§5.4) also show either very weak or no line emission. Thus it is concluded that the optical and infrared observations of the LBDS Hercules radio galaxies, genuinely see the host galaxies' stellar populations at all redshifts.

The cosmological evolution of these stellar populations will be investigated as follows. In section 5.2, the optical and infrared Hubble diagrams will be presented and compared with the evolving spectral synthesis models of Jimenez et al. (1999). These models will then be applied to the colour–redshift diagrams of the sample in order to trace the red envelope of elliptical galaxies (§5.3). Finally, the results of Keck Telescope observations of two of the Hercules sources will be reviewed in section 5.4, with particular emphasis on the ages determined for these galaxies and the implications of these results for the age of the universe and the cosmological parameters H_0, Ω_0 and Λ. The main points will be summarised in §5.5.

5.2 The Hubble diagram

The Hubble diagram was introduced in chapter 1, and is a plot of apparent magnitude against redshift for a population of objects. The original idea had been to use it to measure the density of the universe — if a class of object of known luminosity (a "standard candle") could be identified over a sufficiently large range of redshifts, then the rate at which the sources dimmed with redshift could be measured. This rate depends upon the curvature of the universe, and thus the density parameter Ω_0. However, it was found that the change in brightness of a galaxy due to the evolution of its stellar population dwarfs the change due to the curvature of the universe. The Hubble diagram is now used to measure these evolutionary changes in galaxies, rather than to test a particular cosmology.

The infrared K-band Hubble diagram, or K–z relation, has been used and discussed often in the preceding chapters. The infrared properties of a galaxy evolve much more slowly than the UV/optical properties, leading to a relatively well-defined Hubble diagram in the K-band. It is sufficiently well known for radio galaxies that it formed the basis of the redshift estimations used by Dunlop and Peacock (1990), and was discussed in §4.1.1. The optical Hubble diagrams are more sensitive to evolutionary effects, due to the rapid evolution of the restframe ultra-violet emission in a young, starbursting or active galaxy. These effects can be seen as a large scatter in the diagrams.

It is useful to compare the observed Hubble diagrams with the predictions of evolutionary models for the following reasons. As already noted, powerful radio galaxies are usually identified as giant ellipticals and are thus close to being standard candles. This is seen in the small scatter about the K–z diagrams of Lilly et al. (1985) or Dunlop and Peacock (1990), for example. Thus it is reasonable to suppose that a galaxy that contains a radio source at high redshift, will evolve into the same class of galaxy as the hosts of radio sources at lower redshift — i.e. by studying a radio galaxy sample, we ensure that we are observing the same population of giant ellipticals at $z = 1$ as at $z = 0.5$. If this is correct, then we should be able to consistently model the evolution of these sources over all redshifts.

The Hubble diagrams for the LBDS Hercules sample are presented in figures 5.1 and 5.2 for the optical U^+gri-bands and the infrared JHK-bands respectively. Circles denote sources classified as radio galaxies (G, G?) or of unknown morphology (?), and triangles denote the quasars (Q, Q?). Solid symbols are sources in the 2-mJy sample and open symbols are sources with $1 \leq S_{1.4} < 2$ mJy. U^+ data is only available for those sources that were identified by Kron et al. (1985) on the photographic plates. In figure 5.1(b)–(d), the magnitudes of those sources that were not observed with the Four-Shooter CCD camera have been transformed from the $J^+F^+N^+$ magnitudes of Kron et al. using equations [2.8].

The data have been compared with the galaxy spectral evolution models of Jimenez et al. (1999), as shown in the figures, for a cosmology of $H_0 = 50$ km s^{-1} Mpc^{-1}, $\Omega_0 = 0$ and $\Lambda = 0$. The models were scaled so as to match the K–z relation of Lilly et al. (1985) over $0.3 \lesssim z \lesssim 1$, where the majority of the radio galaxies do indeed follow this relation. Specifically, this scaling corresponds to $K \simeq 15.3$ at $z \simeq 0.4$. Both Salpeter and Miller-Scalo initial mass functions (IMFs) were tested and found to make predictions that were not significantly different from one another; the results of the latter are plotted. The redshift of formation was varied over $2 < z_{\rm form} < 10$ and the resulting models were compared with the data. It was found that a high formation redshift, $z_{\rm form} \simeq 10$, was required in order to fit the faintest i magnitudes at $z \simeq 1.5$.

The effects of varying the metallicity were tested by repeating the plots for $Z = 0.0002$, 0.004, 0.02 (solar), 0.05 and 0.1. It was found that the optical–infrared colours of the models become redder with increasing metallicity (figure 5.3a below). In particular, by scaling the models to the data at K, in order to simultaneously reproduce the observed optical (ri) magnitudes of the galaxies at $0.3 \lesssim z \lesssim 1$ a high metallicity model ($Z = 0.05 = 2.5\,Z_{\odot}$) was required. The solar metallicity model produced galaxies that were ~0.5 magnitudes too bright in r and i. It can be seen in figure 5.1 how well the $Z = 0.05$ model fits the locus of the radio galaxies in all bands and over the full redshift range, to $z \simeq 2$. It is somewhat surprising that a high-metallicity model is required to fit the data, so other effects that could cause this behaviour were considered. There is no evidence that the photometry itself is systematically off by half a magnitude. There are no strong emission lines that could artificially brighten all three infrared magnitudes simultaneously at these redshifts. A modest amount of dust extinction would make the r and i magnitudes fainter whilst having little effect on the infrared magnitudes, as required. However, dust extinction is most effective at the shortest wavelengths, in this case U^+, and quite the opposite effect is seen in the U^+-band diagram (figure 5.1a) — these same galaxies are *brighter* than the passively-evolving models predict, inconsistent with dust obscuration. Thus it is concluded that these radio galaxies do in fact have a higher-than-solar metallicity.

It is seen in figure 5.1 that the passively-evolving model (solid lines) predict U^+ and g magnitudes that are too faint to match the data. The models were thus modified to simulate a galaxy with continuing low-level star formation. This was done in a similar manner to the photometric redshift estimation of section 4.3, by adding some fraction f_{5000} of a young burst to the passively-evolving model. The youngest stellar population available was used for this — a 10 Myr-old burst. Burst fractions of $f_{5000} = 0$, 0.005, 0.01, 0.02, 0.05 and 0.2 were used and are plotted in figures 5.1–5.2. The range of observed magnitudes is successfully reproduced by these spectra, demonstrating that these radio galaxies are consistent with being old, passively-evolving populations with typically 0–20% of their luminosity due to ongoing star formation. Note that a solar-metallicity model may be reconciled with the data if a combination of continuous star formation and dust is considered. A solar-metallicity galaxy with a significant starburst contributing $\gtrsim$10–20% to its g-band (5000 Å) flux, may still be able to produce the observed U^+ magnitudes after extinction by an amount of dust sufficient to produce the observed $i - K$ colours.

Several other comments should be made about the optical Hubble diagrams. First, there are about eight radio galaxies with redshifts of 0.1–1 that are several magnitudes fainter than the general population. These objects are consistent with being the less-luminous counterparts to the sources that lie on the main locus of the figures. Their evolution appears to be much the same as the brighter sources — simply move the models up 2–3 magnitudes and these fainter galaxies follow the same trend. The two 15^{th}-magnitude sources at $z \simeq 0.025$ do not lie on the Hubble relation due to poor magnitude measurements — they are more extensive than the apertures used to measure them.

The two faint sources at $z < 0.1$ that stand out are 53W042 ($z_{\text{phot}} = 0.02$) and 53W068 ($z = 0.048$). 53W042 has a secondary peak in its estimated redshift distribution (figures 4.8 and 4.9) at $z = 1.60$, which would appear to be the correct redshift based on the Hubble diagram here. 53W068 was discussed in §3.3 — it has an unusual spectrum with three tentative line identifications, however its position on the Hubble diagrams suggests that either the features were misidentified, or possibly that the wrong spectrographic source was observed. It is interesting that a photometric estimate for this source places it at $z_{\text{phot}} = 0.25$, consistent with the low-luminosity sources on the Hubble diagrams. Both these results suggest that the

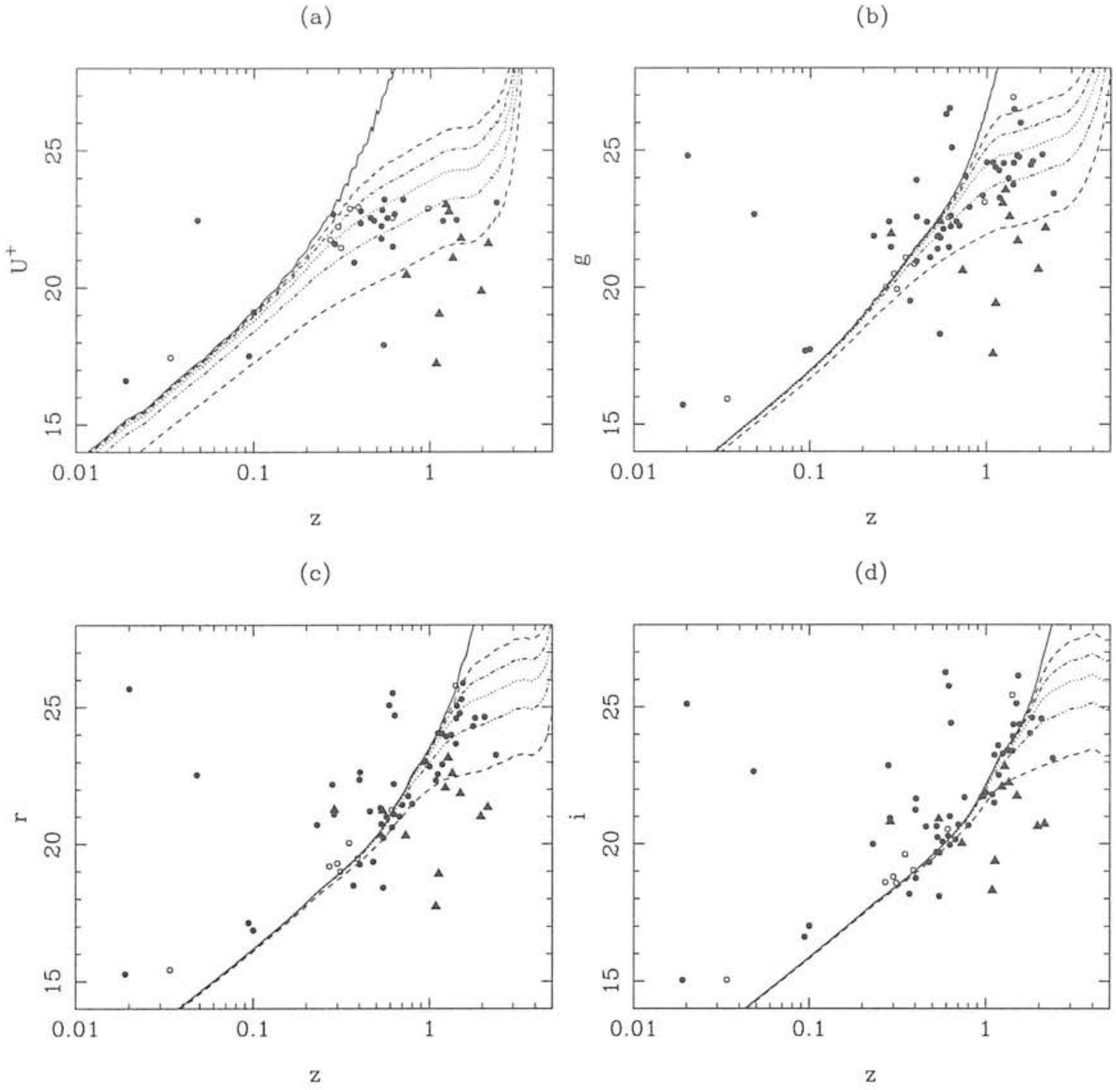

Figure 5.1 Optical Hubble diagrams for the LBDS Hercules sample. (a) Photographic U^+ magnitudes from Kron et al. (1985); this figure is incomplete at $U^+ \gtrsim 23$ as CCD observations were not made in the U-band. (b)–(d) Four-Shooter Gunn *gri* magnitudes, and photographic $J^+F^+N^+$ magnitudes transformed to the Gunn system. Triangles are quasars; circles are galaxies and sources of undetermined morphology. Filled symbols are sources in the 2-mJy sample; open symbols are sources with $1 \leq S_{1.4} < 2$ mJy. Evolving Jimenez et al. (1999) models are plotted for a cosmology of $H_0 = 50$ km s^{-1} Mpc^{-1}, $\Omega_0 = 0$, $\Lambda = 0$, $z_{\rm form} = 10$. The models have a Miller-Scalo IMF, 2.5× solar metallicity and burst fractions of $f_{5000} = 0$ (solid line), 0.005 (dashed), 0.01 (dot-dash), 0.02 (dotted), 0.05 (dot-dot-dot-dash) and 0.2 (lower dashed line).

redshift estimation technique devoloped in §4.3 could be improved by incorporating apparent magnitude information into the fitting. This idea had originally been rejected due to the large scatter in the K–z diagram, however the adoption of a very broad K–z, and perhaps r–z, relation to impose an additional constraint on the photometric fitting could help to reject some

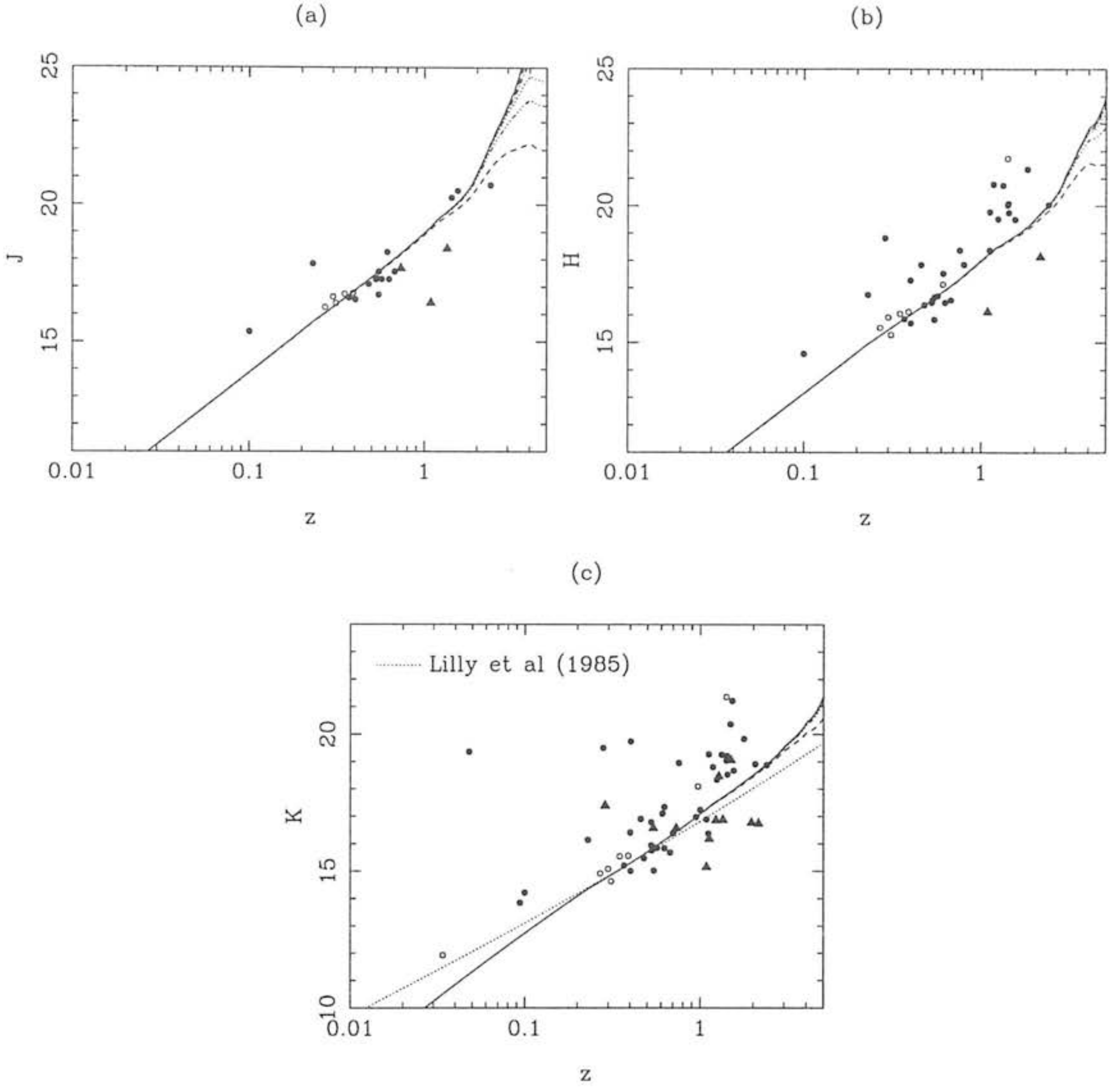

Figure 5.2 Infrared Hubble diagrams for the LBDS Hercules sample. (a) J magnitudes are only available for one-third of the sample. (b) H magnitudes are only available for one-half of the sample. (c) Nearly complete K magnitudes are available, only ~10% of the sample is missing from this plot. Data points and models are the same as in figure 5.1. The dotted line in (c) is the K–z relation from Lilly et al. (1985).

of the secondary peaks in the redshift distributions.

The infrared Hubble diagrams for the Hercules sample are shown in figure 5.2, with the same models as above. In addition, the K–z relation of Lilly et al. (1985) in plotted in figure 5.2(c) for comparison. The J–z diagram is very incomplete (only ~1/3 of sources have J magnitudes), but it does show how well the $z \simeq 0.3$–1 radio galaxies follow the model predictions. The H-band diagram contains more sources, but again is only about half complete. Nearly all (90%) of the sources have K magnitudes, so it is particularly interesting to compare the K–z diagram with that of brighter surveys. At $z \lesssim 1$, the LBDS radio galaxies follow both the models and Lilly's K–z relation for the 3CR and 1-Jansky radio galaxies, the exceptions being the eight under-luminous sources pointed out in the optical Hubble diagrams. Recall that the PSR galaxies are also consistent with this relation (Dunlop and Peacock 1990), over the same redshift range. The K-band is least affected by the AGN, and so provides the best window through which to view the stellar populations of these galaxies, especially within such a restricted redshift range $0.1 < z < 1$. The K–z diagram thus suggests that the host galaxies of radio sources are largely the same over four orders of magnitude in radio flux, from the 3CR to the LBDS.

At $z \gtrsim 1$ the models and data diverge quite significantly. The models are ~1–4 magnitudes brighter than the data at $1 \lesssim z \lesssim 2$. Although the two highest redshift radio galaxies (53W002 at $z = 2.390$ and 53W081 at $z = 2.060$) do lie exactly on the model predictions in K, at optical wavelengths they (or at least 53W002) tend to be brighter than the model. The agreement between model and data at all redshifts in the optical and at lower redshifts in the infrared, suggests that the high-redshift disagreement in K originates in the spectra of the young models (ages $\lesssim 8$ Gyr) at restframe wavelengths of $\sim 1\ \mu$m. This is presumably related to the well known problem of modelling the AGB population in stellar synthesis codes. If luminous AGB stars are generated too rapidly in the early stages of the models, then this could explain the bright K-magnitudes predicted in figures 5.2(b)–(c).

Note that changing the cosmology does not easily remove this high-redshift disagreement. In order to produce fainter galaxies at high redshift, they need to be made older which means either increasing the formation redshift or changing the cosmology to make an older universe. The models that are shown formed at a redshift of $z_{\text{form}} = 10$ which is only 1.4 Gyr after the big bang, already at the high end of the range of currently accepted values of z_{form}. The choice of cosmology is also such as to maximize the age of the universe (20 Gyr), indeed a Hubble constant of 65 km s^{-1} Mpc^{-1} would be more realistic giving a maximum age of 15 Gyr. The only way to accommodate an older universe would be to have a non-zero cosmological constant Λ. Whilst this is possible, the current evidence favours a failure of the models (at long wavelengths and young ages) rather than the cosmology, as the simplest explanation.

5.3 The red envelope

A second useful method of tracing the cosmological evolution of galaxies is the colour–redshift diagram. As with the Hubble diagram, the observations can be compared with the predictions of spectral synthesis models in order to both test the models and place limits on the allowed cosmological parameters. For example, Dunlop et al. (1989a) modelled the $R - K$ colours of the PSR radio galaxies as a function of redshift, concluding that the reddest colours required a very old galaxy (~ 18 Gyr) and high formation redshift ($z_{\rm form} \simeq 20$).

In figure 5.3 the observed $r - K$ versus redshift diagram is plotted for the LBDS sources, together with the models of Jimenez et al. (1999). Figure 5.3(a) illustrates the effect of varying the metallicity from $Z = 0.0002$ to $Z = 0.1$. As is well known, the models become redder with increasing metallicity. It was noted in the preceding section that the Hubble diagrams were best fitted by the $2.5\,Z_\odot$ model and it is seen here that this model roughly follows the upper envelope of the data, although some of the radio galaxies need an even higher metallicity of $\sim 5\,Z_\odot$. At $z \lesssim 1$ the $r - K$ colours of the LBDS galaxies are spanned by these models, suggesting that the colours can be explained as a variation in metallicity, with the bluest galaxies being consistent with a passively-evolving population of very low metallicity (1% of solar). At higher redshifts, the scatter in optical–infrared colours cannot be due solely to variations in the metal content of the galaxies.

The effect of varying the redshift of formation is shown in figure 5.3(b) for values of $z_{\rm form} = 2$, 3, 4, 5 and 10. It is found that varying the formation redshift does not change the red envelope significantly (although it was noted above, §5.2, that the faintest i magnitudes can only be reproduced with $z_{\rm form} \simeq 10$). The models reach their peak $r - K$ colour within $\lesssim 1$ Gyr after the formation of the galaxy, and then evolve along much the same $r - K$ locus, whatever the value of $z_{\rm form}$. It is interesting to compare this result with the models of Guiderdoni and Rocca-Volmerange (1987), which are unable to reproduce the reddest colours ($R - K > 5$–6) without assuming a very high formation redshift $z_{\rm form} \simeq 20$. It was these models that led Dunlop et al. (1989a) to conclude that the reddest radio galaxies in the PSR sample were ~ 18 Gyr old, based on a 1 Gyr burst with solar metallicity. The Jimenez et al. (1999) models successfully reproduce the reddest colours in the current sample (colours that are comparable to those in the PSR) for a galaxy that was formed 11–13 Gyr ago.

The burst models that have so far been considered, assume that the entire stellar population forms instantaneously and then passively evolves without further star-formation. This is a somewhat unphysical model, although it has become the "standard" model of spectral synthesis codes (see §1.5). To produce a more realistic star-formation history, the models were

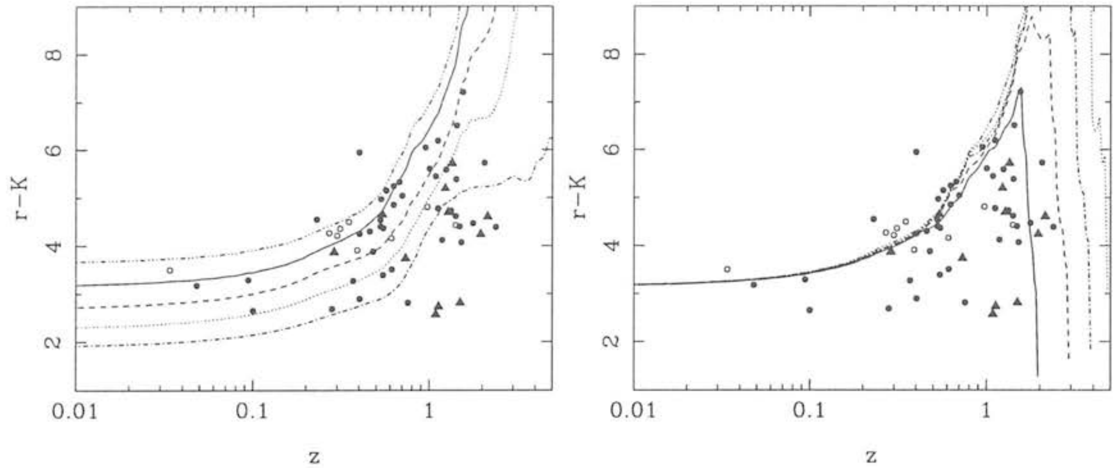

Figure 5.3 **(a) Left:** Model $r-K$ colours as a function of metallicity: $Z = 0.0002$ (dot-dash), 0.004 (dotted), 0.02 (solar, dashed line), 0.05 (solid) and 0.1 (dot-dot-dot-dash). Formation redshift is $z_{\rm form} = 10$. **(b) Right:** Model $r - K$ colours as a function of formation redshift: $z_{\rm form} = 2$ (solid line), 3 (dashed), 4(dot-dash), 5 (dotted) and 10 (dot-dot-dot-dash). Metallicity is $Z = 0.05 = 2.5\,Z_{\odot}$. Triangles are quasars; circles are galaxies and sources of undetermined morphology. Filled symbols are sources in the 2-mJy sample; open symbols are sources with $1 \leq S_{1.4} < 2$ mJy. All models are Jimenez et al. (1999) burst models with Miller-Scalo IMF and without ongoing star formation ($f_{5000} = 0$), for a cosmology of $H_0 = 50$ km s^{-1} Mpc^{-1}, $\Omega_0 = 0$ and $\Lambda = 0$.

again modified so as to simulate a small amount of continuous star-formation at all redshifts. A fraction f_{5000} of a 10 Myr-old population was added to the passively-evolving model, as in the previous section. Figure 5.4 shows the results of this model for f_{5000} = 0–0.2, compared with the observed $g - r$ and $r - K$ colours of the Hercules sample.

The first point to note about this figure is how well the $f_{5000} = 0.005$ model traces the red envelope of both the $g - r$ and $r - K$ colours, with few exceptions. This suggests that there is at least a small amount of ongoing star formation in all the radio galaxies at $z \gtrsim 1$, contributing $\sim 0.5\%$ of the total flux at 5000Å. Some of the galaxies have considerably more star-formation — perhaps as high as 50% of the light at 5000Å if the blueward scatter in the $r - K$ versus z diagram is to be attributed to star-formation. It was seen in figure 5.3(a) above that the blueward scatter could also be explained if the metallicity of these sources was very low. A combination of both low metallicity and significant ongoing star-formation is probably the best explanation for the observed colours of the bluest galaxies at all redshifts.

From a cosmological viewpoint, it is the red envelope of the colour–redshift distributions which is most interesting. The reddest sources at any redshift are the oldest sources, at least to the extent that their colour is due to the stellar population and not due to dust obscuration or

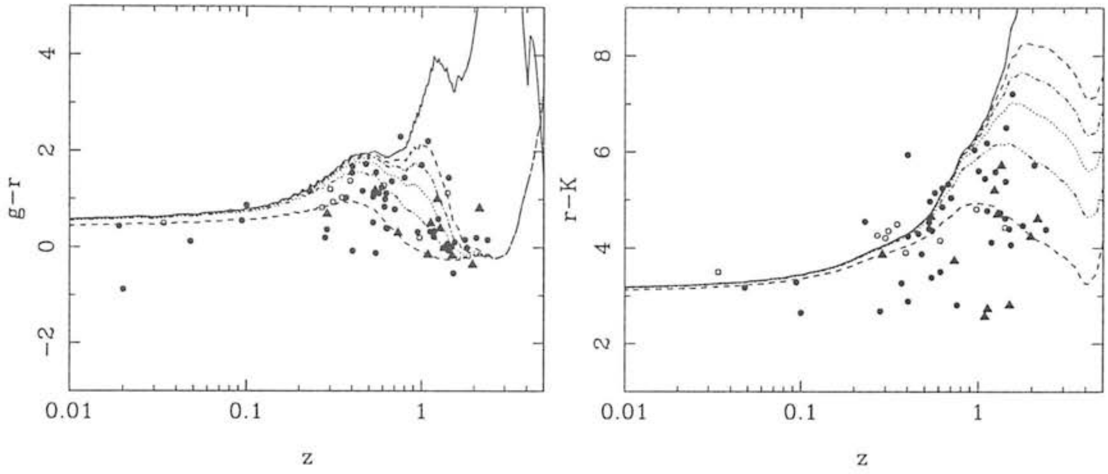

Figure 5.4 (a) **Left:** $g - r$ colours and (b) **Right:** $r - K$ colours as a function of redshift for the LBDS Hercules sample. Symbols are the same as in figure 5.3. Evolving Jimenez et al. (1999) models are shown (Miller-Scalo IMF, $z_{\rm form} = 10$, $Z = 2.5\,Z_\odot$) for starburst fractions of $f_{5000} = 0$ (solid line), 0.005 (dashed), 0.01 (dot-dash), 0.02 (dotted), 0.05 (dot-dot-dot-dash) and 0.2 (lower dashed line). Cosmology as before.

emission line contamination. The universe must, of course, be at least as old as the objects that it contains so if one can trace the ages of galaxies as a function of redshift one can place strong limits on the age of the universe directly, and thus indirectly one can constrain (combinations of) the cosmological parameters H_0, Ω_0 and Λ. The reasons for believing that the LBDS radio galaxies do not have artificially red colours due to emission lines were discussed in §5.1 above. It thus remains to consider if there is any evidence for dust absorption in these sources, and in particular if the handful of $r - K > 5$ galaxies could be reddened due to such dust.

At redshifts $z \lesssim 1$ a fair fraction of the radio galaxies in the sample have U^+-band observations that are invaluable in testing for the presence of dust. Short-wavelength ultraviolet radiation is absorbed by dust and re-radiated in the mid-infrared, thus a galaxy that has been reddened by dust will have very red UV–optical colours. The ~ 25 galaxies at $z = 0.3$–1 that have U^+ magnitudes all have UV–optical colours of $U^+ - g \simeq 0$–2, fully consistent with the spectral evolution models shown in figure 5.4, for $f_{5000} = 1$–20%. If these sources did have significant dust obscuration then it would be seen as a reddening of the data with respect to the models, thus it is concluded that the LBDS radio galaxies at $z \lesssim 1$ are not affected by dust. Note that there were only about six sources in this redshift range (20%) that were detected at g but not at U^+, thus this test was not significantly biassed against objects that were too faint in U^+ to have been detected (e.g. sources obscured by dust).

Having established that the lower redshift galaxies are not reddened due to dust, this result can be extrapolated to higher redshifts, concluding that the $z \simeq 1$–3 sources are not significantly reddened either. Whilst there may be objections to such an extrapolation, it is at least partly justified on the basis of the $g - r$ versus z diagram of figure 5.4(a). Both the $z < 1$ sources and the $z > 1$ sources are enclosed by the models in this diagram — this would be unexpected if the high-redshift sources differed significantly from the lower-z ones.

Given that the available data is consistent with the $r - K$ colours being due to stellar emission, the red envelope of figures 5.3–5.4 may be used to investigate the cosmological parameters allowed by the data and models. It was noted above that the burst models become very red in $r - K$ within a giga-year of the burst. Thus the formation redshift is not significantly constrained by the data — the high-redshift sources simply require $z_{\rm form} \geq 2$–3, for $H_0 = 50$ km s^{-1} Mpc^{-1} and $\Omega_0 = 0$. The bluer, lower-z sources can be formed at lower redshifts than this. The strongest limits on the allowed cosmologies actually come from the reddest galaxies at $0.3 < z < 0.7$, which have $r - K \simeq 4$–5. At these redshifts the r-band measures the flux of a galaxy just *above* the 4000-Å break. It requires quite an old galaxy ($\sim$ 6–7 Gyr) to produce a red $r - K$ colour over this wavelength range, where the galaxy spectrum is very flat (in f_λ). Thus the age of the universe must be $\gtrsim 6$ Gyr at $z \simeq 0.7$ in order to accommodate these radio galaxies. This would only be possible in a critical universe ($\Omega_0 = 1$) for a low Hubble constant $H_0 \lesssim 50$ km s^{-1} Mpc^{-1}. Recent measurements that find $H_0 \simeq 65$ km s^{-1} Mpc^{-1}, are thus incompatible with a high-density universe. In an open universe ($\Omega_0 = 0$) these red sources at $z \simeq 0.7$ can be produced for all values of $H_0 \lesssim 80$ km s^{-1} Mpc^{-1}.

At higher redshifts ($z \gtrsim 1$) the r-band measures a galaxy's flux shortward of the 4000-Å break, in the region of the spectrum which evolves most rapidly. Red $r - K$ colours are therefore easier to produce with a much younger galaxy at these redshifts. The observed $r - K$ colours of the reddest sources (53W069 with $r - K = 6.5$, 53W091 with $r - K = 7.2$) are consistent with a 1–2 Gyr-old burst model at a redshift of $z \simeq 1.5$. This does not make a significant restriction on the cosmology — all open universes are allowed, and a critical universe is old enough to contain these sources for $H_0 \lesssim 80$ km s^{-1} Mpc^{-1}.

It was found in the previous section (§5.2) that the Jimenez et al. (1999) models predicted K magnitudes that were too bright at high redshifts ($z > 1$). It is useful to consider how this affects the modelling of the red envelope and the conclusions drawn from it. If the model K magnitudes are made fainter to match the data, then the predicted $r - K$ colours will become bluer by 1–1.5 magnitudes at $z \simeq 1.5$. This will bring the models closer to the red envelope of the data and allow the high-redshift sources to be used to constrain the cosmology. It can be seen from figure 5.3(b) that a somewhat higher formation redshift would be required, $z_{\rm form} \geq 3$–4, if the models are made bluer. A smaller fraction of ongoing star-formation would be needed in order to fit the $r - K$ colours of the bluer sources. The reddest galaxies would probably lie on the locus of a passively-evolving model (the solid line in figure 5.4b), and would be more sensitive to small changes in the cosmology. Thus an improvement in the spectral sythesis models at high-z would enable this radio galaxy sample to place quite stringent constraints on the allowed cosmological parameters.

5.4 The oldest galaxies in the universe

It is seen in the colour–redshift diagrams above that there are several very red sources with $r - K > 5$ in the LBDS Hercules sample. The measurement of redshifts for these objects was a high priority goal of this project, as they were potentially at very high redshift. Section 3.2 described observations of these sources made by the author at the William Herschel Telescope in 1995. Those observation were unsuccessful in obtaining good enough spectra to measure redshifts from. Around the same time, H. Spinrad and colleagues observed some of these objects at the Keck Telescope. The results of those observations and the subsequent analysis, in which the author was involved, will be summarised in this section.

The LBDS radio galaxy 53W091 is a steep-spectrum, double-lobed FRII radio source with a 1.4 GHz flux of 22.1 mJy. It was identified with a faint ($r \simeq 25.9$), red ($r - K \simeq 7.2$) galaxy in the Palomar and UKIRT images presented in chapter 2. In the summer of 1995, the source was observed with the LRIS spectrometer at the 10 m W. M. Keck Telescope, Mauna Kea, Hawaii by H. Spinrad, A. Dey and D. Stern, with a total integration time of 5.5 hours (Dunlop et al. 1996; Spinrad et al. 1997). The spectrum is shown in figure 5.5, where it is compared with the UV spectra of two nearby elliptical galaxies (M 32 and NGC 3610). A redshift of 1.552 ± 0.002 was determined from the continuum shape, the two spectral breaks at 2640 Å and 2900 Å restframe wavelengths, and the Mg II 2800 absorption feature. There are no emission lines detected in the spectrum, showing that the observed optical emission is not dominated by the AGN.

The best-fitting spectral synthesis models yield an age of $\gtrsim 3.5$ Gyr for this galaxy. Spinrad et al. (1997) used the spectral models of a number of authors (Jimenez et al. 1999; Bruzual and Charlot 1993; Worthey 1994; Guiderdoni and Rocca-Volmerange 1987) to determine the age of the stellar population in 53W091. The models were assessed with respect to how well they predicted the overall spectrum, the spectral breaks at 2640 Å and 2900 Å, a UV colour index defined over $2000 < \lambda < 3200$ Å, and the $R - K$ colour. The models gave a very wide range of ages (2.2–4.7 Gyr) and most had difficulty providing a self-consistent age for all the different features tested. The age derived for this galaxy, made it the oldest object yet

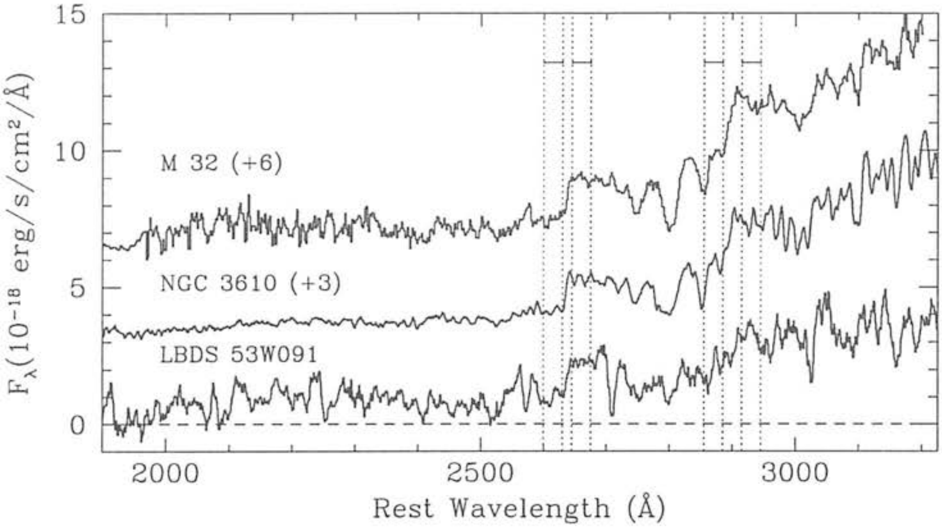

Figure 5.5 Restframe spectrum of 53W091 ($z = 1.552$) compared with the spectra of two nearby ellipticals, M 32 and NGC 3610 (whose spectra have been offset for clarity). The four bands indicate the spectral ranges that define the 2640 Å and 2900 Å breaks. (Spinrad et al. 1997).

observed at $z > 1$. Only certain cosmological expansion times are consistent with the age of this galaxy. In particular, for $\Omega_0 = 1$, a Hubble constant of $H_0 \lesssim 45$ km s^{-1} Mpc^{-1} is required. For an open universe with $H_0 = 50$ km s^{-1} Mpc^{-1} and $\Omega_0 = 0.2$, the minimum formation redshift for 53W091 is $z_{\rm form} \gtrsim 5$.

The following year (1996), a second source from the LBDS Hercules sample was observed at the Keck Telescope (Dey 1997; Dunlop 1999). 53W069 has a 1.4 GHz flux of 3.7 mJy, an r magnitude of 25.0 and an optical–infrared colour of $r - K = 6.5$ (see chapter 2). The LRIS observations revealed it to have a very similar spectrum to 53W091 (figure 5.6). 53W069 has a redshift of 1.432 and a best-fitting age of $\gtrsim 4.5$ Gyr from the models of Jimenez et al. (1999). In addition to the spectral fitting, the (restframe) UV spectrum of this galaxy was compared with individual stellar spectra, via a comparison of the spectral breaks and absorption lines of Fanelli et al. (1992). This initial work was performed by the author, and an updated version was presented by Dunlop (1999). The stellar absorption features seen in 53W069 are overall consistent with those of a G0V–G5V star. Independent of any particular spectral synthesis model, this requires that the stellar population must evolve sufficiently so that the UV light is dominated by a G0 star. Of course, it remains a population synthesis problem to determine how old a stellar population must be before the integrated spectrum is no longer dominated by hotter stars.

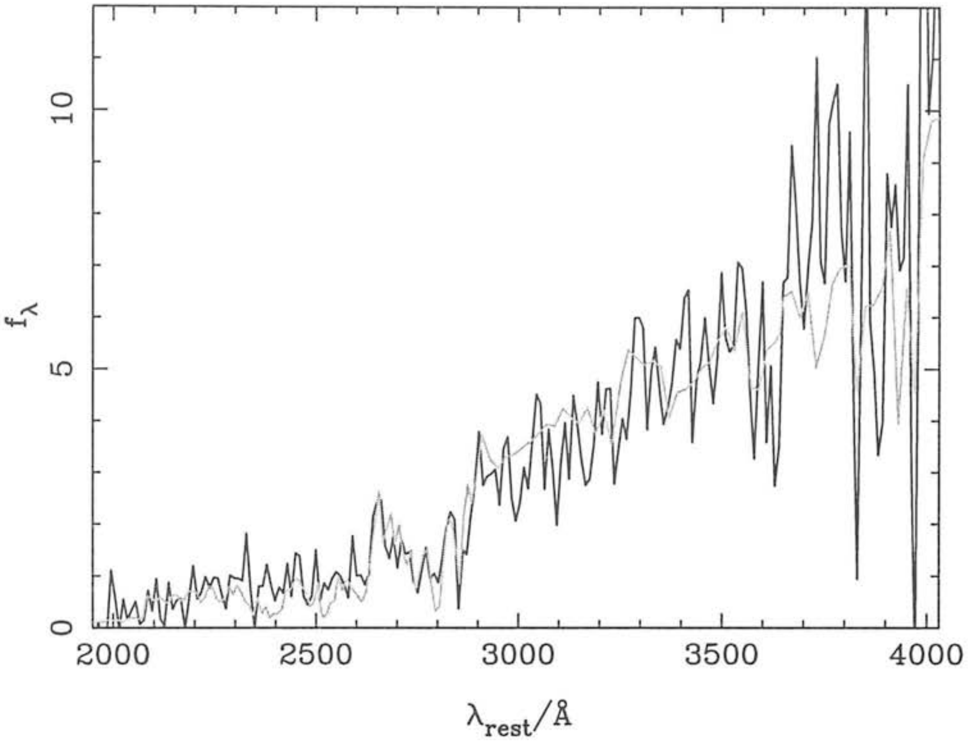

Figure 5.6 Restframe spectrum of 53W069 (black line) and the best-fitting spectral synthesis model (grey line) of Jimenez et al. (1999). The redshift is $z = 1.432$, and the model is a burst of age 4.25 Gyr (solar metallicity). (Dunlop 1999).

The age of 53W069 is a little older than 53W091 and thus it requires either a somewhat older universe or a higher formation redshift. 53W069 is about 1 Gyr older than 53W091 at their respective redshifts; the difference in cosmological time between the redshifts of the two radio galaxies is 0.3–0.5 Gyr; and thus 53W069 must have formed 0.5–0.7 Gyr earlier than 53W091. For an open universe ($\Omega_0 = 0$) with $H_0 = 50$ km s^{-1} Mpc^{-1}, a formation redshift of $z_{\mathrm{form}} \geq 5$ is required. For a higher density or a larger Hubble constant z_{form} must be larger still. For $H_0 = 65$ km s^{-1} Mpc^{-1}, the age of 53W069 places an upper limit on the density of $\Omega_0 < 0.2$. If one considers a critical-density universe with a cosmological constant ($\Omega_{\mathrm{total}} = \Omega_0 + \Omega_\Lambda = 1$), then the age of 53W069 places a *lower* limit on the value of Ω_Λ. For $H_0 = 65$ km s^{-1} Mpc^{-1}, a limit of $\Omega_\Lambda \gtrsim 0.6$ is required (see figure 18 of Spinrad et al. 1997). This is in conflict with the upper limits on Ω_Λ from *HST* counts of elliptical galaxies (Driver et al. 1996), measurements of the cosmic microwave background (White and Bunn 1995), gravitational lens statistics (Kochanek 1996) and high-redshift supernovae (Perlmutter et al. 1997), all of which require $\Omega_\Lambda \lesssim 0.5$–$0.8$. A lower Hubble constant of $H_0 \leq 55$ km s^{-1} Mpc^{-1} is required in order to bring the lower limit derived from the radio galaxy ages into consistency with these results.

Recall that these calculations are based on a galaxy age derived from an instantaneous burst model — realistically, the galaxy will take time to form and so these results place *lower* limits on the age of the universe. In addition, the models only measure the age of the most recent episode of star formation, so if these galaxies had undergone several such episodes their ages would be older still.

The old ages of these two LBDS radio galaxies have important implications for cosmology and galaxy formation — completely ruling out the mathematically elegant cosmological model of $\Omega_0 = 1$ and $\Lambda = 0$, for all recent measurements of the Hubble constant. Thus the age determination of these galaxies has been investigated, and challenged from essentially two directions. First, Chambers (1997, priv. comm.) claimed that polarized light had been detected in 53W091. This would be evidence that the optical/infrared emission contained a (possibly significant) fraction of scattered light from the AGN and that the optical spectrum was not due only to stellar light — this would clearly call into question the reliability of the model fitting. However, subsequent observations at UKIRT failed to detect such polarization, supporting the original conclusion that the light from 53W091 is stellar in origin (Dunlop 1999).

The age of 53W091 has also been challenged on the basis of the accuracy of the spectral synthesis models. Bruzual and Magris (1997, 1998) used the latest (1997) version of the population sythesis models of Bruzual and Charlot (1993) to recalculate the age of the radio galaxy. Fitting the models to the optical–infrared colours they determined an age of 1–2 Gyr for the stellar population of 53W091. This is not in conflict with the results of Spinrad et al. (1997), however, as the authors demonstrated in that paper that the $R-K$ colour predicted by most of the population synthesis models yields an age that is less than the ages derived by other means. Indeed, it was seen in figure 5.3(b) above that the $r-K$ colours of 53W091 and 53W069 can be reproduced by the Jimenez et al. (1999) models within 1–2 Gyr. Due to the uncertainties in modelling the late stages of evolution, the $R-K$ colour alone is not the best measure of the age when there is also detailed information available in the (restframe) UV such as spectral breaks and the slope of the UV continuum.

Bruzual and Magris (1997, 1998) also compared the strength of the observed 2640 Å and 2900 Å breaks with the predictions of their models, and found an age of $\sim$ 2 Gyr for the galaxy. It is important to note, though, that in calculating the strength of the breaks, Bruzual and Magris used different definitions of the break amplitudes than were used by Spinrad et al. (1997). In particular they used broader wavelength regions each side of the breaks, that *virtually overlap* the breaks themselves. Given that each break has a finite width of $\sim$ 10 Å (see figure 5.5), it is almost inevitable that at least part of the break fell within Bruzual and Magris' measurement of the continuum, leading them to underestimate the true break amplitude and thus the age of the galaxy.

In conclusion, whilst there is considerable uncertainty in the age determinations of individual spectral features and colours, average ages based upon multiple diagnostics and several different population synthesis models can be calculated. This yields ages of 4.5 Gyr and 3.5 Gyr for 53W069 and 53W091 respectively, making them the oldest galaxies yet observed in the high-redshift universe.

5.5 Summary

The main results of this chapter can be summarised as follows:

- The evolution of the majority of the LBDS radio galaxies can be modelled by a passively-evolving burst, plus an additional starburst component contributing 1–20% of the emission at 5000 Å.
- The optical/infrared magnitudes of the brighter galaxies are comparable to those in the 3CR, 1-Jansky and PSR surveys, although there is a significant scatter towards fainter magnitudes.
- The Jimenez et al. (1999) models predict galaxies that are too bright in K at high redshifts, possibly due to an excess of giant stars early in the evolution of the stellar population.
- The upper envelope of optical–infrared colours is best modelled by a high-metallicity ($2.5\,Z_{\odot}$) population — solar metallicity models predict galaxies that are ~ 0.5 magnitudes too blue in $r-K$.
- Models with a combination of ongoing star formation and low metallicity successfully span the range of observed $r-K$ colours.
- The red envelope of the $r-K$ versus redshift diagram at $z \simeq 0.7$ imposes a limit on the age of the universe at that redshift of $\gtrsim 6$ Gyr.
- The formation redshift is not significantly constrained by the $r-K$ colours of the radio galaxies. The models predict very red colours ($r-K>5$) within ~ 1 Gyr of formation at high redshift, thus requiring formation redshifts of $z_{\rm form} \gtrsim 2$–3.
- Keck spectra of the two reddest galaxies (53W069 and 53W091) reveal them to be ~ 4 Gyr-old at $z \simeq 1.5$, placing significant constraints on the age of the universe.
- In order to accomodate the oldest galaxies at $z \simeq 0.7$ and $z \simeq 1.5$, the universe must either have a low density ($\Omega_0 \lesssim 0.2$) or a significant cosmological constant ($\Omega_\Lambda \gtrsim 0.6$, if $\Omega_0 + \Omega_\Lambda = 1$), for recent measurements of the Hubble constant of $H_0 \simeq 65$ km s^{-1} Mpc^{-1}.

Chapter 6

A group or cluster of galaxies at z=2.39

The results of deep J, H, K imaging of the field around the $z = 2.390$ radio galaxy 53W002, are presented. At this redshift, the 4000-Å break falls between the J and H bands, thus the infrared observations are designed to identify potential evolved galaxy cluster members by a red $J - H$ colour. Out of the 42 objects detected in the field down to a magnitude limit of $K \simeq 20$, there are 10 galaxies with $J - H > 1.0$ and $K > 18.8$, redder and fainter than the radio galaxy, and consistent with having a spectral break at $z \simeq 2.4$. Two of these reddest galaxies were also identified as possible cluster members from *Hubble Space Telescope* and ground-based narrow-band Lyman-α imaging, and have subsequently been confirmed spectroscopically. The strengths of the inferred 4000-Å breaks in these objects are compared with the predictions of spectrophotometric models of elliptical galaxy evolution and the implications for cosmology of the derived galaxy ages are discussd.

6.1 Introduction

One of the most important challenges in cosmology is to determine the formation epoch and subsequent evolution of elliptical galaxies. Until recently it has only been possible to attempt this via the investigation of powerful radio galaxies, such as those found in the widely-studied 3CR survey (Spinrad et al. 1985) or the Parkes Selected Regions (Downes et al. 1986; Dunlop et al. 1989b). However even the weakest of these sources, at redshifts of cosmological interest, are strong radio emitters compared to the vast majority of galaxies. This results in their normal stellar properties being contaminated by the embedded active nucleus producing extensive emission line regions and distorted morphologies (McCarthy et al. 1987).

Ideally one wants to study radio-quiet galaxies at high redshift and there are now a number of ways to do this. One method is to look at less powerful radio sources selected from low flux-limited samples such as the Leiden-Berkeley Deep Survey, in an attempt to identify the power at which the stellar continuum of radio galaxies is unaffected by the active nucleus. This has been the topic of the preceding chapters. The discovery of two ~ 4 Gyr-old galaxies at $z \simeq 1.5$ in the LBDS (§5.4), clearly demonstrates the usefulness of this technique. 53W091 is devoid of emission lines and was the first galaxy with late-type stellar absorption features to have been discovered at such a large look-back time, placing unparalleled constraints on cosmological models (Dunlop et al. 1996; Spinrad et al. 1997). One can also use radio galaxies or quasars to locate distant clusters. This technique has been successfully used by Dickinson (1995; 1997) in his discovery of the cluster surrounding the radio galaxy 3C324. Imaging of the field revealed an excess of red galaxies ($R-K \simeq 6$) around the radio source, with simple E/S0 morphologies and colours consistent with an evolved stellar population. Keck spectroscopy has enabled redshifts to be measured for a large number of the objects in the field and has confirmed that many of these red galaxies are members of the cluster at $z = 1.21$.

An important breakthrough in the search for high-redshift galaxies was the discovery by Steidel et al. (1995) of a substantial population of star forming galaxies at $3.0 < z < 3.5$, selected using a custom set of broadband filters designed to identify the presence of a Lyman-limit break at these redshifts. The successful confirmation of their redshifts via deep Keck spectroscopy (Steidel et al. 1996b) proved that this technique is very efficient at selecting galaxies at $z > 3$, and has led to further applications of the method (for example, Steidel et al. 1996a; Lacy and Rawlings 1996; Stevens et al. 1998). However, this selection method is strongly biassed towards blue star-forming objects, and a similar bias is also present in narrow-band searches designed to identify high redshift objects via strong emission lines (Hu et al. 1996; Malkan et al. 1996). This is unfortunate since the passively evolving stellar population of a galaxy can be masked with relative ease by even a small starburst, and it is the reddest, oldest, most-passive systems at any redshift which are of greatest importance for constraining the epoch of elliptical galaxy formation and the age of the Universe.

In order to find these passively evolving galaxies one needs a selection technique that is sensitive to an old stellar population rather than a young one. Such a diagnostic is the 4000-Å break — the step in a galaxy's spectrum due to Balmer continuum absorption, calcium H and K lines and the iron G-band. The strength of the break is indicative of the age of the stellar population — an evolved galaxy will show a large break, whereas a young or star-forming galaxy will have a much weaker break. This should be contrasted with the Lyman-limit break at 912 Å used by Steidel et al. (1996b), which is strong for a young galaxy but very weak for an old one. Thus these two breaks provide complementary selection methods, one biased towards blue active galaxies and one biased towards red passively-evolving galaxies.

It is not necessary to produce customized filters such as were designed by Steidel et al. (1995), so long as one is prepared to be limited to a few redshifts for which the break falls between the standard filters: $z \sim 1.6$ for I & J, $z \sim 2.7$ for J & H, and $z \sim 3.8$ for H & K for example. Figure 6.1 illustrates how the J and H filters approximately bridge the break for a galaxy at $z \simeq 2.4$. This led to the idea of using near-infrared imaging to identify galaxies with a strong break on the basis of their infrared colours.

The target chosen for this project was the field around the radio galaxy 53W002 at a redshift of 2.390. Whilst at this redshift the break lies just within the J filter, it is nethertheless sufficiently close that an evolved galaxy is predicted to be a magnitude redder in $J - H$ than a star-forming galaxy. In addition, this radio galaxy was found to be a member of a group or cluster of galaxies at $z \simeq 2.4$ (Pascarelle et al. 1996a; Windhorst et al. 1996) and as such the field has been extensively studied, providing a wealth of optical data to complement the infrared observations.

As the most distant known radio galaxy in the Leiden-Berkeley Deep Survey (Windhorst et al. 1991), 53W002 has itself been the subject of extensive investigation (§2.1.2). Pre-refurbishment *Hubble Space Telescope* imaging found that its surface brightness profile is well described by an $r^{1/4}$-law with scale-length $r_e \simeq 10$ kpc, and with a stellar population ~ 0.3–1 Gyr old, consistent with a formation redshift of 2.5–4 (Windhorst et al. 1992; Windhorst et al. 1994). Ground-based follow-up work led to the serendipitous discovery of a companion galaxy at the same redshift as the radio galaxy — object A at $z = 2.397$. Further *HST* and ground-based imaging in redshifted Lyman-α revealed a total of eighteen potential cluster members (including 53W002), and spectroscopic redshifts of $z \simeq 2.39$ were subsequently measured for three more radio quiet objects (Pascarelle et al. 1996b). The compact size of these

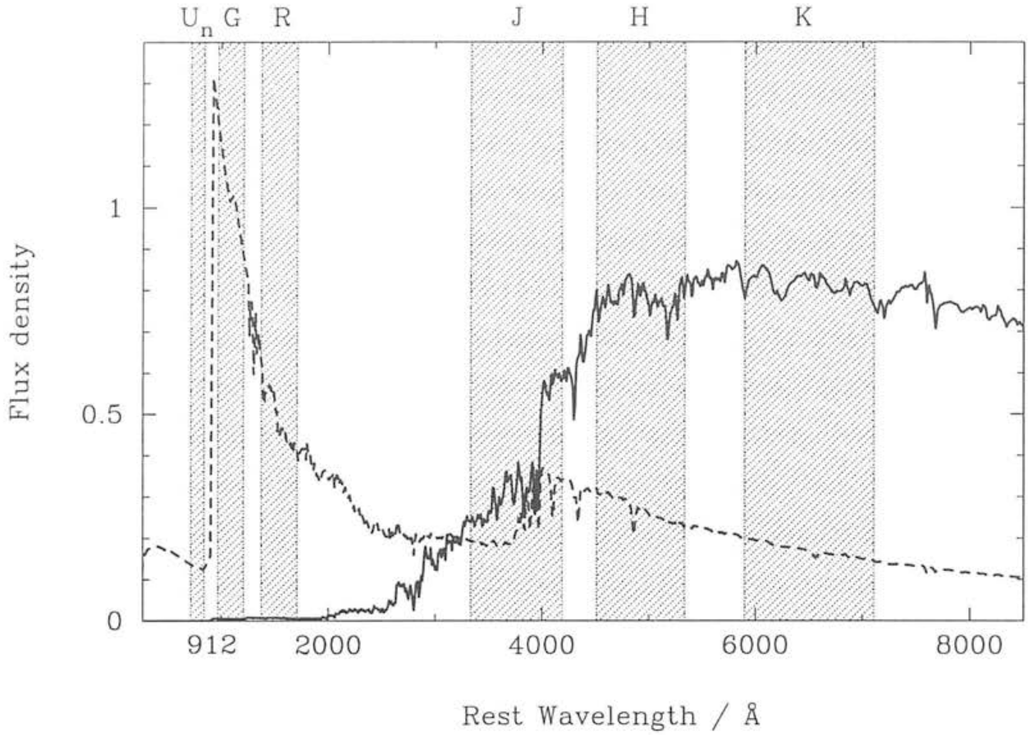

Figure 6.1 Comparison of the Lyman-limit (912Å) and 4000-Å break selection techniques. The two spectra are Guiderdoni and Rocca-Volmerange (1987) models of ages 1 Gyr (dashed line) and 9 Gyr (solid line). Shading denotes the filter bandpasses at redshifts of 3.25 for U_n, G, R, and at 2.39 for J, H, K.

sources ($r_{\rm HL} \lesssim 0\farcs1$–$0\farcs2$, or $\lesssim$ 0.5–1.0 kpc at $z = 2.39$ for $H_0 = 80$ km s^{-1} Mpc^{-1}, $q_0 = 0.5$) and their faint luminosities ($L \lesssim 0.1$–$1\ L^*$) has suggested that they may be the subgalactic-sized progenitors of massive ellipticals or spirals, consistent with a hierarchical model of galaxy formation. Once again though, the selection technique used to find these cluster members is biased towards those galaxies with strong Lyα emission, and is insensitive to any passively-evolving cluster members. The complementary search for such passive galaxies presented in this chapter, thus allows one to investigate the full range of star-formation activity in this cluster at a redshift of 2.39.

In the next section the observations and the data reduction procedure are described. Section 6.3 reports the results of the photometry and the selection of potential evolved cluster members on the basis of their red colours. These results are discussed in the light of the work by Pascarelle et al. (1996b) and Francis et al. (1998). In section 6.4 the strengths of the inferred 4000-Å breaks in these red objects are compared with the predictions of spectrophotometric models of elliptical galaxy evolution, and their sizes are compared with model galaxy profiles.

Finally, the implications of these results for galaxy evolution and cosmology are discussed (§6.5).

6.2 Observations and data reduction

The field surrounding 53W002 was observed by J. S. Dunlop and the author at the 3.8 m UK Infrared Telescope, Mauna Kea, Hawaii on 25–27 May 1995, using the near-infrared imaging camera IRCAM3. The first night was entirely lost due to bad weather, but the remaining time was clear with seeing of 0.8–1.2 arcsec. IRCAM3 has a 256×256-pixel InSb array, and the observations were made using a pixel scale of $0\farcs286$ pixel^{-1}.

The field was imaged in four quadrants. Within each quadrant, a standard jittering procedure was used to obtain a median-filtered sky flat-field simultaneously with the data. Nine 3-minute exposures were made, each offset by $11''$ from the first position, resulting in an area of 50×50 arcsec^2 with a maximal exposure time of 27 minutes, surrounded by a border of lower signal-to-noise data. This was repeated two or three times for each filter (J, H and K) in each quadrant, giving total exposure times of either 54 or 81 minutes per filter.

Observations of the UKIRT faint standard star FS27 (M13−A14) were taken at the beginning of the third night. Photometric zero-points for the other three regions were fixed from these observations using several bright sources which appeared in the lower signal-to-noise areas of two or more of the regions.

The jittering procedure resulted in sets of nine frames in which the sources were located in different positions on the array in each frame. The nine exposures were then stacked and median filtered to produce a sky flat-field concurrent with the observations. In addition, several alternative methods of producing an accurate flat-field were investigated. These included: (i) using the mean of the nine frames after rejecting the pixel values which deviated most from the mean; and (ii) calculating the median after first removing the bright sources by interpolating across them from the local background. None of these alternatives, however, was successful in removing the $10''$–$20''$ variations in the sky, and so the median-filtered sky flat-field that is usually used in infrared imaging was adopted.

The reduction thus consisted of the following steps performed using the on-line reduction package at the telescope, IRCAM3_CLRED: (i) subtraction of a dark frame observed prior to the nine-exposure sequence; (ii) division of each exposure by the normalised median-filtered sky flat-field; (iii) airmass correction; (iv) construction of a mosaic from the nine exposures, taking the mean of overlapping frames after rejection of known bad pixels. The multiple exposures of each quadrant in the same filter were then combined, taking their mean. Finally, the four

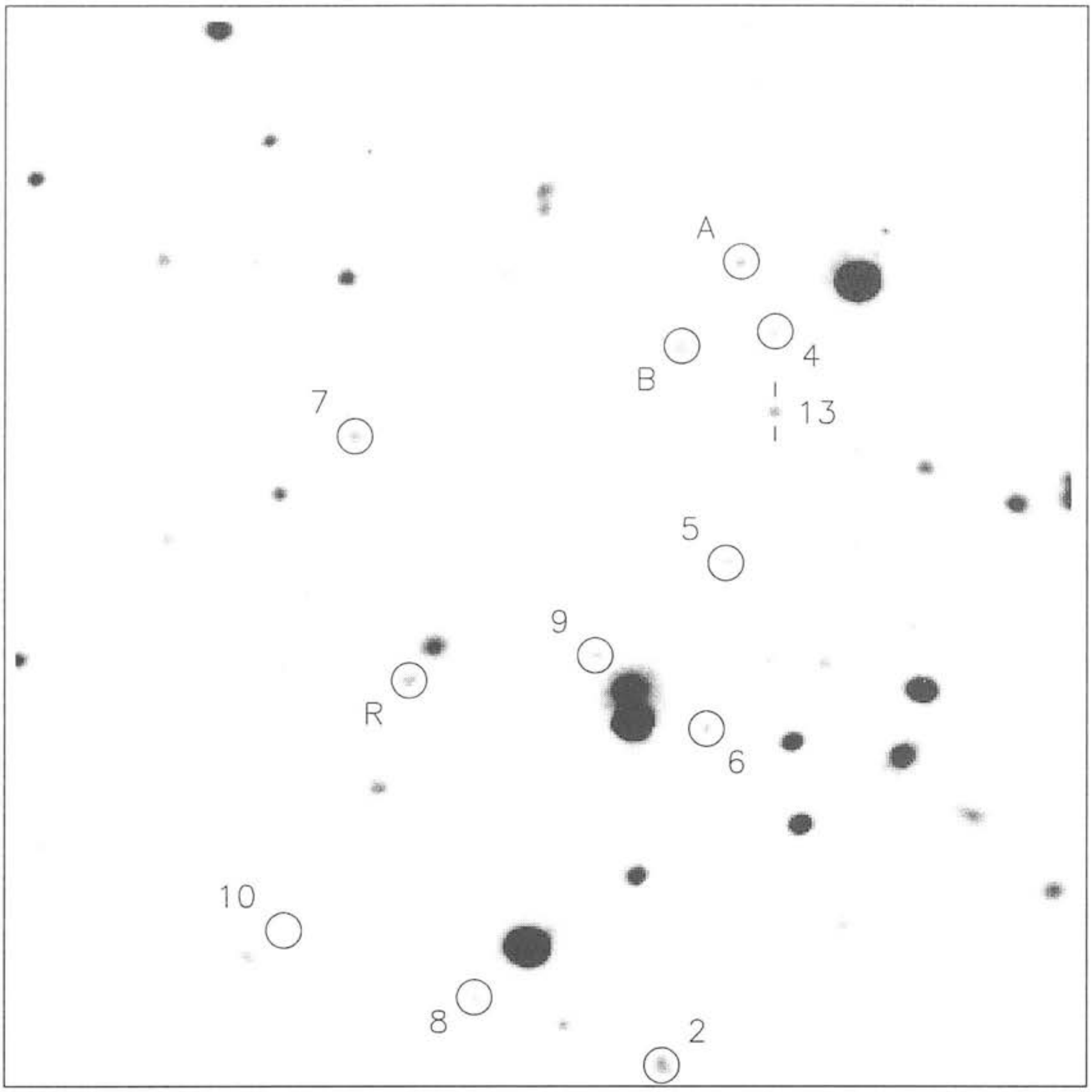

Figure 6.2 The field around 53W002. Circles identify the radio galaxy (R), and infrared-selected potential cluster members (A,. . .,10, as in table 6.1). Sources A and B are spectroscopically confirmed at $z = 2.4$. A, B and 13 are sources detected at K that also show excess Lyα emission in narrow-band optical filters (Pascarelle et al. 1996b). This grey-scale plot is the sum of the individual sky-subtracted J, H and K images, scaled such that the radio galaxy has equal counts in each filter, and smoothed by a 0.″3 gaussian. North is to the top, east to the left, and the image is 103×105 arcsec^2.

quadrants were mosaiced together, registration (to within 0.″3) was achieved using the bright star which appeared on the edge of all four quadrants. The poor signal-to-noise area around the outside of the jitter pattern was truncated, resulting in final images of 100×100 arcsec^2 in each of J, H and K. The combined image ($J + H + K$) is presented in figure 6.2.

Magnitudes for the sources were measured in a 3.″5 aperture using routines in IRAF

(Tody 1993) and KAPPA (Currie 1998). The local background for each object was determined by the mean of four or five measurements of the sky around the source, in an aperture of the same size. The repeatability of the photometry was tested by Dunlop and the author independently calculating magnitudes for a selection of faint sources across the field — the results were found to be in good agreement. Comparison of the magnitudes for the radio galaxy ($J = 20.70 \pm 0.19$, $H = 19.77 \pm 0.28$ and $K = 18.81 \pm 0.12$) with those of previous observations ($J = 20.70 \pm 0.28$, $H = 19.84 \pm 0.29$ and $K = 18.61 \pm 0.17$; Windhorst et al. 1994) are in excellent accord.

The identification of sources was made by eye, using the images both before and after smoothing by a one-pixel ($0\farcs3$) gaussian. The completeness of the identifications, and errors in the photometry, were investigated in the following manner. One of the confirmed cluster members (object A) was extracted from the K-band image, smoothed with a one-pixel gaussian and used as a model galaxy. This model was then scaled to a variety of known magnitudes (from $K = 19.0$ to $K = 20.5$ in steps of 0.5) and added into the K frame at twelve positions across the image. Photometry was performed on the model galaxies in the same way as for the real objects. With a 2-σ detection threshold, eighty per cent of the model sources were recovered at $K = 19.9$, with the completeness falling to fifty per cent by $K = 20.2$. There was no evidence for any systematic errors in the photometry overall, nor from one quadrant to another.

Coordinates for the sources in the field were calculated using a six-coefficient linear fit in ASTROM (Wallace 1994). Reference coordinates for five objects were taken from the ground-based and *Hubble Space Telescope* observations of the field described in Windhorst et al. (1991) and Pascarelle et al. (1996a). Errors in the astrometry were estimated to be $\pm 0\farcs5$, based upon the RMS of the fits and comparison with the positions of two further field galaxies in Windhorst et al. (1994).

6.3 Infrared selection of potential evolved cluster galaxies

There were 42 objects detected in the K-band, of which 36 are above the 80% completeness limit. Of these 42 sources, a sample of 10 galaxies with $J - H > 1.0$ and $K > 18.8$ was isolated. These objects are redder and fainter than the radio galaxy, and are consistent with the presence of a 4000-Å break at $z = 2.4$. The infrared colour–magnitude diagram is presented in figure 6.3, and the data are summarised in table 6.1. The selection criteria are based on the following: (i) radio galaxies can have a significant contribution to their blue flux arising from the embedded active nucleus, so one would expect any passively evolving galaxy at the same redshift, in the absence of an AGN, to possess a stronger 4000-Å break and hence have a redder colour; (ii) the radio galaxy has above-average optical luminosity ($L \simeq L^*$; Windhorst et al. 1991), so one would expect any companion galaxies to be fainter at K (restframe optical) than 53W002. The selection rules are illustrated on the colour–magnitude diagram.

In section 6.4 the colours of the red cluster candidates will be compared with those predicted by spectrophotometric models of elliptical galaxies, but first model-independent evidence that these ten sources are indeed part of the cluster will be considered. The reddest and third reddest galaxies in the sample (objects A and B; denoted '19' and '18' in Pascarelle et al. 1996b) are the only two sources in the cluster, that are detected at K, which have been shown via optical spectroscopy to lie at the same redshift as the radio galaxy. The other spectroscopically confirmed members were either not detected in the K-band or lay outside the infrared field. The remaining eight of our ten red galaxies have not been identified as Lyα emitters and neither have they been observed spectroscopically. They are strong candidates for passively-evolving elliptical galaxies at $z \simeq 2.4$, with significant breaks and weak or non-existent Lyα emission. These results show that (i) near-infrared colours can indeed be used to successfully identify high-redshift galaxies on the basis of the strength of the 4000-Å break, and (ii) at least some galaxies posses a significant qbreak at large lookback times, where most galaxies (including 53W002) have been found to be relatively blue.

To complete the comparison of the cluster candidates with those selected on the basis of Lyα emission, note that one further optically-selected source was detected (object 13; Pascarelle et al. 1996b), but it was found to be relatively blue with $J - H = 0.44$. If this source is indeed part of the cluster then the absence of a break suggests that it is actively forming stars, as indicated by its Lyα emission. Of the eighteen optical cluster candidates, eight were undetected at K and six were outside the infrared field.

It is particularly interesting to compare the red $z = 2.39$ candidates with those in the

Table 6.1 Infrared-selected potential cluster members surrounding the LBDS radio galaxy 53W002.

Source	R.A. (J2000)[1] Dec. (J2000)	$J-H$	$H-K$	K
53W002	17 14 14.74	0.93	0.96	18.81
	+50 15 29.0	(0.34)[2]	(0.30)	(0.12)
A	17 14 11.27	1.63	0.97	19.20
	+50 16 08.6	(0.38)	(0.17)	(0.14)
2	17 14 12.37	1.24	0.89	18.81
	+50 14 51.7	(0.24)	(0.25)	(0.15)
B	17 14 11.89	1.20	−.40	20.30
	+50 16 00.6	(0.22)	(0.31)	(0.30)
4	17 14 10.95	1.17	0.18	19.95
	+50 16 01.9	(0.27)	(0.27)	(0.25)
5	17 14 11.53	1.16	−.05	20.47
	+50 15 39.7	(0.45)	(0.46)	(0.26)
6	17 14 11.79	1.11	0.61	19.59
	+50 15 23.8	(0.50)	(0.42)	(0.21)
7	17 14 15.19	1.07	1.10	19.08
	+50 15 52.5	(0.33)	(0.23)	(0.16)
8	17 14 14.22	1.05	0.43	19.64
	+50 14 58.5	(0.37)	(0.37)	(0.30)
9	17 14 12.88	1.04	0.20	19.49
	+50 15 31.1	(0.30)	(0.31)	(0.16)
10	17 14 16.09	1.00	0.65	20.35
	+50 15 05.2	(0.71)	(0.67)	(0.45)

[1] Astrometry errors are ±0.5-arcsec. [2] Colour and magnitude errors are shown in parentheses.

2139−4434 cluster of Francis et al. (1997, 1998). Three galaxies (B1, B2, B4) at a redshift of 2.38 were discovered via narrow-band Lyα imaging, and confirmed spectroscopically. B1 has the same infrared magnitudes as object A here, and (after making a correction for the AGN contribution in A) the two galaxies have comparable optical magnitudes. The colours of all three galaxies ($J-K$ = 2.1–2.8) are also comparable to the four reddest sources around 53W002 ($J-K$ = 1.9–2.6), although the mean colour of the sources here is a little less at $J-K = 1.7$. The 2139−4434 cluster also contains three systems of damped Lyα absorbers (seen in the spectra of three background quasars), and a further three extremely red objects ($R-K > 5$) have been found in addition to the red Lyα emitters (Francis et al. 1998). This cluster extends over ∼ 10 Mpc, with the neutral hydrogen clouds, Lyα emitters and red

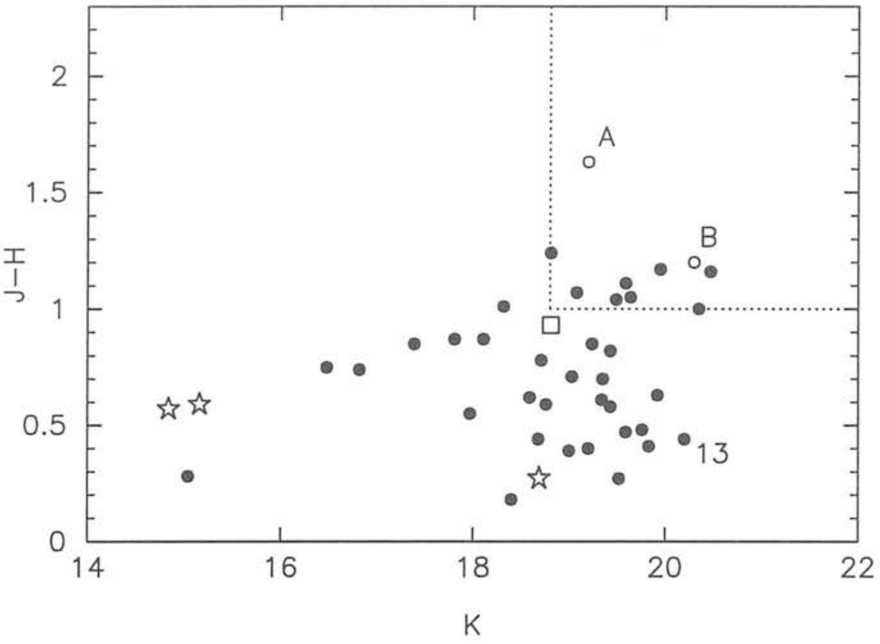

Figure 6.3 Colour–magnitude diagram for the 42 sources in the field detected at K. The radio galaxy is denoted by a box; spectroscopically confirmed members of the cluster by a hollow circle (A & B); source 13 was also identified by narrow-band Lyα imaging; and a star denotes a source which appears stellar on the *HST* image of Pascarelle et al. (1996b). Dotted lines show the criteria used to select potential cluster members ($J - H > 1.0$, $K > 18.8$).

galaxies having an overdensity ≥ 2.5–7. The implied mass of the cluster is much larger than that predicted by CDM models at this redshift, requiring that the formation of Lyα absorbers and galaxies in this system was strongly biassed.

Before turning to investigate the evolution of the ten infrared-selected sources, there are two other possible explanations for their red $J - H$ colours that must be considered, rather than an intrinsically strong 4000-Å break. The first possibility is that the red colour could be due to dust in a lower redshift galaxy. This can be effectively eliminated by considering the $H - K$ colours of these sources. With the exception of 53W002 and object 7, all the sources have $H - K$ colours that are bluer than their $J - H$ colours. For a low-redshift ($z \lesssim 1$) galaxy, both the infrared colours are expected to have similar values of $(J - H) \simeq (H - K) \simeq 1$ (compare figures 2.9d–e). If such a source were to be reddened by dust then one would expect the $H - K$ colour to be reddened as well as the $J - H$ colour, as they both measure the galaxy's flux above the 4000-Å break where the spectrum is relatively flat. Since such a reddening of the $H - K$ colours of the ten cluster candidates is not seen (even 53W002 and object 7 have $H - K$ colours consistent with being un-reddened sources at $z \lesssim 3$), it is concluded that these sources are not dusty, low-redshift galaxies.

The other possibility is that this apparent step in the spectral energy distribution results from emission line contamination in the H-band, which is artificially causing the red $J - H$ colours. There are just two strong emission lines that could be present in H due to a star-forming or active galaxy at $z \lesssim 3$. These are [O III] at 4959/5007 Å which would be redshifted into H for $2.1 < z < 2.6$, and Hα at 6563 Å would lie in the H-band for redshifts $1.4 < z < 1.7$. Thus it possible that some of the red cluster candidates may be either sources with [O III] emission lying just behind or in front of the group of objects around the radio galaxy at $z = 2.39$, or sources with a strong Hα line at lower redshifts. The only way to eliminate the possibility of line contamination would be to pursue a programme of infrared spectroscopy of the red objects. However, it seems overly pessimistic to suggest that such line contamination would be a significant contributor to the colours of all the red galaxies.

6.4 Evolutionary status of the red cluster galaxies

The implications of a population of evolved galaxies at $z = 2.4$ for galaxy evolution and cosmology will now be considered. In figure 6.4 the result of modelling the evolution of the second reddest of the cluster members is shown. The reddest source, object A, was not used as it is an AGN with $> 75\%$ of its optical flux in an unresolved point source (Pascarelle et al. 1996b). At the cluster redshift, all three infrared filters are potentially contaminated by emission lines in this AGN: [O II] at 1.26 μm (in J), Hβ and [O III] at 1.65–1.70 μm (H), and Hα/[N II] at 2.22 μm (K). Thus the infrared colours of object A are likely to be a poor measure of its age, given that they may be dominated by AGN emission rather than the stellar population.

The dependence of $J - H$ colour on galaxy age was predicted using an updated version of the spectral evolution models of Guiderdoni and Rocca-Volmerange (1987). One of the simplest scenarios to consider is to assume that all the stars formed in a single burst of star-formation of 1 Gyr duration and then evolved passively (i.e. no further star-formation occured). The strength of the 4000-Å break is then determined by the evolution of the main sequence turn-off mass. Figure 6.4 shows the effect on the $J - H$ colour of redshifting ("k-correcting") a galaxy from $z = 0$ to $z = 5$, for galaxies of ages 0.1–6.1 Gyr. The rapid rise increase in the model colour as the 4000-Å break passes between the J and H filters at $z = 2$–2.5 is clearly seen.

It can be seen that at the radio source redshift ($z = 2.390$), 53W002 has the colours of a 0.4 Gyr-old galaxy, in agreement with the age previously inferred from more detailed

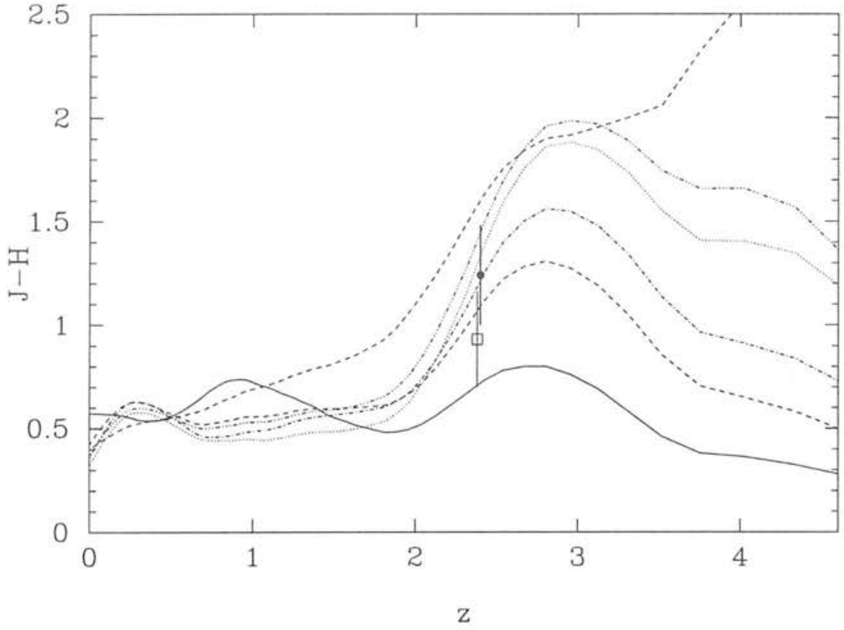

Figure 6.4 The predicted dependence of $J - H$ colour on redshift for a 1 Gyr burst model of galaxy evolution at ages of 0.1 Gyr (solid line), 0.6 Gyr (dashed line), 1.1 Gyr (dot-dash line), 1.6 Gyr (dotted line), 2.1 Gyr (dot-dot-dot-dash line) and 6.1 Gyr (upper dashed line), compared with the observed $J - H$ colour of the radio galaxy (box) and the second reddest companion galaxy at $z = 2.39$ (circle).

spectroscopic information (Windhorst et al. 1991). The second reddest source in the infrared field is predicted to have an age of $1.1^{+1.0}_{-0.6}$ Gyr. For comparison, an Einstein-de Sitter universe is only 2.1 Gyr old at this redshift (for $H_0 = 50$ km s^{-1} Mpc^{-1}). Strictly, these are the times since the cessation of the last starburst and are thus only lower limits to the actual age of the galaxies.

The infrared surface brightness profiles of the red galaxies were also investigated. The point spread functions (PSFs) of the J, H and K images were calculated by fitting a gaussian plus two exponentials to the profiles of the two bright stars in the field. The FWHM of the stars was found to be the same in each filter and in the summed $J + H + K$ image. Thus, the combined image in all three filters was used so as to maximise the signal-to-noise. Radial profiles of the ten cluster candidates were extracted from the summed image, using circular annuli of 0.″3 width. A comparison of the profiles with the model PSF showed that most of the sources were resolved, with the notable exception of object A (the AGN). In order to further reduce the noise in these faint sources, the mean profile of the nine resolved objects was calculated, weighting each point with respect to the inverse-square of its error.

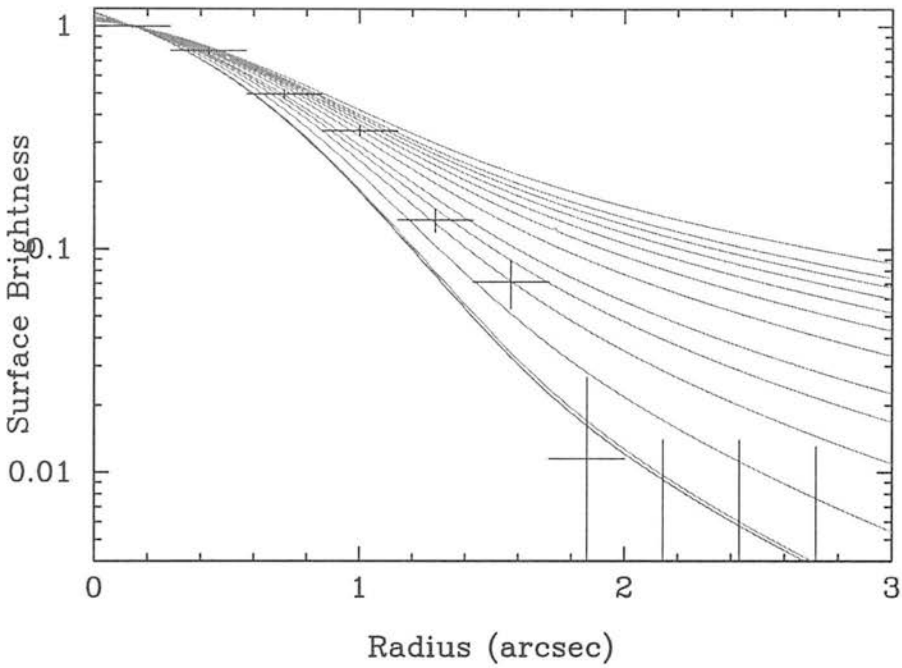

Figure 6.5 The mean surface brightness profile of the nine cluster candidates (excluding object A). The lowest line is the point spread function (PSF), the other lines are de Vaucouleurs profiles convolved with the PSF, for effective radii $r_e = 1,\ 5,\ 10\ldots100$ kpc (in steps of 10 kpc) (bottom to top). The models were caclulated for $\Omega_0 = 1$, $H_0 = 50$ km s^{-1} Mpc^{-1}.

An ensemble of galaxy profiles was calculated and convolved with the model PSF. A de Vaucouleurs profile was used, $I = I_0 \exp\{-7.67\,[\,(r/r_e)^{1/4} - 1\,]\,\}$, with effective radii of $r_e = 1\ldots100$ kpc for a cosmology of $\Omega_0 = 1$, $H_0 = 50$ km s^{-1} Mpc^{-1}. The data and the models are shown in figure 6.5. Comparing the observed profile with the models using a χ^2-fit, gave an average scale-length of $r_e = 25 \pm 15$ kpc, significantly larger than the 0.5–1.0 kpc sizes of the Lyα-selected cluster candidates (Pascarelle et al. 1996b). It can be seen from the figure that the observed mean profile is not fitted particularly well by a de Vaucouleurs model, nor is it by an exponential model. The data are too noisy in order to draw any solid conclusions about the profiles, other than the fact that the red sources are a factor of ~ 10 larger than the Pascarelle et al. objects.

To summarise, ten sources with red $J - H$ colours have been discovered around the radio galaxy 53W002, that are consistent with the presence of a 4000-Å break at the cluster redshift. The ages of the galaxies deduced from the strength of the break are consistent with a 1 Gyr burst model of galaxy evolution, observed at ages of 0.4–1.1 Gyr. With the exception of the AGN (object A), all the sources are resolved and have a significant size (~ 20 kpc). Finally it is noted that all the infrared-selected galaxies and most of the optically-selected ones lie within one arcminute (~ 0.5 Mpc) of one another, consistent with the size of a group or small cluster of galaxies.

6.5 Discussion

In this final section, the infrared view of the 53W002 group will be compared with the optical view presented by Pascarelle et al. (1996b). The results and cosmological implications will also be compared with those drawn from the radio galaxy population that has been the subject of the earlier chapters of the thesis.

Pascarelle et al. (1996b) used the WFPC2 medium-band filter F410M on the *Hubble Space Telescope* to search for redshifted Lyα emitters around 53W002 at $z = 2.390$. They found 18 possible cluster candidates, of which nine have so far been spectroscopically confirmed (Armus et al. 1999; Keel et al. 1999). The candidates are all small, faint objects that the authors call sub-galactic clumps. They suggest that these clumps are in the process of undergoing gravitational collapse and will one day merge to form one or more luminous galaxies. Only three of the Pascarelle et al. objects were detected in the infrared — both AGNs (53W002 and object A), plus object B which may also contain a weak active nucleus. Thus there is no contradiction between the optical and infrared results. If the infrared candidates *are* large, evolved galaxies in the group at $z = 2.39$ then perhaps the Lyα candidates are the "left-overs" of a recently-formed cluster. One could suppose that the majority of the mass over-density in the region has already collapsed into the red objects, leaving a remnant of smaller star-forming clouds that will most likely merge with the larger galaxies in the not too distant future.

The cosmological constraints deduced from these infrared cluster candidates are not as significant as those derived from the radio source population discussed in chapter 5, but there is still some tension between these data and a high-density universe. For $\Omega_0 = 1$ and $H_0 = 50$ km s^{-1} Mpc^{-1}, the best-fit age for the second reddest source is only just compatible with the cosmology. A larger Hubble constant would provide insufficient time for the galaxy to form (~ 1 Gyr) and then evolve to an age of 1.1 Gyr. In agreement with the results of the previous chapter, these reddest sources at $z \simeq 2.4$ favour a low-density universe.

Several cautionary notes must be made about these conclusions. If an instantaneous burst model were used, then the ages assigned to these sources would be lower and there may no longer be a conflict with an $\Omega_0 = 1$ cosmology. More importantly, the redshifts of these sources are unknown. It has been argued that there are good reasons to believe that the candidates are part of the $z \simeq 2.4$ group, but only spectroscopic confirmation of the redshifts can make these results solid.

Chapter 7

Conclusions

7.1 Summary of the thesis

The purpose of this thesis was to address two aspects of the cosmological evolution of galaxies: (i) to confirm or refute the existence of a high-redshift decline in the radio source population beyond $z \simeq 2$; and (ii) to determine if the stellar populations of radio hosts (and massive ellipticals in general) were formed at the same time as the rise in AGN activity. This final chapter will assess the extent to which the purpose has been achieved, and suggest some directions along which the project could be further developed.

An extensive programme of optical and infrared imaging of a 73-source complete sub-sample of the Leiden-Berkeley Deep Survey has been presented. With a 1 mJy flux limit at 1.4 GHz, this sample of weak radio sources promised to probe the radio luminosity function out to higher redshifts and fainter luminosities than has previously been published. Almost complete optical identifications were found for the radio sources, and deep images in $griK$ were obtained for the faintest of these objects that had not previously been identified. A comparison of the K-band magnitude distributions for the LBDS and brighter surveys, revealed that below a flux density of ~ 1 Jy the host galaxies of radio sources do not change significantly — at least with respect to their (restframe) optical/near-infrared magnitudes.

Spectroscopic observations of a sample of sources from the Parkes Selected Regions were processed, in order to reassess the accuracy of the estimated redshifts that underly the evidence for a redshift cut-off in the RLF. It was found that these sources were systematically less luminous in K than had been supposed and their redshifts had, in general, been overestimated. This result enhances the conclusions of Dunlop and Peacock (1990) that there is a decline in the number of powerful radio sources at $z \simeq 2$. The K–z diagram for the PSR sources is more consistent with the results of Eales et al. (1997) for the B2/6C survey than with the results of Lilly et al. (1985) for the brighter 3CR radio sources.

Redshifts were successfully measured for twelve sources in the LBDS Hercules field, bringing the redshift content to 67%. Photometric redshifts were estimated for the remainder of the sample, by fitting a model template spectrum to the observed magnitudes. The observed radio luminosity function was then calculated and compared with the models of Dunlop and Peacock (1990). Two of the models (FF-4 and FF-5) produced reasonable fits to the data, although there was some disagreement between the luminosity-dependence of the data and models. That uncertainty aside, the agreement between the redshift-dependence of the two models and the data appears to confirm the reality of the redshift cut-off at lower radio luminosities than had previously been established. The models predict a cut-off at $z \simeq 1$–2, and there was some evidence in the *observed* RLF of the LBDS sources that the luminosity function may in fact turn over at even lower redshifts, $z \simeq 0.5$–1.

An analysis of the optical and infrared Hubble diagrams, and the $r - K$ colours of the LBDS radio sources enabled several conclusions to be made about the spectral evolution of the sources. It was found that the reddest galaxies at $z \sim 0.7$ can only be formed in a universe that is $\gtrsim 12$ Gyr-old at the present day. Together with limits on the age of the universe at $z \simeq 1.5$ derived from model fitting to the two oldest galaxies observed at high-redshift, these results presented serious problems for a critical density universe. In particular, for a Hubble constant of 65 km s^{-1} Mpc^{-1}, the data either require a low density $\Omega_0 \lesssim 0.2$, or for a critical universe a cosmological constant with $\Omega_\Lambda \gtrsim 0.6$ is necessary. The reddest sources believed to be in a group at $z \simeq 2.4$ were consistent with these conclusions.

With regard to the aims of the thesis, the existence of a cut-off in the radio luminosity function at high-redshift has been tentatively confirmed, although there is still significant uncertainty about the redshift(s) at which this occurs. The reddest of the sources must have formed at very high redshifts and for these objects it does not appear that the rise in AGN activity is associated with the formation of the host galaxy, or at least with the formation of the first stars. It is possible that the stars formed in sub-galactic clumps very early in the universe and that the rise in AGN activity followed the merger of these clumps into massive galaxies (compare the results of Pascarelle et al. 1996b).

7.2 Future prospects

The best method of placing the reality of the redshift cut-off on a more secure basis will be to recalculate the radio luminosity function models. Prior to doing so, the low-luminosity database can be further improved by using the full LBDS survey. The difficulties with using the full survey were pointed out in §4.4.2 — although the data is now available to complete the optical identifications of the full sample, less than half the sources have spectroscopic observations and even fewer have infrared data. Reliable photometric redshifts are harder to calculate in the absence of at least one infrared band, thus the redshift distribution of the whole survey will be of much poorer quality than that of the Hercules sub-sample. The uncertainty in the observed RLF will be greater for this reason, however the much larger number of sources will reduce the statistical errors in calculating the RLF. The net effect may be to produce an RLF that is no more uncertain than that presented in chapter 4. Combining the LBDS survey with the sample used by Dunlop and Peacock (1990), after appropriate scaling to a common frequency, will produce a much more complete dataset than was available to Dunlop and Peacock. One hopes that the new dataset will have sufficient depth, area and luminosity coverage that the issue of the high-redshift decline in the RLF can be unambiguously settled.

The second major improvement to the work presented here, will be to make a more thorough investigation of the spectral evolution of these sources. The high-metallicity models used in chapter 5 require further analysis to determine if they are really necessary — although they appear to be the simplest way to fit the optical–infrared colours that does not mean they are the most physical. Certainly at the highest redshifts, the metallicity must decrease as it takes several generations of stars to build up the metal content of the interstellar medium. The second improvement to the spectral evolution models would be to develop a more realistic star formation history, rather than the instantaneous burst. It is possible to combine the Jimenez et al. (1999) synthetic stellar populations in such a way as to model any desired star formation rate, be it continuous, exponentially-decaying or whatever. A more ambitious approach would be to consider populations of evolving or mixed metallicity.

Now that this sample has been prepared, there are likely to be many scientific questions that it can be used to answer. It is currently one of the most complete radio-selected samples available, in terms of optical and infrared identifications, and redshift content (particularly when the photometric estimates are included). Hopefully it will be widely used.

Bibliography

Allington-Smith, J. R.: 1982, *Mon. Not. R. Astron. Soc.* **199**, 611

Allington-Smith, J. R., Peacock, J. A., and Dunlop, J. S.: 1991, *Mon. Not. R. Astron. Soc.* **253**, 287

Arimoto, N. and Yoshii, Y.: 1987, *Astron. Astrophys.* **173**, 23

Armus, L. et al.: 1999, *Astrophys. J.*, in preparation

Avni, Y. and Bahcall, J. N.: 1980, *Astrophys. J.* **235**, 694

Avni, Y. and Schiller, N.: 1983, *Astrophys. J.* **267**, 1

Baum, W. A.: 1962, in G. C. McVittie (ed.), *I. A. U. Symp. 15, Problems of Extra-galactic Research*, p. 390, MacMillan, New York

Bennett, C. L. et al.: 1996, *Astrophys. J., Lett.* **464**, L1

Berry, M. V.: 1989, *Principles of Cosmology and Gravitation*, IOP Publishing Ltd

Brunner, R. J., Connolly, A. J., and Szalay, A. S.: 1997, *Astrophys. J., Lett.* **482**, L21

Bruzual, G.: 1983, *Astrophys. J.* **273**, 105

Bruzual, G. and Charlot, S.: 1993, *Astrophys. J.* **405**, 538

Bruzual, G. and Magris, G.: 1997, in *Cosmological Parameters and Evolution of the Universe*, IAU Symp. 183, Kyoto, Japan, p. 56

Bruzual, G. and Magris, G.: 1999, *Astrophys. J., Lett.*, submitted

Charlot, S., Worthey, G., and Bressan, A.: 1996, *Astrophys. J.* **457**, 625

Cheng, E. S.: 1994, in J. M. Pasachoff et al. (eds.), *The Farthest Things in the Universe*, Cambridge University Press

Connolly, A. J., Csabai, I., Szalay, A. S., Koo, D. C., Kron, R. G., and Munn, J. A.: 1995, *Astron. J.* **110**, 2655

Connolly, A. J., Szalay, A. S., Dickinson, M., SubbaRao, M. U., and Brunner, R. J.: 1997, *Astrophys. J., Lett.* **486**, L11

Currie, M. J.: 1998, *KAPPA — Kernel Application Package (SUN/95.12)*, Starlink Project, Rutherford Appleton Laboratory

Dey, A.: 1997, in N. Tanvir, A. Aragón-Salamanca, and J. V. Wall (eds.), *The Hubble Space Telescope and the High Redshift Universe*, p. 373, World Scientific

Dicke, R. H., Peebles, P. J. E., Roll, P. G., and Wilkinson, D. T.: 1965, *Astrophys. J.* **142**, 414

Dickinson, M.: 1995, in H. Hippelein, K. Meisenheimer, and H.-J. Röser (eds.), *Galaxies in the Young Universe*, p. 144, Springer-Verlag, Berlin

Dickinson, M.: 1997, in N. Tanvir, A. Aragón-Salamanca, and J. V. Wall (eds.), *The Hubble Space Telescope and the High Redshift Universe*, p. 207, World Scientific

Donnelly, R. H., Partridge, R. B., and Windhorst, R. A.: 1987, *Astrophys. J.* **321**, 94

Downes, A. J. B., Peacock, J. A., Savage, A., and Carrie, D. R.: 1986, *Mon. Not. R. Astron. Soc.* **218**, 31

Draper, P. W. and Eaton, N.: 1996, *PISA – Position Intensity and Shape Analysis (SUN/109.8)*, Starlink Project, Rutherford Appleton Laboratory

Driver, S. P., Fernandez, A., Couch, W. J., Odewahn, S. C., Windhorst, R. A., Phillipps, S., Lanzetta, K., and Yahil, A.: 1998, *Astrophys. J., Lett.* **496**, L93

Driver, S. P., Windhorst, R. A., Phillipps, S., and Bristow, P. D.: 1996, *Astrophys. J.* **461**, 525

Dunlop, J. S.: 1997, in N. Jackson and R. Davis (eds.), *High Sensitivity Radio Astronomy*, p. 167, Cambridge University Press

Dunlop, J. S.: 1999, in H. J. A. Röttgering, P. Best, and M. D. Lehnert (eds.), *The Most Distant Radio Galaxies*, Proceedings of the Royal Netherlands Academy of Sciences, in press, Kluwer, Dordrecht

Dunlop, J. S., Guiderdoni, B., Rocca-Volmerange, B., Peacock, J. A., and Longair, M. S.: 1989a, *Mon. Not. R. Astron. Soc.* **240**, 257

Dunlop, J. S. and Peacock, J. A.: 1990, *Mon. Not. R. Astron. Soc.* **247**, 19 (DP90)

Dunlop, J. S. and Peacock, J. A.: 1993, *Mon. Not. R. Astron. Soc.* **263**, 936

Dunlop, J. S., Peacock, J. A., Savage, A., Lilly, S. J., Heasley, J. N., and Simon, A. J. B.: 1989b, *Mon. Not. R. Astron. Soc.* **238**, 1171

Dunlop, J. S., Peacock, J. A., Spinrad, H., Dey, A., Jimenez, R., Stern, D., and Windhorst, R. A.: 1996, *Nature* **381**, 581

Eales, S., Rawlings, S., Law-Green, D., Cotter, G., and Lacy, M.: 1997, *Mon. Not. R. Astron. Soc.* **291**, 593

Eales, S. A.: 1985, *Mon. Not. R. Astron. Soc.* **217**, 149

Eales, S. A., Rawlings, S., Puxley, P. J., Rocca-Volmerage, B., and Kuntz, K.: 1993, *Nature* **363**, 140

Efsthathiou, G.: 1990, in J. A. Peacock, A. F. Heavens, and A. T. Davies (eds.), *Physics of the Early Universe*, Proceedings of the 36th Scottish Universities Summer School in Physics, p. 361, SSUSP Publications

Ellis, R. S.: 1997, *Ann. Rev. Astron. Astrophys.* **35**, 389

Faber, S. M. and Jackson, R. E.: 1976, *Astrophys. J.* **204**, 668

Fanelli, M. N., O'Connell, R. W., Burstein, D., and Wu, C.: 1992, *Astrophys. J., Suppl. Ser.* **82**, 197

Fernández-Soto, A., Lanzetta, K. M., and Yahil, A.: 1999, *Astrophys. J.*, submitted

Francis, P. J., Woodgate, B. E., and Danks, A. C.: 1997, *Astrophys. J., Lett.* **482**, L25

Francis, P. J., Woodgate, B. E., and Danks, A. C.: 1998, in S. D'Odorico, A. Fontana, and E. Giallongo (eds.), *The Young Universe: Galaxy Formation and Evolution at Intermediate and*

High Redshift, A. S. P. Conference Series, Volume 146, pp 496–503, Astronomical Society of the Pacific

Freedman, W. L. et al.: 1994, *Nature* **371**, 757

Green, R. F.: 1989, in C. S. Frenk, R. S. Ellis, T. Shanks, A. F. Heavens, and J. A. Peacock (eds.), *The Epoch of Galaxy Formation*, NATO ASI Series C vol. 264, p. 121, Kluwer Academic Publishers

Gregory, P. C. and Condon, J. J.: 1991, *Astrophys. J., Suppl. Ser.* **75**, 1011

Guiderdoni, B. and Rocca-Volmerange, B.: 1987, *Astron. Astrophys.* **186**, 1

Gunn, J. E. and Peterson, B. A.: 1965, *Astrophys. J.* **142**, 1663

Gwyn, S. D. J. and Hartwick, F. D. A.: 1996, *Astrophys. J., Lett.* **468**, L77

Hall, P. B., Osmer, P. S., Green, R. F., Porter, A. C., and Warren, S. J.: 1996, *Astrophys. J.* **462**, 614

Hamuy, M., Phillips, M. M., Suntzeff, N. B., Schommer, R. A., Maza, J., and Aviles, R.: 1996, *Astron. J.* **112**, 2398

Hartwick, F. D. A. and Schade, D.: 1990, *Ann. Rev. Astron. Astrophys.* **28**, 437

Helling, C., Jørgensen, U. G., Plez, B., and Johnson, H. R.: 1996, *Astron. Astrophys.* **315**, 194

Henden, A. A. and Kaitchuck, R. H.: 1982, *Astronomical Photometry*, Van Nostrand Reinhold Company Inc

Hogg, D. W. et al.: 1998, *Astron. J.* **115**, 1418

Hu, E. M., McMahon, R. G., and Egami, E.: 1996, *Astrophys. J., Lett.* **459**, L53

Hubble, E.: 1929, *Proc. Nat. Acad. Sci.* **15**, 168

Humason, M. L., Mayall, N. U., and Sandage, A. R.: 1956, *Astron. J.* **61**, 97

Impey, C.: 1998, in S. D'Odorico, A. Fontana, and E. Giallongo (eds.), *The Young Universe: Galaxy Formation and Evolution at Intermediate and High Redshift*, A. S. P. Conference Series, Volume 146, pp 391–396, Astronomical Society of the Pacific

Jimenez, R., Dunlop, J. S., Peacock, J. A., Padoan, P., MacDonald, J., and Jørgensen, U. G.: 1999, *Mon. Not. R. Astron. Soc.*, submitted

Keel, W. C. et al.: 1999, *Astrophys. J.*, in preparation

Keel, W. C. and Windhorst, R. A.: 1993, *Astron. J.* **106**, 455

Kim, A. G. et al.: 1997, *Astrophys. J., Lett.* **476**, L63

Kochanek, C. S.: 1996, *Astrophys. J.* **466**, 638

Koo, D. C.: 1985, *Astron. J.* **90**, 418

Koo, D. C. and Kron, R. G.: 1982, *Astron. Astrophys.* **105**, 107

Kron, R. G.: 1980, *Astrophys. J., Suppl. Ser.* **43**, 305

Kron, R. G., Koo, D. C., and Windhorst, R. A.: 1985, *Astron. Astrophys.* **146**, 38

Kurucz, R. L.: 1992, in B. Barbuy and A. Renzini (eds.), *The Stellar Populations of Galaxies*, IAU Symposium 149, p. 225, Kluwer, Dordrecht

Lacy, M. D. and Rawlings, S.: 1996, *Mon. Not. R. Astron. Soc.* **280**, 888

Laing, R. A., Riley, J. M., and Longair, M. S.: 1983, *Mon. Not. R. Astron. Soc.* **204**, 151

Lanzetta, K. M.: 1991, *Astrophys. J.* **375**, 1

Lanzetta, K. M., Yahil, A., and Fernández-Soto, A.: 1996, *Nature* **381**, 759

Leavitt, H. S.: 1912, *Harvard College Obs. Circ.* **173**, 1

Lewis, G. and Irwin, M.: 1997, *Spectrum: Newsletter of the Royal Greenwich Observatory, Royal Observatory Edinburgh, and the Isaac Newton Group, La Palma* **12**, 22

Lilly, S. J.: 1989, *Astrophys. J.* **340**, 77

Lilly, S. J., Le Fevre, O., Crampton, D., Hammer, F., and Tresse, L.: 1995, *Astrophys. J.* **455**, 50

Lilly, S. J. and Longair, M. S.: 1984, *Mon. Not. R. Astron. Soc.* **211**, 833

Lilly, S. J., Longair, M. S., and Allington-Smith, J. R.: 1985, *Mon. Not. R. Astron. Soc.* **215**, 37

Loh, E. D. and Spillar, E. J.: 1986, *Astrophys. J.* **303**, 154

Longair, M. S.: 1984, *Theoretical Concepts in Physics*, Cambridge University Press

Madau, P., Pozzetti, L., and Dickinson, M.: 1998, *Astrophys. J.* **498**, 116

Maddox, S. J., Efstathiou, G., Sutherland, W. J., and Loveday, J.: 1990, *Mon. Not. R. Astron. Soc.* **242**, 43P

Malkan, M. A., Teplitz, H., and McLean, I. S.: 1996, *Astrophys. J., Lett.* **468**, L9

Mather, J. C. et al.: 1990, *Astrophys. J., Lett.* **354**, L37

McCarthy, P. J.: 1993, *Ann. Rev. Astron. Astrophys.* **31**, 639

McCarthy, P. J., van Breugel, W. J. M., Spinrad, H., and Djorgovski, S. G.: 1987, *Astrophys. J., Lett.* **321**, L29

Metcalfe, N., Shanks, T., Campos, A., Gardner, J. P., and Fong, R.: 1996, *Nature* **210**, 10

Mobasher, B., Rowan-Robinson, M., Georgakakis, A., and Eaton, N.: 1996, *Mon. Not. R. Astron. Soc.* **282**, L7

Mould, J. R. et al.: 1991, *Astrophys. J.* **383**, 467

Navarro, J. F., Frenk, C. S., and White, S. D. M.: 1995, *Mon. Not. R. Astron. Soc.* **275**, 56

Neuschaefer, L. W.: 1992, *The Angular Two-point Correlation Function of Galaxies Down to 25th Mag*, PhD Thesis, Arizona State University

Neuschaefer, L. W. and Windhorst, R. A.: 1995a, *Astrophys. J.* **439**, 14

Neuschaefer, L. W. and Windhorst, R. A.: 1995b, *Astrophys. J., Suppl. Ser.* **96**, 371

Neuschaefer, L. W., Windhorst, R. A., and Dressler, A.: 1991, *Astrophys. J.* **382**, 32

Oort, M. J. A.: 1988, *Astron. Astrophys.* **193**, 5

Oort, M. J. A., Katgert, P., Steeman, F. W. M., and Windhorst, R. A.: 1987, *Astron. Astrophys.* **179**, 41

Oort, M. J. A., Steemers, W. J. G., and Windhorst, R. A.: 1988, *Astron. Astrophys. Suppl. Ser.* **73**, 103

Osmer, P. S. and Smith, M. G.: 1980, *Astrophys. J., Suppl. Ser.* **42**, 333

Ostriker, J. P.: 1993, *Ann. Rev. Astron. Astrophys.* **31**, 689

Padovani, P. and Urry, C. M.: 1992, *Astrophys. J.* **387**, 449

Pascarelle, S. M., Windhorst, R. A., Driver, S. P., Ostrander, E. J., and Keel, W. C.: 1996a, *Astrophys. J., Lett.* **456**, L21

Pascarelle, S. M., Windhorst, R. A., Keel, W. C., and Odewahn, S. C.: 1996b, *Nature* **383**, 45

Peacock, J. A.: 1985, *Mon. Not. R. Astron. Soc.* **217**, 601

Peacock, J. A. and Gull, S. F.: 1981, *Mon. Not. R. Astron. Soc.* **196**, 611

Peacock, J. A., Jimenez, R., Dunlop, J. S., Waddington, I., Spinrad, H., Stern, D., Dey, A., and Windhorst, R. A.: 1998, *Mon. Not. R. Astron. Soc.* **296**, 1089

Peebles, P. J. E.: 1988, *Astrophys. J.* **332**, 17

Peebles, P. J. E.: 1993, *Principles of Physical Cosmology*, Princeton University Press

Penzias, A. A. and Wilson, R. W.: 1965, *Astrophys. J.* **142**, 419

Perlmutter, S. et al.: 1997, *Astrophys. J.* **483**, 565

Pierce, M. J., Welch, D. L., McClure, R. D., van den Bergh, S., Racine, R., and Stetson, P. B.: 1994, *Nature* **371**, 385

Press, W. H., Teukolsky, S. A., Vetterling, W. T., and Flannery, B. P.: 1992, *Numerical Recipes in Fortran 77: The Art of Scientific Computing*, Cambridge University Press, 2nd edition

Rawlings, S., Saunders, R., Eales, S., and Mackay, C.: 1989, *Mon. Not. R. Astron. Soc.* **240**, 701

Richards, E. A., Kellermann, K. I., Fomalont, E. B., Windhorst, R. A., and Partridge, R. B.: 1998, *Astron. J.* **116**, 1039

Roche, N., Eales, S., and Rawlings, S.: 1998, *Mon. Not. R. Astron. Soc.* **297**, 405

Rowan-Robinson, M. M.: 1968, *Mon. Not. R. Astron. Soc.* **138**, 445

Sandage, A. R.: 1968, *Astrophys. J., Lett.* **152**, L149

Sandage, A. R.: 1988, *Ann. Rev. Astron. Astrophys.* **26**, 561

Sandage, A. R., Saha, A., Tammann, G. A., Labhardt, L., Panagia, N., and Macchetto, F. D.: 1996, *Astrophys. J., Lett.* **460**, L15

Sawicki, M. J., Lin, H., and Yee, H. K. C.: 1997, *Astron. J.* **113**, 1

Schmidt, M.: 1968, *Astrophys. J.* **151**, 393

Schutz, B. F.: 1990, *A First Course in General Relativity*, Cambridge University Press

Scoville, N. Z., Yun, M. S., Windhorst, R. A., Keel, W. C., and Armus, L.: 1997, *Astrophys. J., Lett.* **485**, L21

Shortridge, K., Meyerdierks, H., Currie, M., Lockley, M. C. J., Charles, A., and Davenhall, C.: 1997, *FIGARO - A general data reduction system (SUN/86.15)*, Starlink Project, Rutherford Appleton Laboratory

Slipher, V. M.: 1917, *Proc. Amer. Phil. Soc.* **56**, 403

Smoot, G. F. et al.: 1992, *Astrophys. J., Lett.* **396**, L1

Spinrad, H.: 1986, *Publ. Astron. Soc. Pac.* **98**, 269

Spinrad, H., Dey, A., Stern, D., Dunlop, J. S., Peacock, J. A., Jimenez, R., and Windhorst, R. A.: 1997, *Astrophys. J.* **484**, 581

Spinrad, H. and Djorgovski, S. G.: 1987, in A. Hewitt, G. Burbidge, and L. Z. Fang (eds.), *Observational Cosmology*, Proc. IAU Symp. No. 124, p. 129, Reidel Publishing

Spinrad, H., Djorgovski, S. G., Marr, J., and Aguilar, L. A.: 1985, *Publ. Astron. Soc. Pac.* **97**, 932

Steidel, C. C., Giavalisco, M., Dickinson, M., and Adelberger, K. L.: 1996a, *Astron. J.* **112**, 352

Steidel, C. C., Giavalisco, M., Pettini, M., Dickinson, M., and Adelberger, K. L.: 1996b, *Astrophys. J., Lett.* **462**, L17

Steidel, C. C., Pettini, M., and Hamilton, D.: 1995, *Astron. J.* **110**, 2519

Stevens, R., Lacy, M., and Rawlings, S.: 1998, in S. D'Odorico, A. Fontana, and E. Giallongo (eds.), *The Young Universe: Galaxy Formation and Evolution at Intermediate and High Redshift*, A. S. P. Conference Series, Volume 146, pp 225–228, Astronomical Society of the Pacific

Strauss, M. A., Davis, M., Yahil, A., and Huchra, J. P.: 1992, *Astrophys. J.* **385**, 421

Tanvir, N. R., Shanks, T., Ferguson, H. C., and Robinson, D. R. T.: 1995, *Nature* **377**, 27

Thuan, T. X., Windhorst, R. A., Puschell, J. J., Isaacman, R. B., and Owen, F. N.: 1984, *Astrophys. J.* **285**, 515

Tody, D.: 1993, in R. J. Hanisch, R. J. V. Brissenden, and J. Barnes (eds.), *Astronomical Data Analysis Software and Systems II*, A. S. P. Conference Series, Vol. 52, p. 173, Astronomical Society of the Pacific

Tully, R. B. and Fisher, J. R.: 1977, *Astron. Astrophys.* **54**, 661

Urry, C. M. and Padovani, P.: 1995, *Publ. Astron. Soc. Pac.* **107**, 803

Wagoner, R. V.: 1973, *Astrophys. J.* **179**, 343

Walker, T. P., Steigman, G., Schramm, D. N., Olive, K. A., and Kang, H.: 1991, *Astrophys. J.* **376**, 51

Wall, J. V., Shimmins, A. J., and Merkelijn, J. K.: 1971, *Aust. J. Phys. Astrophys. Suppl.* **19**, 1

Wallace, P. T.: 1994, *ASTROM — Basic astrometry program (SUN/5.14)*, Starlink Project, Rutherford Appleton Laboratory

Weinberg, S.: 1993, *The First Three Minutes*, Flamingo/Harper–Collins

White, M. and Bunn, T.: 1995, *Astrophys. J.* **450**, 477

White, M., Scott, D., and J., S.: 1994, *Ann. Rev. Astron. Astrophys.* **32**, 319

Williams, R. E. et al.: 1996, *Astron. J.* **112**, 1335

Windhorst, R. A.: 1984, *Faint Radio Galaxy Populations*, PhD Thesis, University of Leiden

Windhorst, R. A., Burstein, D., Mathis, D. F., Neuschaefer, L. W., Bertola, F., Buson, L. M., Koo, D. C., Matthews, K., Barthel, P. D., and Chambers, K. C.: 1991, *Astrophys. J.* **380**, 362

Windhorst, R. A., Fomalont, E. B., Partridge, R. B., and Lowenthal, J. D.: 1993, *Astrophys. J.* **405**, 498

Windhorst, R. A., Gordon, J. M., Pascarelle, S. M., Schmidtke, P. C., Keel, W. C., Burkey, J. M., and Dunlop, J. S.: 1994, *Astrophys. J.* **435**, 577

Windhorst, R. A., Keel, W. C., and Pascarelle, S. M.: 1998, *Astrophys. J., Lett.* **494**, L27

Windhorst, R. A., Kron, R. G., and Koo, D. C.: 1984a, *Astron. Astrophys. Suppl. Ser.* **58**, 39

Windhorst, R. A., Mathis, D., and Neuschaefer, L.: 1990, in R. G. Kron (ed.), *Evolution of the Universe of Galaxies*, Conference Series Vol. 10, pp 389–403, Astronomical Society of the Pacific

Windhorst, R. A., Mathis, D. F., and Keel, W. C.: 1992, *Astrophys. J., Lett.* **400**, L1

Windhorst, R. A., Miley, G. K., Owen, F. N., Kron, R. G., and Koo, D. G.: 1985, *Astrophys. J.* **289**, 494

Windhorst, R. A., Pascarelle, S. M., and Keel, W. C.: 1996, in R. Bender and R. L. Davies (eds.), *New Light on Galaxy Evolution*, IAU Symp. 171, p. 474, Kluwer, Dordrecht

Windhorst, R. A., van Heerde, G. M., and Katgert, P.: 1984b, *Astron. Astrophys. Suppl. Ser.* **58**, 1

Windhorst, R. A. and Waddington, I.: 1999, in B. Guiderdoni et al. (eds.), *The Birth of Galaxies: Proceedings of the Xth Rencontres de Blois*, in press

Wolfe, A. M. and Prochaska, J. X.: 1998, *Astrophys. J., Lett.* **494**, L15

Worthey, G.: 1994, *Astrophys. J., Suppl. Ser.* **95**, 107

Yamada, T., Ohta, K., Tomita, A., and Takata, T.: 1995, *Astron. J.* **110**, 1564

Yoshii, Y. and Takahara, F.: 1988, *Astrophys. J.* **326**, 1